Pulsars and transients survey, and exoplanet search at low-frequencies with the UTR-2 radio telescope: methods and first results

Iaroslavna Vasylieva

École Doctorale d'Astronomie et d'Astrophysique
d'Île De France

PHD THESIS

to obtain the title of

PhD of Science of Paris Observatory
Specialty: Astronomy, Asprophysics

by

Iaroslavna Vasylieva

Pulsars and transients survey, and exoplanet search at low-frequencies with the UTR-2 radio telescope: methods and first results

prepared at Paris Observatory, LESIA

defended on the 7th of December 2015

Jury :

President :	Didier Pelat	-	LUTh (Meudon)
Reviewers :	Dmytro Lupishko	-	KhNU (Kharkov)
	Roman Motiyenko	-	PhLAM (Lille)
	Lilian Martin	-	Subatech (Nantes)
Examinators :	Michel Tagger	-	LPC2E (Orleans)
	Gilles Theureau	-	LPC2E (Orleans)
Advisors :	Vyacheslav Zakharenko	-	IRA NASU (Kharkov)
	Philippe Zarka	-	LESIA (Meudon)

École Doctorale d'Astronomie et d'Astrophysique
d'Île De France

THÈSE

présentée pour obtenir le grade de

Docteur de l'Observatoire de Paris
Spécialité : Astronomie, Astrophysique

par

Iaroslavna Vasylieva

Recherche de pulsars, transitoires et exoplanètes à basses fréquences avec le radiotélescope UTR-2: méthodes et premiers résultats

préparée à l'Observatoire de Paris, LESIA

soutenue le 7 Décembre 2015 devant le jury composé de

Jury :

Président du jury:	Didier Pelat	-	LUTh (Meudon)
Rapporteurs:	Dmytro Lupishko	-	KhNU (Kharkov)
	Roman Motiyenko	-	PhLAM (Lille)
	Lilian Martin	-	Subatech (Nantes)
Examinateurs :	Michel Tagger	-	LPC2E (Orléans)
	Gilles Theureau	-	LPC2E (Orléans)
Directeurs de thèse:	Vyacheslav Zakharenko	-	IRA NASU (Kharkov)
	Philippe Zarka	-	LESIA (Meudon)

Contents

List of Figures

Acknowledgements

Many thanks for my super-patient supervisors Philippe Zarka and Vyacheslav Zakharenko, for their guidance in science and often in life.
Thanks to Vladimir Ryabov for his help on statistics.
I am infinitely grateful to all colleagues for their invaluable advices and supportive attitude.

Chapter 1

Introduction

Contents

Transient phenomena such as outbursts or variability of cosmic sources at different time scales gave birth to a new branch of astronomy, interested in time-variable phenomena. This new science is studying the cosmic objects as they change. The timescale of such changes varies from nanoseconds to tens of years. All these are relatively short time scales in astronomical terms. Such dynamic events shade light on the variety of physical processes that occur at a range of distances: from cosmic ray showers in the Earth's atmosphere, to gamma-ray bursts from distant galaxies.

1.1 Transient radio sources

Studying transients in radio is promising due to the high time and frequency resolutions of the data acquisition equipment and large instantaneous fields of view provided by the digital beam forming systems of modern radio telescopes. Multiple discoveries of the recent years suggest that there might be many new sources and even new types of sources, available for observations in radio.

On Earth we see the impacts of ultra-high energy particles with the atmospheric atoms, producing intense radio emission [Weekes 2001, Falcke 2003].

In our Solar System examples of transient radio events are solar and Jovian bursts, auroral emissions of the planets and planetary lightning. In the galactic neighbourhood we might be able to detect the radio emissions of magnetized extrasolar planets [Zarka 1997, Farrell 1999, Zarka 2001, Grießmeier 2007]. Flare stars with large magnetic fields exhibit strong radio flares, detectable at radio wavelenghts, similar to solar ones but much more intense. Neutron stars are probably the most numerous and varied class of transient sources in the Galaxy (see the next subsection).

The extragalactic events that produce or might produce detectable radio transients include the elusive fast radio bursts [Lorimer 2007], gamma-ray burst after-

glows, [Usov 2000, Sagiv 2002], supernovae [Colgate 1971], annihilating black holes [Rees 1977] and active galactic nuclei [Aller 1985].

Fig. 1.1 shows representative transient sources of various classes in the so-called 'transient phase space'.

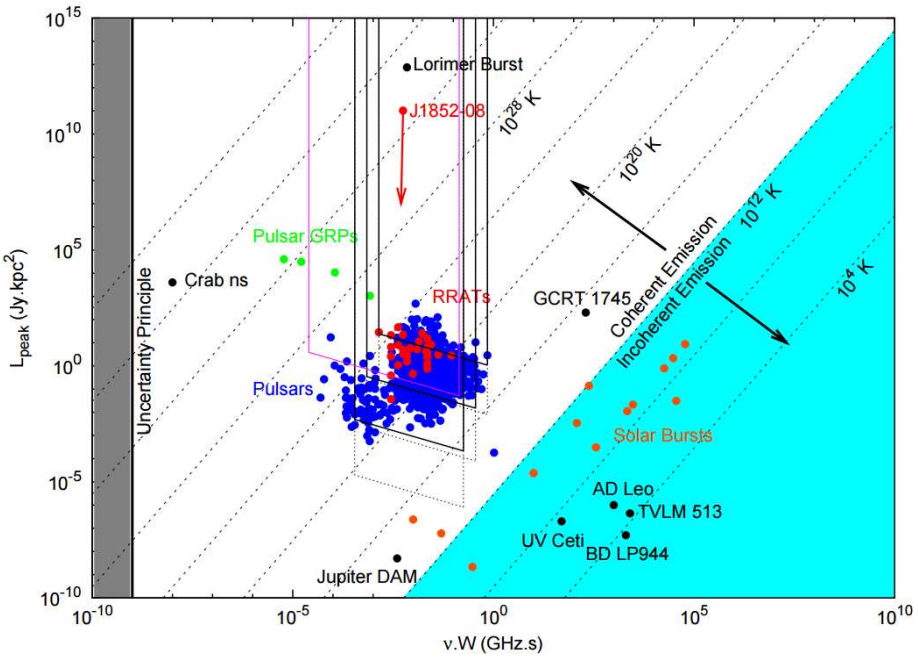

Figure 1.1: Transient phase space [Keane 2011]. Various kinds of transients are plotted versus their energetics. 'Crab ns' stands for nanosecond giant pulses from the Crab pulsar [Hankins 2007]; 'Pulsar GRPs' are pulsar giant radio pulses [Cognard 1996]; 'Lorimer Burst' is the first detected fast radio burst [Lorimer 2007]; the lower right part shows flare stars [Jackson 1989]. The abscissa is the product of emission frequency and duration of a transient event, the ordinate is the intrinsic luminosity, which is the product of flux density and distance to the object squared. These values are related to the brightness temperature T. Lines of constant brightness temperature are shown. The boundary between coherent and incoherent emission mechanisms corresponds approximately to $T = 10^{12}$ K. Sensitivities of the LOw Frequency ARray (LOFAR) to individual pulses from 2 kpc distance (pink box), the Square Kilometer Array (SKA, in project) from 0.1, 1 and 10 kpc (dotted boxes) and the Parkes radio telescope (black boxes) are shown.

1.2 Neutron stars and their radio emissions

Neutron stars are rapidly rotating super-dense remnants of massive stars with strong magnetic fields. It is currently considered that most of them manifest themselves

as radio pulsars that emit strictly periodic pulses across the entire radio spectrum, from decameter [Bruk 1976, Bruk 1977, Zakharenko 2013] to millimeter waves [Morris 1997]. The effect of pulsation can be interpreted as the rotating beam of a lighthouse that turns on when it points to the observer and off when it turns aside. Neutron stars are thought to emit cones of broadband electromagnetic emission from the regions of open field lines near their magnetic poles (Fig. 1.2). Due to their rotation and the misalignment of magnetic and rotation axes, we see the on-pulse emission once per rotation period, when one of the cones emits towards Earth, and off-pulse emission otherwise.

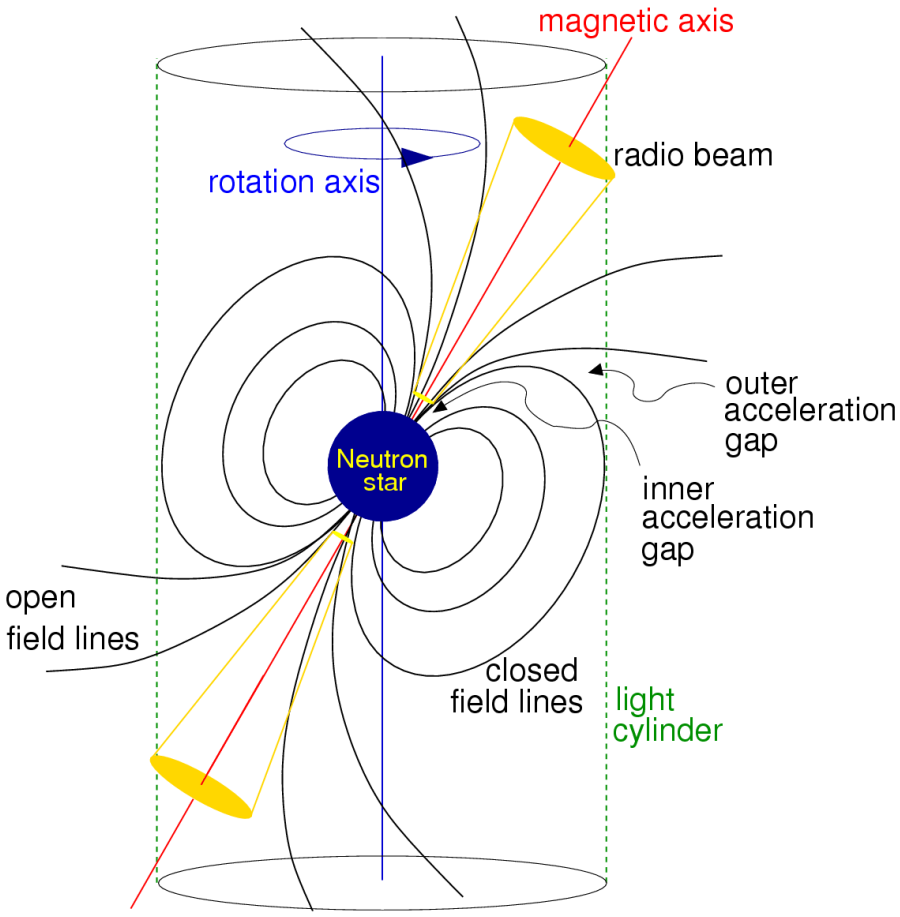

Figure 1.2: Emission model of a neutron star.

Depending on the pulsar orientation, we might see it as a continuum source (when the radiation cone is directed to Earth all the time), as a regular pulsar (when only one of the cones hits the Earth), a pulsar with an interpulse

(when both cones hit the Earth), or not see it at all. Predictions suggest [Vranesevic 2004, Lorimer 2006, Faucher-Giguère 2006] that there should be about 100000 radioemitting neutron stars in our Galaxy, one fifth of which might be favourably oriented so that their radio emission beam points towards Earth for a fraction of their rotation period.

Known pulsar periods range from 1.4 ms to 11.7 s, making two peaks on the histogram of periods (Fig. 1.3). The smaller peak corresponds to millisecond pulsars (MSPs), that are thought to be older than regular pulsars and form a separate population of neutron stars in binary systems.

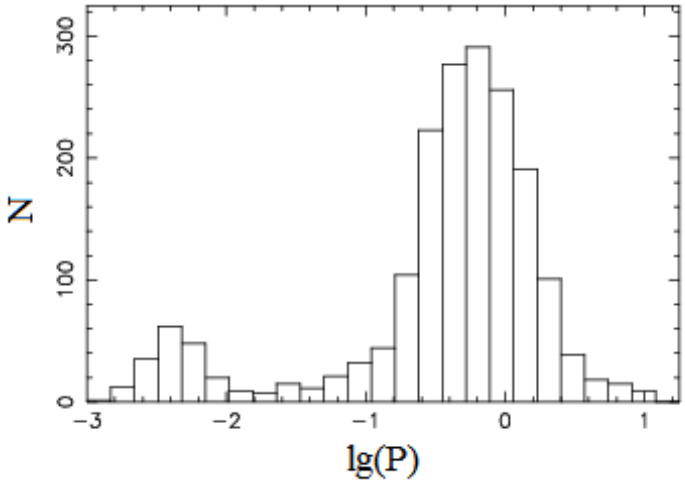

Figure 1.3: Histogram of pulsar periods. The bigger peak corresponds to slow pulsars, the smaller peak to millisecond (recycled) pulsars.

Periods of regular pulsars slowly increase with time, mainly due to losses of rotational energy through electromagnetic emission. The rate of period increase, called the period derivative, directly points to the age of the pulsar. Similar to normal stars, pulsars have an evolution diagram (Fig. 1.4), called "P - Pdot" (or Period-Period derivative) diagram.

Normal pulsars form the largest group on that diagram, the millisecond pulsars form a smaller separate group in the region of small periods. Other groups of neutron stars will be discussed later. Remarkably, there are no detectable objects in the lower right corner. This area is limited by a 'death line'. As the pulsar evolves, it moves lower and to the right in this diagram (i.e. its age and period increase and magnetic field decreases). Eventually the pulsar reaches the death line, where its magnetic field becomes too weak to sustain strong radio emission and thus to slow down the rotation.

The typical spectrum of a regular pulsar is steep, following a power law f^{α}, where f is the frequency and typically $\alpha \in [-4, 0]$ with a mean value $\alpha_{mean} = -1.8$ [Maron 2000]. Usually it reaches a maximum at frequencies between 100 and 200

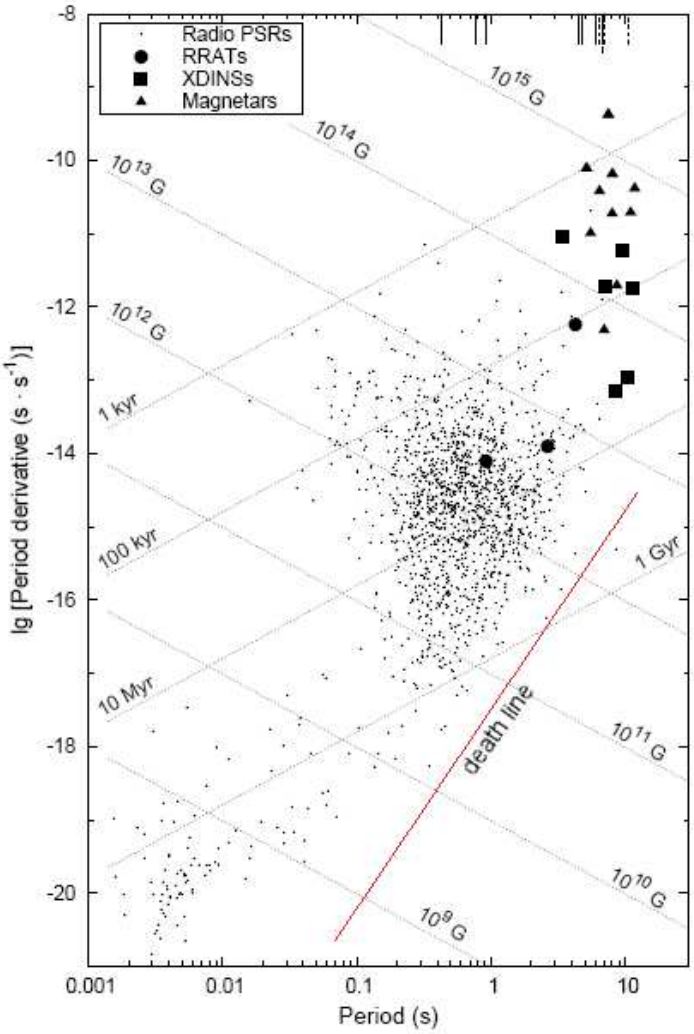

Figure 1.4: Period-period derivative diagram ('P - Pdot'). Regular pulsars form a cluster in the right part of the diagram. Millisecond pulsars are concentrated in the lower left corner. Sloppy lines show the ages and magnetic fields of the neutron stars. This diagram is often used to describe evolution of neutron stars. As a pulsar gets older, it moves to the bottom and to the right in this diagram and eventually crosses the death line. [Kondratiev 2009]

MHz [Kuz'min 1978, Slee 1986, Malofeev 1994] and sharply decreases towards lower frequencies (Fig. 1.5).

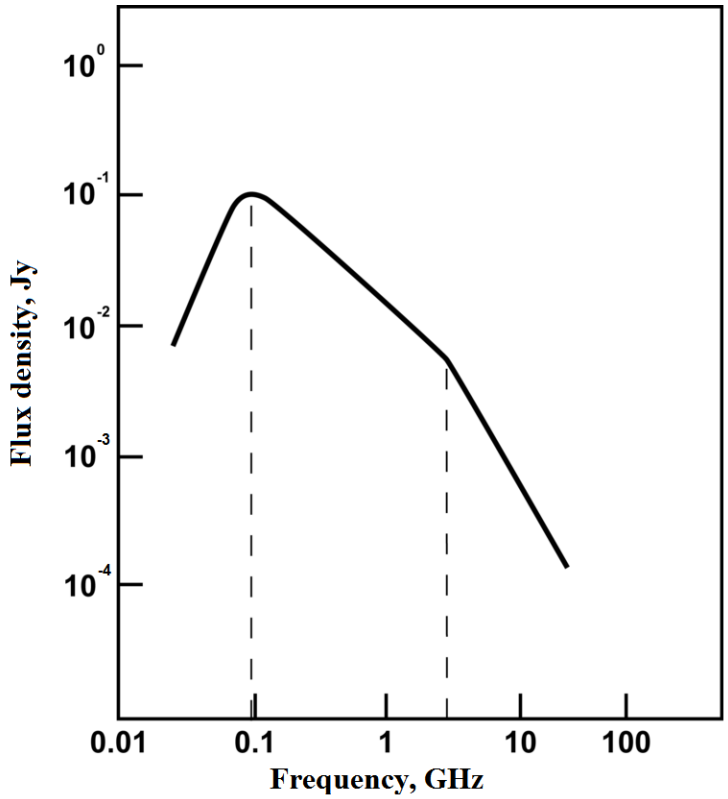

Figure 1.5: Typical pulsar spectrum. It reaches a maximum at the frequencies 100-200 MHz, and drops towards lower frequencies. Around a few GHz, there is the so-called high-frequency turnover.

Spectra of millisecond pulsars do not have a low-frequency turnover, but it does not make them easy to study at low frequencies due to the effects of the propagation medium. Multipath propagation in the interstellar medium caused by inhomogeneities of electron concentration smears pulsar pulses. This effect is called scattering. Additionally, broadband pulses get dispersed, i.e. their low-frequency part is delayed with respect to the high-frequency one. Both of these effects increase their impact at lower frequencies, as $f^{-4.0}$ (normal distribution of inhomogeneities sizes) or $f^{-4.4}$ (Kolmogorov's distribution) for scattering, and f^{-2} for dispersion.

Energy and occurrence rate of pulsar pulses can be diverse. Neutron stars exhibit a range pulse amplitudes, from giant and anomalously intense pulses to complete disappearance of emission (nulls). Some pulsars show short-term nullings, when the pulsar is 'off' for a few pulse periods [Backer 1970], other show long-term nullings (intermittent pulsars), when the pulsar is off for days or weeks [Kramer 2006a], sometimes up to 90% of the time. The latter class of objects becomes more and more nu-

merous [Keane 2011] as the surveys for pulsars and transients become more sensitive. Sometimes a pulsar in a multiple star system stops emitting for some time due to the influence of its companion [Fruchter 1988, Stappers 1996, Lyne 1993, Kaspi 2004]. These phenomena are called eclipses. The most erratically emitting neutron stars are rotating radio transients (RRATs) [McLaughlin 2006], which produce only occasional isolated radio bursts. A separate class of radio emitters that might be related to neutron stars [Mottez 2014] are fast radio bursts (FRBs). These are isolated bursts with large dispersion measures that have not shown any repetition so far.

Several pulsars are known to emit giant pulses [Cognard 1996, Johnston 2003]. The most famous among them is the pulsar in the Crab Nebula. Giant pulses intensity exceeds that of normal pulses by thousand times (see [Knight 2006] for an overview). Anomalously intense pulses [Ulyanov 2006] were detected in the decameter range. They are not as intense as giant pulses and have a different pulse energy distribution. In [Hankins 2003, Hankins 2007] "nano-giant" pulses of the Crab pulsar with subpulse duration of only 0.4 ns were detected. These were the shortest pulses ever detected. Having brightness temperatures of $2 \cdot 10^{41}$ K also makes them the brightest ones.

To date about 2300 pulsars (see ATNF catalog[1]) and ~ 70 RRATs (see RRATalog[2]) are known. This is only a fraction ($\sim 10\%$) of the predicted population. Of course we are yet unable to detect very distant pulsars in the Galactic plane due to propagation effects. Many pulsars may be weak, so the existing pulsar surveys didn't have enough sensitivity to detect them. The transient parameter space is largely unexplored, because this task imposes certain requirements on the radio telescope, such as a large field of view. Thus, surveys and searches remain fully relevant. Almost every survey brings unexpected exotic discoveries, such as new types of neutron star emission patterns or objects that belong to exotic systems, such as pulsar-pulsar binaries [Lyne 2004, Burgay 2003], neutron star-black hole binaries, the black widow systems, the redback systems and the diamond planet systems (review in [Stovall 2014]), allowing to test relativistic gravity [Kramer 2006b, Antoniadis 2013]. Neutron stars are also unique tools for constraining the equation of state of ultra-dense matter [Hessels 2006, Demorest 2010], observing plasma in strong magnetic fields (pulsar magnetosphere [Gavriil 2008, Hankins 2003, Kramer 2006a, Lyne 2010, Hermsen 2013]) and improving our understanding of pulsar radio emission mechanisms. The discovery of bright millisecond pulsars with stable periods is pressing for the operation of pulsar timing arrays, which will attempt to detect gravitational waves. In addition, every discovered pulsar provides a line of sight for studying the interstellar medium and deriving Galactic electron concentration models such as NE2001 [Cordes 2002] or magnetic field models [Han 2006] due to measured Faraday rotation.

Another goal of discovering new neutron stars is to understand their population, evolution and connections between different types of sub-populations.

[1] http://www.atnf.csiro.au/research/pulsar/psrcat/
[2] http://astro.phys.wvu.edu/rratalog

This can be done by simulations [Lorimer 1993, Arzoumanian 2002, Lorimer 2006, Faucher-Giguère 2006], fed with large (preferably unbiased) sample of pulsars.

Discovery of RRATs was unexpected and potentially important for understanding the neutron star evolution and correctly estimating the neutron-star birthrate. It raised many questions about the interconnections of different kinds of neutron stars, such as the link between RRATs and pulsars, RRATs and magnetars (neutron stars with exceptionally strong magnetic fields) [Woods 2006], or RRATs and X-ray dim isolated neutron stars (XDINS) [Walter 1996]. RRATs as well as XDINSs and magnetars have longer periods than normal pulsars. Newly discovered pulsars with long periods ($P > 5$ s) and strong magnetic fields could be of great help for understanding these interconnections. Difficulty of detecting RRATs due to their rare emission suggests that these sources can be quite numerous, even comparable to the size of normal pulsar population. Most recent surveys are aiming to detect a considerable number of RRATs in order to increase the size of their population and draw statistical conclusions from it [Keane 2010, Keane 2011].

Finally, the identification of some radio emitting neutron stars with the sources detected at higher frequencies (X-ray or gamma-ray pulsars) will uncover the relationship between high-energy and radio emission of neutron stars.

All mentioned motivations have driven (and will drive in the future) a number of successful surveys for pulsars and transients.

1.3 Surveys for pulsars and transients in radio

Numerous surveys for pulsars were conducted since their discovery [Hewish 1968] and are being conducted now. Each pulsar survey aims at answering several major questions: (i) how many neutron stars are there in our Galaxy, (ii) what is their spatial distribution and (iii) how diverse is the neutron star population?

Before the discovery of pulsars a number of large-scale radio sky surveys were conducted, none of which led to the detection of pulsars. This was due to the low time resolution and sensitivity of those surveys. Discovery of pulsars encouraged a multitude of high time resolution surveys. Constant improvement of radio telescopes, data acquisition systems and processing tools led to fast increase in the number of detected pulsars that doubled approximately every 4 years [van Leeuwen 2010].

There are two possible survey strategies: (i) targeted searches and (ii) blind searches. Targeted searches usually focus on areas where known or expected neutron stars are located, such as locations of X-ray or gamma-ray point sources [Hessels 2011, Ransom 2011, Keith 2011] and supernova remnants [Staelin 1968, Camilo 2003]. Blind searches are normally performed on large sky areas, such as the Galactic plane or the whole sky accessible to a given radio telescope. Hereafter I will consider blind pulsar and transient surveys.

First surveys attempted to detect individual pulses of pulsars, the same way as they were discovered. Then with the development of computers and processing

techniques the searches became mostly based on pulsar periodicities. In recent years after discoveries of various types of erratically emitting neutron stars, the surveys focused again on isolated dispersed pulses.

Similarly, first searches were made using large low-frequency radio telescopes. They were followed by the ~ 400 MHz surveys made with big dishes (Green Bank, Arecibo), and then by high-frequency (~ 1400 MHz) surveys. Nowadays the attention is again paid to low radio frequencies due to the start of operation of the LOw Frequency ARray (LOFAR).

First pulsar surveys after the Cambridge discovery were done with the largest telescopes of that time, e.g. the Mills Cross radio telescope in Molonglo, Australia [Vaughan 1969, Large 1971], and the dishes at Jodrell Bank [Davies 1970], Arecibo [Hulse 1974] and Green Bank [Stokes 1985, Stokes 1986].

The first Molonglo survey of all southern sky [Vaughan 1969] discovered about 30 pulsars by visual examination of chart records of 4 MHz bandwidth around 408 MHz. The sources drifted through three wide 4^o beams of the East-West antenna of the Mills cross telescope, spaced in right ascension, and were detected first in the 'early' and then in the 'late' beam. No dispersion delay compensation or periodicity search was used.

The next major survey at Jodrell Bank radio telescope, UK [Davies 1970, Davies 1972, Davies 1973], used the dispersion delay between 410 and 406 MHz as a criterion to discriminate between pulsar pulses and impulsive interference. It observed a significant part of the Galactic plane ($-10^o < b < 10^o, 0^o < l < 40^o$ with b the galactic latitude and l the galactic longitude counted from the origin in the direction of Galactic center) in a drifting regime and resulted in the discovery of about 40 pulsars as well as giant pulses of the Crab nebula pulsar. The periodicity search approach was neglected due to its computational complexity.

The 430 MHz survey of the Galactic plane with the Arecibo radio telescope, USA, by [Hulse 1974] was ~ 10 times more sensitive than drift-surveys in Molonglo and Jodrell Bank, because an integration of 3.3 minutes was used at each beam position. For the first time, a computer performed a thorough search in the space of all unknown pulsar parameters: dispersion measure, period and duty cycle (pulse width to period ratio). This resulted in the discovery of 40 pulsars, including the first pulsar in a binary system (PSR1913+16).

In total, 10 years after pulsar discovery, about 150 pulsars were known. The second Molonglo survey [Manchester 1978] doubled this number due to an upgrade of the Mills Cross telescope by a new preamplification system and the use of 11 independent beams. It scanned all the sky below declination $\delta = 20^o$ at 408 MHz and used the Parkes 64-m radio telescope to confirm its detections.

When the discovery of pulsars reached its 20th anniversary, about 350 pulsars were known. The majority of them was discovered around 400 MHz, a frequency at which pulsar flux density is often close to a maximum [Lorimer 1995]. But to substantially increase the number of known pulsars, a deeper survey of the Galactic plane was required. But in the direction of the Galactic plane, propagation effects (dispersion and scattering) that depend on the electron concentration are

strongest. The frequency dependence of propagation effects has a steep power spectrum [Ables 1970] and considerably decreases at high frequencies, therefore a higher observational frequency was chosen to probe the Galactic plane. Major high radio frequency surveys were made at $\sim$ 1400 MHz. Although the flux density is generally higher at 400 MHz, the high-frequency surveys were far more successful due to the aforementioned lower influence of propagation effects and higher contrast between the Galactic background [Lawson 1987] and pulsar radiation.

High-frequency surveys are bound to cover a limited part of the sky, due to the higher directivity of the radio telescopes and the too long time required for the survey of large sky regions by a narrow beam. To speed up the surveys, multifeed antenna systems are used. High frequency observations gave access to the study of more distant pulsars with large DMs, as well as fast (millisecond and recycled) pulsars and pulsars in exotic systems. The first surveys at a frequency around 1400 MHz were conducted at Jodrell Bank [Clifton 1992] and Parkes [Johnston 1992]. They were followed by The Parkes Southern Pulsar survey [Manchester 1996, Lyne 1998], the Swinburne intermediate-latitude pulsar survey [Edwards 2001], and finally Parkes Multibeam Pulsar Survey (PMPS) [Manchester 2001], [Lorimer 2006] and references therein, the most efficient survey so far in terms of number of discovered pulsars ($>$ 800). PMPS used a 13-beam receiving system, recording a continuous 288 MHz bandwidth sampled at 250 μs. It covered part of the Galactic plane ($-5^o < b < 5^o, l = 260^o$ to $l = 50^o$) with 35 minutes integration at each telescope pointing. The archived survey data have been reprocessed several times, and one of the attempts lead to the discovery of RRATs [McLaughlin 2006]. Thereby the Parkes 64-m telescope, equipped with its multibeam broadband receiver, became the most efficient instrument for pulsar search, as it discovered more pulsars than all other radio telescopes together. This success can be explained both by the favorable location of the telescope and a correct combination of equipment and survey strategies.

At the moment, the Parkes telescope is involved in another survey of the entire sky with high time resolution, in liaison with the Effelsberg radio telescope. This survey is called High Time Resolution Universe (HTRU), divided in HTRU-North [Barr 2013] and HTRU-South [Keith 2010]. It also uses 13-beam receivers on both sites and records $\sim$ 400 MHz bandwidth around 1352 MHz with 64 μs time resolution. It is split into three regions by Galactic latitude, low (most sensitive, with 72 minutes integration time), mid (9 minutes) and high (most shallow, 4.5 minutes). So far the survey collaboration reported $\sim$ 200 new discoveries [Keith 2010, Bates 2011, Keith 2012, Burgay 2013, Ng 2014, Bates 2015], the majority of which were made in the HTRU-S survey. The shorter periods and higher dispersion measures of the discovered pulsars, compared to those of PMPS, are the result of higher time and frequency resolutions of the HTRU survey.

A number of other successful surveys were recently carried out or are underway by northern hemisphere radio telescopes. Among these are the PALFA survey at Arecibo as well as the GBT350 and GBNCC surveys at Green Bank.

The PALFA survey [Cordes 2008] started in 2004 at the Arecibo radio telescope

at 1440 MHz, using a 7-beam ALFA (Arecibo L-band Feed Array) receiver. It focuses on the Galactic plane ($-5^o < b < 5^o$), with 268 s integration time for the inner Galaxy pointings ($30^o < l < 78^o$) and 134 s for outer ones ($162^o < l < 214^o$). It discovered a total of 145 pulsars, including 17 MSPs [Lazarus 2015], several Rotating Radio Transients [Deneva 2009] and one Fast Radio Burst (FRB 121102) - the first one not discovered at Parkes [Spitler 2014]. Remarkably, one of the data processing pipelines of the survey used the volunteers' computing network Einstein@Home [Allen 2013] powered by the BOINC [3] platform.

Currently Arecibo is performing the drift-scan 327 MHz survey AO327 [Deneva 2009] in order to cover the declination range $0^o < \delta < 38^o$ of the northern sky.

The GBT350 survey [Boyles 2013, Lynch 2013] is a 350 MHz survey of the sky between -21^o and $+26^o$ in declination using the 100-m Green Bank radio telescope. A distinctive feature of this survey is that it does not track (integrate) any position on the sky - it is a drift-scan survey powered only by Earth's rotation. The choice of this survey method was imposed by the unavailability of the GBT azimuth track during the summer of 2007. The full survey was completed between May and August 2007. Having covered ~ 10300 deg^2 of sky area, the survey revealed 35 new pulsars, including 7 MSPs and 2 pulsars with an unusually large nulling fraction. These discoveries are mostly bright and relatively nearby pulsars. [Karako-Argaman 2015] discovered > 20 RRATs, some of which are relatively nearby (low values of DM). Remarkably, the number of RRAT candidates in the survey is comparable to the number of discovered classical pulsars, which may be an evidence that we underestimate the size of the RRAT population.

The GBNCC (Green Bank North Celestial Cap) survey is underway at Green Bank telescope [Stovall 2014]. It will cover ~ 35000 deg^2, i.e. all the sky above $\delta = -40^o$ in the frequency range 350 ± 50 MHz frequency with 82 μs time resolution. The integration time for each of its 152000 pointings is 120 s. The survey is aiming at detection of pulsars (including nearby millisecond pulsars) and isolated bursts such as FRB or RRAT pulses. About 70 pulsars and 7 RRATs were discovered in the first 20% of survey data.

Another noteworthy survey at GBT was the 350 MHz North Galactic Plane survey [Hessels 2008], which discovered 33 pulsars.

Finally, major expectations are now related to the LOFAR telescope [van Haarlem 2013], which will exhaustively search the northern sky for pulsars during its surveys and monitor it for fast transients over large fractions of the time. Transients are one of the key projects for LOFAR, and the data acquired for other projects will also be examined for transients. Prospects of studying transients and pulsars with LOFAR are discussed in [Stappers 2011]. LOFAR has several dedicated pulsar pipelines, including the standard pulsar pipeline, "Pulp" [Stappers 2011]. Additionally, for identification of isolated dispersed pulses LOFAR has a GPU-based backend, ARTEMIS. First results on pulsars, obtained during the commissioning

[3] http://boinc.berkeley.edu/

phase of LOFAR, can be found in [Hessels 2010, Hassall 2012, Hermsen 2013].

Strategies of pulsar and transient surveys with LOFAR are described in [van Leeuwen 2010]. Two pilot surveys have already been carried out [Coenen 2014] and lead to the discovery of 2 pulsars. The LOFAR Pilot Pulsar Survey (LPPS) observed $\sim$ 10000 deg^2 of the northern sky with 7 incoherently formed 3.7^o beams and 1 hour integration time. Another survey, the LOFAR Tied-Array Survey (LOTAS), covered $\sim$ 600 deg^2 with higher sensitivity and resolution (due to coherent beam forming), and discovered the two aforementioned pulsars.

LOFAR is a 'software' telescope, that can form hundreds of simultaneous narrow beams [Stappers 2011], covering a wide field of view (up to 8400 deg^2 in the "fly's eye" mode). This feature is vital for monitoring fast transients in real time. This can be done in parallel with other observational programs. Additionaly, LOFAR is very agile and is able to change its operation mode setup in less than 1 minute [Stappers 2011]. This opens the opportunity to trigger LOFAR for follow-up observations of transient events detected at other telescopes in other frequency ranges.

All of the above surveys have limitations and selection effects, therefore carrying out new surveys in different frequency ranges and exploring different parts of parameters space is essential to infer correct conclusions about the neutron star population of our Galaxy. The numbers and types of newly discovered neutron stars will shed light on their evolution and constrain the supernova explosion rate. A separate application for the sources discovered in pulsar and transient surveys is to probe the interstellar medium (via dispersion, scattering and Faraday rotation of pulsar pulses).

1.4 Exoplanets and their expected radio emissions

The discovery of Jovian radio emission [Burke 1955] has become a starting point for studies of planetary radio emissions. Soon it became evident that in our Solar System all giant planets (Jupiter, Saturn, Uranus and Neptune) and the Earth itself produce radio emissions (see [Zarka 1998] for a review). Other planetary systems also might have similar conditions for emergence of planetary radio emissions. One concern is whether the radio emission is strong enough to be detectable from the Earth with existing radio telescopes.

Jupiter is a very intense radio source, producing radio emission in a wide frequency band (from few kHz to few GHz). Above a few GHz the radio emission is thermal. At lower frequencies it becomes non-thermal (synchrotron and then cyclotron), being produced by accelerated electrons. It reaches maximum intensity at frequencies below 40 MHz [Zarka 2000]. This low-frequency emission is as intense as the radio emissions from the Sun, because it is generated by a coherent non-thermal mechanism, called the cyclotron maser instability (CMI) [Treumann 2006]. For comparison, the star-planet contrast is typically 10^9 at optical wavelengths, 10^6 in the infrared, but only 10^{1-2} in the low-frequency radio range (for Solar system planets), reaching ~ 1 for Jupiter in the decameter range.

Jupiter's decameter radio emission is seen as very intense mainly because Jupiter is relatively close to the Earth. A basic sensitivity calculation based on the radiometer equation tells us the maximum distance at which we can detect a planet. Assuming the effective area of UTR-2 ($\sim 10^5$ m^2), with integration time of 1 hour in a 10 MHz band, the maximum distance from which we could detect Jupiter on top of Galactic background fluctuations is only ~ 0.1 pc [Zarka 2007]. But interference and ionospheric perturbations will also affect the detection. Therefore in order to be detectable, an exoplanet must be a much stronger radio emitter than Jupiter.

Many theoretical works have been devoted to predicting whether there can be planets producing stronger radio emission than Jupiter. It is currently impossible to build a predictive analytic theory of exoplanetary radio emission due to our poor knowledge of electron distribution functions in the magnetospheres of exoplanets, resulting from specific particle acceleration processes operating there. Existing theories thus rely on studies of the Solar system radio emitting planets, construction of scaling laws that relate the output planetary radio power to the input power into the magnetosphere (from the Solar wind or from the planetary rotation), and extrapolation of these scaling laws to different parameter regimes that may lead to more intense radio emitters.

For Solar System planets, the nonthermal radio emission is produced by: (i) solar wind (or solar coronal mass ejections, CME) - magnetosphere interaction that causes auroral emissions at all magnetized planets, and (ii) magnetosphere-satellite interaction (e.g. between Jupiter and its galilean satellites) [Zarka 2007]. In the latter case, the satellites can be themselves magnetized (case of the "dipolar" interaction Jupiter-Ganymede) or weakly magnetized or unmagnetized (case of the "unipolar" interaction Jupiter-Io). All these interactions can be generally described as the interaction of a plasma flow with an obstacle (magnetized or not) [Zarka 2007].

Although the emissions of Solar system planets have different intensities and spectra, they can be organized in a coherent frame, forming a scaling law. A first scaling law was found between the input solar wind bulk kinetic power into the magnetospheres and their output radio power [Desch 1984]. It was used to predict the power of Uranus' radio emissions, and subsequent measurements by Voyager 2 were in fair agreement with the prediction. A second scaling law was found to relate the incident magnetic power (or Poynting flux) onto the obstacle – magnetosphere or satellite – and the output radio power [Zarka 2001]. If we plot the known values for the average power of Solar System planetary or satellite-planet radio emissions versus the incident magnetic power of either the solar wind on the magnetospheres or the rotating Jovian magnetic field on the galilean satellites, we obtain the 'radio-magnetic' scaling law of Fig. 1.6, that has a slope close to 1.

In Fig. 1.6 [Zarka 2015] the filled circles correspond to auroral radio emissions from Jupiter, Saturn, Uranus, Neptune and the Earth. The radio fluxes are strongly variable over time and frequency, so averaged values (over time, spectrum and radiation pattern) are shown. Although the conditions that produce the radio emissions are different, e.g. the Earth's radio emission is controlled mostly by the solar wind, whereas at Jupiter it is primarily determined by internal magnetospheric processes

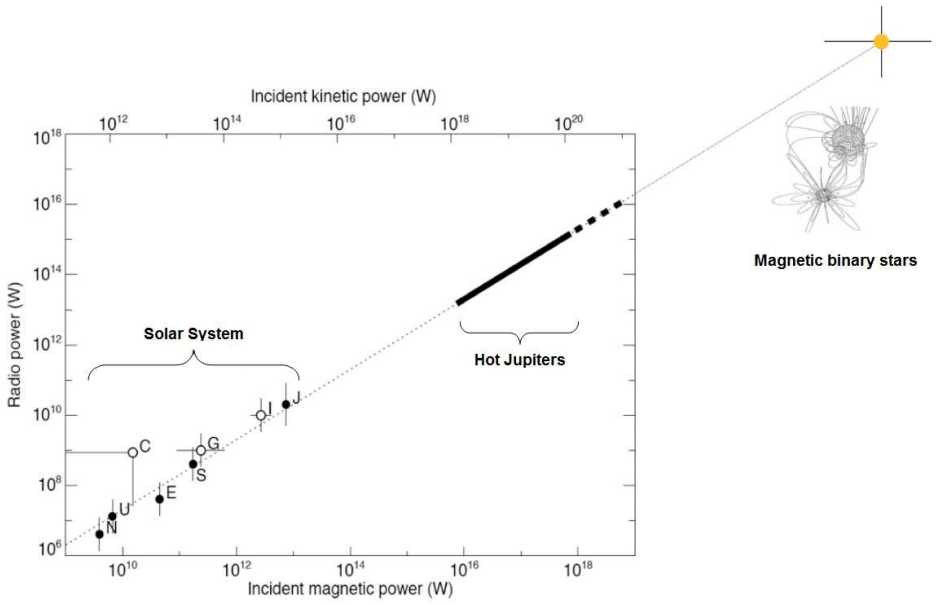

Figure 1.6: Extrapolation of the (radio-magnetic) scaling law for Solar System radio emissions to the parameter regime of hot Jupiters. The known case of one binary star system is also indicated, suggesting that the scaling law holds up to vey large powers. Adapted from [Zarka 2015].

(rotation and mass release from Io), they form a clear scaling law. This law can be extrapolated to a regime of stronger emissions that have a chance to be detected by existing large radiotelescopes. Hot Jupiters, the massive planets close to their host star, can either have a strong magnetic field and interact with the strong stellar wind or interact with a strongly magnetized star through the unipolar interaction mechanism. In both cases they should produce intense radio emission, according to the scaling law ($10^3 - 10^6$ times stronger than that of Jupiter). The radio-magnetic scaling law appears to be valid even for interacting magnetic binary stars, e.g. the RS CVn system $V711\tau$ [Budding 1998].

Application of this scaling law to the known exoplanets, discovered by either radial velocities or transit methods, allows us to make predictions on their detectability by existing large radio telescopes [Grießmeier 2007]. Fig. 1.7 shows that several systems should be detectable with UTR-2 and LOFAR. The maximum frequencies of predicted radio emissions are deduced from exoplanetary mass, as well as measured or assumed planetary rotation. These predictions are order of magnitude indications rather than accurate numbers, but they should allow us to look at the most favourable targets.

The intrinsic planetary magnetic field is thought to be related to the planet's rotation, thus it may decay and vanish if the rotation is too slow. This may well be the case for hot Jupiters, spin-orbit synchronized around their parent star. But even

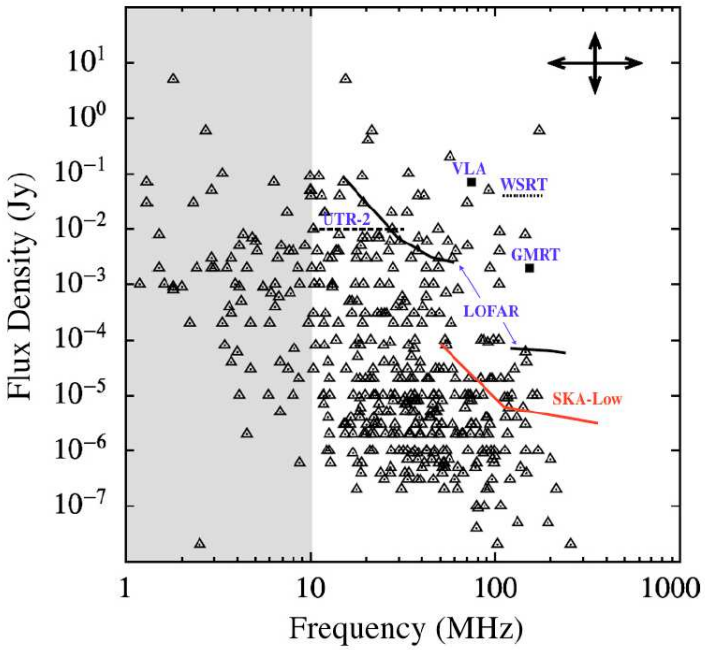

Figure 1.7: Predicted radio flux and maximum emission frequencies for known exoplanets (in 2011). Every triangle is an exoplanet. Lines show the sensitivity of several large radio telescopes. From [Grießmeier 2011, Zarka 2015].

unmagnetized planets have a chance to be detected. Optical spectro-polarimetric measurements show since a few years that there are many strongly magnetized stars with magnetic fields of tens of Gauss (which can be measured by Zeeman-doppler effect) [Fares 2010]. In that case the star-planet system can be seen as a giant analog of the Jupiter-Io system, that can produce similar but more powerful bursty radio emission. Unmagnetized planet may thus induce radio emission in the magnetosphere of their parent star. However, efficient operation of the CMI mechanism imposes that the stellar magnetic field should be 10-100 times stronger than the solar one. In that case, CMI is expected to produce emission at frequencies up to 250-300 MHz. The magnetic field of a star being generally anisotropic, the incident magnetic energy flux at the exoplanet will strongly vary along its orbit, leading to variations of the output radio emission with the orbital phase. The CMI itself generates very anisotropic radio emission beams, and thus the observed radio flux is expected to be modulated with the planetary rotation, likely to be equal to the orbital period for hot Jupiters. Thus, spreading radio observations along the orbital phase of an exoplanet target should in principle allow us to detect these kinds of variations.

A giant analog of the Io-Jupiter system might produce a radio emission $10^5 - 10^6$ times stronger than Jupiter's. Applying this value to the sensitivity calculation, we get a limiting distance of 40 pc for 10 MHz and 1 hour integration at a radio telescope with effective area $\sim 10^5$ m^2.

Note also that other theories have been proposed for exoplanets that are not hot Jupiters. Expanding the frame of magnetosphere-ionosphere interaction at Jupiter, [Nichols 2011] showed that a fast rotating (1 to 3 hours period) Jupiter-like planet, orbiting a star with a bright X-UV output, may also produce intense radio emission.

Conversely, synchrotron emission from the radiation belts of exoplanets is very unlikely to be detected due to its incoherent nature and relatively low flux density, even though at the higher frequency where it is observed the Galactic background and its fluctuations are weaker. Using the radiometer equation we find that a synchrotron emission that is 1000 times more intense than Jupiter's at 1 GHz (and this is not easy to justify theoretically) can be detected from a distance of no more than 2 pc, assuming a telescope effective area $\sim 10^5$ m^2 and 10 hours of integration time within a 10 MHz band.

When a signal from a star-planet system will be detected, the next steps will be to determine if the signal comes from the star or the planet, and then to characterize quantitatively the emission in order to deduce the parameters of the emitting system. Discrimination between the star and the planet is expected to be relatively easy, based on variations at the orbital period and polarization (Jupiter's radio emissions are strongly circularly/elliptically polarized whereas solar emissions are nearly unpolarized).

For characterizing the exoplanetary emission, Hess and Zarka [Hess 2011] used simulations based on the CMI mechanism operating in different star-planet systems (with various magnetic field tilt and offset, orbit inclination, coronal density, etc.) and showed that the shape of planetary signatures – in intensity and polarization

– in the time-frequency plane (i.e. the measured dynamic spectrum of the emission) could give a lot of information about the planet or the star. For example, the maximum frequency constrains the magnetic moment of the planet, the emission morphology indicates the fraction of the auroral oval that emits, the temporal modulation is connected with the revolution period of the planet, the polarization gives information about the inclination of the magnetic field and/or the orbit. In turn, these values can be used to place constraints on planetary dynamos and internal structure, to test directly spin-orbit synchronization, the presence of satellites and the type of planet-star plasma interactions. Large-scale studies of exoplanetary magnetospheres could evolve into a new scientific field of comparative magnetospheric physics.

Another motivating factor for searching exoplanets is that planets having a magnetosphere are more likely to be habitable due to shielding from cosmic rays, stellar wind and CME as well as a more limited atmospheric escape provided by the magnetosphere [Grießmeier 2004].

The idea that planets in other planetary systems can produce radio emission appeared before the actual discovery of exoplanets [Yantis 1977, Winglee 1986], but actual search for radio emission started only in the 21^{st} century. A lot of effort has been spent on trying to detect magnetospheric radio emissions from exoplanets, but no successful unambiguous detection was achieved to date. Detection of such a weak signal whose time-frequency dependence is unknown is a difficult task.

The first searches were untargeted. To date, with about 2000 exoplanets known (discovered using radial velocities and transit methods)[4] there are enough candidates to select from. Successful detection will be followed by characterization of the signal and determination of the aforementioned planetary and stellar parameters.

Several scientific groups in the world try to detect the radio emission from exoplanets with all large radiotelescopes (VLA, GMRT, UTR-2, LOFAR ...). These telescopes are among the most sensitive in the world, and the absence of detection until now is an indication that if the signal exists, it must be weak or the sources observed were not selected successfully among the many possible candidates.

Several detection attempts were made with the VLA [Winglee 1986, Bastian 2000, Farrell 2003, Farrell 2004, Lazio 2007, Lazio 2010], but it has a small effective area (a few thousand square meters) and operates at relatively high frequencies (> 74 MHz). The Tau Bootes and HD 80606 systems were observed, and no detection was obtained, although Tau Boo is one of the favourable hot Jupiters suggested by theoretical predictions. It is expected to emit up to relatively high frequencies (~ 60 MHz, depending on the assumptions about its rotation). An upper limit on Tau Boo radio emission at 74 MHz was ~ 0.1 Jy and 0.048 mJy for HD 80606.

Later observational campaigns were run at the GMRT (India) [Winterhalter 2006, Majid 2006, George 2007, George 2008]. Observed targets were υ And, ε Eri and HD 128311. The first measurements at the fre-

[4] http://exoplanet.eu/catalog/

quency $\sim$ 150 MHz were strongly polluted. Later, GMRT was improved and [Lecavelier des Etangs 2009] obtained maps around HD189733, showing a weak peak (about 2.7σ) close to the position of the target. This planet is a transiting planet, therefore it should be occulted when it passes behind the star, but no decrease of the flux was noted during the occultation. In 2009 the same team observed HAT-P-11B, another transiting exoplanet. A decrease of the signal was observed to coincide with the occultation of the planet by the star (at a $2-\sigma$ significance level), but a subsequent observation in 2010 did not confirm it [Lecavelier des Etangs 2013]. A recent observation of Tau Boo during 40 hours with the GMRT placed an upper limit of $\sim$ 1 mJy on its flux at 153 MHz [Hallinan 2013]. Additionally, the TGSS survey is underway at GMRT (150 MHz), and its first results [Sirothia 2014] have found 4 sources at the expected positions of exoplanets. These targets are currently followed-up to check for the possible contribution of background sources.

Observational campaigns at UTR-2 took place since 1996, with rudimentary receivers until 2006. A few dozen candidates were observed [Ryabov 2004]. An apparently positive but ambiguous result was obtained in 2009 on the Corot-7b super-Earth type planet that has a short orbital period ($\sim$ 20 h). Now UTR-2 is engaged in simultaneous observations with LOFAR, and the amount of observational data continues to increase.

During the first cycles of LOFAR (cycles 0, 1, 2 and 4) after its commissioning, several exoplanet targets were observed by two independent groups (France and the USA). The data on these targets is being processed, confronting with the difficulties inherent to imaging at low radio frequencies. Exoplanets are also searched in the data of the first LOFAR large sky survey (MSSS).

1.5 Motivation and problem statement

The low-frequency range has not been popular for making pulsar surveys because of low expectations on the number of pulsars to be discovered there. The vast majority of pulsars were discovered at frequencies above 300 MHz[5]. Nonetheless the low-frequency range may reveal unexpected transient phenomena as well as different emission properties of known sources. Furthermore, most pulsars and RRATs have been discovered in southern sky surveys or surveys of the Galactic plane. Therefore the northern sky (especially at high Galactic latitudes) may still contain unrevealed nearby objects, due to either insufficient sensitivity of previous surveys or to the sporadic nature of the sources or the unfavorable orientation of the sources' beams. High-sensitivity low-frequency survey of the entire Northern sky may reveal these objects.

Now that LOFAR has come to operation, many observational programs and surveys of pulsars are performed. In its frequency range UTR-2 is more sensitive than LOFAR, and it can thus be used to confirm LOFAR's discoveries and vice

[5] http://www.atnf.csiro.au/research/pulsar/psrcat/

versa. UTR-2 has shown to be sensitive to the majority of nearby regular pulsars [Zakharenko 2013], which motivated us for carrying out a pulsar survey with UTR-2. Such a survey is likely to discover close weak pulsars (with various degrees of nulling) missed out by previous surveys, as well as galactic transient sources. The key task of this new survey, that constitutes the frame of the present work, is thus to record a "snapshot" of the entire northern sky with relatively high time resolution, and search for pulsar and transient signals in it.

The survey is a time-consuming task, usually involving many people. It may take a few years to complete a survey. My goal was to develop automated tools for processing the survey data. A number of software packages, such as PRESTO[6], already exist and are used by other pulsar groups worldwide. Nonetheless these tools are not optimized for low-frequency pulsar observations that require specific methods of interference mitigation and do not tolerate inaccurate dispersion compensation.

The search for exoplanets at radio wavelengths has not been successful so far, either due to the intrinsic weakness and sporadicity of the signal or due to the incorrect selection of candidate targets. An ambiguous result was obtained for Corot-7b after processing its recordings at UTR-2 in 2009. The result of the processing revealed a sinusoidal-like variation of the signal intensity versus the planet's orbital period in the telescope beam directed to the source (*On*), which was absent in the other (*Off*) beam directed 1 degree away from the source (Fig. 1.8). Unfortunately, after some reprocessings with different RFI mitigation algorithms the signature disappeared. Furthermore the calibration of the received flux based on the sky background was performed assuming a good understanding of the gain variations of the telescope resulting from the tracking of the source. The reality is more complex. In order to raise this ambiguity and confirm or refute the detection of Corot-7b, it was decided to build a new processing pipeline based on (i) more thorough RFI mitigation, (ii) no assumption on the telescope response, (iii) comprehensive search algorithms and (iv) comparison with another observation session of the same target performed in 2011.

These two tasks (high resolution full sky survey and full reprocessing of Corot-7b data) imply the development of new algorithms and massive data processing, which can have a large common part (data management and interference mitigation). The developed software should be usable in subsequent searches at UTR-2 and adequate for processing similar time-frequency data obtained by other radiotelescopes (such as LOFAR).

[6] http://www.cv.nrao.edu/∼sransom/presto/

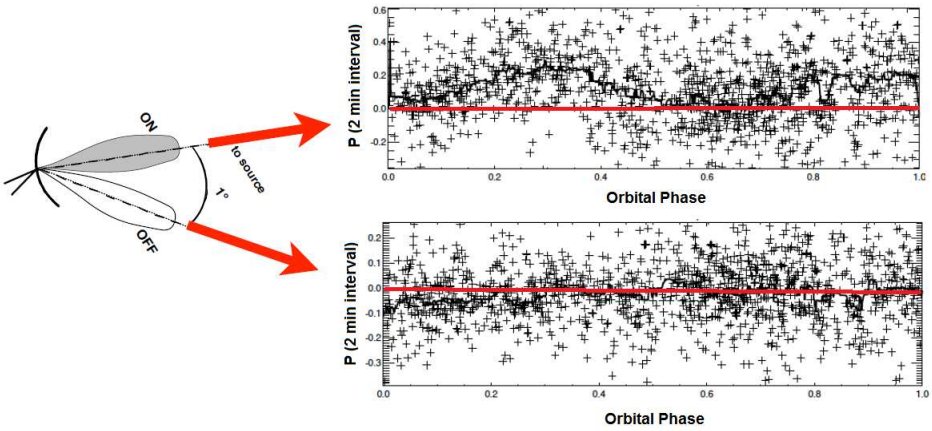

Figure 1.8: Tentative detection of variations in the radio emission from the direction of Corot-7b, with the first version of the "exoplanet pipeline".

Chapter 2

Instrumentation and observations

Contents

The signals of interest, i.e. pulsar pulses, transient bursts and exoplanet radio emission are relatively weak, especially compared to the multitude of ambient terrestrial signals (natural and man-made). Furthermore the study of such signals in the low frequency range is complicated by various hindering factors, such as strong propagation effects through the interstellar medium and the Earth's ionosphere and strong terrestrial interference. Only the use of a large radio telescope with high temporal and spectral resolutions and sufficient effective area (and therefore high sensitivity) may allow to overcome the difficulties and take advantage of the benefits that exist in the low-frequency range.

2.1 UTR-2

The UTR-2 (Ukrainian T-shaped Radiotelescope, version 2) is a large electronically-controlled phased array. It was commissioned in 1970, and since 1972 it has been used regularly for a number of astrophysical research programs. The main areas of study include the Solar system (sporadic solar radio emission, solar corona, interplanetary scintillations, Jovian decameter emission at different time scales, Saturn's lightning temporal structure etc.), the Galaxy (pulsars, transients, absorption lines in interstellar gas clouds, Galactic non-thermal background, flare stars etc.), extragalactic sources (the decameter sources catalogue[1] of the northern sky lists > 4000 extragalactic sources).

Its large effective area, multi (5) beam antenna pattern, extensive beam steering ($\sim 2 \times 10^6$ distinct pointing directions) allowing quasi-continuous radio sources

[1] http://rian.kharkov.ua/index.php/en/decameter-catalogs/95-onr/research/150-catalog-utr-2

tracking, and broad frequency band as well as digital receivers with high time and frequency resolutions make UTR-2 a powerful instrument for decameter radio astronomy.

The detailed characteristics of UTR-2 are:

- effective area: 150000 m^2 at 16 MHz [Braude 1978b]
- geometrical sizes: 1856 m × 52 m (North-South (N-S) array) and 891 m × 52 m (East-West (E-W) array)
- geographical coordinates: $+49^o38'17''$ latitude, $36^o56'27''$ longitude
- polarization: 1 linear (E-W)
- continuously covered frequency range: 8-33 MHz
- half-power beam width: $24'$ (at 25 MHz) in the two planes (N-S and E-W)
- side lobes level (1^{st} side lobe): -13 dB (rectangular current distribution) ... -26 dB (smoothed current distribution)
- number of beam positions: 2048 in v coordinate (N-S direction) × 1024 in u coordinate (E-W direction), see formula (2.1)
- accessible sky: beam can be steered within 180^o in the N-S-direction and 120^o in the E-W-direction
- multibeam capability: up to 5 simultaneous beams separated by $23'$ (at 25 MHz) in the N-S direction
- beam switching (pointing) time: ∼ 10 milliseconds
- dynamic range by third order intermodulations[2] (IP_3) of the pre-amplification system: from ∼ 30 dBm at 25 MHz to 50 dBm at 8 MHz [Abranin 2001]

2.1.1 Antennae field

Due to its large effective area, UTR-2 is the most sensitive radio telescope in the decameter range so far. Compared to the Mills Cross Telescope, the T-shaped configuration of UTR-2 provides the same resolution, but it is more economical in terms of construction. The symmetrical part of the antenna was placed in the direction of the meridian (N-S), because for radio astronomy observations it is usually more useful to receive continuous recording of α (right ascension) than of δ (declination) coordinate, using the rotation of the Earth. Therefore, UTR-2 has the T-shaped configuration shown in Fig. 2.1. It is composed of two rectangular antenna arrays, the bigger of which (N-S) is extended along the meridian and provides the resolution in declination (elevation), and the smaller (E-W), asymmetric with respect to the

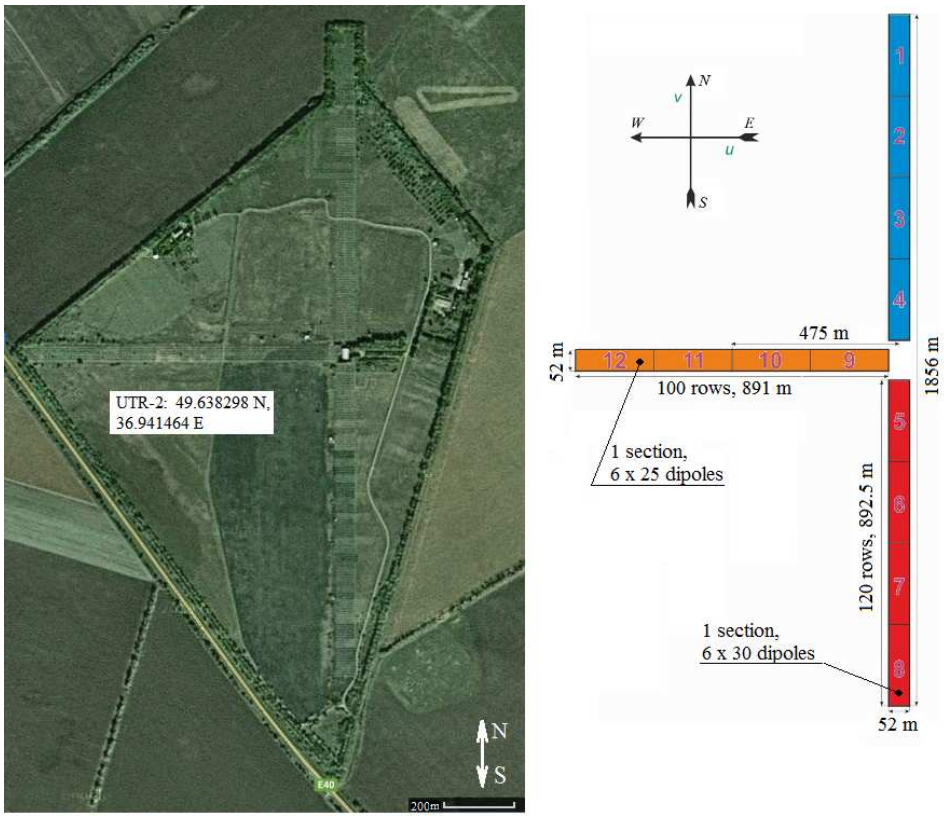

Figure 2.1: Satellite view of the UTR-2 (left panel), section numbers and dimensions (right panel).

center of the radio telescope, is extended along the parallel circle and provides the resolution in right ascension (azimuth).

Beam steering is implemented in the field of view $-1 \leqslant v \leqslant 1$ and $-0.84 \leqslant u \leqslant 0.84$, where

$$u = \cos(\Delta)\cos(A), \qquad v = \cos(\Delta)\sin(A) \tag{2.1}$$

are the directional cosines, Δ and A are the elevation and the azimuth, respectively). Elimination of large grating lobes during the beam steering in the major part of the operating frequency range (10-25 MHz) is provided by the 7.5 m distance between the dipoles in the N-S direction and 9 m in the E-W direction. Accordingly, the N-S antenna consists of 1440 dipoles that form six rows, oriented along the meridian, with 240 dipoles in each row, and the E-W antenna consists of 600 dipoles that form six rows, oriented along parallel with 100 dipoles in each row. In both arrays horizontal symmetrical broadband dipoles of shunt type (Nadenenko dipoles) are used (Fig. 2.2).

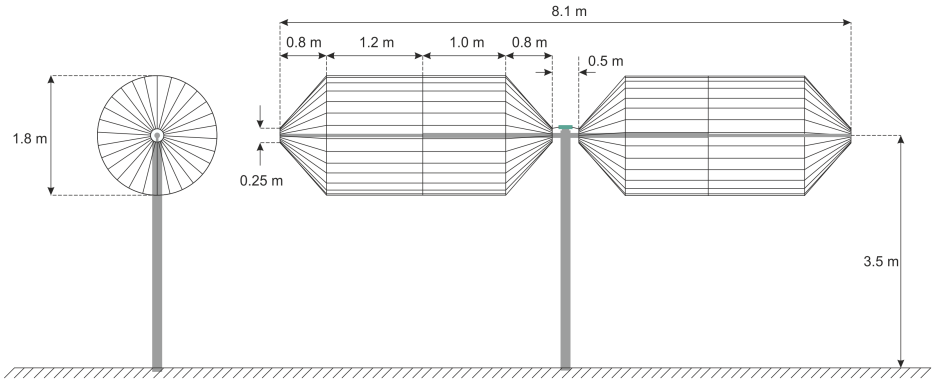

Figure 2.2: UTR-2 dipole shape and dimensions.

Nadenenko dipoles present several advantages: they can be grounded by DC, thus providing lightning protection. Each dipole is a so-called "fat" dipole that provides a broad bandwidth. It is composed of two cylinders made of thirty 8-millimeter galvanized steel wires, converging into cones at the edges in order to reduce mutual coupling between dipoles. All wires are connected in each half of the dipole, and are isolated from the supporting rods by the shunts. The diameter of the dipole is 1.8 m, the length 8.6 m. The supporting vertical rods (masts) are of 3.5 m height. The described dipole dimensions provide a relatively weak dependence of the effective area and the impedance of dipoles on the direction of the beam orientation and frequency. In order to expand the field of view in the declination coordinate, the axes of all the dipoles were oriented along the E-W direction, thus providing measurements of only one linear polarization. The accurate orientation

[2]https://en.wikipedia.org/wiki/Third-order_intercept_point

of the antennae on the ground was performed by means of geodetic methods with an accuracy of a few angular seconds.

The resolving power of the T-shape telescope when operating in the so-called 'modulation' mode (product of the two antennae outputs) can be calculated as follows. The interferometric pattern is defined as:

$$F(u,v) = f_1(u) f_2(v) \cos\left(\frac{2\pi D u}{\lambda}\right), \tag{2.2}$$

where u and v are the directional cosines determined by formula (2.1), $f_1(u)$ is the directional pattern of the E-W arm, $f_2(v)$ is the directional pattern of the N-S arm, λ is the wavelength $\cos(2\pi Du/\lambda)$ is thus the interferometric factor that appears due to the spatial separation of the phase centers of N-S and E-W antennae, D being the distance between the antenna centres. Assuming equal current amplitudes of all the antenna elements, ignoring the directivity of the single dipoles, the influence of ground and taking into account that $D = L/2$ (L is the E-W arm length), the extended expression for the antenna pattern is:

$$F(u,v) \approx \frac{\sin\left(\frac{2\pi D u}{\lambda}\right) \quad \sin\left(\frac{2\pi D v}{\lambda}\right)}{\frac{2\pi D}{\lambda} u \quad \frac{2\pi D}{\lambda} v} = sinc\left(\frac{2\pi D u}{\lambda}\right) \; sinc\left(\frac{2\pi D v}{\lambda}\right). \tag{2.3}$$

Thus, the directional pattern of the T-shaped antenna is symmetrical in both planes and coincides with the directional pattern of a square-shaped array with dimensions $2L \times 2L$. The half-power beam width of the directional pattern at 25 MHz, with $L = 900$ m, $u_{0.7} = v_{0.7} = 1/200$, is equal to $\theta = 24'$.

2.1.2 Phasing system

UTR-2 has a complex beam steering control (phasing) system, which needs to be described in order to understand the data management steps that we follow when trying to detect weak sources, such as exoplanets.

The beam steering control of UTR-2 is based on discrete scanning techniques, because continuous sky scanning is redundant, owing to random errors in the amplitude and phase of currents measured by antennae. The minimal beam shifting step should produce a beam position error much smaller than the beam width.

All variety of electrical beam steering methods can be divided into two major types: (i) systems with the creation of phase shifts between dipoles and (ii) systems with the creation of temporal delay between dipoles. The required value of the phase shift or time delay is provided by either phase shifting devices or variable time delay lines, plugged to each dipole (parallel scheme) or to groups of dipoles (parallel-multilevel scheme). The first phasing method, based on phase shifts, has significant drawbacks: limited bandwidth, complexity of the phase shifters control, dependence of beam control programs on frequency. All these drawbacks are absent in the beam steering method based on delay lines. Each controllable antenna element

is connected to a summator via a delay line that compensates for the spatial advance of its signal with respect to the signal with the maximum propagation delay. This method allows to have a single frequency-independent program for beam steering, bandwidth being limited only by characteristics of individual dipoles, and to resolve signals that have a characteristic length less than the electromagnetic waves travel time along the antenna. Drawbacks of the phasing system based on delay lines are complexity and big electrical losses. The latter can be compensated by the introduction of a pre-amplification system.

The UTR-2 phasing system is constructed on the temporal delays principle. It includes 439 delay blocks (that are nevertheless called "phase shifters", by convention) with variable cable length delay lines. The delay lines are built on a binary principle: n cells provide 2^n different time delay values. All phase shifters are placed underneath the antenna arms in three underground tunnels (collectors) and controlled by a single central control panel. In order to control the beam automatically according to a given observational program (for example, to follow a cosmic source) the control system computes local angular coordinates for a given object at successive times, and generates code signals to control the phase shifters (Fig. 2.3).

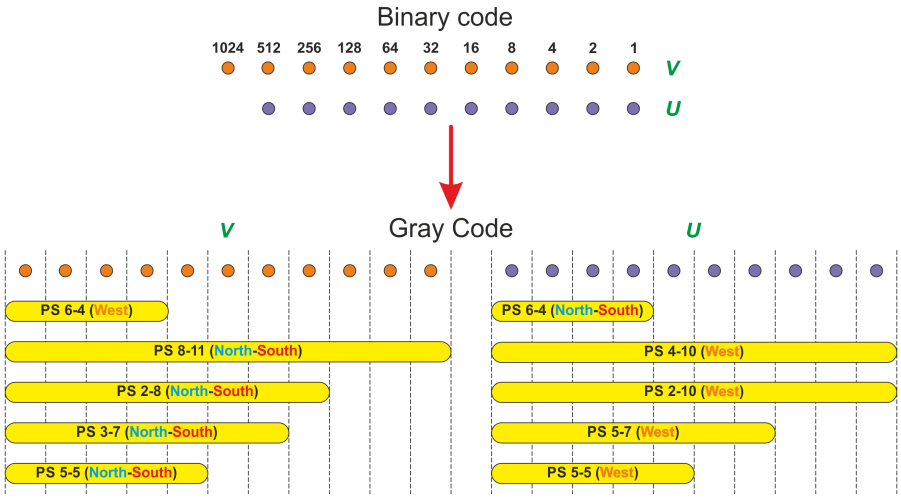

Figure 2.3: UTR-2 beam steering control. The phase shifters installed at UTR-2 are shown along with the control code digits that they use. The more significant digits control lower levels of phasing system, and thus provide larger displacement of the beam on the sky during pointing. Only the biggest phase shifters (PS-8-11, PS-4-10 and PS-2-10) use the least significant bits and thus provide the finest pointing, being switched at every re-pointing. Phase shifters are arrangend in columns that correspond to phasing either in v or in u coordinate.

In order to optimize the phasing system and reduce the cable length (and hence losses), a multi-level tree-structured phasing scheme was organized at UTR-2. At

each level a group of antenna elements is phased, resulting in the formation of a fractional directional pattern of this level. The resulting antenna pattern of the entire antenna array is the product of the fractional directional patterns of all phasing levels. The fractional directional patterns of the different levels are controlled asynchronously, i.e. for each position of the beam all the levels are phased in close but not coincident directions.

Since the distance between the steerable directions of the phasing changes 2-fold from level to level, it is desirable to have a different number of time delays (corresponding to beam positions) at each level, proportional to the distance between the elements, connected by the phase shifters of the given level. At the lower levels of phasing system, combining a small number of close-by elements, the width of the directional pattern is large, and hence the number of beam positions is small. The directional pattern of every higher level is more narrow compared to a lower level and therefore more beam positions are possible. Eventually, at the last level the number of beam positions is equal to the total number of beam positions of the whole antenna array.

Mutual phasing of directional patterns of different levels is made in such a way that for any position of the beam phase errors due to the asynchronous control should be minimal. This corresponds to their position when the maximum of each fractional diagram in the first and last positions is shifted with respect to the edges of the sector by half of the interval between adjacent positions. In Fig. 2.4 the relative positions of the fractional patterns of a three-level phasing system are shown. At the first level there are two beam positions, at the second there are four, at the third - eight. Optimal placement of the factors for the first three positions of the antenna beam is shown in the lower part of the figure.

In the UTR-2 phasing system, phase shifters with fixed phase center are used. In this case, the dipoles are always phased in pairs symmetrical with respect to the phase center. The full length of the discrete delay line is placed between the two dipoles and, during the steering, corresponding cells are switched from one dipole duct to another. Thus the sum of the delays applied to these two dipoles remains constant, i.e. the phase center of the system is fixed. The advantage of such phasing system is the simplicity of its control. The system control is based on supplying voltages to the switching elements, corresponding to the binary representation of the beam position number. The phase shifters with fixed phase center are controlled by the Gray code[3]. In the Gray code when switching to the next number, only one digit changes at a time. For example, the sequence of numbers from 0 to 7 looks in the Gray code as follows: $000, 001, 011, 010, 110, 111, 101, 100$. This allows to extend the durability of the commutable delay lines by minimizing a relay switching rate. The main element of the phase shifter is a time delay switch, consisting of the switching elements (relays) and a segment of high-frequency coaxial cable.

The ability to work simultaneously with five beams, spaced by about a half-power beamwidth of the antenna pattern, was initially intended to cope with refraction of

[3] https://en.wikipedia.org/wiki/Gray_code

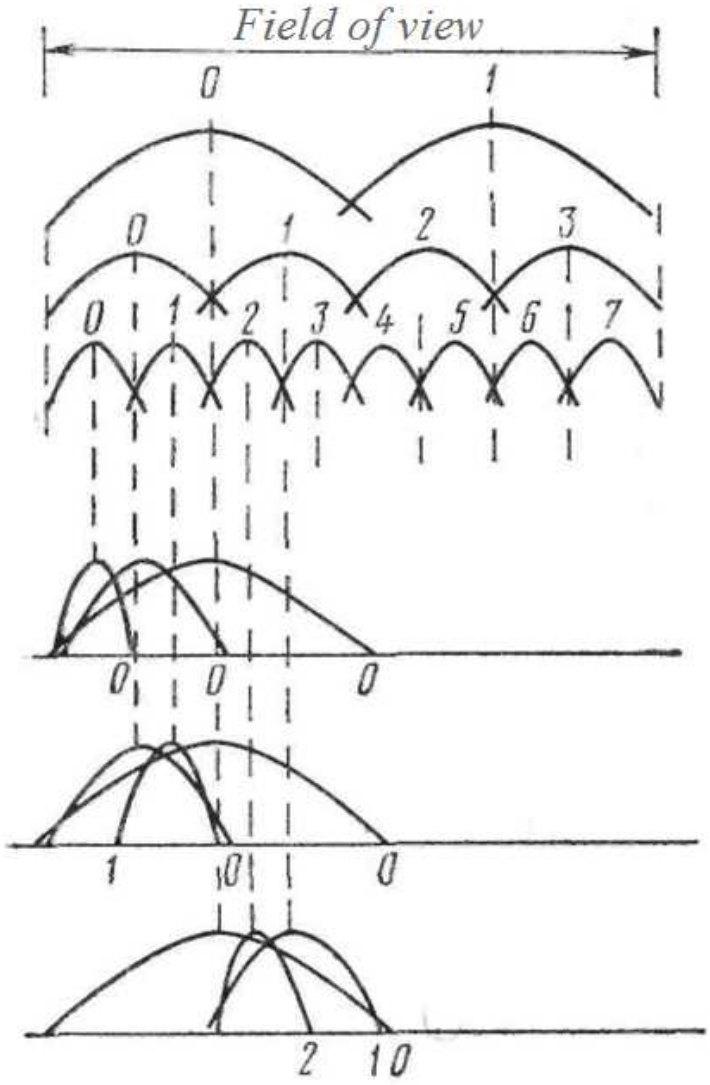

Figure 2.4: Asynchronous multi level phasing. The resulting beam is a product of partial beams of all phasing levels. From one pointing position to anoter, the value of this product changes considerably, causing the "jumps" in background. Three consecutive pointing positions are shown. The lower the phasing level (closer to dipoles), the less frequently it is re-pointed.

radio waves in the ionosphere. Now it is also used to provide rough sky mapping.

Several independent beams can be formed either by phase matrices or by systems of temporal delays. The latter are used at UTR-2. The distance between the dipoles being roughly a half wavelength, the number of beams for UTR-2 may in principle be equal to the number of rows along the longer side of the antenna. However, in the case of a large antenna such systems that provide a broad simultaneous field of view are technically or computationally costly. Another option - the formation of n independent beams with separate management of each of them - is the best in terms of capabilities of the instrument, but is also technically difficult, as it requires the creation of n identical phasing and control systems and, in addition, a substantial increase in the number of antenna amplifiers. At UTR-2 a much more simple method that combines multibeam capabilities and electric control of group of beams is used. The signals of each section of the N-S antenna are split into five identical signals and are transferred to the beamforming block. The beamforming block has 5 phase shifters, working in parallel, each with a fixed delay line. These phase shifters incline the beam to the direction of north and south from the central position with step $\sim 23'$ at 25 MHz. Thus the 1^{st} beam is shifted by $46'$ to the south, the 2^{nd} - by $23'$, the 3^{rd} is not shifted, the 4^{th} and 5^{th} are shifted to the north by $23'$ and $46'$, respectively.

The radio telescope antennae are phased in the aforementioned discrete way. Along the short sides of the antennae, phasing is made by a one-level synchronous scheme, whereas along the long sides it is made by an asynchronous multi level scheme. There is also a third system that provides mutual phasing of the antennae along the u coordinate, which is necessary due to the spatial separation of N-S and E-W antenna centers. To compensate for the losses arising from the large antenna dimensions and thus long delay lines, and to simplify the system of multiple beam forming as well as to reduce the side lobes, both antennae are divided into sections of 180 dipoles in the N-S antenna (30 groups of 6 dipoles) and 150 dipoles in the E-W antenna (25 groups of 6 dipoles). Fig. 2.5 and 2.6 show the phasing scheme of the N-S and E-W antennae respectively.

High frequency relays are used as commutation elements in the phase shifters. Each relay contains 6 switching contacts in one box. Using these relays permits to phase and sum up to six signals at once. The delay lines in the phase shifters are made of 75 Ohm coaxial cable.

Initially, the phasing is carried out along the short sides of the antennas, since in this case each antenna requires only one control system. Therefore in the sections of the N-S antenna the signals of rows of 6 dipoles (1 in Fig. 2.5) are phased and summed first along the E-W direction (u coordinate) by four-digit phase shifters PS-6-4 (2 in Fig. 2.5). In the name PS-6-4, 6 refers to the number of input signals (6 dipoles), and 4 is the number of time delay cells, providing $2^4 = 16$ beam positions in the sector $|u| < 0.84$.

Phasing of one section in v coordinate is implemented as a three-level scheme, pointing 256 beam positions in the sector $|v| < 1$. After the phase shifters PS-6-4 the signals of 5 rows of dipoles in each section are fed to five-digit phase shifters PS-

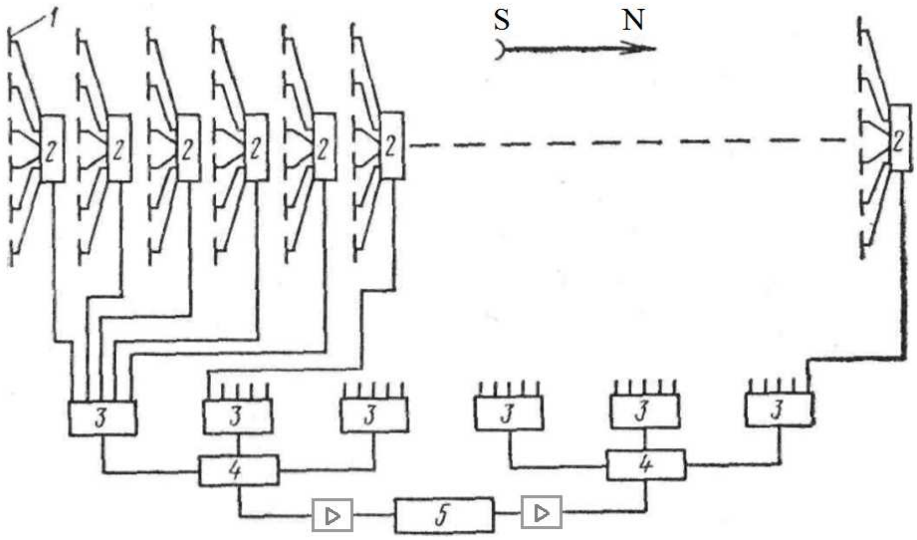

Figure 2.5: Phasing scheme of the N-S antenna section. *1* - dipole; *2* - PS-6-4 (phase shifter with 6 inputs that provides 2^4 beam positions); *3* - PS-5-5; *4* - PS-3-7; *5* - PS-2-8.

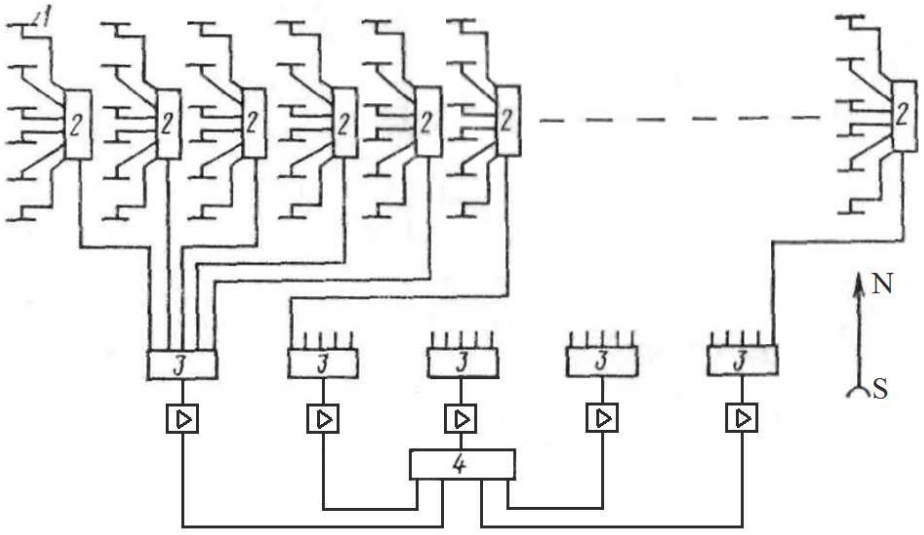

Figure 2.6: Phasing scheme of the E-W antenna section. *1* - dipole; *2* - PS-6-4 (phase shifter with 6 inputs that provides 2^4 beam positions); *3* - PS-5-5; *4* - PS-5-7.

5-5 (3 in Fig. 2.5). Then the six output signals of PS-5-5 are fed to two seven-digit PS-3-7 (4 in Fig. 2.5), and eventually to one eight-digit PS-2-8 (5 in Fig. 2.5). Thus each of the 8 sections of the N-S antenna is phased.

In the E-W antenna sections, the groups of 6 dipoles (1 in Fig. 2.6) are first phased in v coordinate. It is done along the N-S direction by means of 25 phase shifters PS-6-4 (2 in Fig. 2.6), providing 16 beam positions in the sector $|v| < 1$. Phasing in u coordinate is two-level and asynchronous. It is done by 5 five-digit phase shifters PS-5-5 (3 in Fig. 2.6), and eventually one seven-digit phase shifter PS-5-7 (4 in Fig. 2.6), providing 128 beam positions in the sector of $|u| < 0.84$. Further phasing of the signals is shown in the block diagram of the radio telescope (Fig. 2.7).

Phasing between sections 1-12 is performed after amplification of signals by the second stage antenna preamplifiers (2 in Fig. 2.7). Sections of N-S antenna (1-8) are phased in v by the phase shifter PS-8-11, and sections of E-W antenna (9-12) in u by the phase shifter PS-4-10, providing 2048, and 1024 beam positions, respectively. The relative phasing of the two antennae (N-S and E-W) is performed by the phase shifter PS-2-10 after an additional signal amplification by the fourth stage antenna preamplifier (4 in Fig. 2.7).

Fig. 2.7 shows the basic elements of UTR-2. After the fourth stage antenna preamplifiers (4) hybrid couplers are inserted, allowing to have independent outputs of all sections (I and III in Fig. 2.7) as well as groups of 2 and 4 sections (II and IV in Fig. 2.7). Similarly, after a beamforming block that creates 5 beams, the hybrid couplers allow to separate the signals of 5 N-S antenna beams (V) and by means of multiplication with the E-W antenna to form thirty outputs of the radio telescope (VI), six outputs from each beam.

In modulation mode, the signals of the two antennae are multiplied by means of phase modulation in the diode modulators (M in Fig. 2.7) that change the phase of one of the antennae signals by π. The multiplication of the two antenna patterns is obtained by the following expression:

$$(U_1 + U_2)^2 - (U_1 - U_2)^2 = 4U_1U_2. \tag{2.4}$$

In order to ensure high reliability the radio telescope is equipped with an automatic control/troubleshooting system. The overall control system allows to check operability of the telescope as a whole by measuring the precise shape of the directional pattern. The differential control system allows to check the amplitudes and phases of the signals at the outputs of the phasing system.

The large losses that arise in the long connecting cables and phasing equipment of the radio telescope are compensated by a broadband (7.7 . . . 37 MHz) antenna preamplification system. It has four stages with a total gain ranging from 35 dB at the lower end of the frequency range to 70 dB at the upper end. Three suboctave bands and push-pull scheme of amplification module allow to suppress by dozens of dB all even non-linear products - harmonics and combinations. As mentioned above, the non-linearity by third order intermodulation (input IP3) exceeds 50 dBm at 8

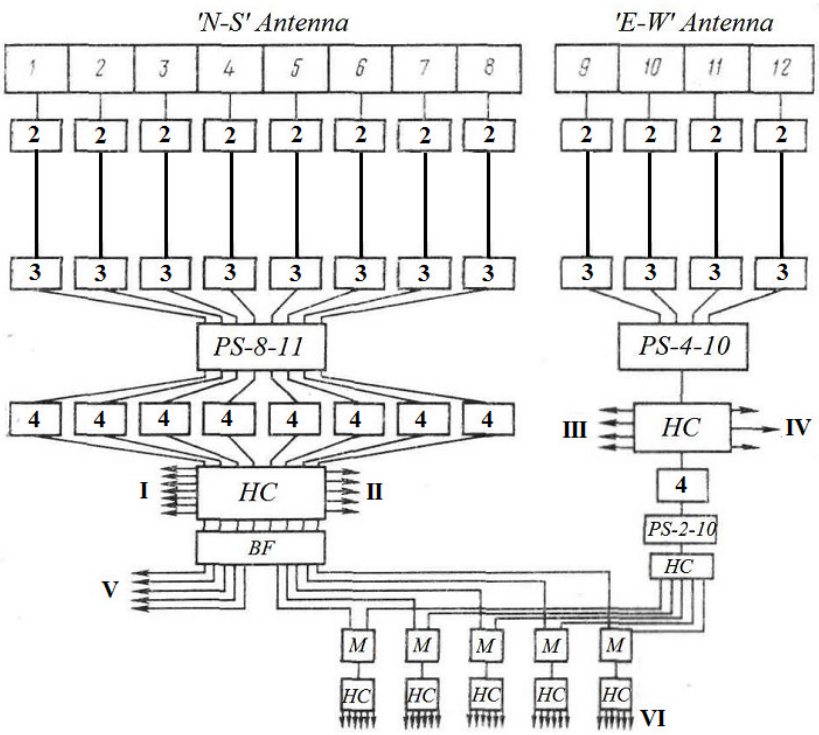

Figure 2.7: Block diagram of the UTR-2. *1-8* - sections of N-S antenna, *9-12* - sections of E-W antenna; *2,3,4* - second, third and fourth stage preamplifiers; *HC* - hybrid coupling devices, *M* - modulators; *BF* - beamforming block; *I-VI* - outputs; *PS-8-11, PS-4-10, PS-2-10* - principal (most beam positions) phase shifters.

MHz. This gives a possibility of permanent operation at all times in the most severe interference conditions.

Since UTR-2 commissioning various components benefited from a significant modernization. This included modifications of the pre-amplification system, data acquisition system, beamforming system and control devices. Since 2014 UTR-2 is fully automatized and available for remote control (under the condition of stable internet connection).

2.1.3 Receivers

The recording equipment changed revolutionarily in mid-2000s with the installation of the DSP-Z receivers [Kozhin 2007], [Ryabov 2010]. These are broadband digital receivers designed and built as part of the first exoplanet radio search programme at the Institute of Radio Astronomy of NASU. At the moment 5 such receivers are installed at UTR-2, one for each telescope beam. They have two-channel inputs with 16-bit analog-to-digital (ADC) converters and FPGA for computing and accumulating instantaneous spectra on-the-fly. All receivers are synchronized by means of both internal and external synchronization. Internal synchronization is based on the intrinsic computer clock (quartz crystals) of each receiver, whereas external synchronization is powered by a rubidium time/frequency standard with relative frequency (in)stability of $\sim 5 \times 10^{-12}$ and GPS pulse-per-second generator. The rubidium standard provides sufficient short-term synchronization, whereas long-term synchronization is done using the GPS clock. All receivers are connected in a single network and can be controlled remotely by sending the executive commands to the corresponding Ethernet port using the TCP/IP protocol.

The receivers can record data in three modes: (i) 'waveform', (ii) 'spectra', (iii) 'correlation'. In 'waveform' mode the data flow from the ADC output is recorded to the hard drive directly, without any processing. The data rate is ~ 264 Mb/s. It determines the maximum output data rate of the telescope ~ 1 Gb/s (5 receivers)

In the second recording mode ('spectra') the input signal is converted into a 2-dimensional (time, frequency) spectrogram. Each slice in the spectrogram (individual spectrum) is obtained by means of Fast Fourier Transform (FFT) of the weighted time series with subsequent averaging selected by observer. The phase information is lost in this mode. The typical data rate at the time resolution of 100 ms is ~ 327 kb/s. The last recording mode ('correlation') provides recording of power spectra of the two channels, along with real and imaginary parts of their complex cross-correlation. The data rate is twice the data rate of the 'spectra' mode.

Parameters of the ADC block of the receiver are given in Table 2.1. The 16-bit resolution of the ADC ensures a high dynamic range allowing operation in an interference polluted environment. A high sampling rate allows recording of a broad band at once. The processing boards are designed for data acquisition, computation of spectra and recording of spectrograms to the hard drive. They have PCI-X interface and are installed into a standard computer workstation, along with the ADC. Board parameters are given in Table 2.1. Parameters of time resolution and

bandwidth of the data recorded by the receiver may be selected in a wide range. The waveform data is recorded at a temporal resolution limited by the clock frequency (15 ns for 66 MHz). Spectra and correlation products can be recorded with temporal resolution between 0.25 and 100 ms. Spectral resolution is fixed at 4 kHz.

Table 2.1: Main parameters of the DSP-Z receiver.

	Parameter	Value
ADC	Number of input channels	2
	Input frequency band	180 MHz
	Input voltage range	± 1 V
	Sampling frequency	$10 - 130$ MHz
	Number of bits	16
	Dynamic range	73 dB
	Intrinsic noise	-117 dB
	Maximum output data rate	2.5 Gb/s/channel
	Receiver-PC interface	SATA
Processing board	Number of FFT points	16384
	Processing rate	8500 spectra/s
	# of integrated spectra per output spectrum	$2 - 1024$
	Maximum output data rate	200 Mb/s

The data format (*.JDS) contains a header with information such as the time of observation, time resolution, sampling rate, frequency range, synchronization method, recording method (waveform, spectra, correlation) etc. These parameters are used in the subsequent data processing. The observer can choose to create data files of specific size or length, rather than record all the observation data in one output file. Usually the file creation is not synchronized with the telescope pointing (when tracking the source). Each created file is supplied with a standard JDS header and the counters containing status information. For example, if the receiver records spectra the counters are placed in the two topmost frequency bins of each spectrum.

2.2 GURT

Modern radio astronomy requires high sensitivity and large continuous bandwidth. Although UTR-2 has been constantly modernized, it has its limitations, mainly its bandwidth and single linear polarization. Therefore the Institute of Radio Astronomy started the construction of a new radio telescope, compatible with UTR-2, but

with a broader frequency range ($8 - 80$ MHz), larger effective area (~ 1.3 km ^{2}), full polarization measurement capabilities and a digital phasing system – the Giant Ukrainian Radio Telescope (GURT).

the first 3 sections of GURT of 25 dipoles each are now fully operational and are used for observations of the Sun, Jupiter, strong radio sources and a few pulsars. Each section includes 5×5 active dipoles phased in analog way (the distance between the dipoles is 3.75 m). For phasing signals between sections, digital phasing will be used. In total there will be > 100 sections (Fig. 2.8).

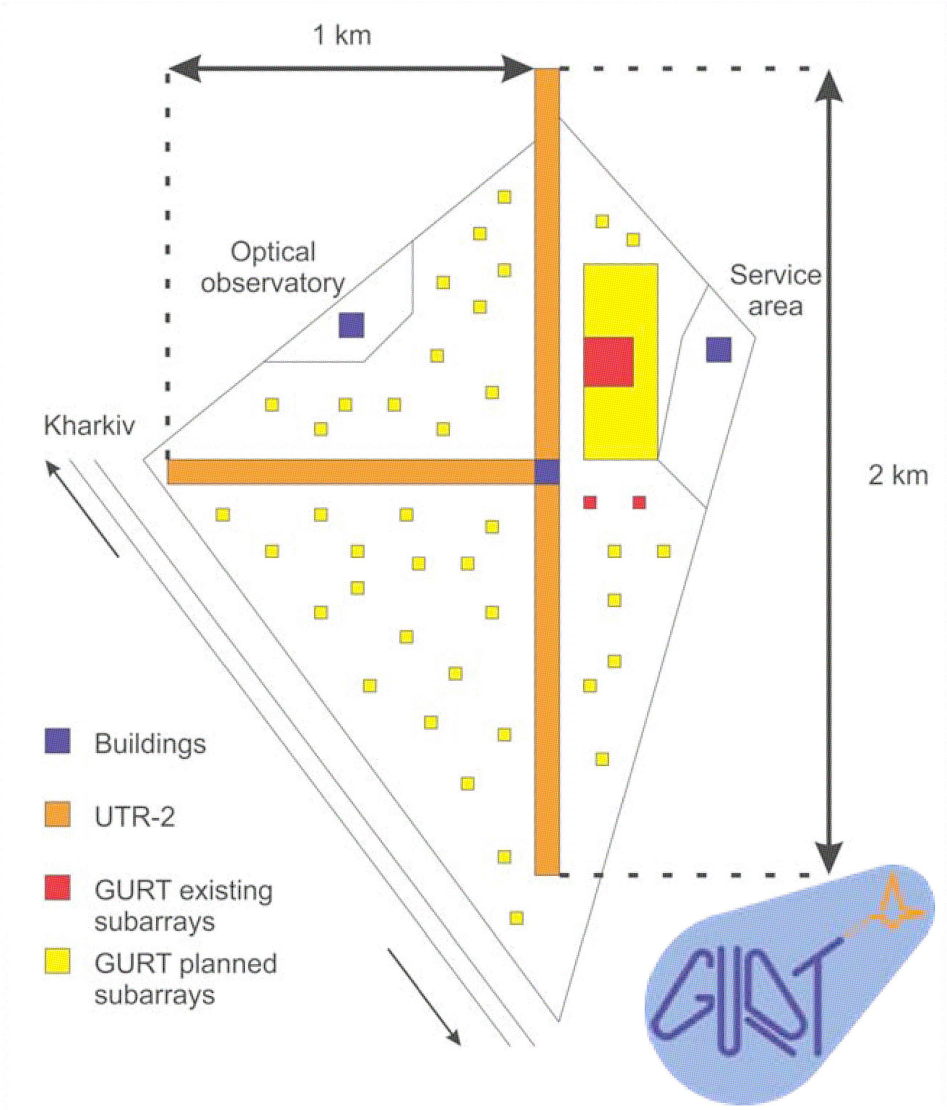

Figure 2.8: Location of existing and planned (in near future) GURT sections. From [Konovalenko 2014].

High interference immunity of GURT will be ensured by high dynamic range of

antenna amplifiers $\sim$ 90 dB (IP3 $\sim$ 30 dBm).

A new modification of receiving equipment, the advanced digital receiver (ADR), has been developed in the Institute of Radio Astronomy to fulfill the needs of this new telescope. Similarly to DSP-Z it has 2 channels and 16 bit ADC, with 160 MHz sampling frequency. It performs real-time 16384 channels FFT, records waveform or computes on-line auto-spectrum, cross-spectrum, sum-difference, and normalization (subtraction of average) of each channel.

In the present work we discuss processing of UTR-2 data only, while mentioning the prospects of observations using GURT as well as LOFAR and NenuFAR radio telescopes.

2.3 Survey for pulsars and transients at UTR-2

Several surveys have been carried out at UTR-2 so far [Braude 1978a, Braude 2002], but the present survey uses a different approach, connected to the lack of confusion effect for pulsars and transients. The survey uses Earth rotation in order to scan different areas of the sky by right ascension coordinates, and the five beams of UTR-2 in order to cover a range of declinations (Fig. 2.9). The difference from the previous surveys is the non-use of the modulation operation mode. Thus, instead of using narrow beams of antenna pattern (obtained by multiplication of the two antenna signals, Fig. 2.10 left) the survey is recorded in the wide crosswise beams of the sum of N-S and E-W antennae (Fig. 2.10 center).

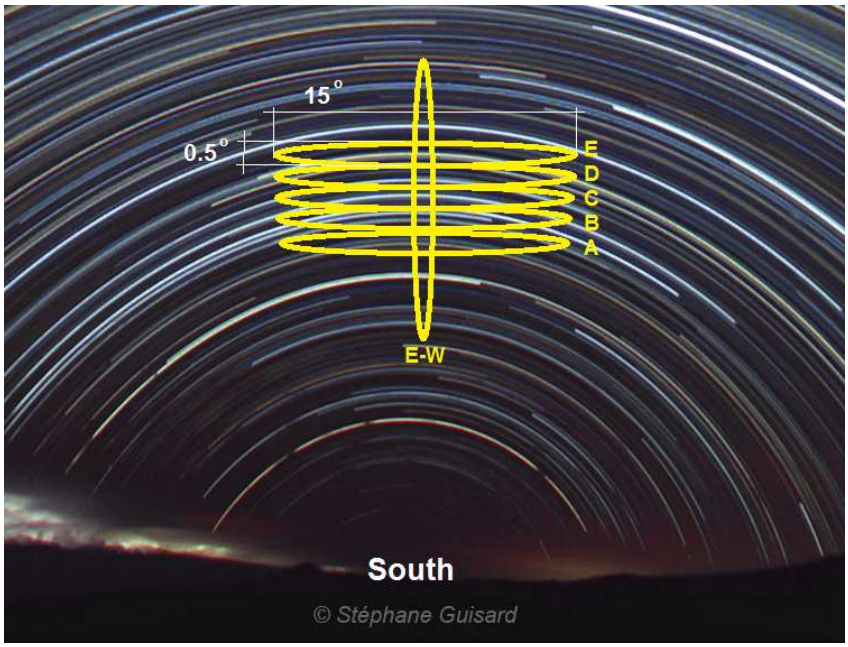

Figure 2.9: Five beams of the N-S antenna (A,B,C,D,E) and beam of E-W antenna of UTR-2 pointed on the celestial meridian.

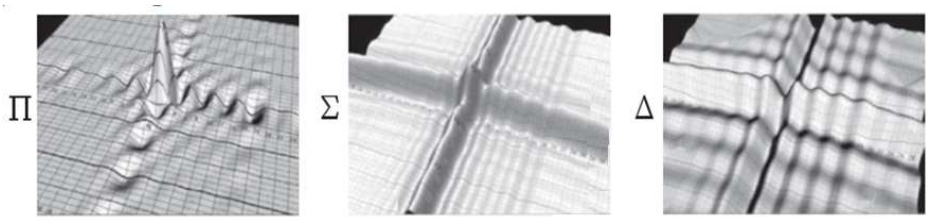

Figure 2.10: Product ("pencil beam"), Sum ("knife") and Difference patterns of the N-S and E-W antennae in the (u, v)-plane (pointing to the zenith direction).

Sources cross this beam during about an hour (Fig. 2.9 left panel), which is advantageous both for pulsars (as we can accumulate a sufficient number of pulses) and for transients (as the probability to detect a transient grows with increasing field of view). Considering that the narrow pencil beam is crossed by a source during 2 minutes, the sensitivity to a periodic source increases significantly when using a wide antenna pattern. For transient sources, though, the accumulation is impossible, and the resulting sensitivity is equal to the instantaneous one, but the field of view is determined by the crosswise pattern of the sum: $30' \times 15^o$ along E-W direction and $1^o \times 15^o$ along N-S direction, which is approximately 100 times larger than the pencil beam ($30' \times 30'$).

The use of 5 beams speeds up the survey and allows to track the same source as it crosses different beams. The centers of the 5 beams are placed in the local meridian plane. The total width in the declination coordinate, occupied by the 5 beams, is 2.5^o. Each day the beams are lifted up by 2.5^o from South to North, and a new strip of the sky is recorded. Thus, in ~ 40 days of continuous recording the whole Northern celestial hemisphere will be covered. As we want to have better interference conditions and weaker influence of the ionosphere, the 40 full days transform into the 80 nights with 6 month interval between the two observational sessions of 40 nights each. We selected the lowest declination (-10^o) that we wanted to record in the survey, from the condition of losing no more than half of the antenna effective area compared to the zenith direction when steering the beam to that position (coordinates of UTR-2: $49^o38'10''$ N, $36^o56'29''$ E).

The survey temporal resolution was chosen to be 8 ms, based on the typical scattering time constants for the pulsars in the decameter range. Only a few of pulsars have this parameter less than 8 ms, therefore almost all the pulses that we receive will be smeared by more than 1 time resolution point. There is no need to make the time resolution higher, but it also shouldn't be much lower, because for short periods of pulsars we need to have at least a few dozens points to resolve a period. In this survey we don't search for millisecond pulsars that are hardly detectable in the decameter range. We focus on the relatively close objects with periods $> 50 - 100$ ms.

The survey frequency range is $16.5 - 33.0$ MHz, the upper half of the UTR-2 frequency range. It is divided into 4096 partial frequency channels, i.e. the frequency

resolution is about 4 kHz. It has been chosen due to better interference conditions (especially in the evening and morning hours) and due to the fact that the majority of pulsars have weak emission below 15 MHz.

Initially we scanned the range of dispersion measures from 0 to 30 pc cm^{-3} (which corresponds to $1-2$ kpc maximum distance to the sources with low galactic latitudes). After that, the range of dispersion measures can be extended up to 100 pc cm^{-3} if it proves useful (e.g. to search for more distant transients). For recording and processing one snapshot of northern sky, the required disk space is $\sim 80-100$ Tb that results in ~ 40000 hours of processing time on a single workstation.

2.4 Observations of known exoplanets at UTR-2

Observations of known exoplanets are made at UTR-2 since 1996. They started with the use of an acousto-optical spectrum analyzer (an analog fast multichannel receiver), and eventually continued using DSP-Z. The common approach that was followed in every observation is the use of the '*On-Off*' principle. It means that there is a potential signal of interest and a reference signal that are processed together. The signal of interest in this case is radio emission coming from the direction of a known exoplanet. The reference signal may be the signal coming from another close-by direction of the sky. Therefore observations are made with two beams, separated by 1^o (Fig. 2.11). Having 5 beams of the N-S antenna of UTR-2, we chose the central (3rd) beam as '*On*' beam, and the 1st or the 5th beam (that don't have overlap with the central beam) are the reference signal ('*Off*').

Another way to obtain a reference signal is to use the difference signal of N-S and E-W antennae. The difference antenna pattern has a minimum in the direction to the source, so it amplifies the signals coming only from the parts of antenna patterns that are not common (i.e. all but the pencil beam). The difference signal represents the Galactic background around the source. The signal of interest is contained in the sum and product signals.

The last way to get a reference signal is a time-dependent one, when the source is kept in the beam for a known part of time. The other equal part of the time, the source is not in the telescope beam. In the case of UTR-2 the source (at the celestial equator) crosses the beam (at the level of HPBW) in about 2 minutes. Thus, in order to track the source, antenna beam position should be switched every 2 minutes. In order to realize the temporal '*On-Off*' scheme, the antenna pointings should be done more seldom (e.g. once every 4 minutes), so that the source drifts through the beam and goes beyond it.

In the present work we use the first two methods (spatial '*On-Off*' and use of the difference signal). The majority of known exoplanet observations were recorded in 'spectra' mode of the DSP-Z receiver. Records in 'correlation' mode also took place, but the algorithms of their processing applied to the exoplanet search have not been finalized yet. Waveform data have never been recorded for the purpose of detecting exoplanet radio emission as we need to integrate the signal in time and frequency

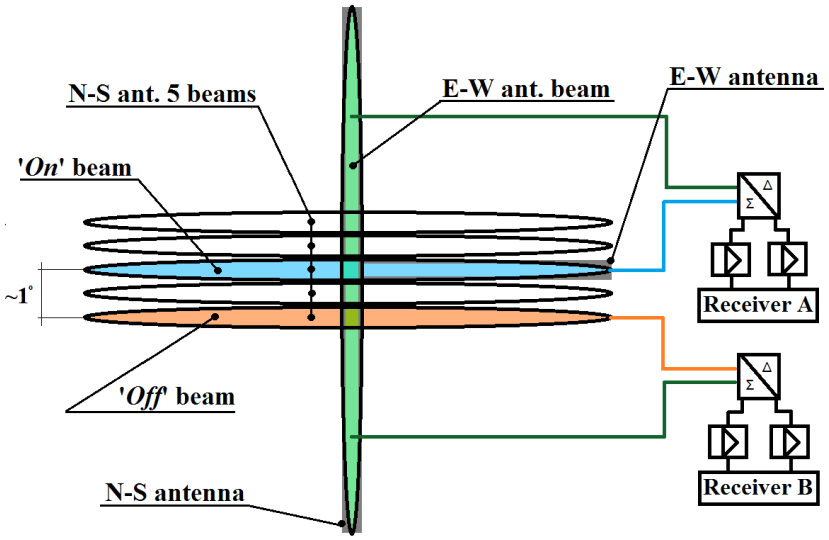

Figure 2.11: Setup of exoplanet observations. *On* beam (central beam of N-S antenna) is directed to the targeted exoplanet. Its output together with the output of E-W antenna are fed to Sum/Difference couplers, amplified and recorded by the receiver A. *Off* beam is directed 1^o aside and after coupling with E-W antenna its output is recorded by receiver B.

for high enough sensitivity. The time resolutions of the data recordings were in the range $20 - 40$ ms. The typical frequency band of observations was $12 - 33$ MHz or $16.5 - 33$ MHz, depending on the interference situation. All the exoplanet records at UTR-2 that are stored up to now and deserve a new processing occupy about 30 Tb of disk space.

Chapter 3

Pre-processing pipelines

Contents

A pre-processing pipeline is a number of automatized steps to prepare data for further analysis. It includes correction for instrumental effects and other hindering factors as well as reducing the data dimensions where possible. Usually it is referred to as data reduction, after which only the useful minimum of information is retained in the data.

As observations are carried out in decameter range (the lowest frequency range of the electromagnetic spectrum, available for ground-based observations), the signals of interest are distorted by strong influence of propagation effects, perturbed by the ionosphere and contaminated by numerous Radio Frequency Interference (RFI). At decameter wavelengths a good spatial resolution (which is determined as λ/D, where λ is wavelength, D - antenna aperture size) can be achieved only having an enormously large antenna array. UTR-2 being one of the largest existing radio telescopes, has minimum width of antenna pattern main beam $\sim 30'$. It means that a quite large area of the sky is captured by the beam, which might contain other sources besides the source of interest. Large antenna arrays are very complex instruments that are difficult to calibrate and that can produce unexpected instrumental effects. All aforementioned factors should be taken into account when studying faint astrophysical sources such as pulsars and exoplanets.

Observations at UTR-2 are made with 1-5 DSP-Z receivers, each of which has two input channels and may produce data with different time resolutions. Data is recorded in form of file(s), containing the header with main technical information, followed by the time-frequency arrays (dynamic spectra) of the two channels. During

one observational night of the pulsar/transient survey $\sim$ 180 Gb data is recorded by each of the 5 receivers. In 80 nights of survey it results in more than 70 Tb of data to be processed. Furthermore, all suspicious signals that resemble signatures of pulsars or transients (hereafter 'candidates'), will be re-observed in a follow-up observation session, in order to confirm or refute their detection. This will further increase the volume of survey data.

Observations of exoplanets were quite diverse, and the total data volume, accumulated since installation of DSP-Z receivers at UTR-2 is about 30 Tb. The fraction of Corot-7b data among them is small ($\sim$ 600 Gb in November 2009 and $\sim$ 1 Tb in November 2011), but we aim to have software tools that will be applicable for all existing data. Having this big data volumes, automation of pre-processing is vital. Manual processing becomes very time consuming and not feasible.

We developed a generic software for eliminating hindering factors and reducing the data. For compatibility reasons, both pre-processing pipelines (for pulsar/transient survey and exoplanet search) are written in Interactive Data Language (IDL). Previous analogs of these pipelines were also written in IDL and now various cross-tests are possible. In addition, IDL is a powerful visualization tool, which is vital for selecting candidates in the pulsar/transient survey and examining the data in different ways in the exoplanet search. Because of the different nature of studied objects (neutron stars and exoplanets) the algorithms vary in the two pre-processing pipelines, but nevertheless they have a large common part.

3.1 Common parts of the pipelines

As all data was recorded at UTR-2, a large common part of both pipelines is file management. DSP-Z equipment at UTR-2 evolved since first installation in 2006 through 3 versions of DSP-Z ('.jds', initially 'Jupiter data system') format. Each .jds file contains a header followed by two-channel data in the format of a dynamic spectrum (with dimensions FREQUENCY, TIME (f,t)). Formats of the header and status fields are different for the 3 different generations of DSP-Z. The format of the data itself has a modified floating point notation. In order to have high dynamic range, the floating-point coefficient is extended at the expense of several bits allocated for the exponent.

The recordings of exoplanet candidates were made at different stages of receivers modernization. In contrast, pulsar/transient survey was started in 2010, and all data are recorded with the same version of DSP-Z receiver. The file reading programs work with all DSP-Z versions and transform a data file into dynamic spectrum, an array with (time, frequency, intensity) coordinates that represents how signal intensity varies with time at different frequencies of telescope operation range. Fig. 3.1 shows an example of dynamic spectrum containing Jupiter radio emission.

Data can also be calibrated in the same way for both pulsar/transient survey and exoplanet search, as the underlying observational principles are similar. In the present work we use sky calibration, although for better RFI mitigation and

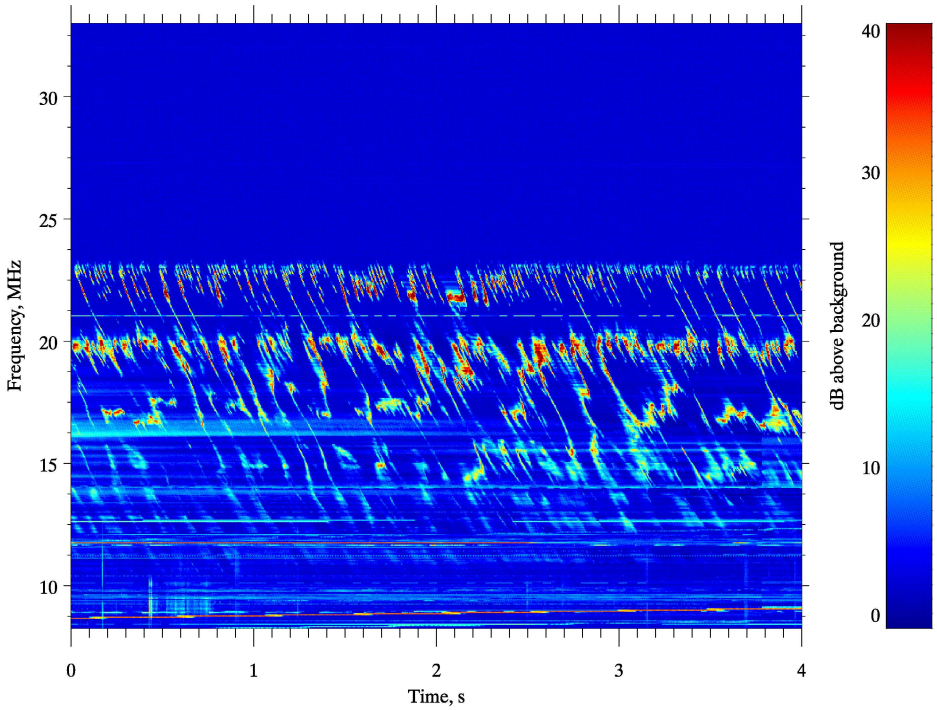

Figure 3.1: An example of dynamic spectrum with Jovian radio emission. Powerful drifting bursts in the frequency range 8-33 MHz have a rich time-frequency structure.

more accurate estimation of flux density there will be need for instrumental calibration. A major verification of UTR-2 and upgrade of calibration system are ongoing [Ulyanov 2015].

The radio frequency interference mitigation is a crucial step in radio astronomy data processing. Radio astronomy is aimed at detecting signals with various intensities. Sometimes the signal is quite intense, like solar flares and sporadic Jupiter radio emission, but more often it is very weak, even down to micro-Jansky level [Fomalont 2002]. In both studies we try to detect weak signals from distant cosmic sources on the background of strong terrestrial man-made and natural interference. The situation gets worse with decreasing observational frequency. Interference in the decameter range are numerous and intense (sometimes exceeding the sky background by 70-90 dB, assuming 4 kHz channel width). The only way to reduce their impact is to use high dynamic range devices on all signal path (through the telescope) and to apply sophisticated RFI mitigation algorithms. Currently the major radio telescopes use 12- or 16-bit ADCs at different stages of data acquisition. Comprehensive modernization has been done at UTR-2 [Abranin 2001] to increase its dynamic range and linearity. Now the analog part of the telescope is fully invulnerable to RFI, but the bottleneck is the digital equipment. The digit capacity and dynamic range provided by 16-bit ADC at UTR-2 is not enough to fully eliminate the impact of the RFI. Possibly, Using a 20-bit ADC could provide a considerable improvement in the quality of the data, and possibilities of RFI mitigation.

Every radio telescope has its own RFI environment that depends on the operating frequency and location (distance to cities, latitude etc.). Therefore at each instrument there should be a particular RFI mitigation pipeline. Although there is no universal RFI mitigation routine, the existing algorithms can be adjusted to the specific instrument. For example, if the observer is concerned only by strong RFI, with an intensity largely exceeding the useful signal, it is possible to specify a threshold, above which the samples should be removed from the data.

UTR-2 is located quite close to inhabited localities, and ~ 60 km from the big city of Kharkiv. The main producers of RFI are broadcasting radio stations, vehicles (ignition arcing), radars, ionosphere sensing stations, portable radio transmitters etc. Despite the telescope's operating range is 8-33 MHz, we can see the impact of the RFI from lower frequencies. The nonlinear element with lowest dynamic range (ADC in our case) produces at the output combination frequencies along with harmonics of input signals. For example, if there are two RFI signals at frequencies f_1 and f_2, at the output of the amplifier we will have such combinations as $2f_1 \pm f_2$ and $2f_2 \pm f_1$ etc. that can be in the telescope frequency range. Sometimes all frequency range is contaminated as a result of presence of several extremely intense interfering signals.

In addition to local RFI signals, the telescope receives ones that have been reflected from the ionosphere and the ground (propagated through the ionospheric channel). The limiting frequency, below which the signal is reflected back to the ground, depends on the ionization of the ionosphere, which is connected to the solar activity. During the night the RFI level drops dramatically, leaving mostly local

signals in the telescope frequency band.

In the UTR-2 data, except for the case of strong contamination, the RFI normally lie either along the frequency axis (short wide-band RFI) or along the time axis (narrow-band RFI) in the dynamic spectra. The exceptions are only chirp signals and signals of ionosphere sensing stations. Unfortunately, no RFI database has been created so far at UTR-2, but the data processing of major surveys (including the decameter catalog survey and the present pulsar/transient survey and large data sets of exoplanets observations) may give a lot of useful information about RFI as a by-product.

All the described peculiarities apply both to pulsar/transient survey and exoplanets recordings. Therefore, data in both situations might be cleaned in a similar way, only taking into account the different time resolutions and bandwidths of the data. A fundamental difference is that RFI mitigation of observations of exoplanets must be more severe to exclude any possible source of spurious signal, as we don't know how the signal of interest might look like.

In [Fridman 2001] the five major RFI mitigation techniques are listed: (i) thresholding in the time-frequency domain, (ii) utilization of filtering techniques, (iii) use of reference channels, (iv) spatial filtering and (v) cancellation of outliers in probability distribution of the power spectrum. In the present work for RFI mitigation purposes we mostly rely on techniques from the first category, while we also use other methods for reference (or confirmation of detection) at the post-processing stage.

The algorithms for identifying where data contains RFI become more and more sophisticated and computationally costly. They can vary from the simple comparison of each data point with calibration data to pattern recognition, advanced machine learning and neural networks. A successful method of RFI recognition should be able to identify RFI at least as good as the human eye. The human eye is not a perfect tool, because after removal of strongest RFI, the contrast of the dynamic spectrum changes, and it turns out that there are more interference in the data than what we could see before, but it is a good starting point. We composed a toolkit of several existing RFI flagging methods, that have different advantages and complement each other. We modified them to fit better the exoplanet search in UTR-2 data. Below I will describe two RFI mitigation tools that we have chosen for RFI cancellation in both pulsar/transient survey and exoplanet search pipelines:

- PATROL (simplified version of [Zakharenko 2013])
- Sum(Var)Threshold method (used in the LOFAR AOFlagger) [Offringa 2010], [Offringa 2012a]

They are parameterized, according to the nature of studied objects and specifics of the telescope. We combined them together to fully utilize their advantages and compensate for their drawbacks. And we developed a way to dynamically (adaptively) adjust the severity of RFI flagging depending on the input data.

3.1.1 Flagging polluted frequency channels and time intervals

The first method, called PATROL (Pulsars And TRansients Overall Lookup), was originally a part of RFI cancellation software, developed for data of known pulsar census at UTR-2 [Zakharenko 2013]. It is very fast, and it flags the whole bad frequency channels and time intervals in the dynamic spectrum. Bad frequency channels usually contain the signals of broadcasting radio stations, especially at the frequencies below 20 MHz and around 27 MHz, either local or reflected from the Earth ionosphere. These channels can be characterized either by anomalous mean value (generally high) or by anomalous variance (either large or small). Therefore, for identification of bad channels PATROL requires the values of mean (μ) and standard deviation (σ) of each channel, calculated from the raw (uncalibrated) data. If taken after flattening, these channels (that are also contained in the average spectrum, and divided by it) will be not as outstanding. μ and σ are calculated iteratively in each frequency channel, excluding the values above 3 σ_{it} at each iteration, until there are no more peaks left to exclude. Having μ and σ values for each channel, and dividing σ/μ, we get the dependence as in Fig. 3.2.

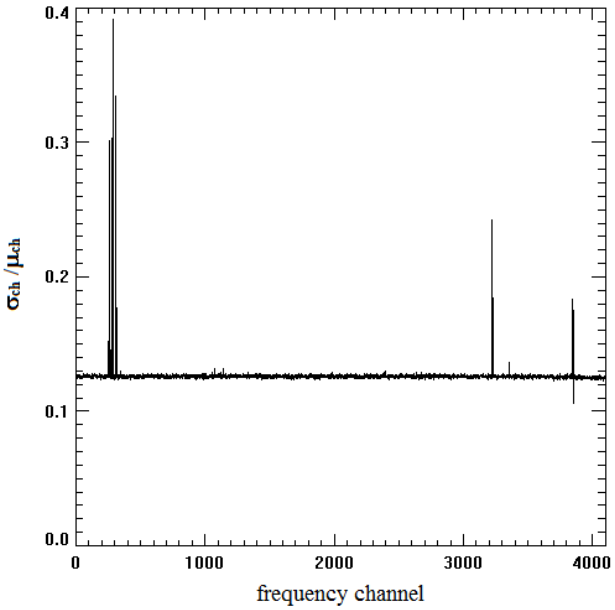

Figure 3.2: An input vector for PATROL - the standard deviation in each frequency channel divided by its mean. Peaks are frequency channels with highly variable intensity, dips are channels of high constant intensity. Both types of channels most likely contain RFI.

Here the maxima are all the channels with high variance and low mean value, and the minima are the channels with highly intense quasi-constant signals. This representation allows to detect both types of bad channels, as they are outliers in

this graph. All the other channels have approximately same mean value, as μ and σ are correlated ($\sigma = \frac{\mu}{\sqrt{b\tau}}$, where b and τ are frequency and time resolutions, respectively), and therefore, if the value at certain channel is strongly (3-4 standard deviations of the distribution of e.g. fig. 3.2) different from the mean, then we consider that channel contaminated.

The situation with polluted time intervals is more simple. Usually there are only short wideband spikes, produced by the telescope equipment or nearby vehicles or natural sources such as lightning. They significantly exceed the average fluctuations of background noise, and even the weakest are visible by eye, although are not easy to eliminate. If we integrate a dynamic spectrum over frequency, producing an integrated time series, we will see peaks at the positions of every wideband spike. Every frequency channel contains a part of this spike, and contributes to the resulting peak, so then the peaks are significantly above the average value. They are detected using a threshold of 2.7 - 3.0 standard deviations above the running average of the time series.

Sometimes a channel is affected part of the time, and then the transmission is stopped (as in the case of walkie-talkie). The signal can also have a linear frequency modulation (as in the case of ionosphere sensing stations), so its frequency decreases or increases with time, affecting many adjacent frequency channels for small periods of time. Also a dynamic spectrum can have low-intense spots or intensity fluctuations due to ionospheric effects. Unfortunately, the described types of RFI are either missed out by the PATROL RFI flagging module (if they are weak) or flagged along with the whole channels and time intervals containing them (which is also bad as we lose many useful data points). Fig. 3.3 a) shows a calibrated 2-minute data frame containing RFI and the result of RFI flagging by PATROL - the 'mask', which is an array of 0 (polluted pixels) and 1 (clean pixels) weight.

3.1.2 Flagging patches in time or frequency direction

Another method, called SumThreshold method [Offringa 2010], was developed by A. R. Offringa as the default LOFAR RFI mitigation pipeline. It is a very effective but time-consuming tool. The method is multi-purpose: by slightly varying its parameters, it can be tuned at different kinds of RFI. With default settings it performs quite well on LOFAR and WSRT data, with 95% recognition accuracy and about 0.1% probability of false positive flagging [Offringa 2010]. The method is described in detail in [Offringa 2012a], in section 'The SumThreshold method'. It is based on the CuSum method ([Page 1954, Basseville 1993]) and the similar VarThreshold method [Offringa 2012a], [Offringa 2010].

The main idea is that usually RFI form connected shapes either in frequency or in time direction. A set of thresholds is applied to the data, separately in time and in frequency direction, and the connected shapes of samples exceeding each threshold are found. A combination of N samples (either in time or in frequency direction) is entirely flagged as containing interference if all its samples (VarThreshold method) or its average (SumThreshold method) exceeds the threshold T_N (given in absolute

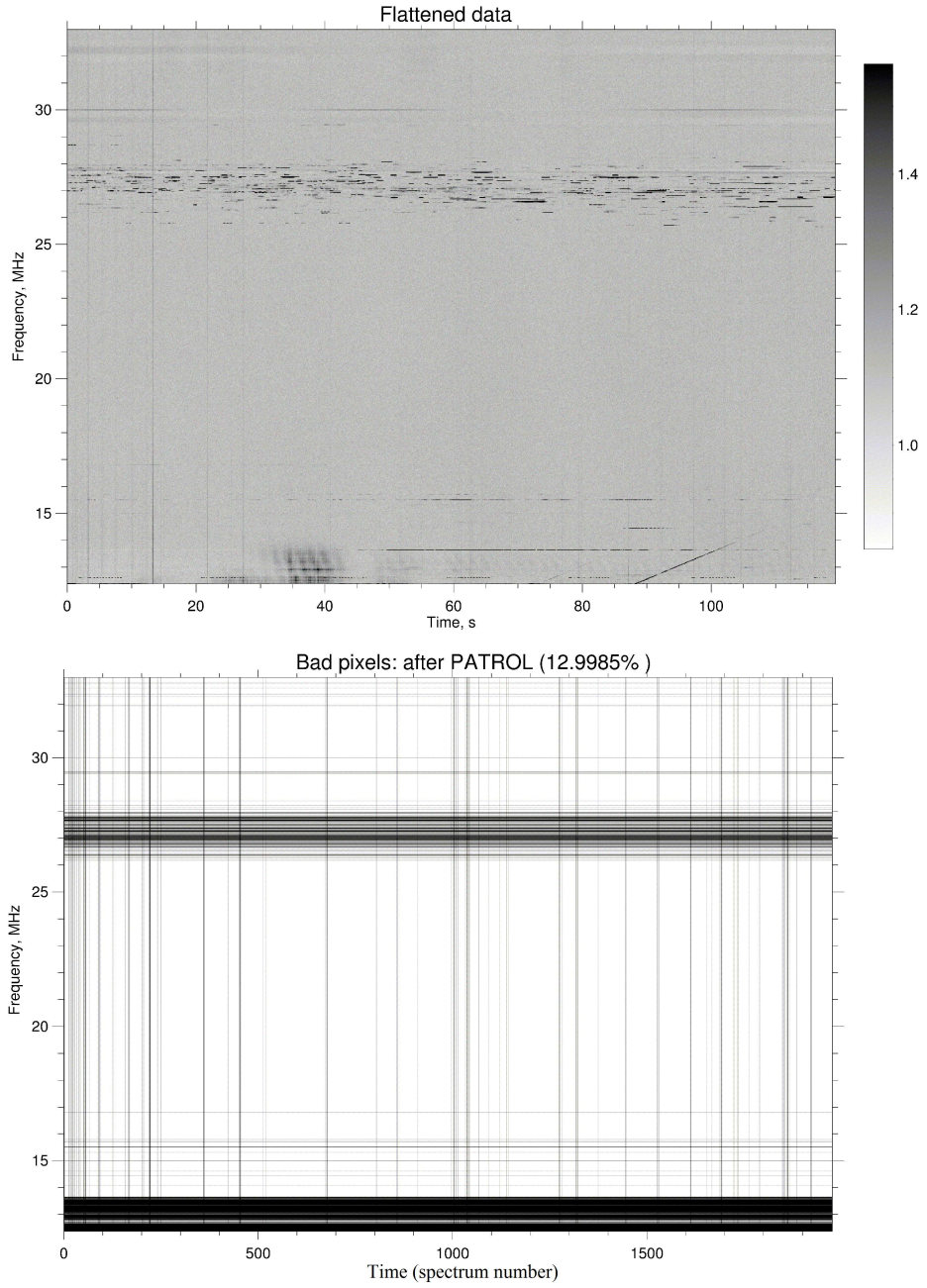

Figure 3.3: Normalized (flattened) dynamic spectrum (upper panel) and the resulting mask of bad pixels after RFI flagging by PATROL (lower panel). $\sim 13\%$ of the pixels have been flagged

value or relative to the standard deviation σ of the data). The sliding window size N is increased from iteration to iteration, and the larger is N, the lower is the threshold T_N, applied to the samples or their average. In the original VarThreshold method [Offringa 2010]

$$T_N = \frac{T_1}{a^{\log_2 N}}, \tag{3.1}$$

where T_N is the threshold for a combination of N pixels, T_1 is the threshold for a single pixel (default value $T_1 = 10$), and $a = 1.5$ is an empirical coefficient. N is thus the size of the sliding window (taken as powers of 2: 1, 2, ..., 64). The flagger passes multiple times (equal to the number of thresholds and window sizes) through each frequency channel (time direction) and then through each instantaneous spectrum (frequency direction) in the time-frequency plane, flagging increasingly weaker interference. Then the bad pixel mask of horizontal passes is merged (multiplied) by the bad pixel mask of vertical passes. The result of running this flagging method on the same calibrated data fragment as in Fig. 3.3 a) is shown in Fig. 3.4.

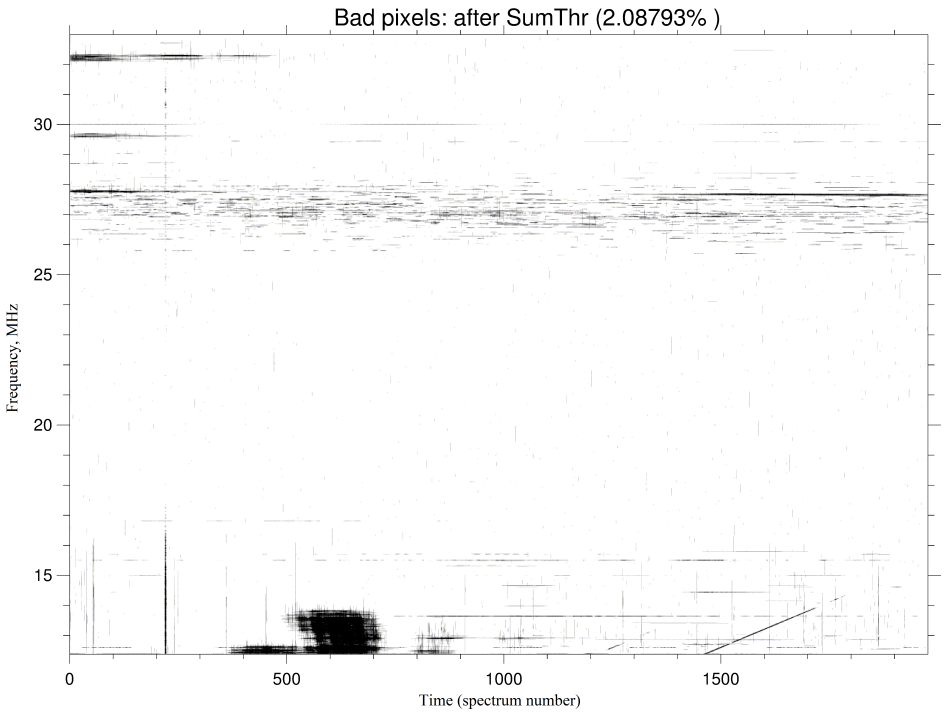

Figure 3.4: Resulting bad pixels mask after RFI flagging by SumThreshold: $\sim 2\%$ of the pixels have been flagged.

3.2 Specifics to Pulsar/Transient survey pipeline

A pre-processing pipeline for the survey is composed of:

- RFI mitigation (including sky calibration)
- dedispersion and data reduction

The differences between the pulsar/transient survey and the exoplanet search pipelines start with different observation strategy: the survey is in drift-scan mode, in which the beam is fixed and drifts through the sky due to Earth rotation, whereas exoplanets are continuously tracked by a steerable beam. The file management is easier for the survey, because the observation is uninterrupted, there are no abrupt changes in the background intensity (due to rephasing of the telescope) and the antenna effective area stays the same. As during the observations we don't have telescope pointings, we are not bound by the intervals between the pointings, and we can choose an arbitrary duration of data to process at once. The optimal size of the elementary dynamic spectrum to process from the standpoint of running time and efficiency of RFI recognition is 1024 instantaneous spectra. It is also consistent with the time-scale of the ionospheric fluctuations, so that the ionosphere can be considered constant within the elementary dynamic spectrum.

The detection of pulsars or transients should be also easier, compared to exoplanets, because the signal of interest is often repetitive (or periodic - for pulsars) and dispersed. These two properties are in favour of detecting new sources, because we know exactly how their signals might look like in the time-frequency plane. Nowadays a great variety of neutron star types is known. Regular pulsars emit short pulses every rotation period, pulsars with nullings emit not every period, intermittent pulsars might sometimes 'switch off' and stop emitting for thousands of periods, Rotating RAdio Transients (RRATs) emit one pulse in hundreds of periods. But generally the property of periodicity greatly facilitates detection of neutron stars in their different incarnations, especially normal pulsars. For normal pulsars, due to the possibility of accumulation of periods, sensitivity increases as $\sqrt{N_p}$ observed pulsar periods. As periods are short (milliseconds to seconds), in 1 hour of observation it is possible to accumulate several thousands of individual pulses. Practically, for this accumulation we need to know the pulsar period with high precision and have a high time resolution of the data, in order to resolve the period with enough data points and to avoid aliasing.

At decameter wavelengths we do not see individual pulses for the majority of pulsars, except for the closest ones and those that emit so called anomalously intense pulses [Ulyanov 2006] and giant pulses. But we still can detect them, because the weak radiation is present at the same longitudes in every period and shows up after accumulation. Other transients likely consist of individual pulses (or pulses that reoccur sporadically) that can be of various intensity. Only frequency integration favours the detection of such events.

Both pulsar and transient signals are strongly dispersed, which becomes most apparent in the decameter range. The dispersion delay should be compensated prior to spectral data integration. The pulses are lapsed in the time-frequency plane, which makes them different from the terrestrial interference, which are usually either

vertical (broadband) spikes or horizontal (narrowband) emitters. Thus, dispersion is another supporting factor for detecting pulsars and transients.

Despite the aforementioned helpful properties of pulsar radiation, interference is a serious hindering factor that reduces the dynamic range, introduces spurious periodicities and biases the data distribution. At the pre-processing stage we should remove as much RFI signatures from the data as possible, while not removing the dispersed pulsar/transient pulses.

3.2.1 RFI mitigation

Survey observations were intentionally planned during night hours of autumn-winter periods to avoid strong contamination by RFI and strong ionospheric effects. Therefore, survey data is rather clean with moderate inclusions of RFI-active periods in the evenings and mornings. Only when the wide crosswise beam of antenna pattern is tilted low, close to the horizon, it picks much terrestrial interference. The majority of the survey data contains persistent narrowband RFI from broadcasting radio stations and occasional wideband RFI from nearby vehicles or very distant terrestrial lightning, reflected multiple times under the ionosphere. Short RFI patches (as those from radars) and rare scintillations of strong cosmic sources, coming from the side lobes, also take place. Thus, RFI mitigation routines should be oriented at these RFI types and leave the useful data intact. It shouldn't just remove all bright signals in the dynamic spectrum, as transient signals might also be quite intense. For the present survey pipeline we assumed that it is better to retain some weak RFI rather than to remove useful signal during RFI mitigation. The second requirement is that RFI mitigation should be fast, in order to have the possibility of real-time processing.

Thus, we built the RFI mitigation process in three steps: (i) data calibration and normalization, (ii) detection of short patches in time and frequency directions and (iii) detection of entirely polluted frequency channels and spectra.

The first stage is combined with estimation of the mean and standard deviation in each frequency channel, described above in the section 3.1.1. In each frequency channel data is divided by the channel mean and is made zero-mean (by subtracting 1).

To deal with the second step, the best algorithm is SumThreshod, described above. It detects both short spikes and side lobe sources scintillations (that can also be decomposed to straight vertical and horizontal lines). The precaution is to not use a small window size at the same scale as the pulsar pulse. Due to finite time and frequency resolutions (8 ms and 4 kHz, respectively), pulsar pulse can be decomposed to small 'steps' - combinations of a few points in time or frequency directions. The characteristic size of these steps depends on the dispersion measure. After testing SumThreshold with different window sizes on recordings of several pulsars, the most appropriate set of window sizes was empirically chosen as $\{2, 8, 16, 128, 256\}$ for frequency direction and $\{1, 2, 4, 8, 64\}$ for time direction. Historically, we started to use SumThreshold with its default settings, and the single pixel threshold $T_1 = 10$

and decided to keep the same parameters for all the survey data. The third step is given to PATROL for detection of bad frequency channels and spectra with thresholds ($\mu \pm 4\sigma$) and ($\mu \pm 3\sigma$), respectively. The 'bad' values, flagged by SumThreshold and PATROL, and replaced by the median calculated only over 'good' values in each data fragment.

Each 1024-spectra fragment is cleaned by the described succession of steps and sent to a single output file, having the same header as the original data files. From the 2-channel receiver output, we process only the first channel - the Sum. The resulting file size is usually 90 Gb. For real-time processing the size of the created output file is the same as that of an unprocessed file. Then, consecutive cleaned files are concatenated for the convenience of further dedispersion. At this stage, we don't reduce the clean data neither in time nor in frequency. We need high time resolution, because the events we look for are short. In addition, if we find a pulsar candidate, even without reduction its period will occupy a few to a few hundreds time resolution points only. We need a high frequency resolution for more accurate dedispersion.

The images of original and clean dynamic spectra are kept as a reference for further processing steps. The percentage of bad pixels in the whole night of observations is stored in a log file. Typically, for one night of survey observations we mask out about 5% of data. On an average workstation, RFI mitigation takes about the same time as observation.

Fig. 3.5 shows the results of RFI mitigation for a typical data frame in the survey: Fig. 3.5 a) before, Fig. 3.5 b) after processing. Compared to a previous version of RFI mitigation routine (used in [Zakharenko 2013]), we gain a factor of 1.5 to 1.8 in signal-to-noise ratio of detected known pulsars. In Fig. 3.6 efficiency of the two routines (old and new) is compared on three known pulsars.

3.2.2 Dedispersion

Dispersion of radio waves is caused by the ionized interstellar medium because its refractive index is frequency dependent. It is characterized by dispersion measure (DM) which is defined as the integrated column density of free electrons on the line of sight (between observer and pulsar)

$$DM = \int_{line\ of\ sight} N_e dl. \tag{3.2}$$

Dispersion results in the slower propagation (and later time of arrival) of the same pulsar pulse at lower frequencies, compared to higher frequencies (see Fig. 3.7). The difference of arrival time at two frequencies f_1 and f_2 can be computed as

$$\Delta t = K \left(\frac{1}{f_1^2} - \frac{1}{f_2^2} \right) DM, \tag{3.3}$$

where $K = 1/2.410331 \times 10^{-4}$ MHz^2 cm^3 s/pc [Backer 1993]. Using equation (3.3) and knowing precisely the DM value, it is easy to compensate for the dispersion

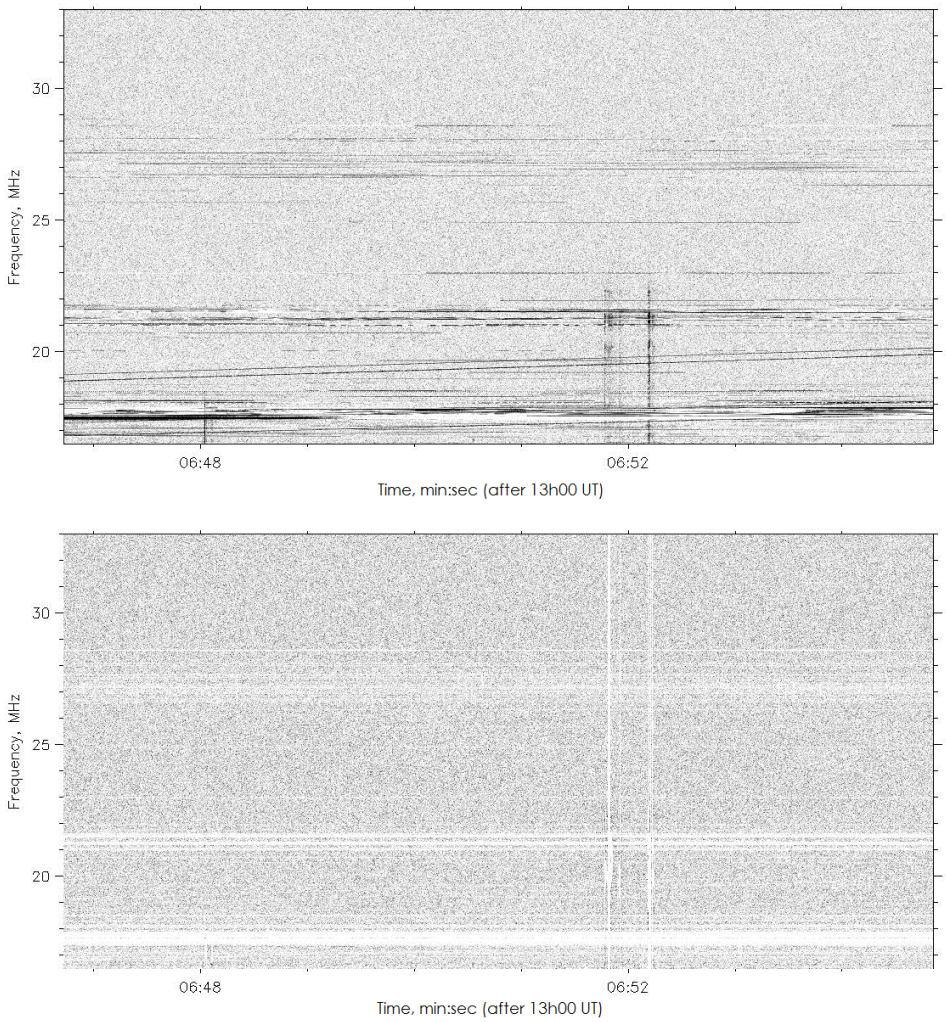

Figure 3.5: Normalized dynamic spectrum of data from the pulsar/transient survey acquired on 11/1/2014 during the daytime (13h UT), before (upper panel) and after (lower panel) RFI mitigation.

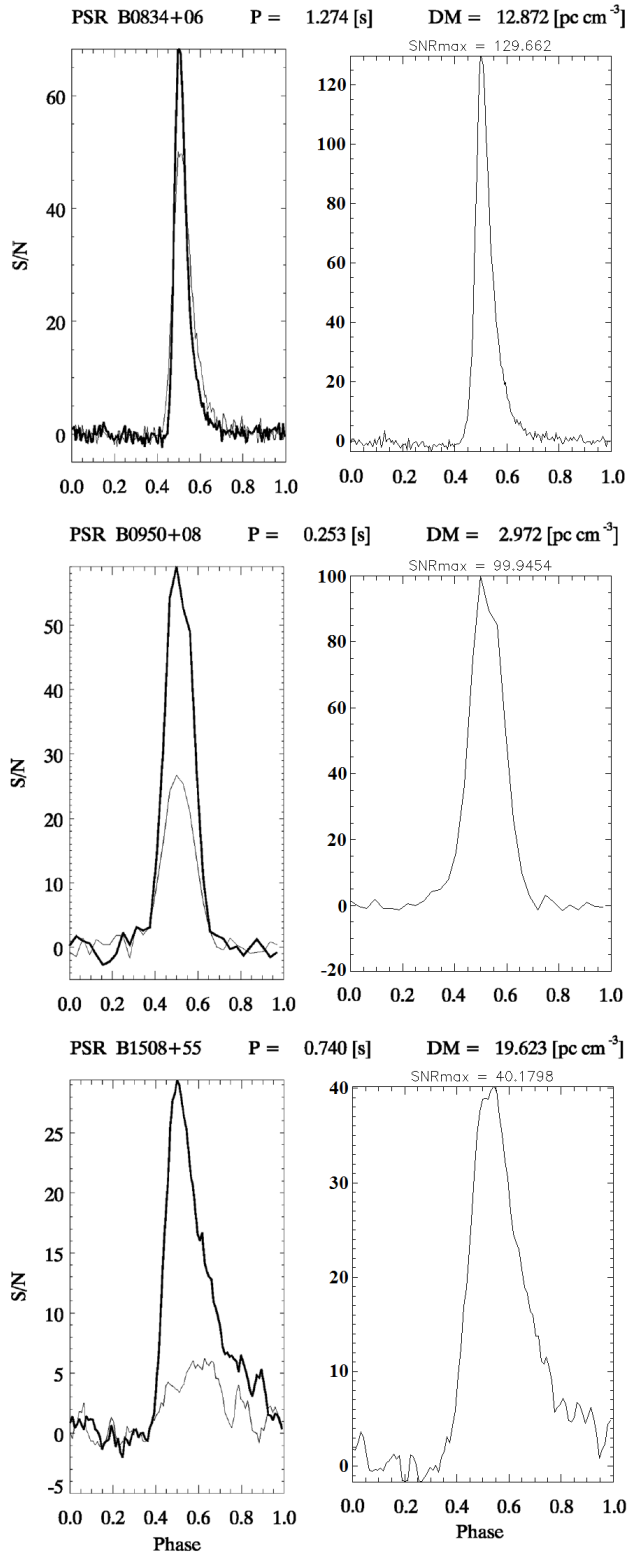

Figure 3.6: Average pulse profiles of three known pulsars (PSR B0834+06, PSR B0950+08 and PSR B1508+55) after RFI mitigation from [Zakharenko 2013] (left panels) and from the present work (right panels).

delay, by shifting the signal at each frequency, with respect to the highest frequency in the observed range. After this shift the pulse becomes aligned at all frequencies (as it was at its emission in the pulsar magnetosphere) and it becomes possible to accumulate the signal via frequency integration. This method is called incoherent dispersion compensation as opposed to coherent dedispersion [Hankins 1975], which introduces the frequency-dependent phase shift to the signal waveform. The coherent method is computationally costly, while the incoherent method is inaccurate due to the finite frequency resolution of the data. For the purposes of the survey, and with the time and frequency resolutions used, the accuracy of incoherent method is enough.

The result of incoherent dedispersion of a data fragment with pulsar pulses is presented in Fig. 3.7.

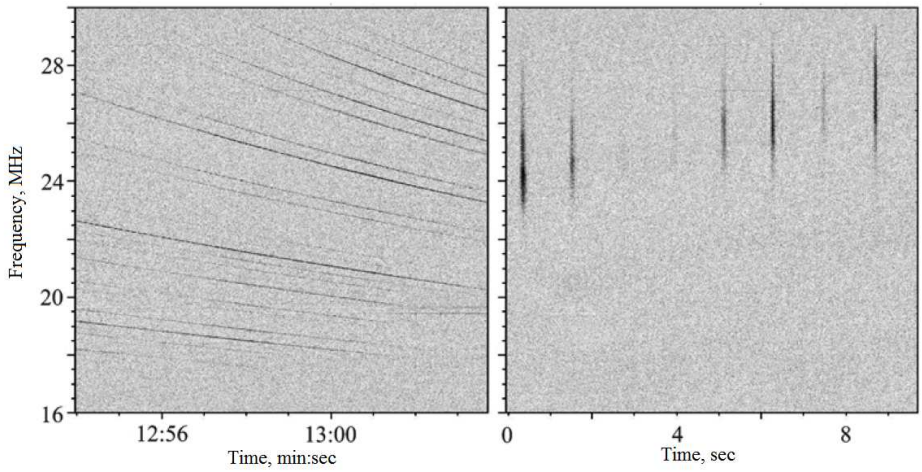

Figure 3.7: Pulsar pulses before dispersion delay compensation (left panel) and after it (right panel).

When dispersion measure is unknown, we have to explore a range of DMs with a certain step, trying to get the best pulse alignment parallel to the frequency axis. If dispersion delay is under- or over-compensated like in Fig. 3.8 top and bottom panels [Zakharenko 2013], the signal-to-noise ratio (SNR) of pulsar pulse after frequency integration is less than that of correctly dedispersed pulse (middle panel).

For distant sources with large values of DM, observed over a sufficient bandwidth, even a small inaccuracy in the DM compensation leads to significant decrease in SNR. Therefore, the step at which we explore the different DM values in the survey should be small. On the other hand it is determined by the time resolution of the data. The time shift between the upper and lower frequency channels should be greater than one time resolution point. Furthermore, the step size (and corresponding by the number of such steps) is limited by the requirement on the processing time, which should be the least possible. Taking the aforementioned factors into account, our choice was to start with a blind dedispersion in the range $0 < \mathrm{DM}$

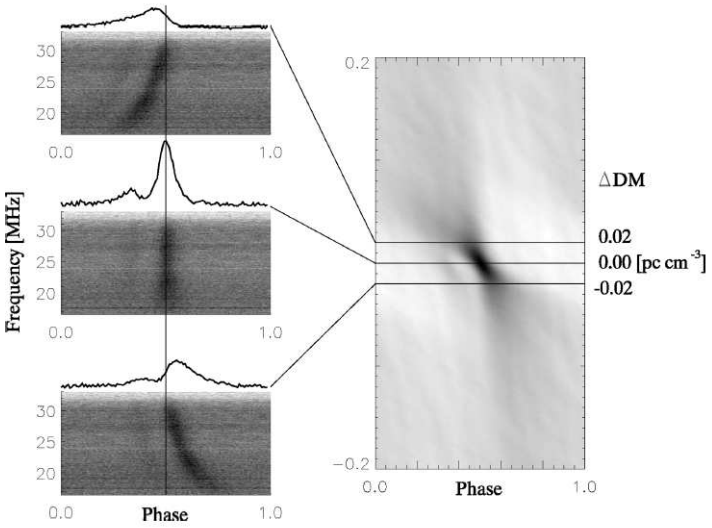

Figure 3.8: Dispersion delay compensation: correct (middle left panel), undercompensated (lower left panel), overcompensated (upper left panel), and SNR after spectral integration (right panel).

< 30 pc.cm^{-3} with a step size 0.01 pc cm^{-3} that leads to $\sim 10 - 15\%$ maximum decrease in SNR when we are not at the right DM value. It corresponds to 3000 'trial' values of DM. For each DM value, a set of time shifts is applied to the 4096 frequency channels of the data, according to equation (3.3). The table of these shifts for all individual DM values are pre-computed for faster processing, and stored in a binary file to which dedispersion program refers permanently. The program goes serially through each DM step, performs a frequency-dependent shift and integrates the shifted data fragment over frequency. This is repeated 3000 times, and as a result the data is reduced by a factor ~ 1.4 as 4096 frequency channels turn into 3000 integrated time series, each for a different DM value. If there is a strong pulsar in this picture, it will look like a series of pulses, bright and narrow at the correct DM of the pulsar, and more smeared with reduced intensity as the DM moves away from the actual pulsar DM. A transient event will look like a single pulse of the same shape.

The dedispersion program is written in C++ language for reasons of speed and future compatibility with NVidia CUDA technology for parallel processing on graphics (GPU) cards. The program can be fed by a concatenated cleaned file or by multiple separate files (for real-time processing). It allocates space for time shifting the data, up to the maximum possible shift (that corresponds to $DM = 30$). If working with multiple files, it bufferizes in memory a part of the next file in order to fill the gap that is formed in the current file by frequency-dependent time shifting.

When run on a computer workstation as a single process, dedispersion occupies $\sim$ 5 Gb of RAM and takes ~ 7 times longer than observation time. So, if a workstation

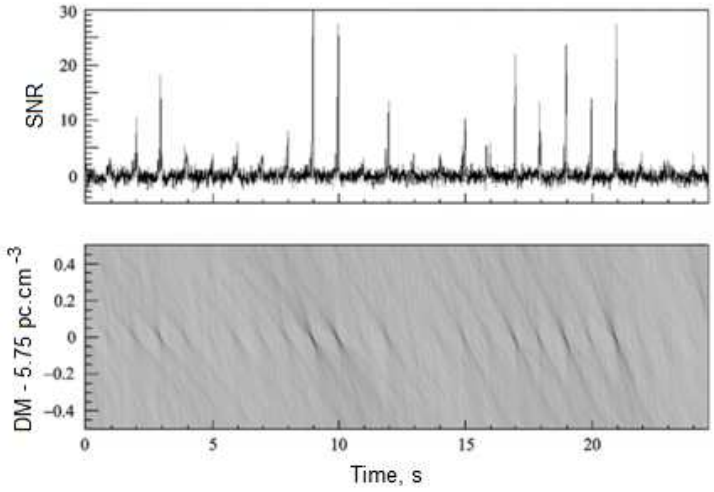

Figure 3.9: Individual pulses of PSR B0809+74 in the DM versus time plane (lower panel). Time series corresponding to the DM = 5.75 pc cm^{-3}, the correct DM value for PSR B0809+74 (upper panel).

has > 40 Gb of RAM, 7 copies of the program can be launched in parallel and real-time dedispersion can be achieved, if a powerful enough CPU is used (e.g. Intel Core i7). Each copy of the program will, in this scenario, process different part of an observation. Having completed RFI mitigation, the IDL launcher initializes and launches several copies of C++ program, depending on the amount of RAM available.

We attempted to launch quasi-real-time processing at UTR-2, but two UTR-2 servers had not enough RAM for real-time dedispersion of 5 receivers data flow. Data dedispersion is the longest and most computationally costly part of the whole survey data processing. But it is also the ideal procedure for the parallelization, because the same action is repeated many times (for different DM trials) with the same data fragment. Currently only the use of graphic cards can allow to compensate for dispersion in real time. The estimated acceleration using the graphic cards is going to be × 60 times [Tkachov 2013].

With the current state of equipment and software it is possible to do RFI mitigation on-line. Thanks to the fragmented structure of raw data, we can start processing almost on the fly - immediately after the recording of the first file. After each file reached its full size, it was sent to the pipeline.

Eventually the on-line processing hasn't been fully implemented at UTR-2 due to network errors, limited RAM and disk space, but we hope that it will be included in the default configuration in the near future.

3.3 Specifics to Exoplanet pre-processing pipeline

The pre-processing pipeline for the exoplanet search includes the following steps:

- file management
- RFI mitigation
- data reduction

Observations of exoplanets are done in tracking mode, where the source is constantly kept within the main telescope beam. As the beam width is 0.5 degree, the minimum time required for a cosmic source to cross it due to Earth's rotation is 2 minutes. Every 2 minutes the configuration of antenna phase shifters is thus changed. As UTR-2 has asynchronous phasing with respect to data recording, the background value can change abruptly from pointing to pointing. These jumps may exceed by far all the variations in the useful signal we are looking for. Therefore the 'jumps' in background, if not treated properly, introduce bias and destroy the signal searched for. To remove this effect, we should process each 2-minute interval between telescope pointings separately.

As in the case of weak pulsars, the emission can be well under the noise level, but it can still be detectable after certain integration in time and frequency. But whereas even very weak pulsars can be reliably detected by coherent summation of many periods of their emission (when the signal is accumulated in-phase, and the noise is added up randomly), exoplanet signal is not expected to be periodic and but rather to reoccur episodically as in the case of radio emissions of Solar System planets. Taking this into account, and because predicted exoplanetary radio emission levels are very low, the pipeline should be tuned for the detection of weaker signals, rather than stronger ones. This is the key difference with the pulsar/transient pipeline.

As discussed above, another factor that favours detection of pulsars and transients, as compared to exoplanets, is their dispersion measure. The DM of exoplanets, which we consider as candidates to have detectable radio emission, is typically lower than that of the closest pulsars (DM < 2 pc.cm^{-3}), because these are close-by objects. Therefore, dedispersion is not a vital discriminating factor for detecting exoplanets, but it is still worth trying to include it as an additional identification criterion. The distance to the exoplanets that we observed is known, and it is possible to predict their approximate *DM* value from the model of Galactic free electron concentration NE-2001 [Cordes 2004]. If the maximum of the received signal corresponds to this value of *DM*, it can be an evidence of the detection of exoplanet radio emission.

Predictions suggest [Zarka 2007] that radio emission (auroral and satellite induced) can be in the form of bursty signals similar to Jupiter's bursts. But the emission most likely will not be visible by eye on the dynamic spectrogram, because it is intrinsically weak and hidden by background fluctuations caused by the ionosphere or beam deformations convoluted to the inhomogeneous sky background (confusion). We rather expect to detect it as a time variable excess of radio emission

not seen in a control ('empty') part of the sky observed simultaneously. Thus owing to the multibeam capability of UTR-2, all exoplanet observations were performed with simultaneous beams directed to the target (*On* beam) and to a nearby control region (one or several *Off* beams). Time variations of the *On* signal should be consistent with the geometry of the emitting system relative to the observer. A reliable criterion of emission detection is thus a modulation by the orbital period of the exoplanet around its parent star, which means that there are regular conditions that take control the generation or visibility (due to its anisotropic beaming) of this radio emission at certain positions of the planet along its orbit.

Before the present work, the first processing pipeline developed for exoplanet search at UTR-2 [Zarka 2002] was a complex parameterized procedure, processing the whole series of observations of a given target from end to end. Its parameters (RFI mitigation thresholds, calibration by the sky background, dedispersion trial range and time and frequency integration parameters) were selected for each processing run. The RFI mitigation algorithm developed for that purpose (ZURFIM, see below) required long tuning in order not to remove too much useful signal, while at the same time removing RFI down to a level close to the background noise. Weak broadband RFI and the weaker edges of strong RFI were particularly challenging. ZURFIM removed $10-15\%$ of data in 'good' observing conditions (night-time) and up to 30% in the evening or morning hours. The inconvenients of this first pipeline were the absence of a unique low level preprocessing (RFI mitigation, integration), imposing a new end-to-end run for every other set of parameters. Absence of a unified file management of input data files made the pipeline vulnerable to spurious recordings (that in some cases caused the run to fail). Finally the calibration by the sky background was performed through a linear fit of the backgound level at each frequency during every 2-minutes interval between pointings. This introduced time variations to the final signal time series in which spurious instrumental behaviour revealed to be very difficult to disentangle from cosmic signal variations. As a consequence, the tentative detection of the radio emission from Corot-7b displayed on Fig. 1.8 must be confirmed by a complete, more robust reprocessing of the data.

Ideally, pre-processing should be blind, applied with the same parameters to all types of data. It should also be as simple and clear as possible. The post-processing (discussed in the next chapter) should be flexible, and fast to modify and re-run. It makes a need of the two separate stages in the pipeline, pre- and post-processing.

These were the guidelines for creating a new pipeline (version 2). Additional requirements included that it should be easily manageable, portable, cross-platform and possible to be used in stream processing. The new pipeline has been written in IDL in order to be compatible with the previous versions of the pipeline, to have a possibility of cross-tests. IDL provides good visualization and easy file management capabilities. It also allows to create a simple graphical interface consisting of widgets, required to facilitate the reuse of the program by other users.

The pre-processing stage, described in this chapter, should be a conversion of data from an actual DSP-Z receiver, which receives at high resolution both useful signal and RFI to data of hypothetical 'perfect' receiver, with lower time and fre-

quency resolution, receiving only signal and Galactic background. Compared to the previous pipeline, we improved and unified the file management, RFI mitigation and introduced data reduction to a fixed time and frequency resolutions for all data.

Detection of an exoplanet's signal is indeed not expected to be possible at high time-frequency resolution (that provides too low sensitivity). Data are acquired at these high resolutions ($\sim$ 20 msec $\times$ 4 kHz) for the sole purpose of efficient RFI mitigation, after which they can be rebinned with coarser time and frequency resolutions for tentative signal detection and scientific analysis.

3.3.1 File management

The file management part of the pipeline (also referred to as data reader) should be very fast and simple, so that the processing time at this stage is mostly determined by data reading. We built it from several separate simple blocks each consisting of an independent subroutine. Blocks should have a possibility to work standalone.

The DSP-Z receiver works in three modes [Ryabov 2010] : (i) spectrum analyzer, (ii) full correlation and (iii) waveform. Observations discussed in the present work, were made in the spectrum analyzer mode. For convenience, the data flow is generally split into separate consecutive files. For different purposes, the observer can select different sizes of output files (usually 2 Gb, i.e. a long integer capacity).

The main block of the data reader decodes the header of the data (it is compatible with all previous versions of .jds format) and reads the two channel data from the requested part of selected data file (from 1 spectrum, starting at any position, to the whole file). It converts data from .jds format to standard IDL double variable type and outputs the dynamic spectrum with its corresponding time and frequency axes as well as status information for each spectrum in the data. The time axis is given in Julian date, which allows absolute timing of each spectrum. This block is a subroutine of another block that reads one 2-minute interpointing interval (IPI) - the basic unit of pre- and post-processing.

The telescope pointing time is not synchronized with file creation, therefore one IPI can be spread across two consecutive files. A dedicated program determines whether the selected files are consecutive or not. It is done via the status information coded in the two uppermost frequency bins of each spectrum. Along with the overflow flags, microsecond counter and ADC cycle counter, one of the status fields is the number of issued spectra since the start of observation that is used to check the file consecutivity. If the interpointing interval is shared between two consecutive files, then the two counterparts are concatenated together and processed as a whole.

The start of each pointing is identified by another dedicated routine in the pipeline. By default, it builds an integrated time series for each file (over the whole frequency range), and folds it modulo 2 minutes (the time interval between telescope pointings). Then in the folded time series, the spike with the highest intensity coincides with the pointing times.

During the pointing, many relays in the phase shifters switch at the same time, causing sparking, which results into a powerful wide-band burst of radio emission

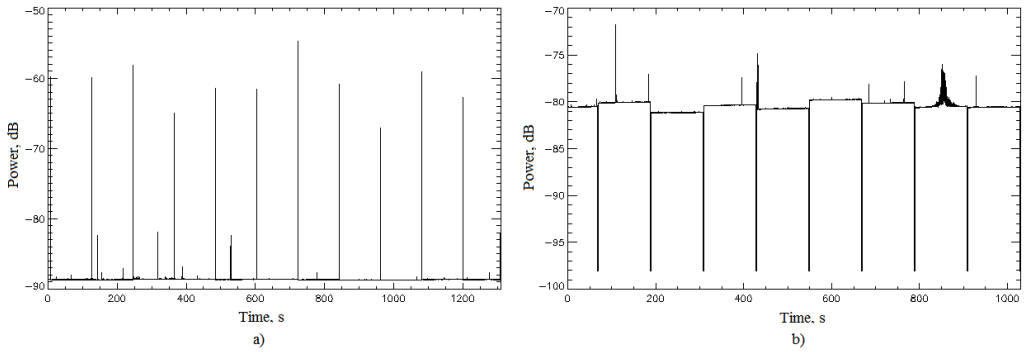

Figure 3.10: Integrated time series of 1 file: with normal antenna pointing signatures (a) and with the strobe-killer circuit (b).

(Fig. 3.10, a). This burst is usually the most powerful event within a 2-minute interval, and its detection points to the initial phase of the periodic pointing signals within the file. Knowing the initial phase, and that the time between the adjacent pointings is 2 minutes, we can determine the number of pointings in the file along with the start and the end of each inter-pointing interval. Some observations were done using a 'strobe-killer' circuit, which disconnects the antenna output from the receivers at the time of antenna pointings. This results in a drop of received power during these intervals, instead of an intense peak. These dips are detected by thresholding (the typical threshold used is $\mu - 17\sigma$).

The above described file-mapping program creates an IDL save set file with information about each data file, its consecutive neighbours and pointing positions within it. This information is then used to read a part of the file, corresponding to any requested interpointing interval (identified by its number within the file). The time required for mapping one 2-Gb data file is typically about 200 seconds.

After this save set has been created for each file in the data set, further processing takes place. The last (incomplete) IPI of each file is appended to the first (also incomplete) IPI of the next file.

3.3.2 RFI mitigation

The ultimate goal of RFI mitigation is to remove all RFI signatures of natural and artificial origin from the data, while keeping the useful signal intact. Usually it is impossible to achieve this goal completely. As aforesaid, in order not to suppress transient signals (if any) it is better to be less severe in the RFI mitigation of the survey data. For exoplanets we consider that it is better to sacrifice a part of signal, but remove as much RFI as possible. If any RFI is left in the data, it may distort the signal and prevent detection or lead to spurious detection.

For the purposes of the pre-processing pipeline, we only flag the position of bad data points in the time-frequency plane (hereafter bad pixels), and then ignore them

at integration stages. The flags are stored in a so-called bad pixel map that has the same size as a data frame but consist only of 0 and 1, where 1s correspond to 'good' pixels - pixels containing only Galactic background noise and useful signal, which at the resolution of the observations is likely to be hidden within Galactic background fluctuations, whereas 0s are at the positions of pixels containing RFI. Thus, the sole purpose of RFI mitigation is to build a bad pixel map for each IPI. It can also be called 'bad pixel mask', because when multiplied by the data, it replaces bad pixels by zeros.

3.3.2.1 Dynamic spectrum flattening

In order to apply the RFI flagging methods from sections 3.1.1 and 3.1.2, the dynamic spectrum should be flat, i.e. there should be no large-scale variations in time and frequency. For UTR-2 data the frequency inhomogeneity is dominant, due to the shape of the frequency dependent response (gain) of UTR-2. The contrast between the most and the least intense parts of the time-frequency tile is comparable to the power of the RFI to be identified. To overcome this problem, the data tile is usually divided by the average (over the whole IPI) frequency response of the telescope (i.e. an average spectrum).

We use a more robust method in the present pipeline. Instead of an average spectrum we compute a reference intensity spectrum made of the 10% quantile of the distribution of intensities at each frequency. We can assume safely that the 10% intensity quantile (intensity level exceeded by 90% of the measurements) in each frequency channel consists of clean data values, because contamination by RFI must exceed 90% of the pixels in a given channel in order to impact this 10% quantile. We divide the data tile by this reference spectrum. Hereafter this operation is referred to as flattening. Note that the average level of the dynamic spectrum after flattening is slightly higher than 1, because the intensity defined by the 10% quantile is lower than the mean. More precisely, for a Gaussian distribution with moments (μ, σ), the level of the 10% quantile is $\sim (\mu - 1.3 \times \sigma)$. The mean of flattened data is thus $\frac{\mu}{\mu - 1.3 \times \sigma}$. The ratio μ/σ is equal to $\sqrt{b \times \tau}$ with, for our observations, b=4 kHz and τ=20 msec. With these values, we obtain a mean of the flattened data equal to ~ 1.17

The flattening corrects for the spectral response of the telescope but not for time variations. This is done on purpose because slow time variations may be caused by the ionosphere, beam deformation, or a real signal, whereas fast time variations (spikes) are flagged by the RFI mitigation routine. Alternatively, a surface fit could be used to fit the whole data background and to correct for both time and frequency variations as in [Winkel 2006].

3.3.2.2 ZURFIM RFI flagging method

In this pipeline we use a third flagging method, ZURFIM, in addition to PATROL and SumThreshold, mainly as a preparatory stage for RFI flagging.

ZURFIM (Ze Ultimate RFI Mitigator) is able to detect broadband spikes, radio stations, linear frequency modulated signals, spots, and to deal with various scales of RFI patches in the data. In addition, it is quite fast. It has been created by P. Zarka for the first processing of observations of exoplanets, but it can be tuned, depending on the signal of interest, e.g. for pulsars. Its principle is somewhat similar to SumThreshold but makes use of time-frequency segments of arbitrary lengths and applies arbitrary thresholds. It is based on a set of integrations applied to data in time and frequency directions, after flattening by a 10% intensity reference spectrum. First it identifies bad frequency channels in the dynamic spectrum (those that contain more than 90% of bad pixels) by means of subtracting the running average from the reference spectrum with subsequent thresholding at 4σ of the residuals. Then, in a selected number and order of successive passes data is integrated in time or frequency, and the RFI are flagged in the reduced time-frequency tile above the thresholds specified for each iteration.

Integrating data in time helps to flag narrowband RFI, either strong (if the integration factor is small), or weak and persistent (if the integration factor is large). Integrating in frequency serves to flag brief spikes, strong if the integration factor is small, and weak broadband when it is large. The only drawbacks are that (i) it flags too many pixels at the tile edges and (ii) it has to be manually tuned for each type of observed source. For example, when observing Saturn Electrostatic discharges, frequency pre-integration should not be large, otherwise the useful broadband signal will be eliminated. For using ZURFIM on pulsars, the key precaution for not erasing pulses is to choose an integration factor in time or frequency large enough so that each resulting pixel contains one pulse.

3.3.2.3 RFI classification

Each of the above RFI flagging methods plays a specific role in the pre-processing pipeline. As the level of interference varies with the time of the day, the season, or the state of the ionosphere, different depth of cleaning should be used during the processing. The RFI mitigation program evaluates to which category (out of 3 or more) a given dynamic spectrum belongs to. For each category, we tune the RFI mitigation routines differently, applying more severe thresholds to more contaminated data. Depending on the degree of contamination of each IPI and on the type of RFI that affects it, there is a set of rules for the classification. It is a classification based on a figure of merit (FoM), where the FoM of an IPI depends on its statistics (median value, mean value, mean-median difference, standard deviation, number of values, exceeding a 4σ threshold). We also check for the presence of spots with ZURFIM (as it is fast and reliable for that purpose).

The FoM ranges from 0 to 100, where 0 is clean data, and 100 corresponds to completely useless data due to strong RFI contamination. Out of 100 points maximum, the major part (from 0 to 36 points) is given to the result of ZURFIM, that is, the percentage of flagged data samples. If it is large ($> 7\%$) then most likely there are spots in the dynamic spectrum (likely to be strong radio sources or

emitters in side lobes, or ionospheric scintillation). The next criteria by relevance are the mean value μ over all dynamic spectrum (that should be close to 1 after data flattening – see section 3.3.2.1) and the standard deviation (that depends on data time resolution). Each of them gets from 0 to 18 points out of 100. Finally, the data median (that should be also around 1 and not differ much from the mean) as well as the number of peaks that exceed $\mu + 4\sigma$ get from 0 to 14 points each. The attributed FoM values are empirical, chosen by the visual inspection of RFI mitigation results.

The idea of this approach emerged when we ran the described RFI flaggers on a large data set, and plotted histograms of percentage of flagged points. All the histograms had several peaks. For example, in the histogram (Fig. 3.11) derived using ZURFIM we see 4 peaks. These peaks correspond to dynamic spectra with different types of RFI. As the lowest peaks correspond to few cases, we finally defined 3 categories of RFI contamination for processing Corot-7b data.

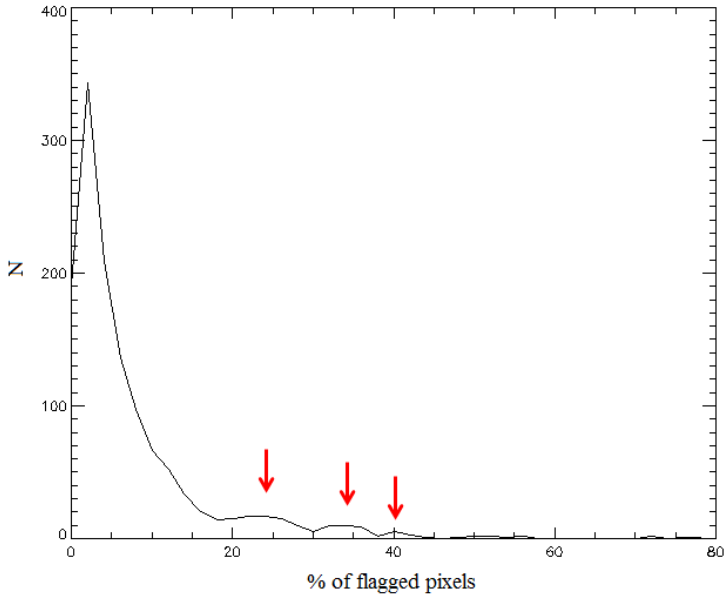

Figure 3.11: Histogram of percentage of pixels flagged by ZURFIM per IPI (Corot-7b 2009 data set, receiver A). Peaks (red arrows) correspond to different RFI types in the data.

The first category includes relatively clean IPIs having only rare narrowband and wideband interference or very weak spots. A typical example is shown in Fig. 3.12.

The typical IPI that belongs to the second category is shown in Fig. 3.13. It contains middle sized intense spots and/or numerous wideband and narrowband RFI and ionospheric sounding station signatures (slanted lines).

The IPIs of the third category are strongly contaminated by the interference that affects large patches both in time and frequency directions (Fig. 3.14).

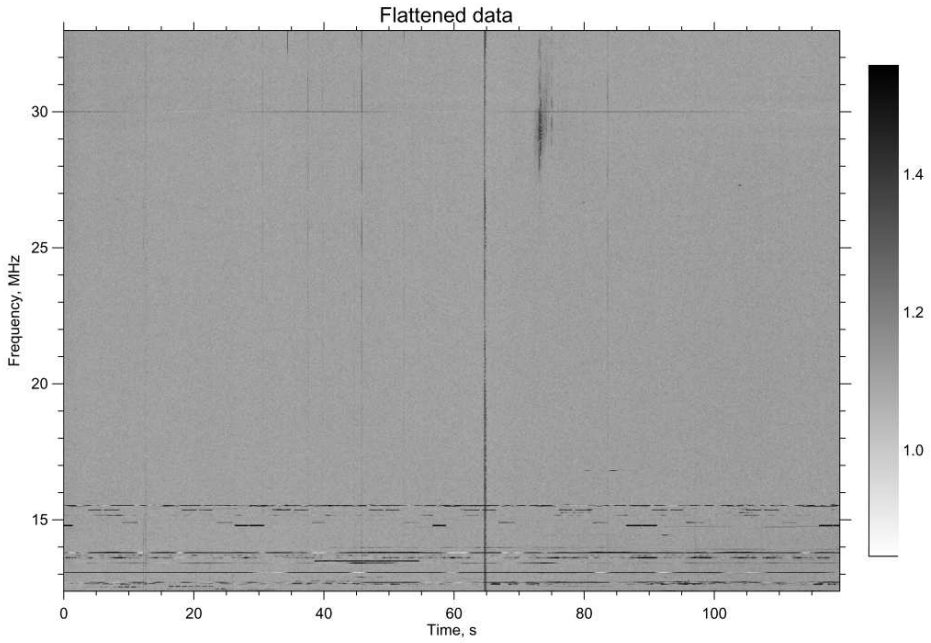

Figure 3.12: Dynamic spectrum classified in the first (least severe) RFI contamination category.

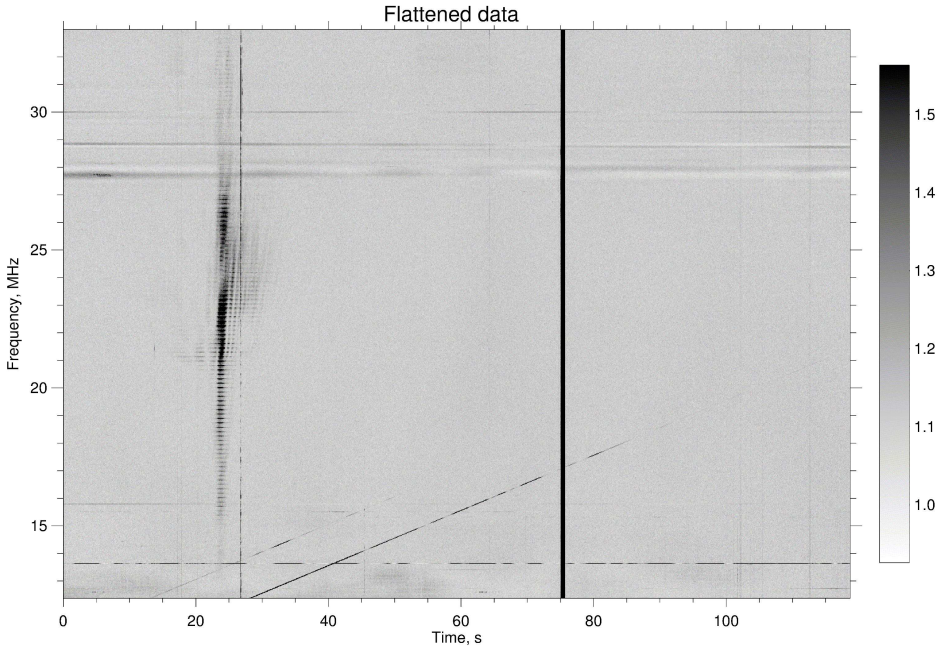

Figure 3.13: Dynamic spectrum that belongs to the second (medium) RFI contamination category.

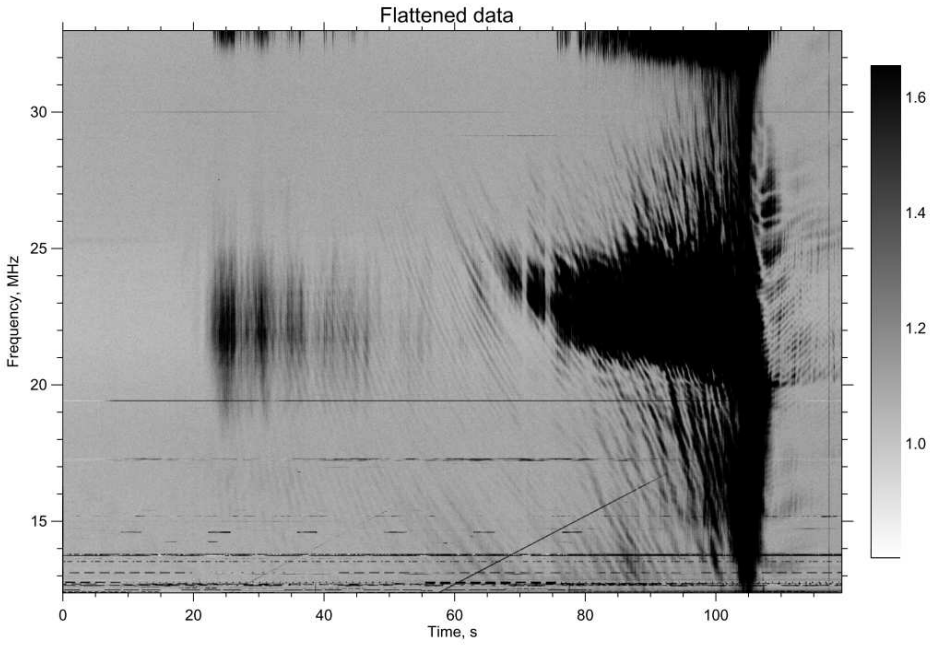

Figure 3.14: Dynamic spectrum that belongs to the third (most severe) RFI contamination category.

In the VarThreshold and SumThreshold methods (section 3.1.2) the default parameters $T_1 = 10$ (σ) and $a = 1.5$ that give satisfactory results with LOFAR and WSRT data [Offringa 2010]. These values were chosen empirically for the aforementioned radio telescopes, but they are likely not to be adapted to the lower frequency range of UTR-2. Thus we attempted to derive independent probabilistic estimates of the value of the threshold versus the size of the sliding window. As the problem is actually complex, because it relies on the fraction of a gaussian distribution exceeding a variable threshold, we derived only approximate expressions based on simple assumptions. These expressions are different for the VarThreshold and SumThreshold methods.

We consider a series of n pixels of data $x_i \in X$, $i = 1...n$, containing normal gaussian noise ($\mu = 10$, $\sigma = 1$) and RFI. We want to suppress the RFI, while suppressing the minimum of gaussian noise peaks. At the highest resolution, i.e. considering all individual pixels, the corresponding threshold t_1 should be defined so that the probability $P(x_i > t_1) = p_1 = \frac{1}{n}$. In this way, no more than one noise peak out of n pixels will generally be removed. In IDL, t_1 is derived as GAUSS_CVF(p_1).

For VarThreshold, we estimated the probability to find one occurrence of N consecutive pixels, all above a given threshold t_N, from the probability p_N that one pixel is above that threshold. There are N possible arrangements of these N consecutive pixels, that are all independent have each have a probability p_N to be above t_N, resulting in a probability $\simeq N p_N^N$ of occurrence of N consecutive pixels,

all above a given threshold t_N. As we want that probability to be equal to p_1, we find in that case $p_N = (p_1/N)^{1/N}$, from which we derive t_N.

For SumThreshold, to find the threshold t_N above which we expect to find no more than one occurrence of N consecutive pixels, whose average is above the threshold, we estimated the number of independent pixels resulting from the averaging of the series $x_i \in X,\ i = 1...n$ by a sliding square window of width N. This number of independent pixels was estimated by adding the number of non-overlapping windows ($\sim n/N$) weighted by 1 with the number of overlapping windows ($\sim n - n/N$) weighted by $1/N$. We find a number of independent pixels $n_i \sim n(\frac{2N-1}{N^2})$. We derive the threshold t_N so that the probability $P(x_i > t_1) = \frac{1}{n_i} = \frac{p_1}{(2N-1)/N^2}$. In IDL, t_N is derived as GAUSS_CVF($\frac{p_1}{(2N-1)/N^2}$).This threshold is then divided by $\sqrt{N}$ to take into account the reduction of the standard deviation of the noise X due to averaging.

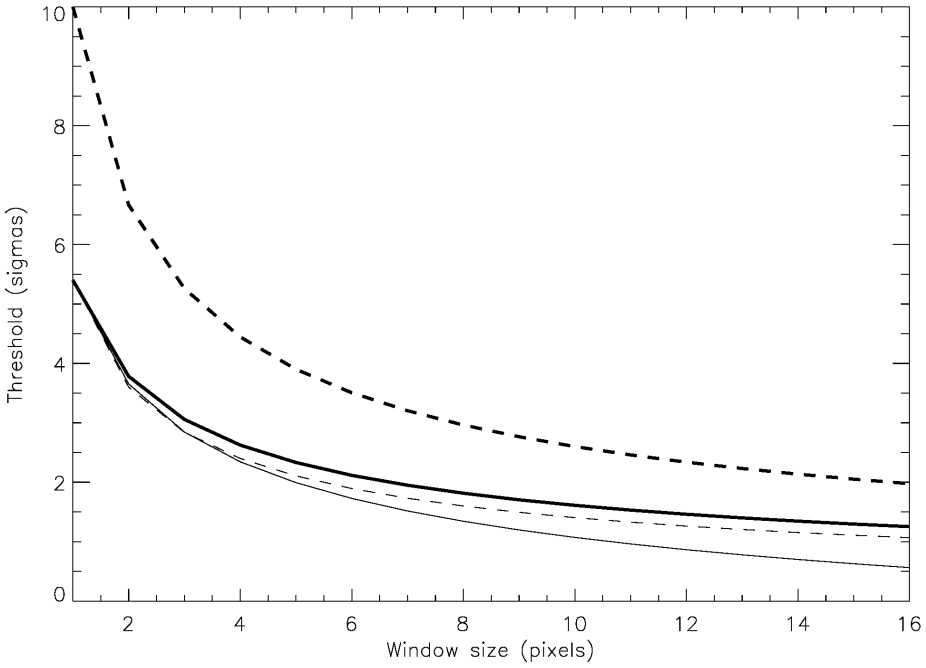

Figure 3.15: Variation of the threshold versus window size to be used with VarThreshold and SumThreshold. The boldface dashed line is the threshold from [Offringa 2010] with default parameters. The lightface dashed line is scales to T_1=5.4 (σ), corresponding to one gaussian noise peak per 5000×6000 pixels dynamic spectrum. The boldface solid line is the threshold that we computed for use with SumThreshold and the lightface line that for VarThreshold (both for the same T_1 of 5.4). They are consistent and possibly better adapted that the single threshold curve from [Offringa 2010].

Fig. 3.15 compares the variation of the threshold versus window size as defined

in [Offringa 2010] with the ones we derived above. With the default value $T_1 = 10$, VarThreshold and SumThreshold are not severe enough for the heavier RFI pollution at low frequencies that is encountered at UTR-2, as compared to the RFI environment of LOFAR and WSRT. It is thus necessary to considerably lower T_1. The expression of the threshold that we derived above for SumThreshold proves to be remarkably close to that empirically proposed in [Offringa 2010] with a common value of T_1, but without any free parameter a, and additionally it provides some clue about how choosing the value of T_1, via the probability to have one noise peak above T_1 in one processed data block. The threshold variation that we derive for VarThreshold starts from the same value of T_1 but evolves with the window size towards lower values of threshold, as can be expected from the more stringent condition required by VarThreshold to identify a series of N consecutive pixels as an RFI. T_1 is the only adjustable parameter that allows us to tune the severity of RFI mitigation with VarThreshold and SumThreshold. Fig. 3.15 uses T_1=5.4 (σ), corresponding to one gaussian noise peak per 5000×6000 pixels dynamic spectrum.

We tested via simple simulations the performances of VarThreshold and SumThreshold with the above-defined thresholds on normal gaussian noise, and the observed behaviour is as expected. In the pipeline, we only use SumThreshold. For accelerating the processing we do not use all consecutive window sizes (powers of 2), but instead we chose the most relevant ones for the scales of RFI we encounter in our data: $\{8, 16\}$ for the frequency direction and $\{2, 8, 16\}$ for the time direction.

We use SumThreshold for all 3 categories of RFI contamination, adjusting only T_1 (and the values of T_N accordingly, following Fig. 3.15). For the second category the threshold values are taken as displayed in Fig. 3.15. For category 1 they are multiplied by a factor $\sqrt{2}$, and for category 3 they are divided by the same factor. These multiplication factors were chosen empirically.

Then for all categories we launch the PATROL flagger with thresholds 3 and 2.5 for removing remaining bad frequency channels and spectra, respectively. The reason why we run SumThreshold before PATROL is that when a time or frequency slice is only partly contaminated by a strong RFI, PATROL might flag all this slice, even though there is a part of good data in it. SumThreshold will only remove the patch containing RFI, and then this patch will not be taken into account by PATROL.

The figure of merit points and category limits were chosen empirically, by the visual inspection of the cleaning quality of many IPI of the Corot-7b observation campaign of 2009 and by testing them on weak pulsar data, with performances quantified by the resulting signal-to-noise ratio of the average pulse profile. The visual inspection was made first on the IPI strongly affected by interference, and then on relatively clean ones. If the current parameters lead to efficient cleaning of all RFI in the 'dirty' IPI, they were tested for not being too severe with clean data fragments.

The test of the entire RFI mitigation pipeline on pulsars (Fig. 3.16) has shown that for strong pulsars it performs less well than the dedicated tools, but the weaker the pulsar, the better the performance. This behaviour is expected and desired for

us, as exoplanet signals (if any) should be very weak.

Although the described classification routine is developed for UTR-2 data, it will be applicable to beamformed data from other radio telescopes.

Strong RFI generally contain weaker edges or there are weaker gaps between stronger counterparts of the same RFI. These features also have to be removed, but they are sometimes left out by the RFI flagging program. To deal with this situation, mask expansion methods are used. In [Offringa 2012b] the Scale Invariant Rank (SIR) operator is suggested. It takes as an input one line of the bad pixel map either in time or in frequency direction, and, depending on an 'aggressiveness' parameter s ($0 \leq s \leq 1$) flags the surrounding N pixels if $(1-s)N$ pixels have been flagged previously.

We implemented it and although it performs well on our data, it took considerable processing time ($\sim$ 70 seconds for 1 IPI). Thus we developed a simpler method, based on morphological mask dilation. It identifies the connected patches in time or frequency direction, flagged by RFI flagger and expands each patch larger than m pixels by n pixels on each side. In the pipeline we use the parameters $\{m = 10, n = 5\}$ for the time direction and $\{m = 12, n = 5\}$ for the frequency direction. This operation takes about 2 seconds for 1 IPI. It is not scale invariant, but the RFI at UTR-2 usually have a relatively small range of scales. Mask expansion is not used by default in the pipeline, but can be used if requested.

The DSP-Z receiver has two input channels, and usually we process data from both channels (Sum and Difference of N-S and E-W signals), and we create bad pixel masks for the two channels separately. Our tests show that the RFI might be different in the sum and difference channels (e.g. Fig. 3.17), because the resulting S and D antenna patterns have different side lobes and differ in the area of pencil beam (D does not contain the pencil beam - PB). Therefore, some RFI, coming from the direction of PB or certain side lobes, may be weak (but still present, and hard to flag) in D, but stronger in S. RFI coming from the direction of other side lobes may be stronger in D and weaker in S. But as physically the input signals from which S and D are constructed are the same (N-S antenna and E-W antenna signals), the RFI are present in both outputs (S and D), and we need to remove them, by merging the bad pixel masks created for S and for D. The merging operation in this case is identical to the logical 'AND': if at least one of the individual masks has 0 at certain position, the resulting value in the merged mask will be also 0.

In Fig. 3.17 red colour denotes bad pixels in S only, blue - in D only, and green - the common bad pixels for S and D. Bad pixel maps are indeed different. In Sum (red) we can see the pulsar pulses, whereas in difference they are absent. But some narrowband (and wideband) interference are unique for either the sum or the difference channel.

3.3.2.4 Noise statistics

In Fig. 3.17 individual bad pixels (not organized in lines) are distributed randomly, as noise peaks, and only a few of them are common for both channels. To obtain

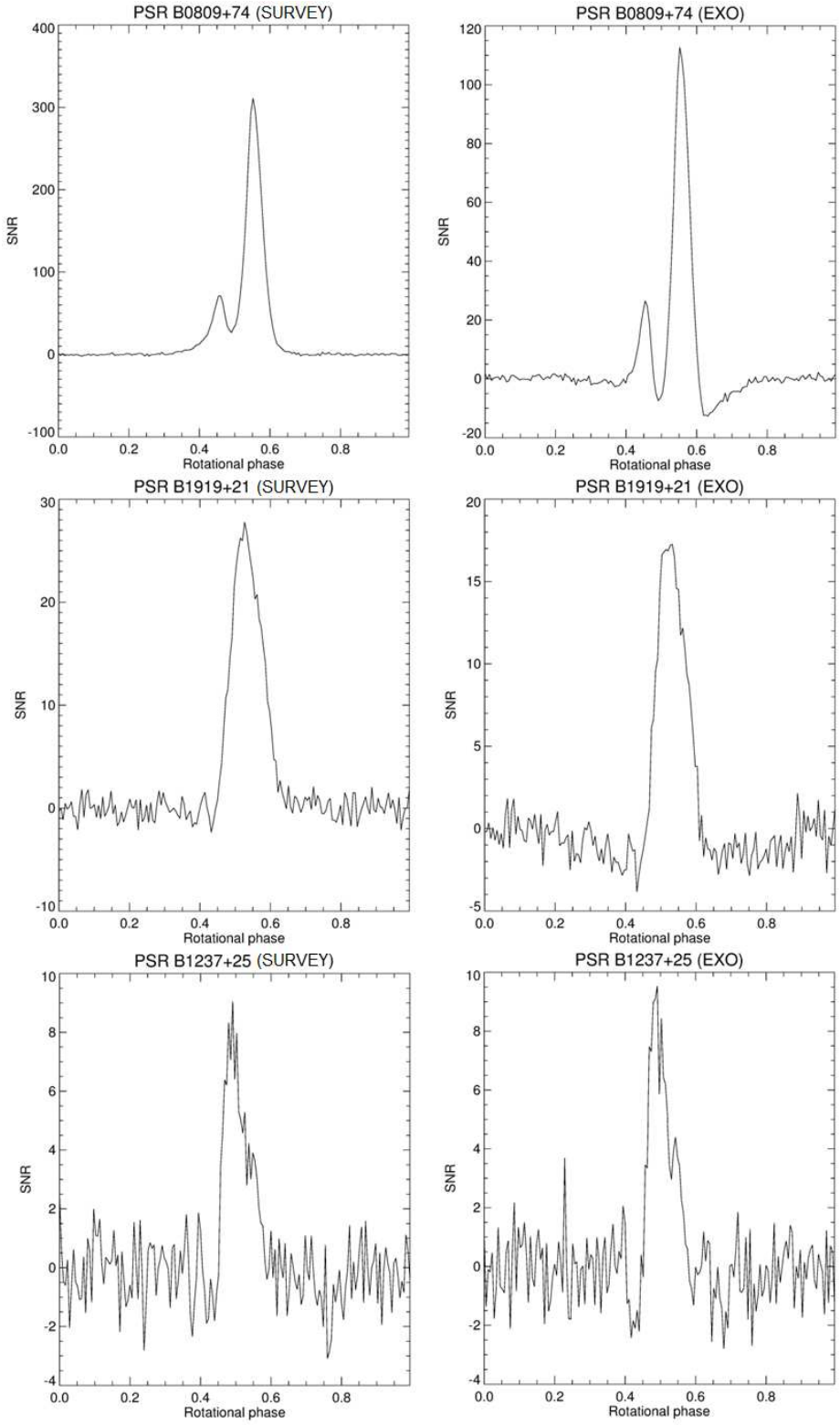

Figure 3.16: Test of RFI mitigation routine developed for exoplanet search on pulsar data. Comparison of SNR of strong (upper panels) medium (middle panels) and weak (lower panels) pulsar after RFI mitigation by the survey pipeline (left panels) and exoplanet pipeline (right panels). RFI mitigation from exoplanet pipeline is more efficient for weak pulsars that do not emit strong pulses. Dips around the main pulse are due to effects of RFI mitigation that eliminates the pulse along with adjacent pixels.

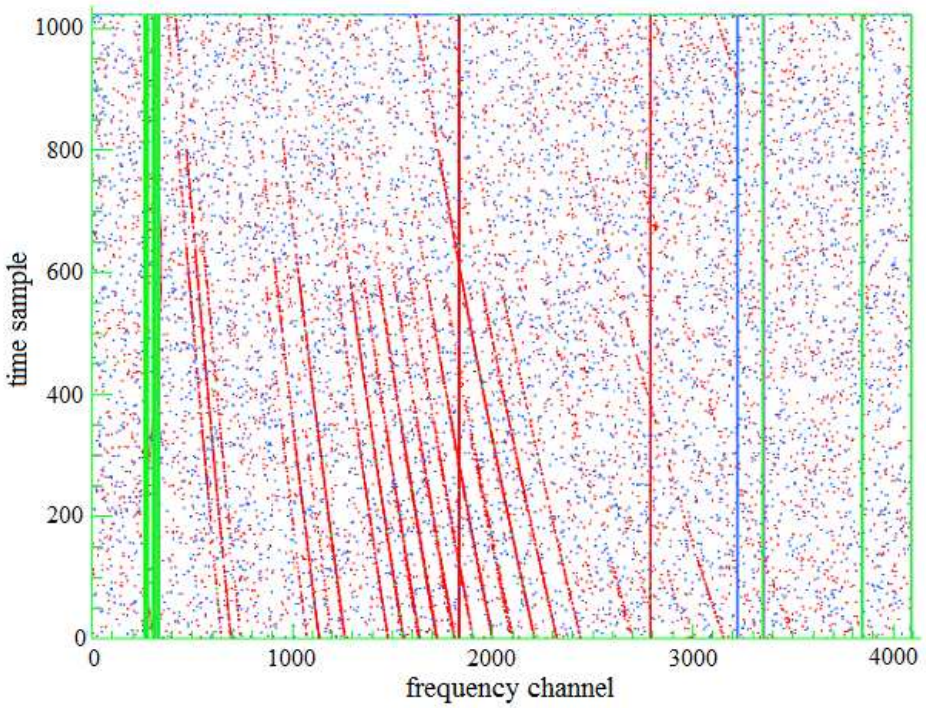

Figure 3.17: Data points exceeding the 3.5 standard deviations threshold in sum (red), difference (blue) and both sum and difference (green) data.

this figure, samples were flagged if they exceeded a threshold $\mu + 3.5\sigma$, where μ is the median of the array, and σ is its standard deviation. The number of individual flagged samples seems too large compared to expected noise peaks at 3.5σ level for a gaussian noise distribution. It implies that the data distribution is not Gaussian. Indeed, if we compare the number of pixels flagged in the RFI-free part of the dynamic spectrum with that in a simulated data array of same size with Gaussian distribution, they differ by a factor of ~ 3. In the array with Gaussian distribution much less data points exceed the $\mu + 3.5\sigma$ threshold, and the factor relative to the number of pixels flagged in real DSP-Z data depends on the time resolution of the data.

All RFI flagging methods used in our pipeline involve thresholding. Usually the RFI are more intense or more variable than the sky background noise, therefore applying some threshold to the data mean or variance can help to filter them out. The threshold should be selected so that few useful data are above it and the minimum possible amount of RFI is below it. To make a proper thresholding, one must have a good knowledge of the distribution of clean data intensity. If it is Gaussian, then it is easy to select and apply thresholds, since there is well-defined dependence of the number of removed values (which are above the threshold) on the threshold value. For example, selecting the threshold of $\mu + 3\sigma$, where σ is standard deviation, the fraction of removed data exceeding this threshold is $\sim 0.135\%$. If we do not know the statistics of the data distribution and apply the same thresholds to it as we would apply for normally-distributed data using empirical values of the variance or σ, we risk either to remove too many useful samples (if the distribution is shifted to the right, like a Rayleigh, or a Rice distribution) or to retain too many RFI contaminated pixels (if the distribution is shifted to the left).

This problem first emerged when we noticed that too many isolated pixels were flagged in the dynamic spectrum (as in Fig. 3.17 comparing S and D). It is very unlikely that the large excess of flagged isolated pixels are actual RFI, short-lived and narrowband. So there must be an excess of high-intensity values in the data as compared to a Gaussian distribution. Indeed, when we plot the distribution of pixel intensities in a clean flattened dynamic spectrum, it is different from a Gaussian distribution (Fig. 3.18).

This distribution actually does not correspond to any standard distribution. Its shape varies from Rayleigh (when a low number of spectra are averaged, i.e. at high time resolution) to Gaussian (high number of averaged spectra/low time resolution), according to expectations from the central limit theorem. The central limit theorem states that when we add up a sufficiently large number of independent random variables, the resulting distribution tends to be Gaussian.

In our case, the initial voltage oscillations at the output of the antenna are normally distributed (as cosmic signals observed in a band narrower than their natural width are essentially gaussian noise). At the receiver input, the signal is digitized by the ADC and, in the spectrum analyzer operating mode, a Fast Fourier Transform (FFT) is applied to the signal within a sliding window of N=16384

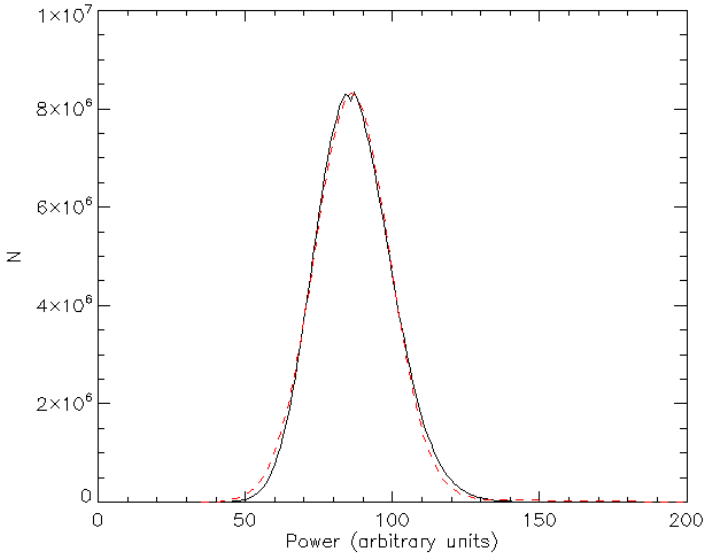

Figure 3.18: Data distribution in 1 flattened file (black line) and an attempt to fit it by a Gaussian (red dashed line). Data distribution is asymmetric and has a high-value 'tail'.

samples, multiplied by a Hamming window function:

$$w(k) = 0.54 - 0.46 \cos\left(\frac{2\pi k}{N}\right), \tag{3.4}$$

where $k = 0, 1, \ldots, N-1$.

The absolute value of the FFT is taken and squared to obtain the intensity values. The result is called an elementary spectrum. Then the sliding window is shifted by half its size and the FFT with squaring is performed again. This procedure is repeated n times, where n is the number of averagings, specified by observer to define the time resolution δt of the data. Then n consecutive elementary spectra are averaged, and only the resulting spectrum is recorded. As consecutive spectral intensities at a given frequency are nearly independent, with $n = 2$ one would obtain a Rayleigh distribution of intensities in each frequency channel. As n increases the distribution evolves towards a Gaussian one.

In order to obtain the exact shape of the distribution for any given time resolution, we simulated the receiver output for different numbers of averaged spectra. The procedure of simulation is the following. We simulated 100 million raw spectra in order to average them after with any number of averagings. We assumed that the input signal has been digitized by the ADC, and the values produced are normally distributed with zero mean and standard deviation 1 (without loss of generality as the data is eventually normalized to $\mu = 0$ and $\sigma = 1$). To calculate each spectrum, we generated a series of 16384 normally distributed values and multiplied them by

the Hamming window function. Then FFT was taken and the component corresponding to the frequency 25 MHz was selected. The data was then shifted by half of its size (the second half of the array - 8192 values - is retained, and is followed by newly generated 8192 normally distributed values) and the procedure is repeated 100 million times. Having obtained 100 million raw spectra, we could average any number of them. In the DSP-Z receiver the number of averaged spectra (n) is tunable, from 2 (implying 0.25 ms time resolution) to 800 (100 ms time resolution), with a step of 2. We didn't simulate all of them, but the 13 representative values spanning the whole range of used values: $\{2, 4, 8, 16, 32, 64, 80, 128, 162, 256, 324, 512$ and $800\}$. For each value of n we wanted to obtain 10 millions of recorded spectra (created from raw spectra by means of averaging). For large values of n, we had not enough raw spectra to produce recorded spectra (e.g. $10^7 \times 800 = 8 \cdot 10^9$ which is more than the 100 million raw spectra that we generated). Therefore we had to reuse the raw spectra, by shuffling them.

The histograms of the simulated data for 3 different values of n are shown in Fig. 3.19.

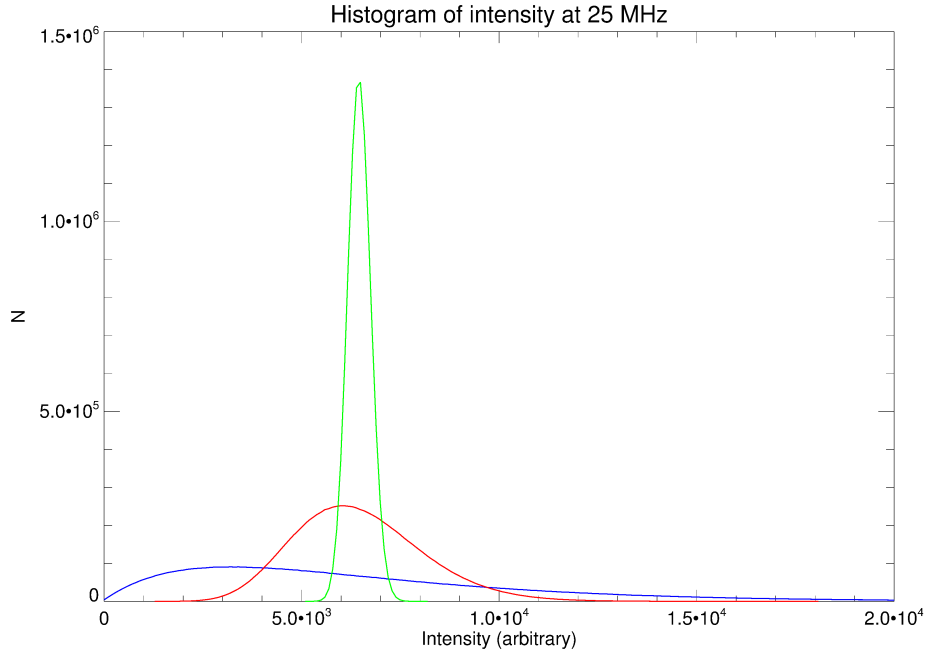

Figure 3.19: Data distribution in a single channel at 25 MHz frequency: for $n = 512$ averaged elementary spectra ($\delta t = 64$ ms, green), $n = 16$ ($\delta t = 2$ ms, red) and $n = 2$ ($\delta t = 0.25$ ms, blue).

A series of 81 thresholds (from 2 to 10σ, with σ computed from the simulated data, above average with step 0.1) was then applied to each set of simulated data to examine the fraction of values, which are above each of the thresholds. This fraction was considered as the probability that the recorded values exceed the threshold, and

with the GAUSS_CVF function (built in IDL) we got the corresponding Gaussian distribution cutoff (threshold).

In this way we established a correspondence between thresholds expressed in σ for a Gaussian distribution (of which we have a good intuitive grasp) and thresholds of the distribution of DSP-Z data. In the processing pipeline, we want to provide thresholds in number of Gaussian σ, independent of the time averaging (resolution) of the data. Thus we used above simulation to build a mapping from Gaussian threshold and number of averaged spectra n, to the threshold for the actual data distribution, above which the same fraction of data will be eliminated, as in the Gaussian distribution, above the input threshold.

The simulation was precise only up to a threshold of 5σ. Above this value, we hit saturation (size of simulated data - 10 million values - was not big enough to encounter a noise peak exceeding a higher threshold, given the small probability of it). In order to extend the simulation to a 15σ level, we fitted it to an expression $Y = P_0 + P_1 X^{P_2} + P_3 X$ where X is a real data threshold, and Y is a Gaussian threshold, corresponding to it. We used the MPfit fitting toolkit for IDL [Markwardt 2009] with initial parameters $\{0, 2, 0.5, 1\}$. A least-square minimized set of fit parameters was obtained for each value of n and used for extrapolation to 15σ.

The fit, plot together with original data, is shown in Fig.3.20.

We obtained thus a good fit for the above 13 values of n. The surface of this mapping from DSP-Z threshold to Gaussian threshold is presented in Fig.3.21.

In order to be able to convert thresholds for other values of n, outside those indicated above, a fit of the surface in the direction of n is required. We supply the conversion program with a value of n and Gaussian threshold σ_G and get the actual threshold for the data σ_{DSP-Z} by interpolation.

3.3.3 Data reduction

After the RFI flagging toolkit has created a bad pixel mask m for a given data frame x (a merged mask for S and D acquisitions), we reduce this mask (Σm) and the data multiplied by this mask ($\Sigma\ (x \cdot m)$), in order to facilitate further data manipulations (and ultimately save disk space). For exoplanet data, the date resolution is reduced from 20 msec $\times$ 4 kHz to 100 msec $\times$ 100 kHz, implying a reduction by a factor 125 of the data volume, allowing for fast and flexible post-processing.

The data and the mask are reduced and stored separately, so when the data reconstruction is needed, the reduced data should be divided by the reduced mask. Each reduced mask bin is a weight to the corresponding reduced data bin. After reconstruction, each resulting data point is an average of a high resolution data bin, taken only on its 'good' (non-polluted) pixels. For example, for a data array:

$$x = \begin{matrix}[1 & 4 & 2 & 9 \\ 10 & 1 & 4 & 8]\end{matrix}$$

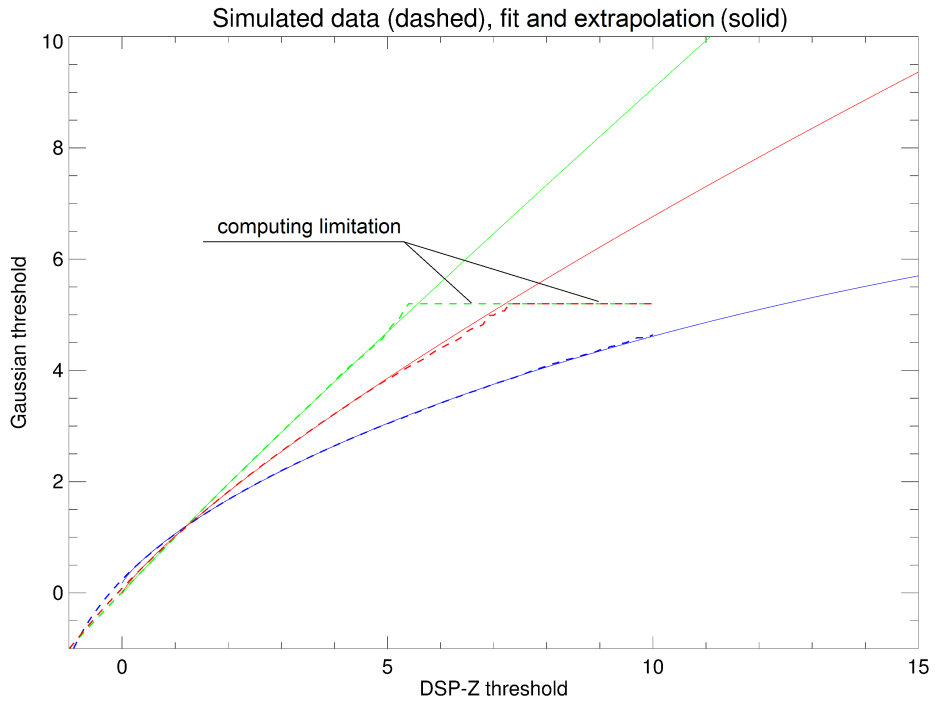

Figure 3.20: Simulated (dashed lines) relations between Gaussian threshold and actual threshold for real data with $\delta t = 64$ ms ($n = 512$ averaged elementary spectra, green), $\delta t = 2$ ms ($n = 16$, red) and $\delta t = 0.25$ ms ($n = 2$, blue) time resolutions and their fits (solid lines).

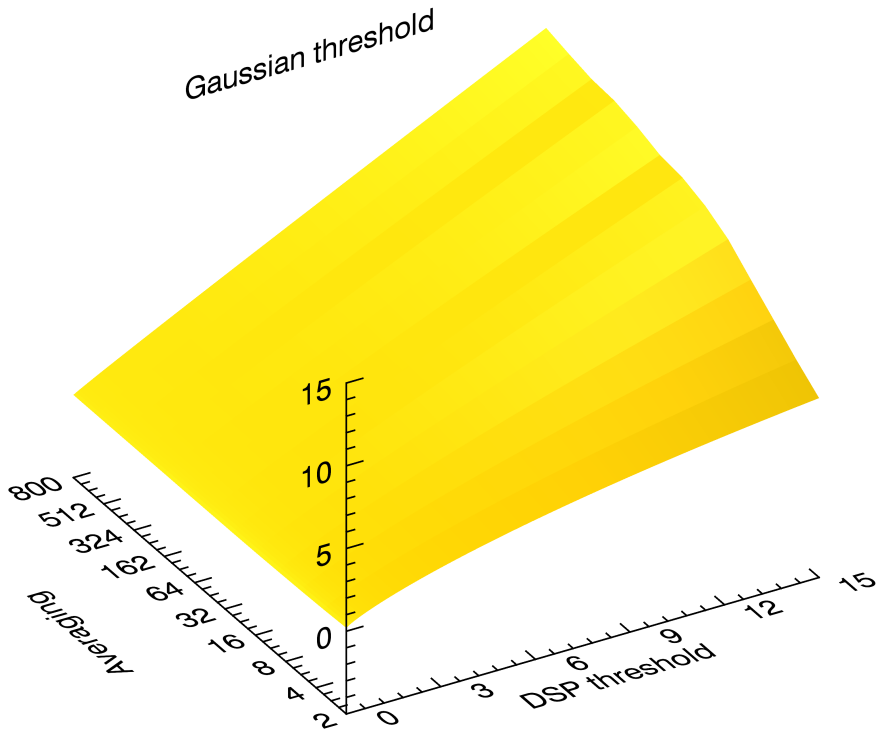

Figure 3.21: Relation between Gaussian threshold and actual data threshold for different time resolutions (number of averaged elementary spectra (n) in the DSP-Z receiver).

We assume that RFI values are > 7. Then the mask of 'bad' pixels will be:

$$m = \begin{matrix}[1 & 1 & 1 & 0 \\ 0 & 1 & 1 & 0]\end{matrix}$$

After multiplication of the data array by the mask, we get:

$$x \cdot m = \begin{matrix}[1 & 4 & 2 & 0 \\ 0 & 1 & 4 & 0]\end{matrix}$$

which after 2-fold reduction in each dimension becomes:

$$\Sigma\ (x \cdot m) = [1.5 \quad 1.5]$$

The reduced mask (weight) is:

$$\Sigma\ m = [0.75 \quad 0.5]$$

Division of the reduced data by the reduced mask allows us to obtain an array with unbiased mean, each value of which represents an average over 'good' pixels in the first and the second 2×2 bins, respectively:

$$x' = \frac{\Sigma\ (x \cdot\ m)}{\Sigma\ m} = [2 \quad 3]$$

The reason why we store both reduced arrays $\Sigma\ (x \cdot m)$ and $\Sigma\ m$ instead of their ratio x' is that is x', all pixels have the correct mean computed on good pixels, but variances in inhomogeneous across the array x' because each pixel results from integration of a variable number of good pixels. When we want to further integrate (reduce) x' during the post-processing (next chapters), simply rebinning it ($\Sigma\ x'$) is incorrect because we would then average with an equal weight pixels that result from the averaging of a different number of high resolution pixels, and that must be adequately weighted for being further averaged. Retaining $\Sigma\ (x \cdot m)$ and $\Sigma\ m$ does exactly this. When we want to further integrate x over time and/or frequency, we can simply rebin (reduce) these two arrays as $\Sigma\Sigma\ (x \cdot m)$ and $\Sigma\Sigma\ m$, and then divide the former by the latter to obtain:

$$x" = \frac{\Sigma\Sigma\ (x \cdot\ m)}{\Sigma\Sigma\ m}$$

Each pixel of the resulting array $x"$ is correctly weighted, exactly as if computed directly from the high resolution data x, without loss of information due to the intermediate reduction step. Variance is still variable from pixel to pixel in $x"$, which is unavoidable due to the masking of bad pixels. After flattening of the data (see next chapters) and subtraction of 1, resulting in zero-mean data, the variance can be corrected by multiplying each pixel of the reduced array (e.g. x') by the square root of its weights ($\Sigma\ m$) and then dividing it by the average of the square root of the weights over the whole array [Zarka 1997].

Reduced data and masks are easy to manipulate the data as then can be loaded at once into computer RAM (e.g. for the Corot-7b 2009 campaign, the original data ∼600 Gb is reduced to ∼5 Gb). The original (not reduced) mask can also be stored together with reduced data, as it occupies a little space: it is a byte array type of the same size as the high resolution data x (float data), but as it contains only 0s and 1s, it can be stored in bits, reducing the size of the stored file by another factor 8. We wrote the IDL programs converting bytes-to-bits and bits-to-bytes on the fly.

The described two stages of pre-processing (RFI mitigation and data reduction) do not bias the data in any way, and do not require any a priori assumptions about the signal or hardware. At the output we get data that could have been recorded by a hypothetical 'perfect' RFI-immune receiver, working with 0.1 sec time resolution and 100 kHz frequency resolution. We do not expect to have intrinsic signal width or variations time scale smaller than these resolutions. Data is stored without any dedispersion, but dedispersion can be performed on the reduced data, which is acceptable for the DM values that we expect from the exoplanet signals.

Chapter 4

Post-Processing and Results of the pulsar/transient survey

Contents

The first positive results were obtained already at the preparatory stage of the survey [Zakharenko 2013]. The aim of this stage was to identify the detectability of known pulsars with UTR-2 prior to try to discover new ones.

Detection of a known pulsar implies obtaining a reliable shape of its average pulse profile (an example of average pulse profile of PSR B0809+74 is shown in the upper left panel of Fig. 4.1), through coherent folding of all dedispersed data with the pulsar period and integration over all frequencies. Detection of pulsars is eased by their unique properties as dispersion ($\sim 1/f^2$) and periodicity. Periods and coordinates of pulsars are measured very precisely in high-frequency observations, whereas dispersion measures are not always as accurate as needed for a low-frequency detection. Individual pulses may appear at different longitudes (phases) of the pulsar rotation period, but there is a preferential longitude where pulses occur most often, which corresponds to the maximum of the average pulse profile. Each pulsar has a unique average pulse profile (its fingerprint) that should correspond to the properties of its emission region, although we do not know yet the exact correspondence rules. Some profiles have multiple components (e.g. main pulse, precursor and interpulse as in [Gil 1994]), other may show subpulse drift [Drake 1968, Weltevrede 2006]. The profiles evolve with an observation frequency (this can be seen for various pulsars in the European Pulsar Network database [1]) revealing changes in the average pulse shape or intensities of the components. Often profiles get broader at low frequencies. For instance, in [Bilous 2015] the width of the PSR B0809+74 profile at ∼150 MHz (Fig. 4.1, lower right panel) is less than in [Zakharenko 2013] at ∼25 MHz (Fig. 4.1, upper left panel). There are various theoretical models attempting to explain the structure of pulse profiles and their behaviour (e.g. [Ruderman 1975, Rankin 1986, Dyks 2005, Petrova 2010]), but none of them encompasses all the observed diversity of pulse profiles.

[1] http://www.epta.eu.org/epndb/

During the above precursor study a full sample of pulsars with DM $\leqslant 30$ pc.cm^{-3}, period $P \geqslant 0.1$ s and declination $\delta \geqslant -10^o$ (which resulted in 74 sources in total, according to the catalog [Manchester 2005]) was observed with UTR-2. Out of this sample, we detected 40 pulsars, for 30 of which it was for the first time in the decameter range. This study became a basis for the present pulsar/transient survey that helped us to select the survey parameters. The processing pipeline, used in this study was slightly different from the one described in chapter 3, mainly because the pulsar parameters (DM and P) were known. The pipeline included RFI mitigation, dedispersion and folding with the pulsar period of the time series integrated over the whole frequency range. The RFI mitigation also used PATROL (section 3.1.1), but did not use SumThreshold. Compared to the RFI mitigation used in the current pulsar/transient survey pipeline, its performance was approximately 1.7 times less good (compare upper and lower left panels of Fig. 4.1). Dedispersion was first applied with a single DM value (the one from the catalogue), but subsequently it was found that the catalog values have inaccuracies that are critical at decameter wavelengths and prevent detection of the pulsar. This was the major reason for previous failures to detect known pulsars at decameter wavelengths. To deal with this problem, a range of DM values around the catalog DM was explored (Fig. 4.1, upper right panel). The observation mode was also different from the drift-scan mode we used in the survey. Each source was tracked (by the maximum of *Sum* antenna pattern) for 90 minutes. The sensitivity of the targeted search was higher than in the survey, because the sources were located in the diagram of both antennae (N-S and E-W), compared to the sources, passing across one of the N-S antenna beams in the survey, and the integration time was longer. For further details of the observations and processing, please refer to the first paper in Appendix A. During this study we confirmed that an intrinsic broadening of the average pulse profile (not due to scattering) takes place at low frequencies, as compared to higher frequencies (Fig. 4.2). This is attributed to the increasing beaming fractions of pulsars (according to radius-to-frequency mapping or another emission region model). This effect, along with the high detectability of nearby slow pulsars (55% of the sample with aforementioned parameters) were the principal motivations to conduct the described pulsar/transient survey. In addition, the DM range (from 0 to 30 pc.cm^{-3}) is not restrictive. The measured scattering time constants τ_{sc} for the pulsar profiles and the scattering spectral indices α_{sc} were lower than expected, and showed that detection of pulsars is possible up to DM = 70 pc.cm^{-3}. For transients this range can be extended up to 100 pc.cm^{-3}.

Post-processing is a step aimed at concluding about detection (or non detection) of the source(s) via extracting all possible useful information from the preprocessed (RFI mitigated and integrated or dedispersed) data. Post-processing of pulsar/transient survey data is intrinsically different from that of exoplanet observations, because the signal should be often visible by eye (especially transients), and we have a model of the signal we are looking for. Therefore, post-processing of survey data is very well-defined, using dedicated methods for extracting dispersed transient and repetitive signals, in contrast with post-processing of exoplanet records that is

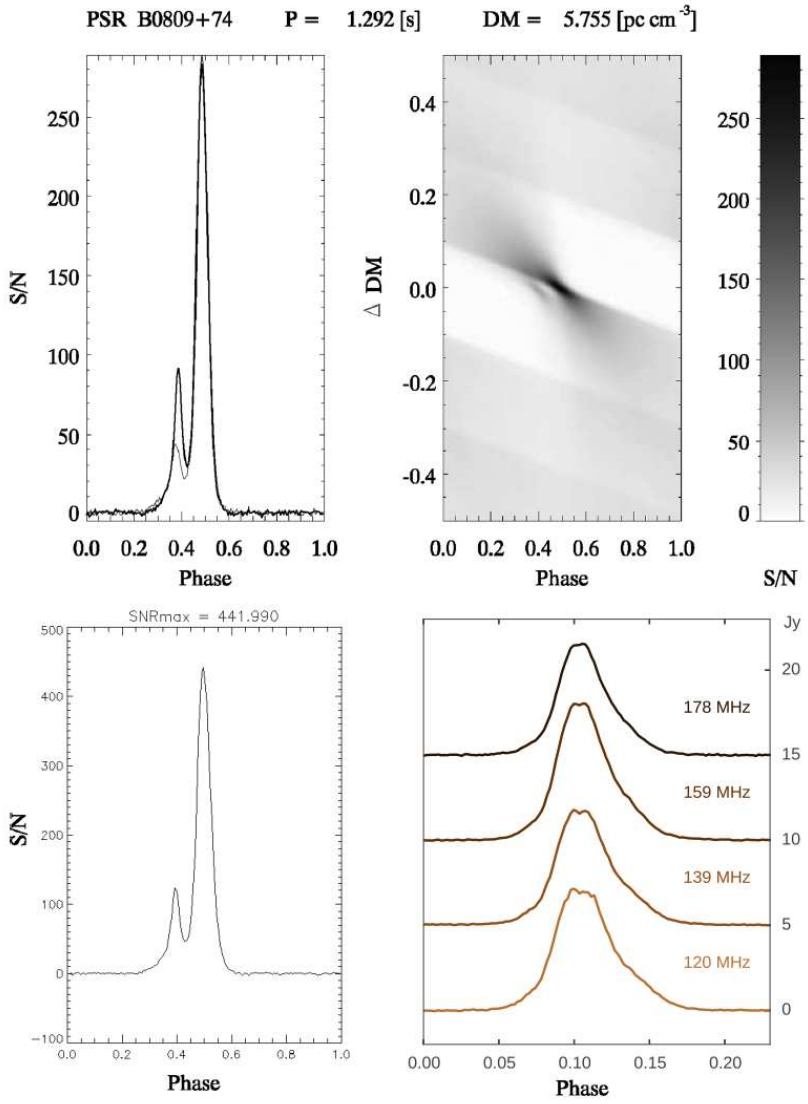

Figure 4.1: Upper panel: detection of PSR B0809+74 in [Zakharenko 2013] at 25 MHz with SNR $\sim$ 290. Lower left panel: re-processing of the same data with the RFI mitigation described in chapter 3 increased SNR by a factor of $\sim$1.5. Lower right panel: PSRB 0809+74 observed with LOFAR HBA ([Bilous 2015], $\sim$150 MHz), illustrating the pulse profile broadening at 25 MHz (profile width at 10% of maximum level is $\sim$0.3·Period) as compared to 150 MHz ($\sim$0.1·Period).

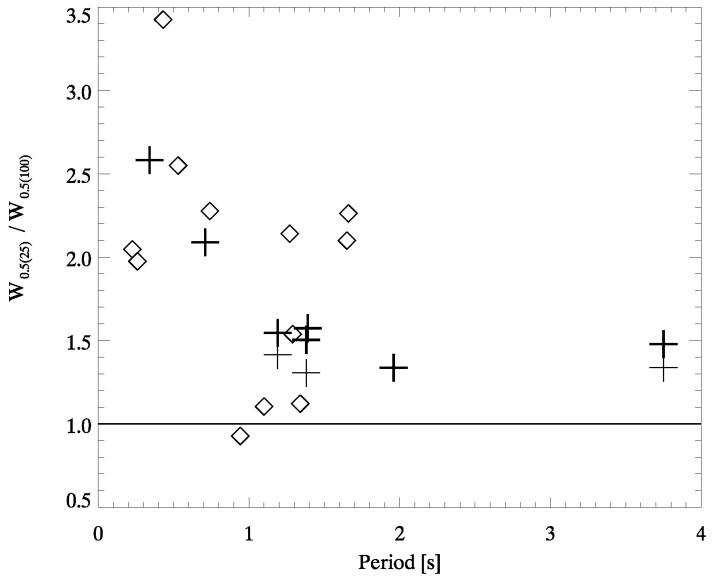

Figure 4.2: Pulsar profile (half-power pulse width) widening at 25 MHz, compared to 100 MHz as a function of pulsar period ([Zakharenko 2013]). Diamonds denote the increase in pulse width of pulsars detected at UTR-2, crosses are the values, extrapolated from [Thorsett 1991]. All values except one are above 1, so widening is observed.

more general and exhaustive.

At the moment more than 90% of planned sky area has been surveyed (Fig. 4.3). We have covered all the northern sky but the circumpolar region, an area with high background noise close to Galactic center and the area around the strong radio source Cyg A.

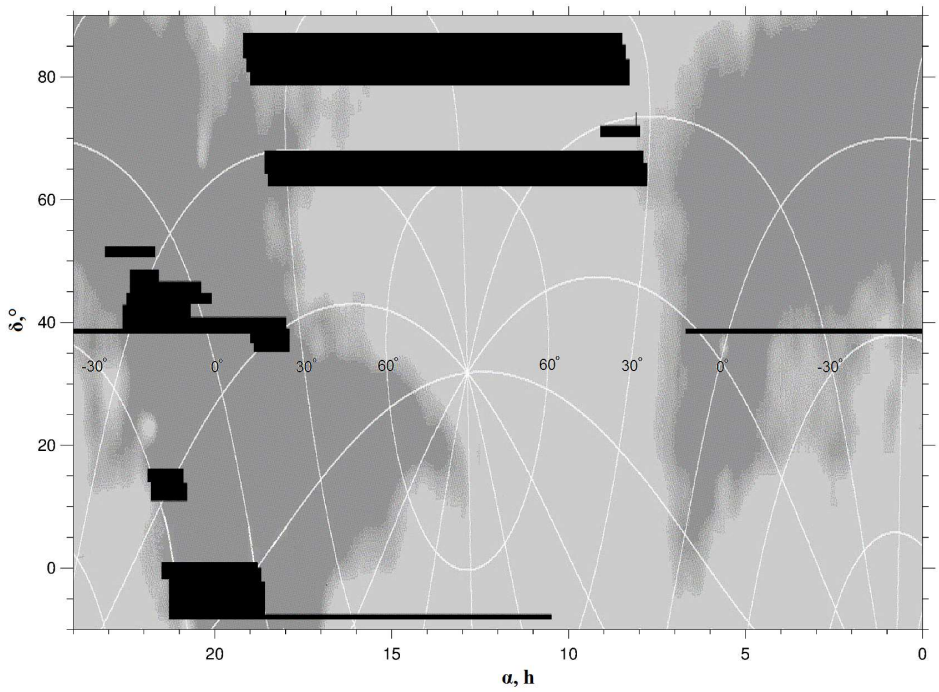

Figure 4.3: Fraction of the sky observed in the survey. The sky region $-10^o < \delta < 90^o$ is shown in shades of grey (adapted from the continuum map of the northern sky [Sidorchuk M., private communication]). Darker regions indicate the higher Galactic background temperature. Lines of Galactic coordinates are superimposed. All this area but the black strips has already been surveyed.

About 75% of recorded data have been pre-processed (i.e. cleaned from the RFI and dedispersed). After dedispersion the pipeline branches into two post-processing tasks:

- Search for individual dispersed bursts
- Search for periodic pulses

Up to now, we focused mainly on the first task (individual bursts), but the methods for periodicity search are also presented.

4.1 Search for individual bursts

The results of de-dispersion are represented versus the coordinates (DM, time), containing 3000 time series integrated over frequency, corresponding to 3000 different DM values, each of 2^{16} points length ($\sim$ 520 seconds).

The first stage of post-processing is the search for powerful events in the "time - dispersion measure" plane. Here we mean by "events" the points (pulses after dedispersion and frequency integration) that exceed certain threshold in a time series. Time series may contain long-term variations caused by changes in Galactic background and ionosphere during the observation session, which should be removed for correct selection of the threshold when searching for bursts. It is done by means of high-pass filtering, i.e. subtraction of low-pass filtered time series from the original one. We retain all variations that are shorter than $\sim$ 4 seconds. We also assume that due to scattering in the interstellar medium we will not encounter short spikes with timescale of $\sim$ 1 sample (8 ms). So we filter short time scales as well, by computing a running average over 4 adjacent data samples. Thus the shortest scale of "events" becomes 32 ms. These filtering parameters have been chosen empirically, when processing test data sets of known pulsars recorded in the same way as the survey data.

After these two filterings (high-pass and low-pass), a data frame of 2^{16} points is divided into 16 smaller subframes $\sim$ 32.5 sec each. Each of the resulting 3000 time series in the subframe is checked for events exceeding a $\mu + 5.5\sigma$ threshold, where μ and σ are the mean and standard deviation of the time series, computed iteratively, by discarding outstanding peaks at each iteration until the noise level is reached. If an event exceeding the aforementioned threshold is found, its parameters (SNR, DM and time of occurrence since the start of observation) are recorded in an output 'database' file. Each such event can potentially be a giant or anomalously intense pulse of a pulsar, or a RRAT signal. It can be also a signal of completely unknown origin, because such a survey is the first one conducted at decameter wavelengths. Selecting a 5.5σ threshold is also an empirical compromise. If a lower threshold is chosen, too many spurious events leak into the database, such as weak RFI signatures or the edges of pulsar pulses smeared in a range of adjacent DMs around the true pulsar DM.

For better visualization and further visual inspection, a red circle is drawn at the location of every detected event. The radius of the circle is proportional to the factor by which the actual signal exceeds the 5.5σ threshold. Usually events occupy several adjacent time resolution and DM points, each producing a circle, therefore circles overlap in the compressed scale and form red disks. The image of the subframe with superimposed event circles is stored for further candidate selection. An example of such image is shown in Fig. 4.4. A disk at DM $\sim$ 22.7 pc.cm^{-3} is an example of a transient candidate.

An example of pulsar detection (in a series of consecutive pulses) is shown in Fig. 4.5. Events with different intensity repeat at the same value of DM=12.88 that corresponds to the DM of PSR B0834+06 [Zakharenko 2013].

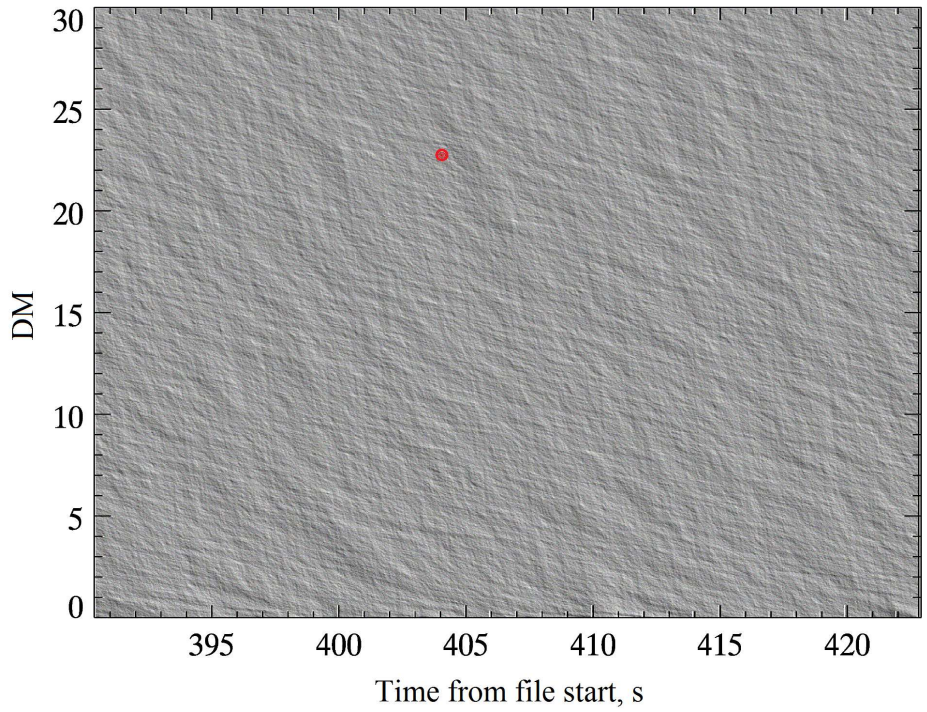

Figure 4.4: Result of the individual pulse search program. The red disk in the upper part of the diagram is an example of transient candidate with DM$\sim$ 22.7 pc.cm^{-3}.

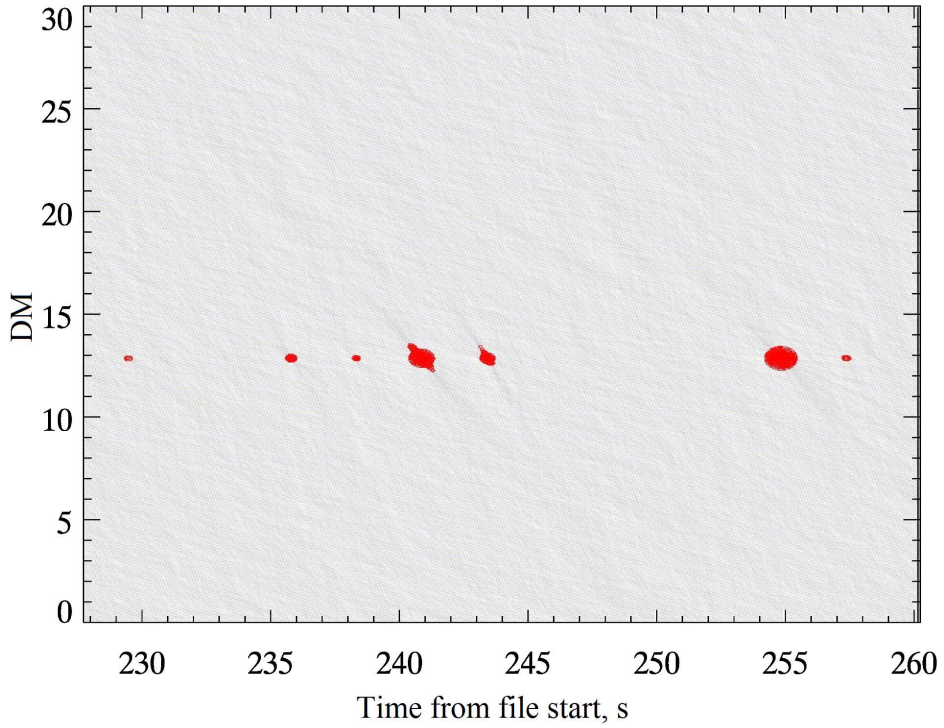

Figure 4.5: Result of the individual pulse search program. A sequence of red circles at DM=12.88 is an example of pulsar detection.

A data subframe with residual interference is shown in Fig. 4.6. The events form a connected shape, spreading on a range of DM values, and producing many false-positive events.

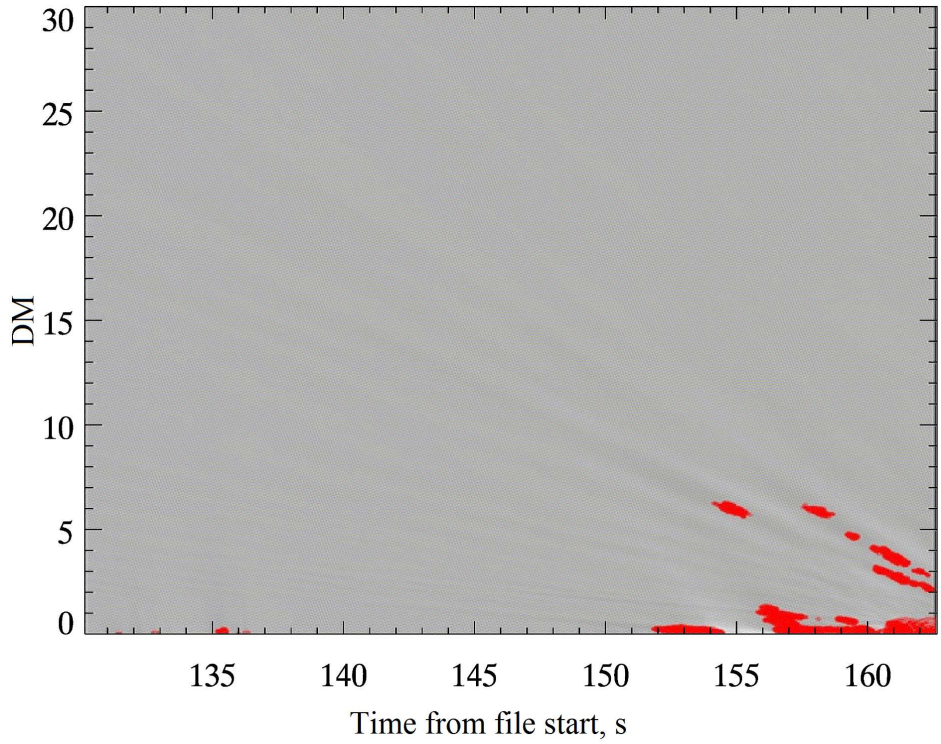

Figure 4.6: Result of the individual pulse search program. Red circles that form an extended structure indicate residual broadband RFI.

Sometimes, RFI not eliminated during the pre-processing can form a shape that mimics a real signal, concentrated in a small range of DM values (Fig. 4.7, upper panel). These events are misleading, and could be confused with a strong transient candidate. To solve the ambiguity, we return to the raw data and dedisperse the raw dynamic spectrum with respect to the DM value at which the event appeared. If the signature of the event after dedispersion is parallel to the frequency axis, then it is a signal whose time-frequency behaviour agrees with the dispersion law (3.3), therefore most probably it is a cosmic source. If after dedispersion the event forms a shape different from a straight line (Fig. 4.7 lower panel), it means that its time-frequency sweep is different from the one induced by propagation through cold plasma of the interstellar medium, and it is most likely a terrestrial RFI.

The parameters (DM, SNR, time) of all events that were identified in the recordings of one receiver during one observational night (13 h) are stored in a single .dat file. This file is then analyzed in order to see at which DM values the events happened. Two summary plots are done for each receiver data for each night of observation. The first one is a scatter plot of DM at which the event happened versus

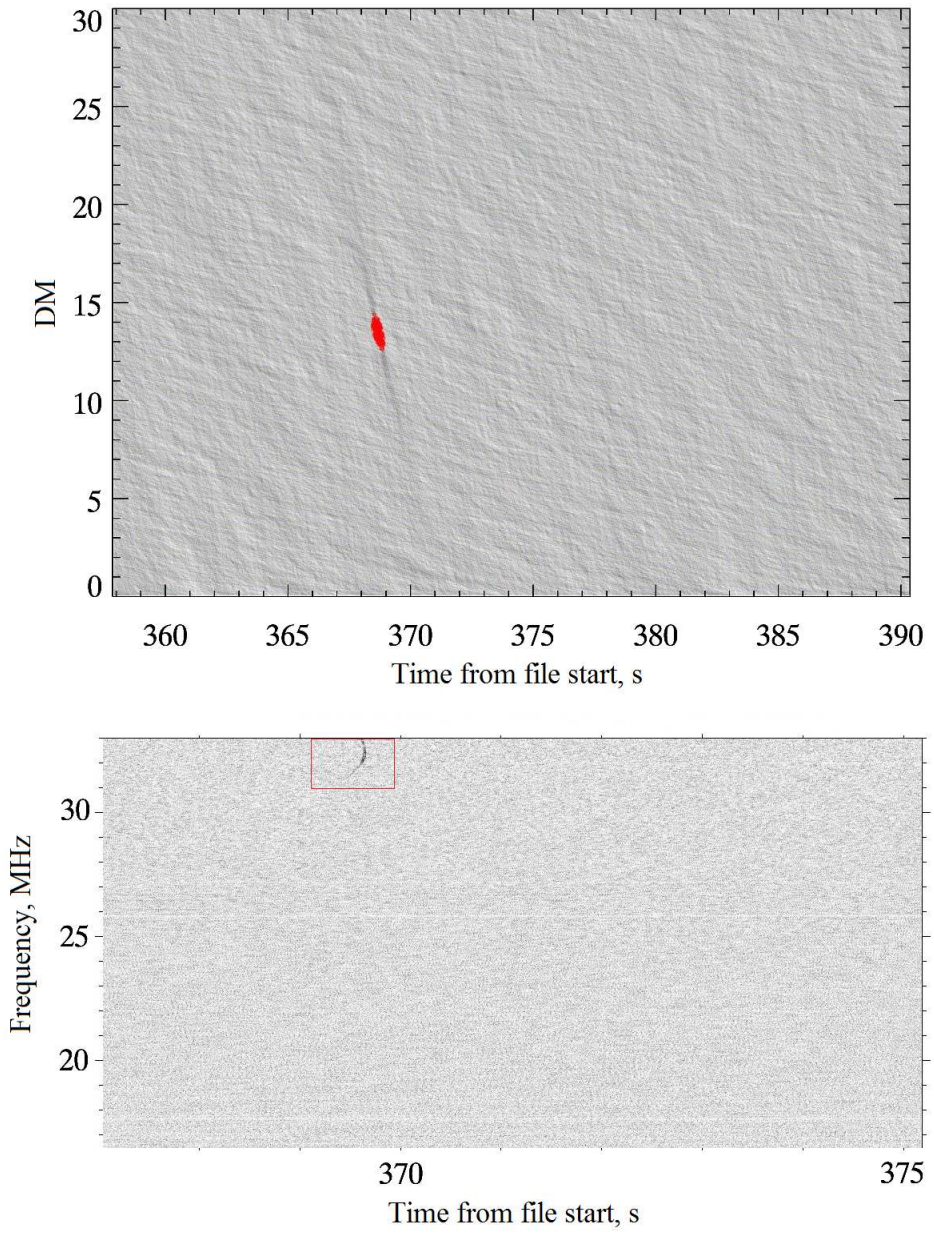

Figure 4.7: Result of the individual pulse search program. Upper panel: the event occupies a small range of DM, but nonetheless is RFI. Lower panel: after dedispersion of the raw dynamic spectrum the event appears to have a time-frequency dependence different from the expected dispersion.

time when it happened. Here SNR of the events is not represented. This plot is mainly used for examining possible RFI residuals. RFI appear at low values of DM, mostly at DM=0. The time scale is very compressed for this plot, but sometimes (as in Fig. 4.8, lower panel) we can see a sequence of pulses, repeated at the same DM value. In this plot there are pulses of PSR B0834+06.

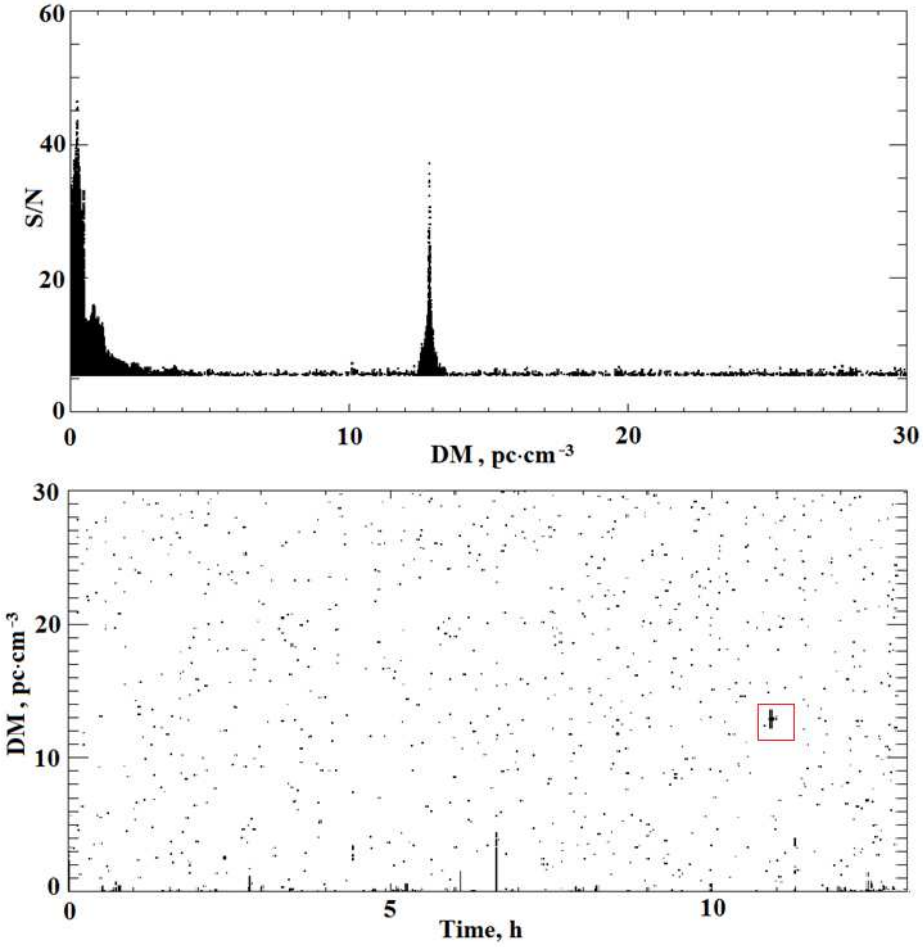

Figure 4.8: Upper panel: summary plot of the event SNR versus DM, The peak corresponds to the DM of PSR B0834+06. Lower panel: summary plot of the event DM versus time of occurrence. The highlighted region contains the events, associated with PSRB0834+06.

The second summary plot (Fig. 4.8, upper panel) is a scatter plot of SNR of each event versus its DM. Each point is an individual event, whose SNR exceeded the 5.5σ threshold. If there is a peak in this summary plot, it means that there were many events with different intensity at the same value of DM. It is a signature of a pulsar or a repetitive transient. The peak in Fig. 4.8 corresponds to the DM of the pulsar B0834+06. The declination $+6^o$, corresponding to a survey code that was

observed that night also confirms that it was this pulsar.

For convenience, this plot is constructed by a program that has an interactive functionality. Clicking on an event (one point of the plot) allows to display its coordinates (DM and SNR). Then, in the vicinity of the selected DM coordinate (DM±0.2 pc.cm^{-3}) the program searches for the event with maximum SNR. It outputs the SNR of this event, the DM value, the time when it occurred and links to a raw data file that contains the event, for visual inspection.

Considering that a typical pulsar pulse has a maximum on the precise value of the pulsar DM and gets smeared at its proximity, the most intense event points are automatically selected at the true dispersion measure of a candidate. Having selected a point in the peak (Fig. 4.8, upper panel), the program will output the correct DM value for PSR B0834+06: DM=12.88 pc.cm^{-3} (with precision equal to the step size = 0.01 pc.cm^{-3}).

Each peak on the plot is then checked to determine if it is a known pulsar or a new source that has not been discovered so far. For this, we compare the candidate DM value obtained from the interactive selection described above, with DM of known pulsars. First, we check the DM values of the 40 pulsars that have already been reliably detected at UTR-2 [Zakharenko 2013]. Then, we check the ATNF pulsar catalog [Manchester 2005]. If no coincidence is found, the source should be re-observed in follow-up observations to confirm or refute the discovery of a new pulsar. If the coincidence by DM is found, but the approximate coordinates of a candidate differ significantly from those of the pulsar from the catalog, the source is also retained for re-observation.

In the fraction of data that we processed, we found 17 pulsar candidates with DM value not associated with DM of any known pulsar (e.g. the one indicated with question mark in Fig. 4.9). Three sessions of follow-up observations were done in attempt to detect these sources again. The sum, difference (and, respectively, the product) of N-S and E-W antennae was used, but this time only three beams (A, C and E) were recorded. Each candidate was observed during 1 h 45 min., far from its culmination ($>$ 1 hour), so that the source could cross all 3 beams consecutively and hence its coordinates could be refined. The antenna was re-pointed every 10 minutes in order to keep the approximate source position within the beam. Thus, an area of 2.5 $\times$ 2.5 degrees^2 was monitored at a time. Unfortunately the individual pulse search has not revealed any events at the dispersion measures associated with the aforementioned sources in the follow-up observations. That can be due to their intrinsic sporadicity or unfavourable conditions of observations (ionosphere refraction that can essentially displace the source, RFI, or observation at low elevation). We hope to reveal these sources by subsequent periodicity search.

4.2 Search for periodicities

Signals of weak pulsars are unlikely to be found by individual pulse search. Detection is possible only using their periodicity via subsequent accumulation at the source

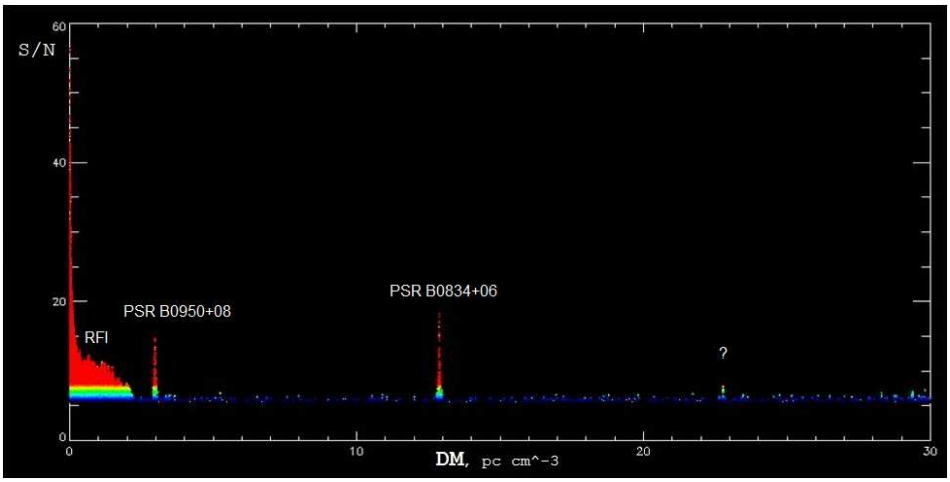

Figure 4.9: Example of summary plot of events SNR versus DM, with detection of 3 sources: PSR B0950+08, PSR B0834+06 and an unknown source at DM $\sim$ 22.7.

periods while it drifts across a wide "North-South" antenna pattern.

There are two main algorithms for pulsar periodicity search: (i) methods based on Fast Fourier Transform (FFT) - for search in the frequency domain and (ii) Fast Folding Algorithm (FFA) - for search in the time domain by means of autocorrelations (see references in [Kondratiev 2009]). Our previous work on the attempt of detecting XDINSs in the decameter range [Zakharenko 2011] led us to the conclusion that the FFA method is optimized only for long periods ($>$ 5 s) and gives more noisy results for short periods compared to FFT (cf. the noise levels above 2 Hz in Fig. 4.10 upper panel, and less than 0.5 s in the lower panel). We assume that periodicity search method should be more efficient for searching normal pulsars in the survey data, rather than RRATs or XDINSs that have long periods of inactivity and will more likely be detected by their individual pulses. Therefore, we chose the FFT method.

Several parameters can be varied for searching periodicities in the data using FFT. First is the data length (time window) that we analyze at a time. If chosen too small, there will be not enough sensitivity to detect pulsar harmonics, whereas if it is too large, there is a risk to accumulate much residual RFI that will suppress the useful signal. Second, the cutoff frequencies for band-pass filtering play an important role. We want to filter out the high frequencies, corresponding to short periods ($<$ 0.05 s) that we know we cannot detect and low frequencies, corresponding to periods longer than $\sim$ 10 seconds, for which sources are very rare.

The periodicities search algorithm proceeds as follows. First, we make the Fourier transform of the dedispersed data (3000 time series at different DM) with an optimal time window (from the standpoint of noise minimization) $\sim$ 520 seconds (that also corresponds to the length of one data file). We obtain 3000 frequency series, corresponding to the 3000 trial DM steps. Similar to the procedure for tran-

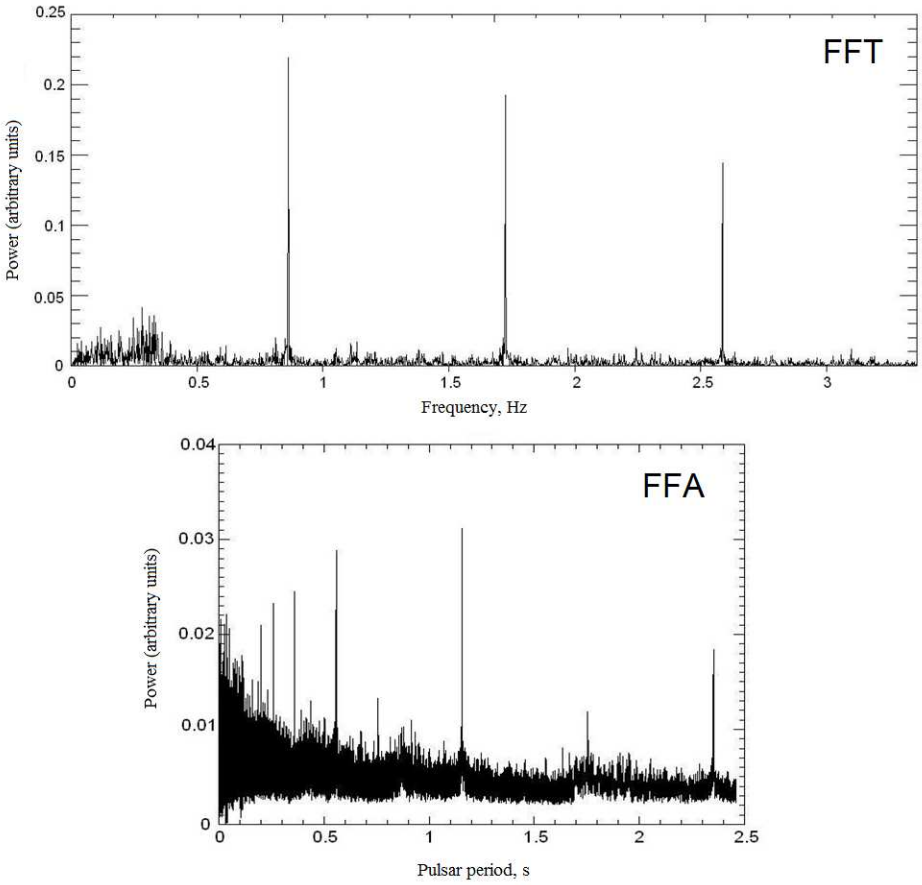

Figure 4.10: Comparison of FFT (top) and FFA (bottom) algorithms for detecting a pulsar period of 1.18 s (PSR B1133+16).

sient signal search, for each value of trial DM, we calculate the standard deviation σ_{FFT}. Values that exceed 10 σ_{FFT} threshold are written to the 'database' and are denoted by red circles on the "frequency - DM" plane. The circle radii are this time proportional to the logarithm of SNR (of each harmonic).

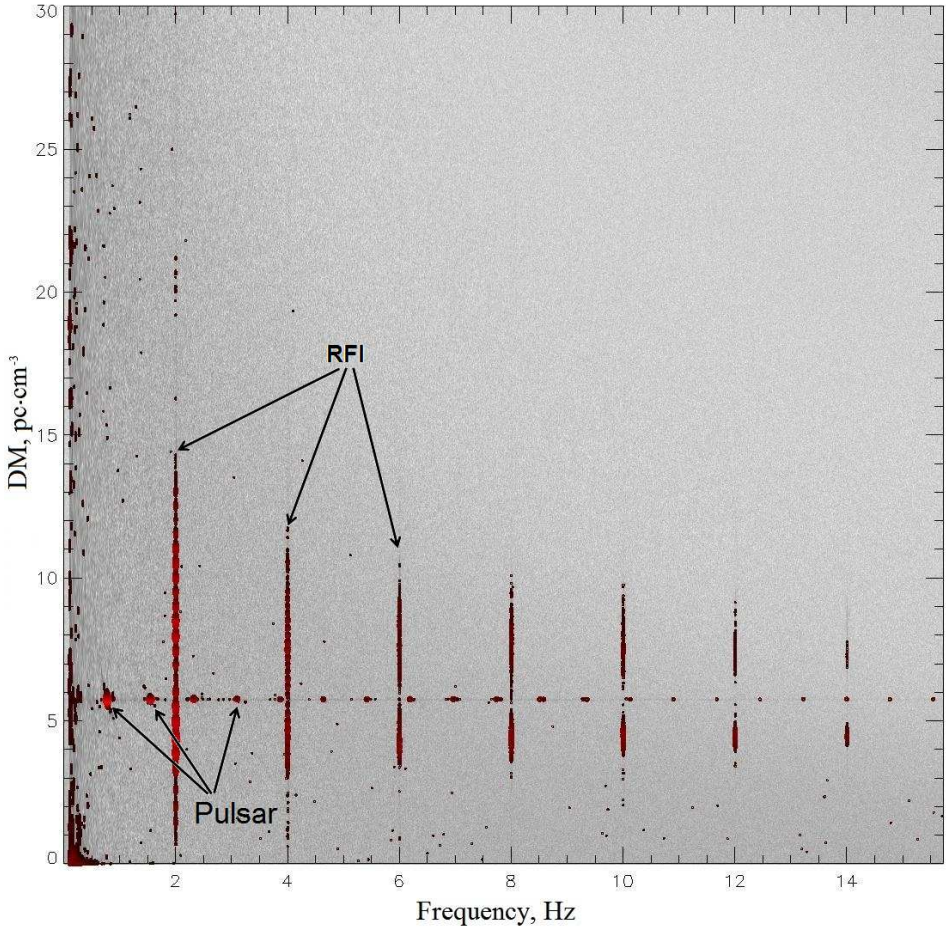

Figure 4.11: PSR B0809+74 detected in a period of bad RFI conditions (morning hours). 20 points on a horizontal line, corresponding to DM = 5.75 are 20 pulsar harmonics. Vertical red lines (producing many false-positives) are signatures of residual periodic RFI.

Fig. 4.11 shows the result of a blind search for periodic signals in the direction of PSR B0809+74. Twenty harmonics of PSR B0809+74 (equidistant points at DM ~ 5.75 pc.cm^{-3}) are detected in spite of the presence of strong RFI, whereas for the majority of the known pulsars we can see only the first few harmonics. From this data we can estimate the potential sensitivity of observations in the survey mode in more detail.

Fig. 4.12 shows an example of processing of 6 consecutive 520-second data files (total of 52 minutes). The two upper panels show the temporal variations of indi-

vidual pulse intensity during the observation. The topmost panel shows the SNR of the pulsar pulses, calculated as a ratio of the on-pulse to the off-pulse part of the period, and smoothed over 10 adjacent periods. In panel b) each vertical slice is one period of the neutron star rotation. The dark horizontal high-intensity strip in the middle is the main pulse window of the pulsar. Panel c) shows the SNR of the first harmonic of the pulsar period in each of the 6 selected data files. The length of the data frame, on which FFT is done corresponds here to the length of one data file (520 s), and it is the optimal value in terms of both resulting SNR and ease of data processing. The lowermost panel shows the simulated response of the source, while it crosses the antenna pattern of the sum of N-S and E-W antennae towards the pulsar. It is a circumpolar source, hence the time of its passage through antenna pattern is longer than for low-declination sources.

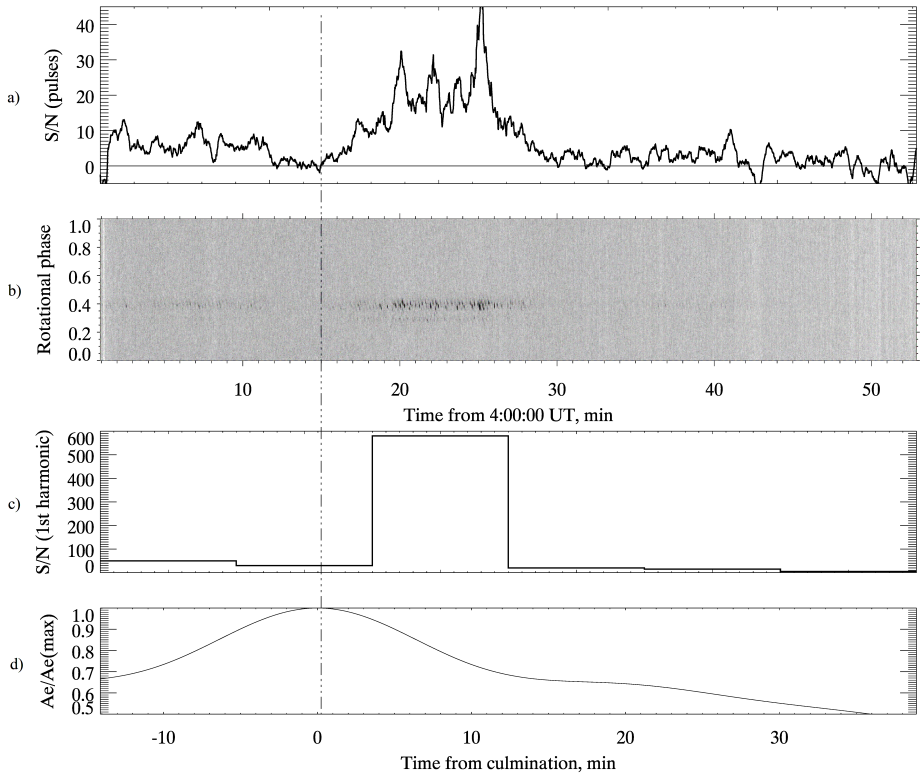

Figure 4.12: (a) SNR of individual pulses of PSR B0809+74 in 6 consecutive data files during its transit across the wide antenna pattern in the survey mode; (b) the intensity of pulses versus pulsar's rotational phase; (c) SNR of first harmonic of the pulsar signal; (d) variation of the sensitivity during the source transit.

In Fig. 4.12 the maximum intensity of individual pulses is reached in the third data file. The Figure proves that the time of maximum intensity of the pulsar radio

emission does not necessarily coincide with its culmination time (dash-dot line, crossing all panels of the plot), when antenna effective area and therefore sensitivity are maximum. This effect demonstrates that the survey concept was correct, in the sense that observations in sum (not product) of the two antennae allows better accumulation of weak pulsar signals. Signal is present in the wide knife-like pattern of the sum of N-S and E-W antennae for more than 40 minutes (see Fig. 2.9 and 2.10 to recall the antenna patterns). If we used a narrow pencil beam (product of the antennae) we would see the pulsar only during 2 minutes around its culmination and we would thus not be able to capture the period of pulsar's maximum intensity. In this active period the first harmonic of the pulsar radio emission reaches an impressive SNR ~ 600.

Pulsar's SNR can be further increased. Fig. 4.13 (upper panel) shows how the pulsar harmonics power depends on the DM value used during dedispersion. As in the time domain, the harmonics power is present not only at the precise value of pulsar DM, but also at several adjacent values of trial DM. Therefore, there is additional room to accumulate the pulsar power, which can be vital for detection of weak pulsars. After summing of 100 adjacent values of DM, the SNR of the first harmonic raises up to ~ 2000 (Fig. 4.13 lower panel - solid black line). Furthermore, if the power of higher harmonics (up to tenth) is added up with the first one, it allows to reach a SNR of ~ 4000 (Fig. 4.13, lower panel - red line). As the average flux density of the above pulsar is about ~ 1.2 Jy, and its signal can reach a SNR of 4000, there are resources for the detection of pulsars at the level of a few mJy with this method.

First runs of the blind periodicity search program have shown that an intolerably large number of residual RFI is left in the data. In contrast to individual bursts search, the use of more severe RFI mitigation is essential. The current RFI mitigation routine for the survey, described in chapter 3, is optimized for transient search. As we decided to apply the same RFI mitigation to all data of one sky snapshot, we first of all focused on detecting transient signals. After the more severe RFI mitigation of the survey data and additional tests of filtering parameters on known pulsars, the described periodicity search program will be launched on the survey data massively.

4.3 Transient candidates from the Survey

Up to now we focused mostly on dispersed individual pulse search when processing the survey data. During the automatic post-processing, a large number of events (hundreds of thousands) were detected and written to our output "database" file. Most of these events were detected at low values of DM and attributed to residual RFI. We excluded from further consideration events with DM$<$1. Nevertheless, close sources also may produce events at low DM values. These events cannot be automatically distinguished from RFI, therefore visual inspection is needed.

The visual inspection program loads images created by the individual pulse

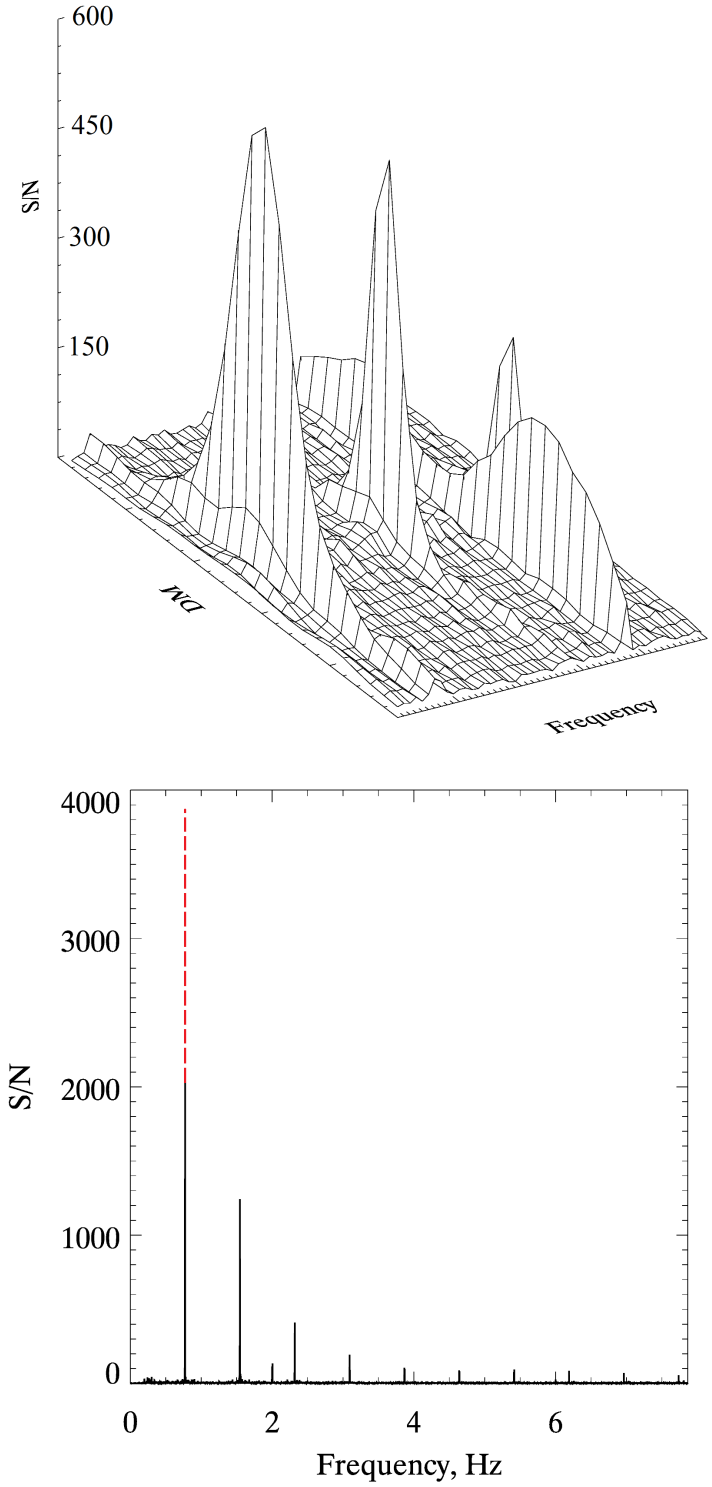

Figure 4.13: Pulsar harmonics' SNR versus DM (upper panel) Harmonics' power is spread over adjacent DM values. After addition of 100 adjacent DMs, SNR at the fundamental frequency reaches $\sim$ 2000 (lower panel, black), and after addition of all higher harmonics' power to the first harmonic it reaches almost 4000 (red dashed line).

search program, one by one. The observer examines the events, denoted by red circles and identifies those, which satisfy the following criteria: (i) events should be isolated, and not part of any structure. All extended structures are most likely produced by RFI. (ii) individual pulses after dedispersion and frequency integration should have a SNR > 6, and (iii) a circle should not be empty (that represents an event in a single time resolution point). Usually the pulses we look for occupy several points of the time series, so the circles overlap and look like filled or partly filled. If an event satisfies all the aforesaid criteria, the observer interactively selects its coordinates (the same way as explained in section 4.1.1). Around the selected coordinates, the event with maximum SNR is found and recorded to a second 'database'.

During the visual inspection, a series of repetitive events at the low value of DM=3.83 pc.cm^{-3} attracted our attention. The events were detected at the survey code, corresponding to $\delta = 63.1355^o$ in the recordings of all 5 telescope beams (Fig. 4.14).

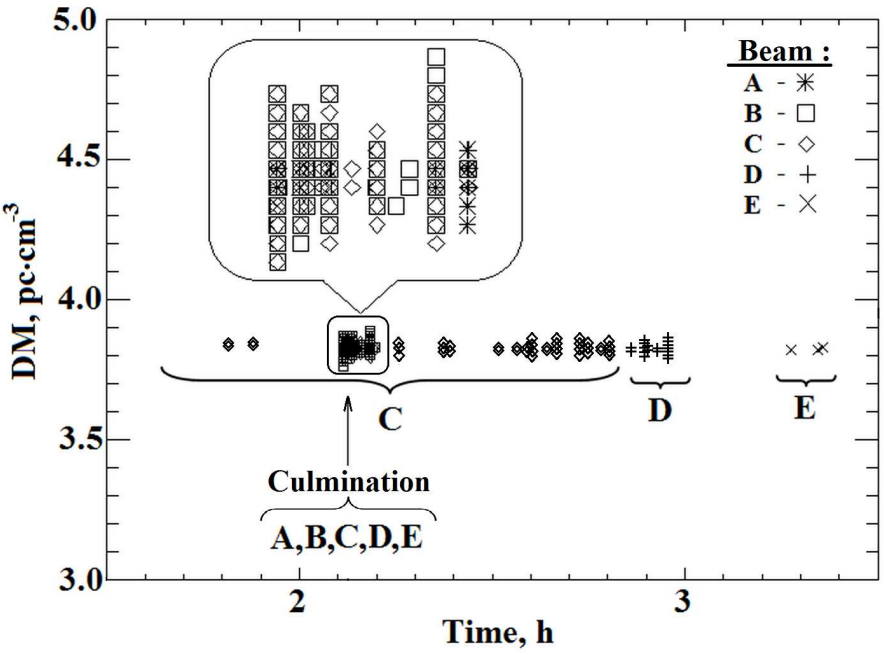

Figure 4.14: Signatures of PSR J0243+6257 in all 5 beams of UTR-2.

An interference may also appear in all five beams simultaneously, but the above source was detected in different beams at different times. First its signature appeared in the central beam, and lasted there for about an hour (which is consistent with the N-S antenna pattern layout). In the middle of the passage of the source across the central beam, for about 4 minutes the events happened simultaneously in all 5 beams. It means that the source was in its upper culmination and crossed the E-W antenna pattern, which overlaps all 5 beams of the N-S antenna (Fig. 2.9).

After the source finished its passage through the central beam (C), it went down from its upper culmination and crossed consecutively the two lower beams (D and E). Each event had SNR of at least 8. Given the time of culmination, we determined the Right Ascension (RA) of the source to be about 2 h 41 min. The declination is explicitly determined by the survey code and the strip in which the source was found (central beam), i.e. about $+63^o$. Thus, knowing the approximate coordinates of the source and its dispersion measure, it was easy to identify the source, using the ATNF pulsar catalogue [Manchester 2005]. It was the pulsar J0243+6257 recently discovered by GBT [Hessels 2008]. This pulsar has never been detected at decameter wavelengths in general and at UTR-2 in particular. Its dispersion measure was not precisely determined (being 4 pc.cm^{-3} in [Hessels 2008]), and therefore it is refined in the present survey. Fig. 4.15 shows the SNR versus DM summary plot (similar to Fig. 4.8, upper panel) for the beam C data, containing a clear peak at DM=3.83 pc.cm^{-3}.

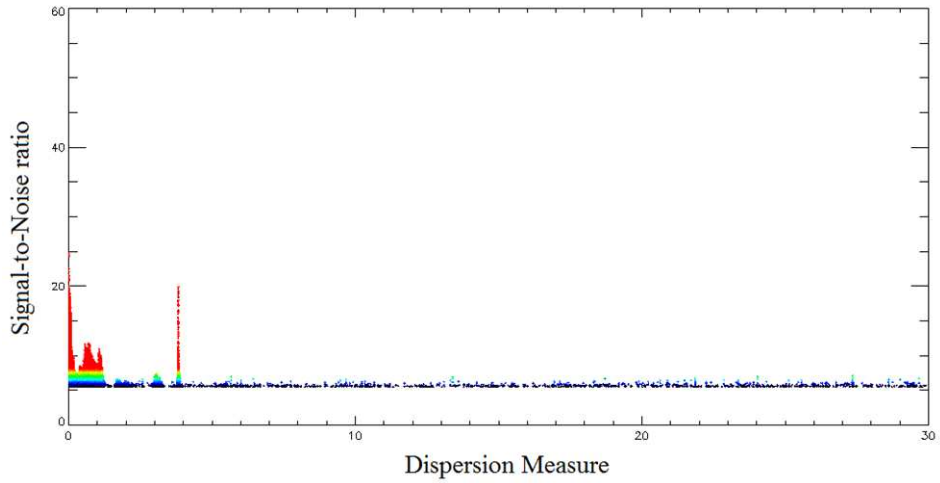

Figure 4.15: Detection of PSR J0243+6257. Precise determination of the dispersion measure = 3.83 pc.cm^{-3}.

Up to now, about 2/3 of the survey records are processed by the automatic search of individual bursts, and about 20% by manual selection (visual inspection). Initial number of detected individual bursts is very high. After the subsequent manual selection, much less candidates was left for further consideration. Furthermore, we excluded all the events associated with known pulsars from the list of candidates using the following method. We compare the DM of each event to the DM of the 40 pulsars from [Zakharenko 2013] that are detected at UTR-2. If the DM of an event lies within 0.1 pc.cm^{-3} of the DM of one of known pulsars, and its declination δ (recalculated to the epoch J2000) is within $30'$, and its right ascension α within 1 hour from the δ and α of the known pulsar, then we remove it from further consideration. During this procedure, we have re-detected 26 pulsars (25 already detected at UTR-

2 [Zakharenko 2013] and the above pulsar J0243+6257). We considered a known pulsar to be re-detected only if there were events corresponding to its dispersion measure in the surveyed sky patch approximately corresponding to its coordinates.

To date we have a 'database' with about 450 individual dispersed events with SNR above 6. All have a frequency sweep in accordance with the dispersion law (3.3). The majority of these events do not belong to new pulsars (i.e. they do not repeat at the same DM value, close in time). These events are placed on the sky map on Fig. 4.16.

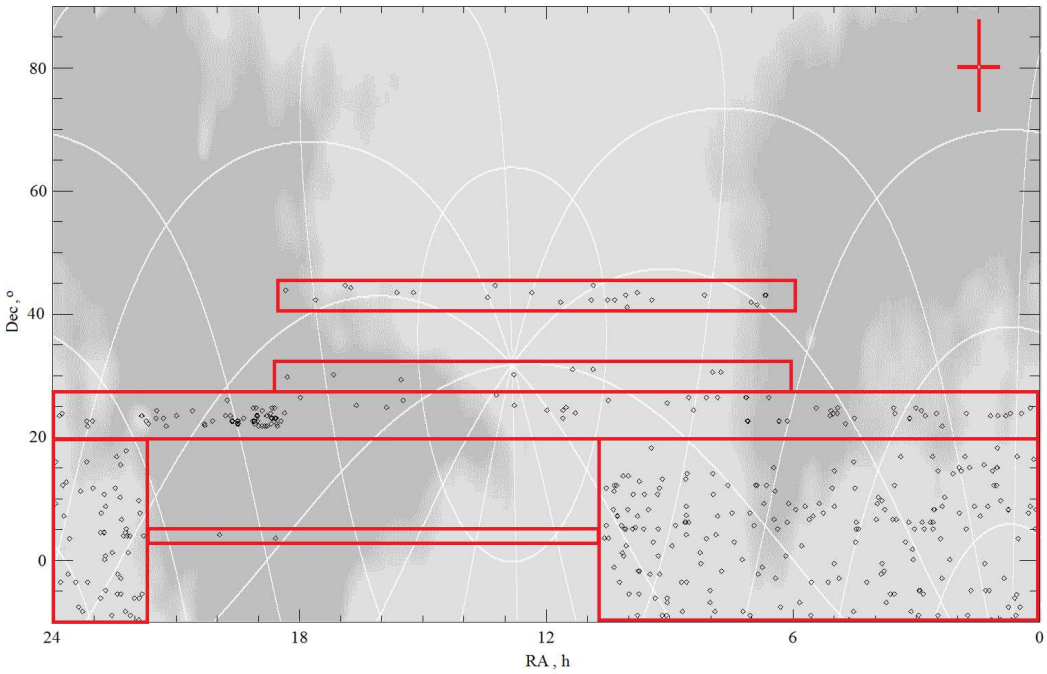

Figure 4.16: Continuum map of the northern sky (darker color corresponds to higher Galactic background temperature, i.e. Galactic disk) with superimposed (approximate) coordinates of $\sim$ 450 transient events that we detected in the processed fraction ($\sim$ 20%) of the survey data (red boxes). A cross in the upper right corner indicates error bars, corresponding to sizes of N-S and E-W antenna beams.

The preliminary localization of the source can be made due to 5-beam observation mode. If it is observed only in one receiver's data, the declination is determined with precision $< 1^o$. On the contrary, if the signal is present in all 5 beams, then it is most probably detected by the common E-W antenna pattern. In this case the right ascension can be determined with the same precision. Then, the beam with maximum signal points to the correct declination of the source. The presence of the source in one of the beams can also be checked, using the difference of the corresponding beam of the N-S antenna and the E-W antenna (see Fig. 2.10). Having the Sum and the Difference channel, the pencil beam can be computed, according

to the formula (2.4), which contains only a sky area of the intersection between the E-W antenna and the given N-S antenna beam.

A preliminary histogram (Fig. 4.17) of detected transient candidates versus galactic latitude (b) resembles what we would expect for real cosmic sources. The source locations follow the Galaxy's disk population, considering that with the current pre-processing limit at DM < 30 we do not go beyond the width of the disc. There is a local maximum at $b = 0^o$. For comparison, the distribution of known pulsars with DM less than 30 pc/cm^3 and a period (p) of > 0.2 s, versus the Galactic latitude, is shown in Fig. 4.18. The histogram looks similar to the distribution of known pulsars, except for the maximum that we find at -50^o.

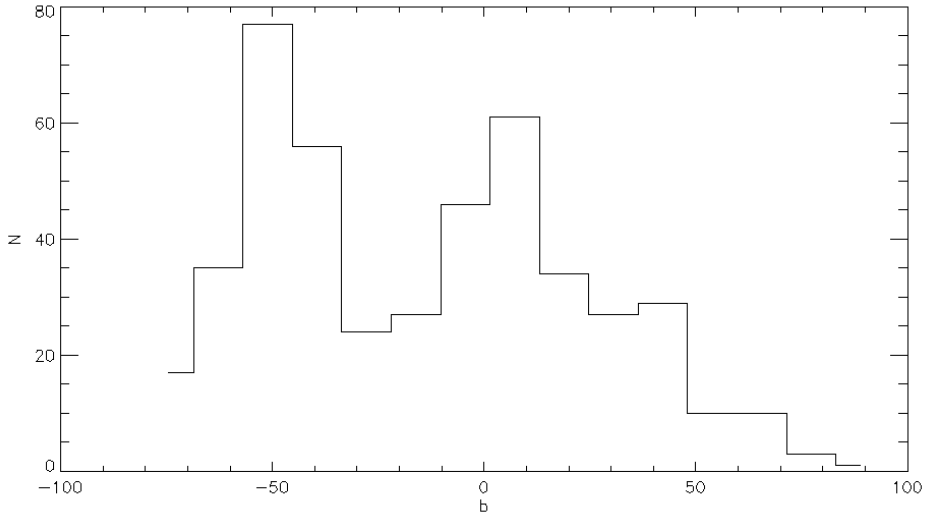

Figure 4.17: Histogram of transients' Galactic latitudes b (^{o}).

We should keep in mind that lower beam positions (corresponding to that maximum at -50^o) have been entirely processed, whereas the higher positions are processed only partly. Therefore detection of other transients will increase all parts of the histogram except for the area of the current maximum. Also for the low beam positions there is larger probability to capture terrestrial RFI as compared to positions closer to zenith. Therefore, another more thorough stage of candidate selection is being done for these regions.

The nature of the transient candidates is yet uncertain, but the shape of the received pulses is very similar to related pulsar pulses. We propose that our detected transients could originate from:

- pulses of neutron stars that are unfavourably oriented in space for higher frequency observations
- RRATs with low dispersion measures that have been misinterpreted as RFI in the high-frequency surveys

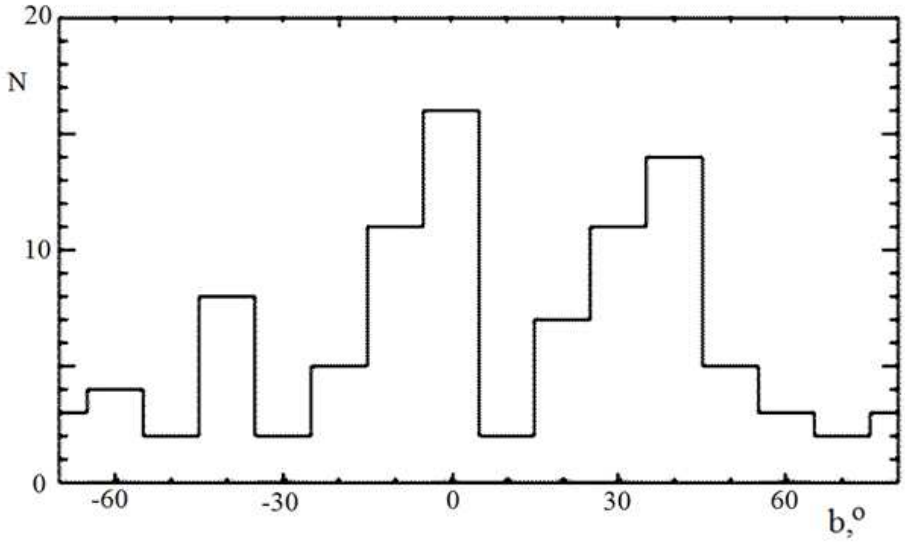

Figure 4.18: Distribution of known pulsars with DM $<$ 30 pc.cm^{-3} and period P $>$ 0.2 s on Galactic latitude b (^{o}).

- pulsars that present an increase of flux density towards low frequencies (such as PSR B0943+10, [Stappers 2011])
- giant pulses of millisecond pulsars (usually flux density of millisecond pulsars grows with decreasing frequency) that are either sporadic or unfavourably oriented. Although giant pulses are short, they will arrive significantly scattered at our frequencies and will be noticeable in the survey data
- anomalously intense pulses of close weak pulsars ([Ulyanov 2012])

To test the neutron star origin of our pulses, a number of tests can be made. Pulsars are expected to have a specific distribution of dispersion measure. While in the Galactic disk, the number of pulsars should vary as the square of the dispersion measure. When we reach the edge of the disk in the direction of pole, the number of pulsars should increase linearly with the dispersion measure. At some distance, the radio emission from pulsars becomes weaker than fluctuations of the Galactic background, and the number of detected pulsars at higher DMs decreases. The predicted histogram for pulsars that should be detected by SKA [Keane 2015] is shown in Fig. 4.19.

Building a similar histogram for $\sim$ 450 detected events show a somewhat similar shape of distribution (Fig. 4.20).

The histogram of known RRATs dispersion measure (Fig. 4.21) resembles the histogram of pulsars. We can see the lack of low-DM (nearby) RRATs. These sources are difficult to discover in high-frequency surveys due to their small dispersion delay between upper and lower bound of the frequency range, and therefore their similarity

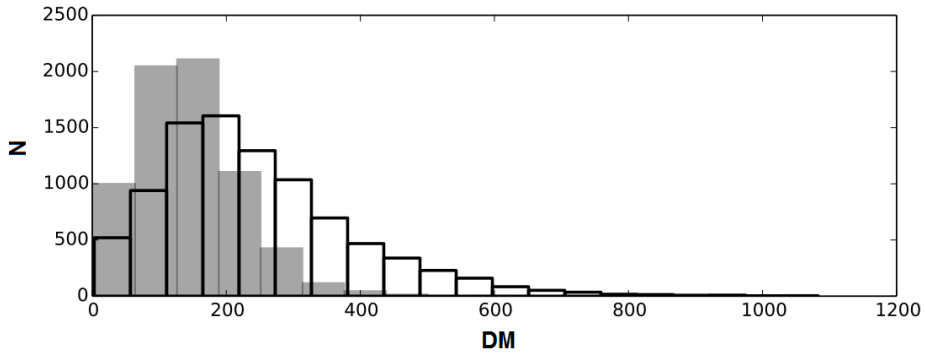

Figure 4.19: Simulated histograms of DM of pulsars, expected to be observed with SKA Phase 1, for SKA1-LOW (dark bars) and SKA1-MID (clear bars) [Keane 2015].

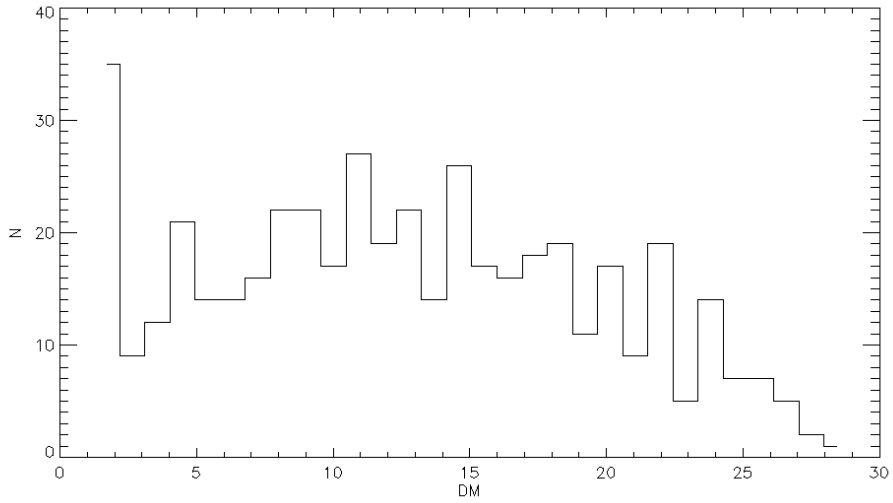

Figure 4.20: Distribution of DM of transient events detected in this study.

with wideband RFI [Kondratiev 2009]. Thus we are interested in a detection of the closest RRAT.

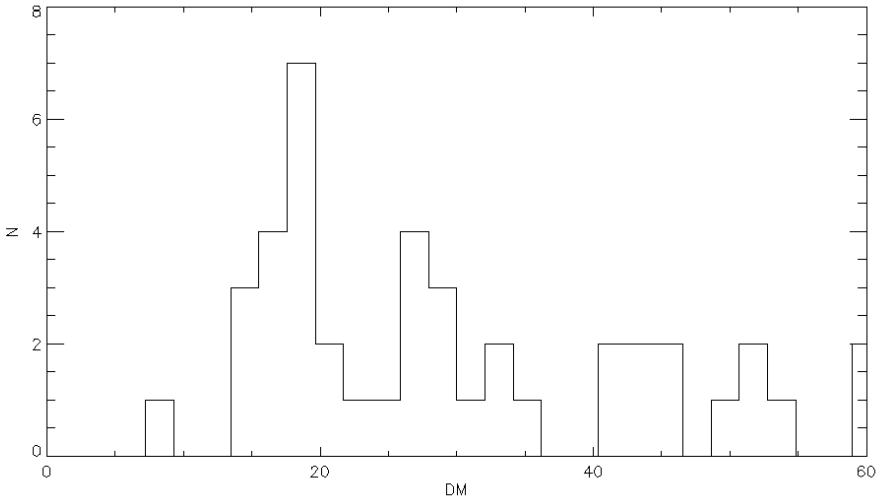

Figure 4.21: Distribution of known RRATs DM.

As the dispersion measure is higher in the Galactic disk (for sources at the same distance) than for other Galactic latitudes, the scatter plot of pulsar DM versus b looks as shown in Fig. 4.22.

Therefore we expect the distribution of DM versus Galactic latitude of our pulses to be similar to that shown in Fig. 4.22, but taking into account the limited DM range explored. Currently this distribution looks like in Fig. 4.23. There are not enough events yet, to draw any conclusion, but the number of events decreases with increasing DM, and events with higher DM tend (slightly) to lower Galactic latitudes. The repeated events are visible as overlapped triangles.

Detection of about 450 transient events in the first 20% of the survey data suggests that there might be many relatively nearby cosmic objects that emit non-repetitive pulses or non-regular low occurrence rate pulses. The ongoing multiparametric analysis is aimed at detailed study and more thorough selection of these events. We assume that after processing of 100% of the data we will have more than 1000 valid transient signals (proven to be non-RFI). With this number of events, we will be able to draw more robust statistical conclusions, such as their distribution versus Galactic latitude, signal-to-noise ratio and dispersion measure as verification criteria.

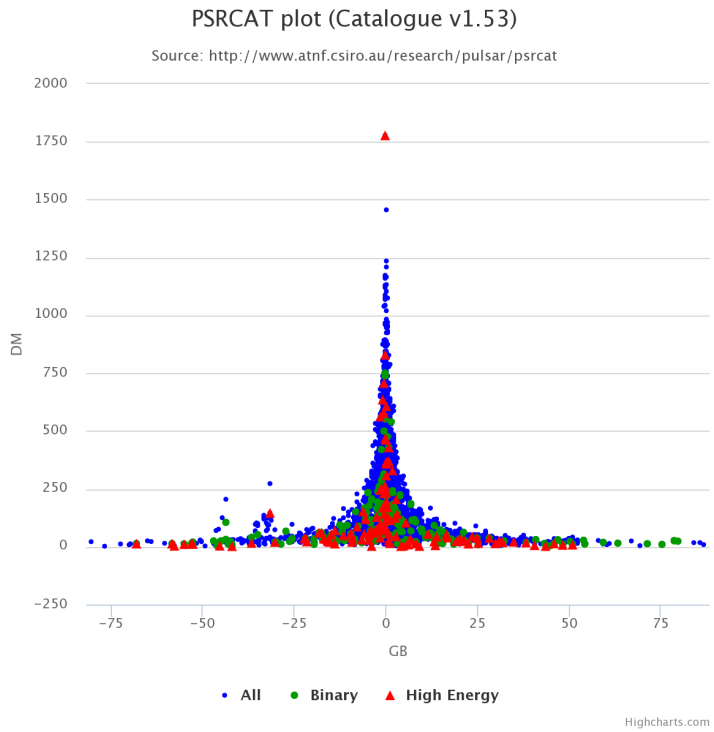

Figure 4.22: DM versus Galactic latitude for pulsars from ATNF pulsar catalog.

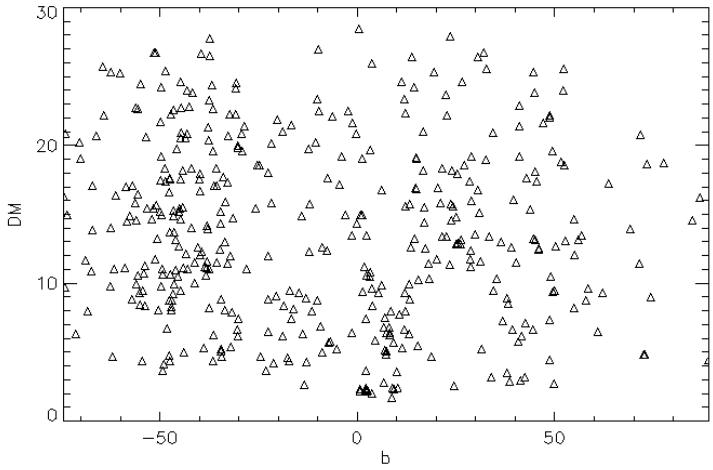

Figure 4.23: DM versus Galactic latitude for the events detected in our survey.

Chapter 5

Post-processing and results on exoplanet search with UTR-2

Contents

At the post-processing stage the aim is to determine whether there is a signal from the targeted exoplanet in the data. For this, we integrate data (in frequency and time) in different ways, usually obtaining 1 value Q_i for each 2-minute inter-pointing interval (IPI), and observe how this quantity (called observable) evolves with the observation time and with the orbital period of the exoplanet. Eventually we compare the behaviour of each observable in the *On* and *Off* beams. If in the *On* beam we see stronger variations of the observable with time or orbital period, than in the *Off* beam, it might be an evidence of presence of magnetospheric or induced emission from the exoplanet.

The example of solar system planets tells us that planetary cyclotron-maser radio emissions are very anisotropic. Thus, an observer should measure regular occurrence or intensity variations as a function of the orbital period. This why we fold the measured values Q_i with the orbital period of the targeted exoplanet. If some regular variation of Q_i versus the orbital phase is detected in the *On* beam only, it will be a strong hint of the presence of an exoplanetary emission. However, our observations of Corot-7b provide a complete coverage of its orbital phase, but with few measurements per phase. As planetary radio emissions are also intrinsically sporadic, this coverage may be insufficient for finding clear evidence of a signal modulation with the orbital phase. Thus we also looked at broadband bursts that, if present in the *On* beam and absent in the *Off* beam, could provide another hint of the detection of exoplanetary radio emission. We expect the detection of a real signal to be not too dependent of the details of the post-processing. Of course, further tests may be required to confirm the origins of the signal.

Ideally, the *On* beam should contain only the source of interest (the emission region of star-exoplanet system), and the *Off* beam should observe only the Galactic background, simultaneously. A signal in the *On* beam may as well be the radio emission of the host star. Again, variations with the orbital period will be an

essential discriminating factor. Additionally, there may be other sources in the relatively wide beam of UTR-2 (especially in Sum (of N-S and E-W antennae) mode), that can contribute to the output flux of either *On* or *Off* beam. Intense radio sources can also create a response from the side lobes of the UTR-2, usually in the form of broadband scintillations. Those might be effectively removed by processing the phase information of data recorded in the correlation mode, not used in the present work. But neither of these sources will have consistent variations with the orbital period of the exoplanet. The first step is thus the detection of a radio emission, and the next step is the discrimination between the planet and the star or other sources in the field, via periodicity, dispersion measure, or polarization studies (the later not at UTR-2).

There is a point source with 1.2 Jy flux density at the edge of the field around Corot-7b corresponding to UTR-2's pencil beam. Fig. 5.1 shows this field from the LOFAR MSSS[1] catalog.

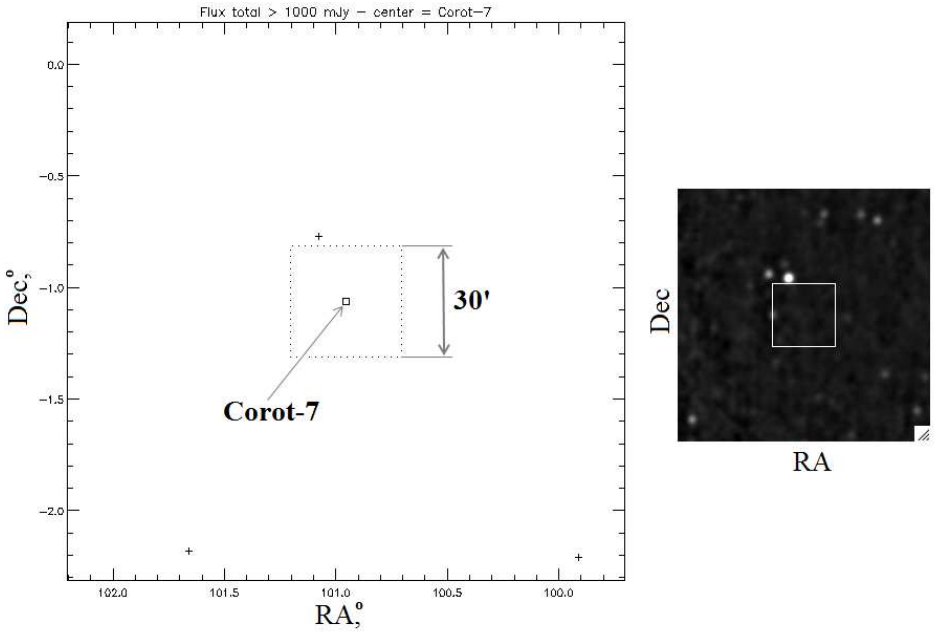

Figure 5.1: Left panel: point sources stronger than 1Jy/beam in the Corot-7b field, taken from LOFAR MSSS catalog. Right panel: the sky map at 120 MHz around the Corot-7b field. Squares in the centers of both images correspond to half-power beam width of UTR-2 pencil beam (∼30')

To confirm or refute the detection of an exoplanetary signal, we need to consider several selections and sky calibration methods applied to the data, and find ways to reduce the data so that the exoplanet signal is highlighted. If the desired signal persists in several observables, under different selections, then it is a good argument

[1] http://msss.astron.nl/

in favor of the detection of a real signal.

The post-processing stages, described below, consists of:

- data selection
- calibration
- computation of observable quantities
- examination of diagnostic plots

5.1 Data selection

Data selection is aimed at eliminating those parts of the data, which are corrupted (either by residual RFI or by instrumental effects) and ensuring that all data included into the analysis have an equal weight (as far as possible).

At the post-processing stage, all the reduced data from an observation set (*On* or *Off* beam) is loaded into the computer RAM as a 4-dimensional data array, whose dimensions are (i) data acquisitions (Sum and Difference), (ii) frequency, (iii) time within 1 IPI ("fast" time), (iv) index of IPI in the observation ("slow" time).

Having two data acquisitions, Sum (S) and Difference (D), we can compute the pencil beam P, according to the formula (2.4): $P \sim S - D$ and the corrected pencil beam P':

$$P' = \frac{S}{\langle S \rangle} \langle D \rangle - D,$$

where $\langle S \rangle$ and $\langle D \rangle$ are spectra integrated over all observational nights for A & B receivers, i.e. with the same hardware (cables/amplifiers/circuit). The corrected pencil beam takes into account a physical difference (offset and variations) between the Sum and Difference channels, especially in the last stage amplifiers that are installed just before the DSP-Z receivers.

The data selection is made in three dimensions: (i) the frequency selection, (ii) the selection of IPI (long time scale) and (iii) time selection within IPI (short time scale). All IPI are approximately the same length (usually 2 minutes of recording), which makes ∼1200 spectra after data reduction. Some IPI don't have an equal length with the other IPI, and hence they are examined closely and may be excluded from further consideration. For example, at the edges of each night of observation, the IPI are usually slightly shorter than 2 minutes. The information contained in the bad pixel maps may be used to eliminate the IPI that contain too many polluted spectra or frequency channels (sometimes the fraction of contaminated data within an IPI exceeds 50%). They are also ignored in further processing. The threshold is set with respect to the RFI mitigation method used. In the latest pipeline version we specify two thresholds: $< 40\%$ (less severe) and $< 20\%$ (more severe) of bad pixels per IPI. The less severe selection usually excludes $\sim 20\%$ of the data, whereas the more severe one excludes about 30% of the data (of the IPI).

Selections in frequency are based on knowledge of the telescope response (resulting from its construction principles), and on our expectations about the signal. We defined the following selections:

- all frequencies, i.e. 12 – 32 MHZ
- $\sim 19-21$ MHz, range where the telescope response is $\geq 80\%$ of its maximum level (this is the peak range of the telescope response)
- $\sim 18-26$ MHz, range where the telescope response is $\geq 20\%$ of its maximum level (corresponds approximately to the second stage of the preamplification system)
- $\sim 12-18$ MHz (low band, in case of low frequency emission only)
- $\sim 18-24$ & $24-31$ MHz (for comparing detection in 2 spectral bands in the main range of the telescope)

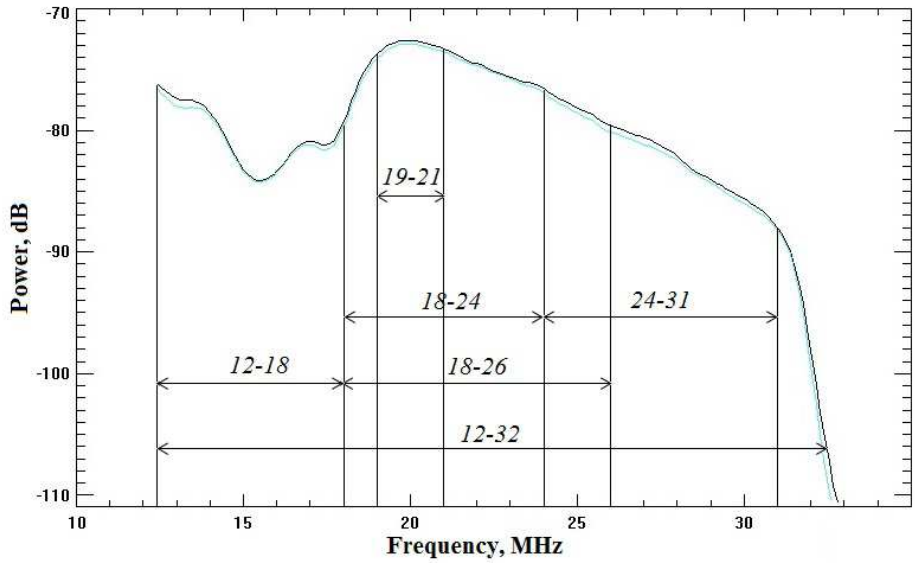

Figure 5.2: Frequency selections applied to the data for highlighting the signal or comparing detection in different spectral subbands.

Further selections require visualizing data in all possible ways. This is also useful for having an idea of the quality of pre-processing. To visualize the 4-dimensional array, we need to reduce it over certain dimensions in order to get either summary 2-dimensional data slices or 1-dimensional cut sets.

Reducing data and bad pixel masks to 2 dimensions can be done by:

a) averaging over frequency (one time-series per IPI) - for selection of clean IPI and clean/stable interval within the IPI (Fig. 5.3);

b) averaging over 'slow' time (one average dynamic spectrum) - for selection of frequency range and clean/stable interval within the IPI (Fig. 5.4);

c) averaging over 'fast' time (one spectrum per IPI) - for selection of frequency and clean IPI (Fig. 5.5).

In these plots we can see which parts of data contain residual RFI or differ in some way from the other data.

The cut sets (line plots) are the following:

a) averaging over fast time and frequency in each IPI → average IPI intensity versus slow time (IPI number) - for selection of clean IPI (Fig. 5.6);

b) averaging of all IPI over (slow time and) frequency → time series versus fast time within the average IPI - for selection of clean/stable interval within the IPI (Fig. 5.7);

c) averaging of all IPI over time (thus over fast and slow time) → average spectrum (amplitude-to-frequency response of the telescope) - for frequency selection (see Fig. 5.2).

From Fig. 5.7 we see that there are more pixels masked at the edges of the IPI, on average. This may be due to unsteady-state processes in the telescope after pointing and due to edge effects in RFI flagging routines, or to a transient excess of RFI. Thus, as a selection in the direction of 'fast time', we can eliminate the first 15 seconds and last 5 seconds of each IPI, i.e. $\sim 16\%$ of the data.

5.2 Sky calibration

For each above selection data should be calibrated before further integration in order to compensate for frequency dependent preamplifiers output, which makes signals at certain frequencies more intense than at the others. The data calibration can be done in several different ways: using a reference source, using a reference noise generator, using a reference antenna, or using the sky signal itself.

UTR-2 was not initially designed to perform continuum measurements, as there is no common part between the N-S and E-W antennae. In the present work we don't expect to measure the absolute flux density of the exoplanet radio emission, but we rather want to make a conclusion about the presence or absence of an emission. At this stage, for the purposes of exoplanet detection, calibration by the sky background (either by data of *On* beam or data of *Off* beam) is sufficient. Data calibration by the sky signal can be done by dividing the data by the averaged telescope response (average spectrum). This process is also called "flattening". Ideally, the averaged response should contain neither a useful signal nor any interference. The data averaging window may vary according to the specific flattening method applied.

In the raw data we have the two data flows (recordings): the Sum (S) of N-S and E-W antennae signals and their Difference (D). From S and D, we obtain the pencil beam P and the corrected pencil beam P'. The average spectrum is computed for each elementary recorded spectrum (S, D, P, P'). Among these

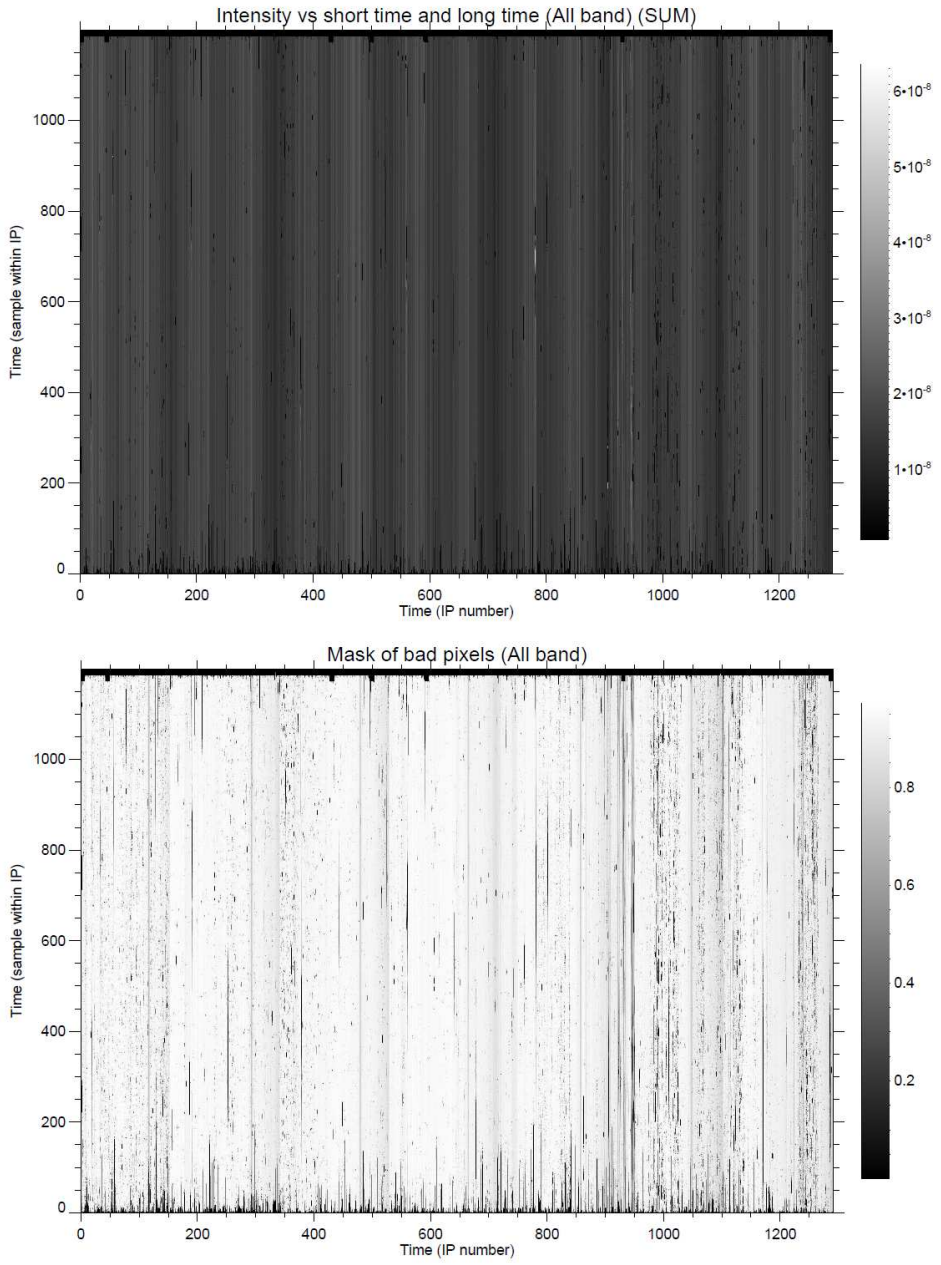

Figure 5.3: Data visualization - data array averaged over frequency. Averaged intensity and mask of bad pixels are represented as a function of slow time (IPI number, abscissa) and fast time (inside an IPI, ordinate).

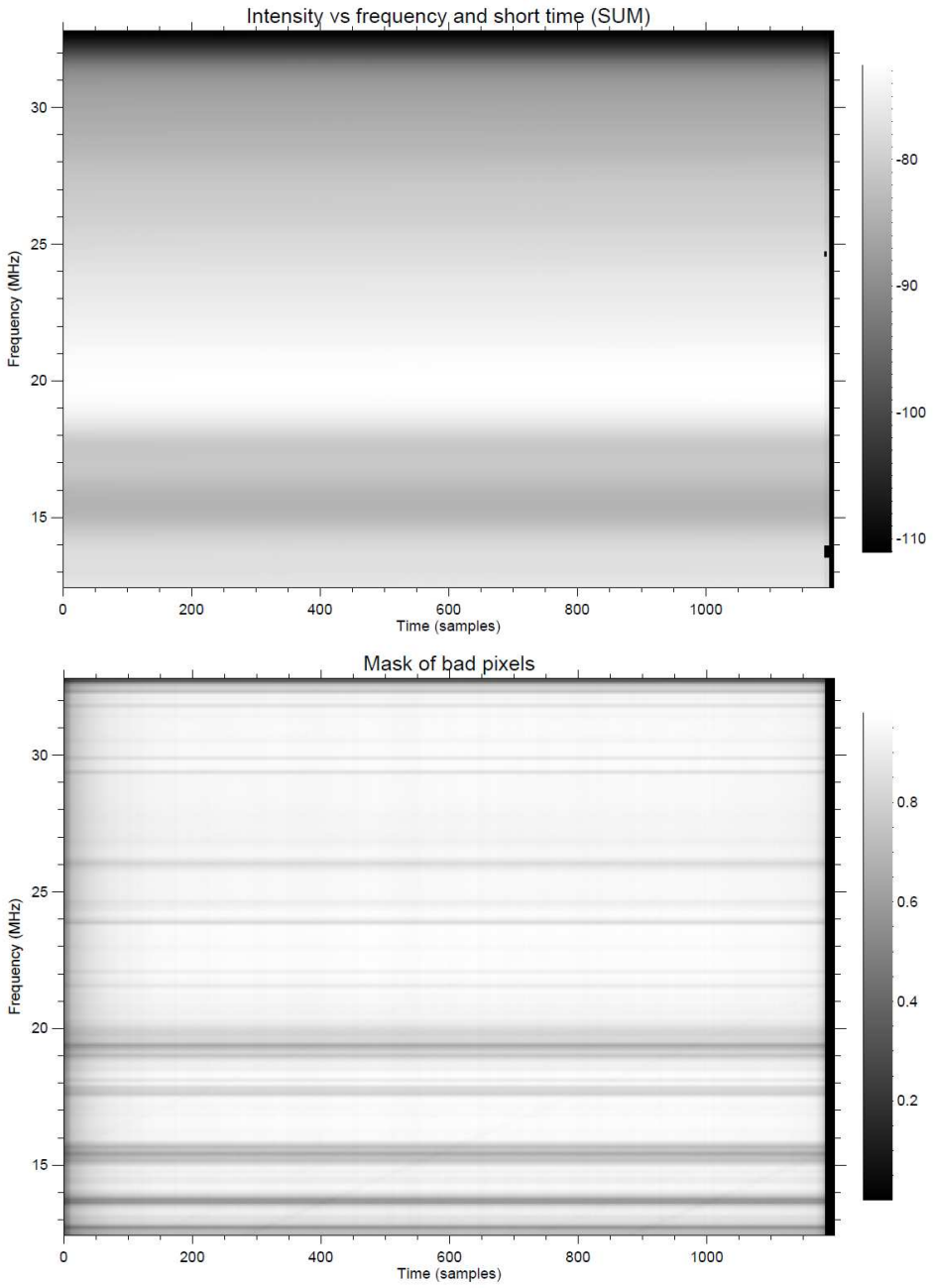

Figure 5.4: Data visualization - data array averaged over slow time. Averaged intensity and mask of bad pixels are represented as a function of fast time (inside an IPI, abscissa) and frequency (ordinate), i.e. they form an integrated 2-minute dynamic spectrum and corresponding integrated mask of bad pixels.

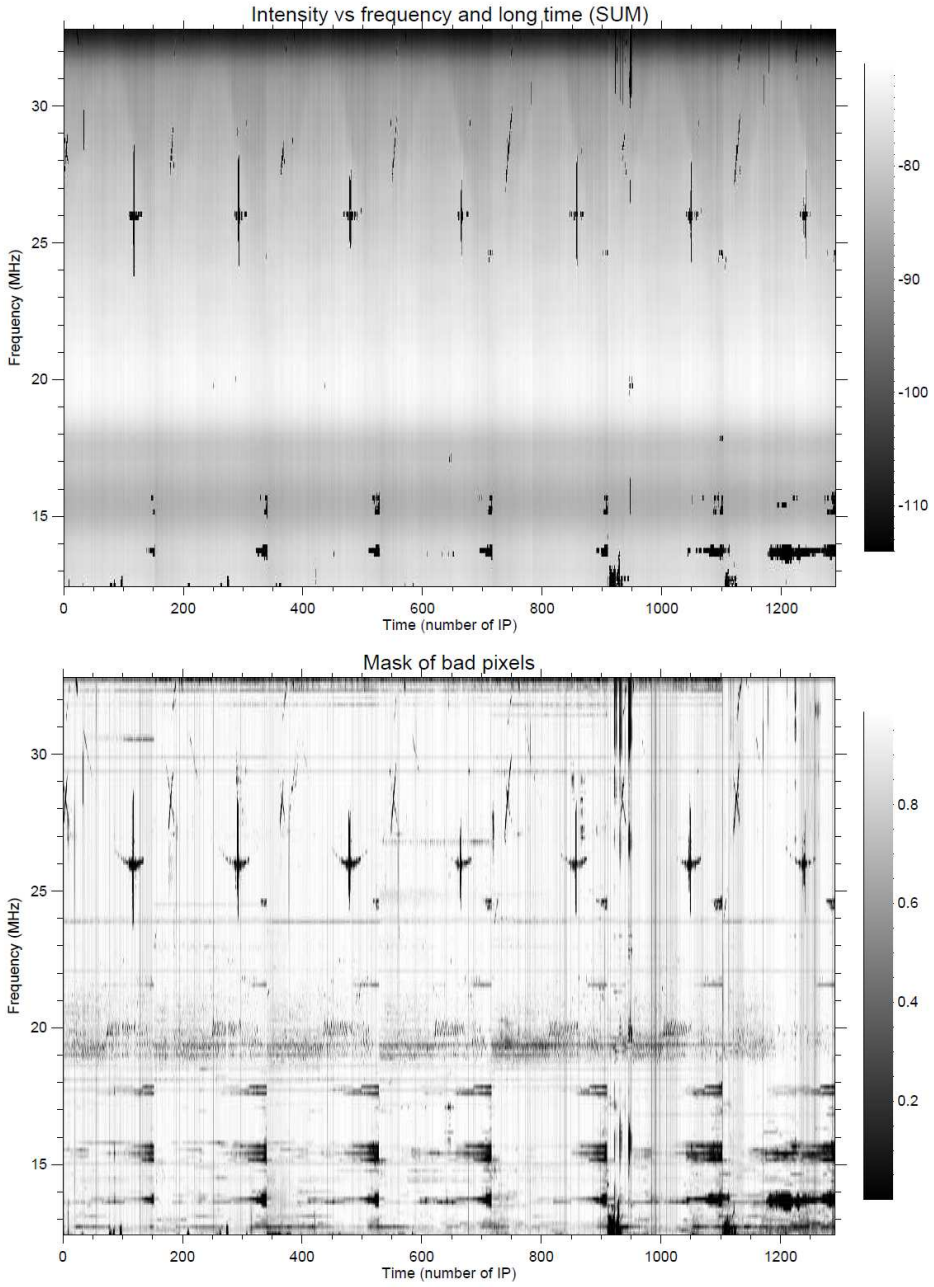

Figure 5.5: Data visualization - data array averaged over fast time. Averaged intensity and mask of bad pixels are represented as a function of slow time (IPI number, abscissa) and frequency (ordinate), i.e. all observation session (7 nights) is shown with a compressed time scale.

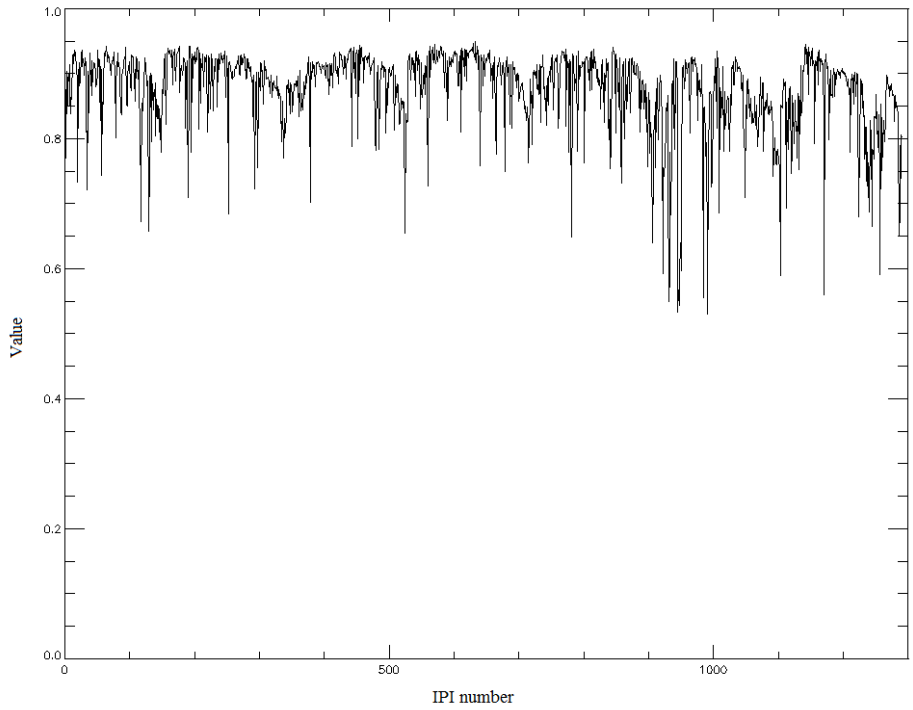

Figure 5.6: Averaged bad pixel mask - illustrates the number of removed data pixels in each 2-minute interval versus the index of such interval (i.e. versus slow time).

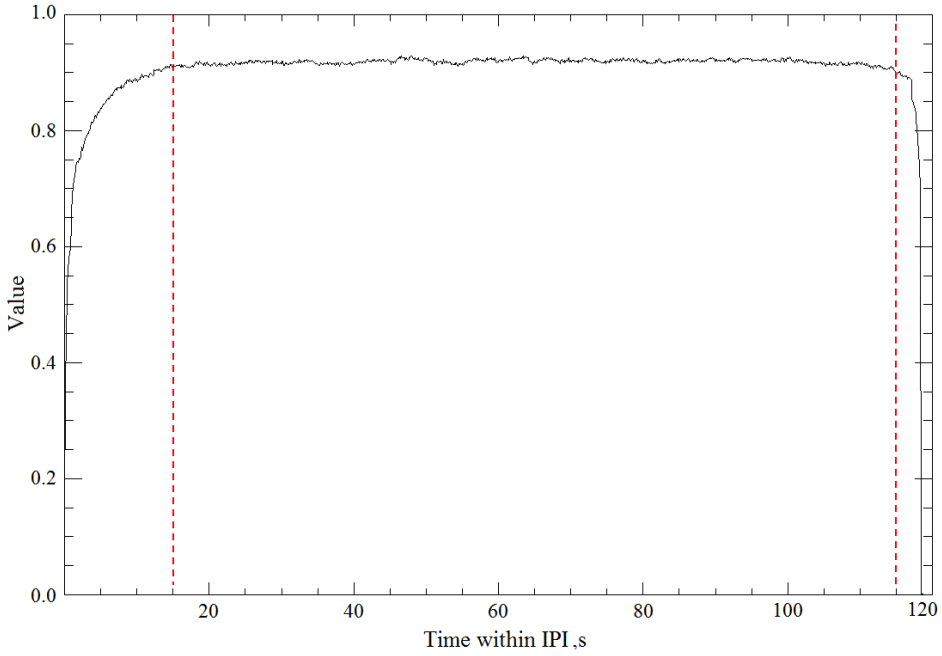

Figure 5.7: Averaged bad pixel mask - illustrates the average number of pixels removed at different parts of the average 2-minute interval (i.e. versus fast time).

spectra, the one that represents the Galactic background is D, where there is in principle no exoplanet signal. Therefore we attempted to calibrate each recorded spectrum either by its own average spectrum or by the average spectrum, computed from Difference ($\langle D \rangle$), and we compared the two ways of flattening. The *Off* beam can also be used as a reference for calibration if balanced with the *On* beam, as it is directed to an empty path of the sky. Each average spectrum is computed taking into account the percentage of bad pixels contained in the reduced bad pixel mask.

We derived the average spectra for data calibration with 4 different time windows:

- 2 minutes (1 IPI)
- 30 minutes (that corresponds to a sliding window centered on current IPI with 15 IPI width)
- 6 hours (whole night of observation)
- average of all IPI recorded at the same local time each night of observation

Alternately, a preliminary flattening can be performed using the average spectrum of all the data (all 7 observation nights). It is rough, because the variations from night to night are quite strong. We used it only for preliminary flattening, which is then followed, for example, by high-pass filtering or other stages of flattening.

We calibrated data of *On* and *Off* beams (*A* and *B* receivers) independently, but in the future, after achieving a better balance (in the hardware) between the beams, we will also be able to calibrate the *On* beam (presumable containing the signal) directly by the *Off* beam (presumably containing only Galactic background).

5.3 Representative observable quantities

After each selection and calibration method, we compute several observable quantities Q_i, examine their evolution with time and with the orbital period of Corot-7b, and compare it for *On* and *Off* beams. Below is the list of observables we defined for this search (following the method of [Zarka 1997]):

- Q_1: total power of each IPI, integrated over all frequencies (12 – 32 MHz)
- Q_2: total power of each IPI, where the integrated time series that results from integration over all frequencies is weighted by a Haar-like function (square window)
- Q_3: same as Q_2 but with weighting by a $sin(x)/x$ function

As the target (Corot-7b) traverses the pencil beam from East to West, due to Earth rotation, during an IPI, the weightings of Q_2 and Q_3 are expected to enhance the signature of the presence of a continuous signal. These first 3 observables (Q_1-Q_3) can be computed for different selections and flattening methods (as described above). The next observables, Q_4 to Q_8, are computed from the high-pass filtered integrated time series obtained from the data of each IPI after frequency integration. Each time series is then normalized by its standard deviation, in order to unify the thresholds applied to the data. High-pass filtering is done via subtracting the low-frequency component (long-term variations) obtained from smoothed data by a sliding window over 2 seconds or 10 seconds.

- Q_4: is simply the normalized time series described above
- Q_5: number of peaks per IPI $>$ threshold τ, compared to number of peaks $< -\tau$
- Q_6: sum of power of peaks per IPI $>$ threshold τ, compared to sum of |power| of peaks $< -\tau$
- Q_7: number of peaks per IPI above a threshold τ and exceeding the corresponding *Off* values by a factor ≥ 2
- Q_8: sum of power of peaks per IPI above a threshold τ and exceeding the corresponding *Off* values by a factor ≥ 2

From these observables, we derive the following diagnostic plots:

- time variation of the observable Q_i during the observations

- smoothed (boxcar-filtered) time variation of Q_i with 3-second sliding window
- variation of Q_i versus orbital phase of the exoplanet
- smoothed (boxcar-filtered) variation of Q_i versus orbital phase with short (6 seconds) and long (12 seconds) sliding windows

The orbital phase of the target source is known, from the time of first transit and the orbital period of the exoplanet[2]. The above plots are superimposed for the *On* and *Off* beam (or for the target and calibrator signal, see below) in order to compare their variations.

With this general method we processed two data sets recorded for the Corot-7b exoplanet in November 2009 and November 2011. In 2009 the source was observed 7 nights, 6 hours each, and in 2011 - 13 nights, 6 hours each. The data set of 2011 is more noisy (contains more broadband RFI, see Fig. 5.8). In both data sets the signal of the *On* beam (receiver A) is more variable than the signal of the *Off* beam (receiver B). Both processed data sets have been recorded in "Spectrum" (Sum/Difference) mode (see section 2.1.3 of Chapter 2 for explanations of data recording regimes). Additionally, the data of 2011 have been recorded in "Correlation" mode in parallel to "Spectrum" mode. This data can allow us to achieve better RFI mitigation, using the phase information, and to confirm the shape of the observed variations (physically different receiver, but the same telescope beam). In this chapter I will focus on the data set of 2009, which is less noisy and has been processed once before present work, so that it is possible to compare our results to earlier ones.

For post-processing of the above data set, we used the entire recorded frequency band ($\sim 12 - 32$ MHz) as a first frequency selection, in order to reduce the total number of diagnostic plots. However we examined the influence of the other two selections - in "fast" time (the edges of 2-minute intervals are removed) and in "slow" time (the whole 2-minute intervals are removed if they contain much interference). Generally, the selection in "slow" time (removal of polluted 2-minute intervals) does not influence strongly the resulting curves, whereas the removal of IPI edges surprisingly does, especially for data of 2011. This indicates either the presence of instrumental effects inherent to UTR-2 or that the removal of IPI edges excluded the contribution of a spurious point source that is present at the edge of the Corot-7b field (Fig. 5.1).

The various flattening (sky calibration) methods used give different results, with the least noisy result obtained for calibration by the average spectrum of each 2-minute interval itself. Calibration by the average spectrum of the whole observation session (e.g. 7 nights) or of 1 whole night (6 hours) or even surrounding 30 minutes introduces large variations, because the background intensity varies strongly from night to night and even from one 2-minute interval to another. Calibration with an average spectrum computed from the 2-minute intervals with the same local time

[2] exoplanets.eu/catalog

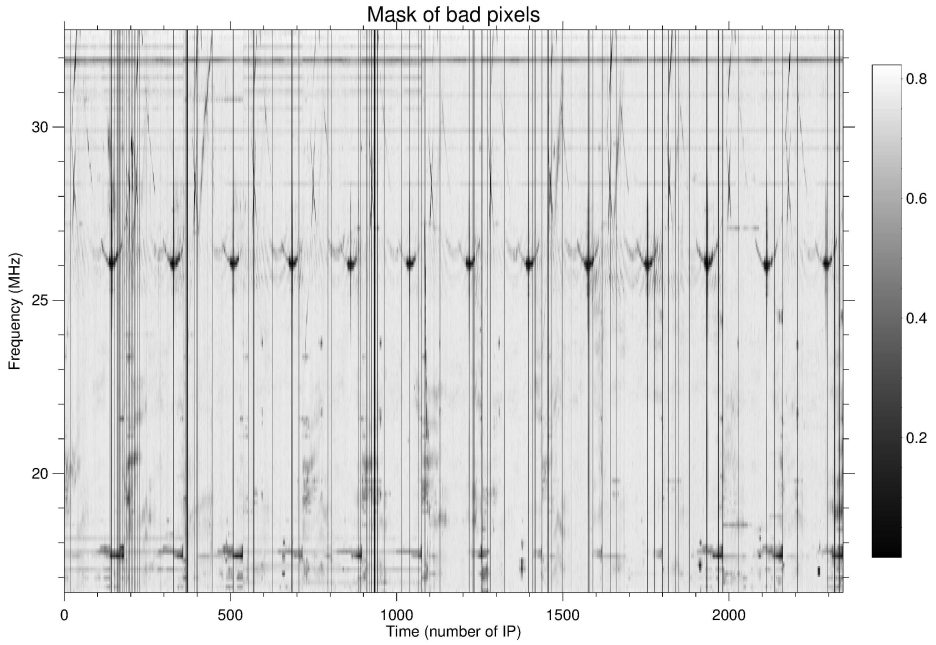

Figure 5.8: Bad pixel mask (Corot-7b, 2011) as a function of slow time (IPI number, abscissa) and frequency (ordinate): the all observation session (13 nights) is shown with a compressed time scale.

each night is noisy, because of the small amount of spectra averaged (7 or 13) and the difference of background values between them.

The data recordings used have different functions in our analysis. Sum data (S_A) (Fig. 2.10) from the *On* beam (receiver A) contains the source (Fig. 2.11) but also contains the large crosswise part of the sky that corresponds to the directional patterns of N-S and E-W antennae, that may contain (residual) RFI and other sources. The Difference (D_A) is all the crosswise pattern except the central part, which is common for N-S and E-W antennae. D_A does not contain the source, only the Galactic background and possibly other sources that are present in S_A, too. Therefore it can be reasonably used for sky calibration. When D_A is subtracted from S_A, we get the Pencil beam P_A (equation 2.4) that contains only the central part of the crosswise pattern that is common for both antennae. It contains less RFI and other sources, and in principle should contain only the useful signal and Galactic background. S_A and D_A channels should be perfectly balanced by UTR-2 electronics, giving a zero difference unless there is a point source in the center. In practice, it is not the case, because the two receiver channels (containing S_A and D_A) are amplified separately by two amplifiers of the same construction but physically different. So the Pencil beam P_A can be useful only under condition of accurate calibration of the S_A and D_A. This is what we try to do by computing a corrected pencil beam P'_A.

The *Off* beam (receiver B) is intended to be used as a reference beam or as a calibrator. The Sum and Difference (S_B and D_B) data acquisitions are useless for calibration/reference purposes, because their wide crosswise antenna patterns include the source (fig.). We consider that only the pencil beams P_B and P'_B from the *Off* beam are useful to be compared with simultaneous data recordings that contain the source.

Data calibration showed more clear results when performed with the $\langle D \rangle$ average spectrum (not containing the source). In this case computing observables for P gives the same result (with offset=1) as for S, because $\frac{P}{D} = \frac{S-D}{D} = \frac{S}{D} - 1$

Taking into account all the selections and flattening methods, we obtain 640 plots per observable Q_1-Q_5, 320 plots for Q_6, 600 plots for Q_7 and Q_8, and finally 800 plots for Q_9-Q_{10}. All these plots were then inspected visually for time variations or meaningful orbital signatures. The ways to automatize the inspection of the plots are still to be devised.

Observables Q_1-Q_3 (as mentioned above) are total intensities of each 2-minute interval, with different weighting (in time direction) within the 2-minute interval. The most interesting plots are the variation, obtained in the P_A, when calibrated by $\langle D \rangle$ versus time and folded versus orbital phase of Corot-7b (Fig. 5.9).

The shape of the *On* curve is similar to what was obtained in the previous processing of this data, before the present work (Fig. 1.8). The folded curve for *Off* beam (receiver B) is more flat, but still has one 2-fold lesser peak. The offset present between curves for A and B receivers is of instrumental origin, and disappears for P', because the physical difference between the two channels has been taken into account. Variation in the *On* beam is enhanced (and slightly deformed), still with

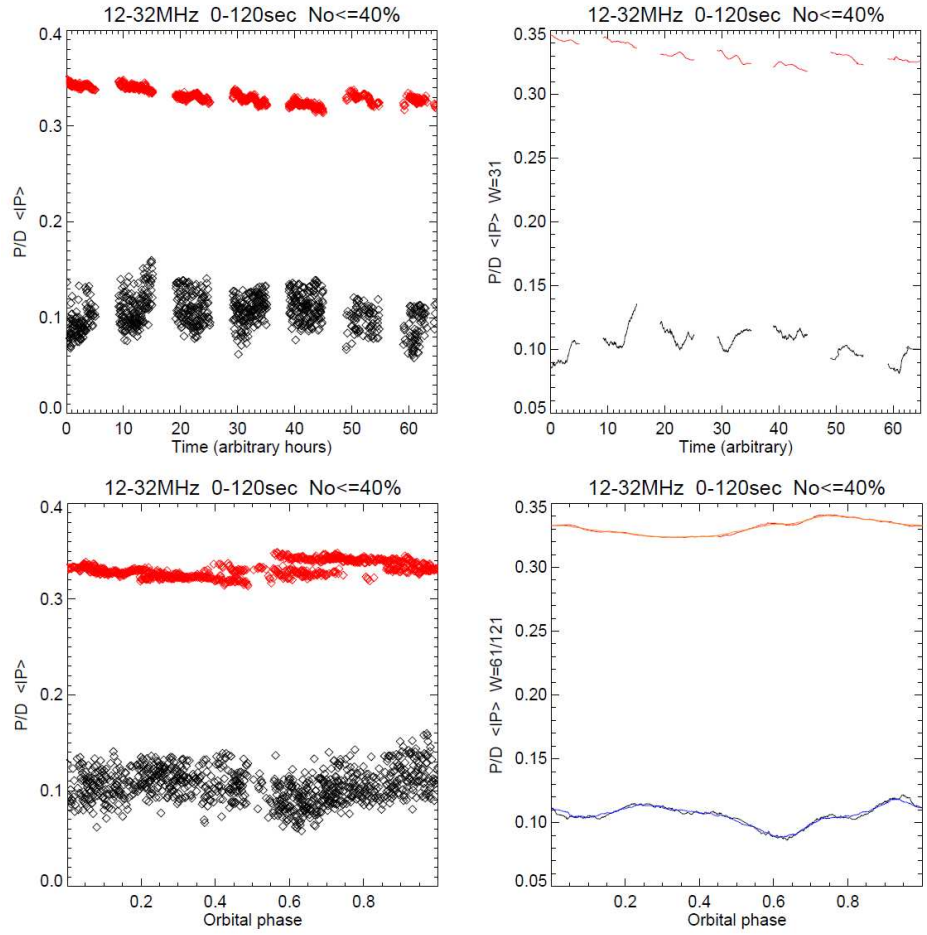

Figure 5.9: Total intensity of 2-minute intervals (Q_1) of *On* pencil beam P_A (black and blue) and *Off* pencil beam P_B (red and orange), represented versus observation time (upper panels, without and with smoothing) and versus orbital period of Corot-7b (lower panels, without and with smoothing). The offset between *On* and *Off* curves is not understood but is necessarily of instrumental origin.

two maxima per orbital period, whereas variation in the *Off* beam becomes more notable and almost comparable with that in *On* beam (Fig. 5.10).

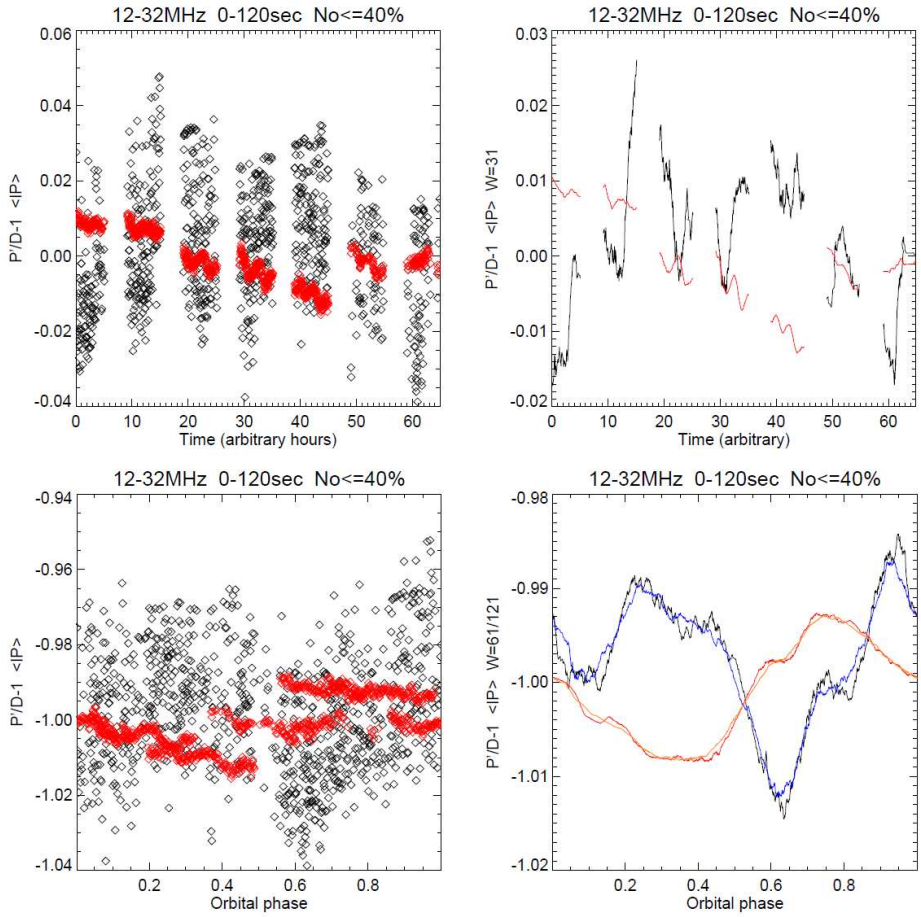

Figure 5.10: Total intensity of 2-minute intervals (Q_1) of corrected *On* pencil beam P'_A (black and blue) and corrected *Off* pencil beam P'_B (red and orange), represented versus observation time (upper panels, without and with smoothing) and versus orbital period of Corot-7b (lower panels, without and with smoothing).

However, when one examines the plots versus observation time, the behaviour of *On* and *Off* data of P' beam is very different. The *Off* curve is composed of quasi-flat curves per night that have different averages. Therefore the resulting modulation in *Off* is more due to variations from night to night than the variation of the signal within one night. Meanwhile in receiver A, a homogeneous scattering of intensities is present every night, drawing the resulting curve. This can be either due to the presence of variable signal in *On* beam or due to instrumental effect, inherent with amplifiers or receivers of UTR-2. If the receivers A and B behave differently, then no conclusion can be drawn. Therefore a future observation should switch the *On* and *Off* receivers and electronic channels. If after such a switching

the variation in *On* beam is still more variable than in *Off*, this would strongly support the existence of a real signal.

The shape of the curve in the *On* beam does not change significantly for P', compared to P. Neither it does for a different calibration approach (flattening by the average spectrum over each night). Generally, this first analysis suggests that for the observable Q_1, the signal in the *On* beam (A) is always more variable than that in the *Off* beam (B). It is also the case for the data of 2011. However, we will not conclude about the presence of the signal until the suggested test, switching receivers A and B, is performed.

If a real continuous signal is present in the observable Q_1 (which is simply the total intensity of each 2-minute dynamic spectrum), then the next two observables Q_2 and Q_3 should highlight that signal, as it increases while drifting across the UTR-2 pencil beam, reaches maximum in the center of the beam, and then decreases symmetrically. Q_2 (which is equivalent to central half of an IPI minus the two edge quarters) highlights the 1-minute central part of each 2-minute IPI with respect to the two edge 30-second quarters. This should also diminish the impact of the point-source located at the edge of the beam (Fig. 5.1). Q_3 reproduces the shape of UTR-2 beam, and gives maximum weight to the central point of the 2-minute interval, decreasing symmetrically on both sides as $\frac{sin(x)}{x}$. These two observables show approximately the same result as Q_1, but with the *On* variations more amplified than the *Off* ones, which is a good sign. The diagnostic plots for Q_3 (P') are shown in Fig. 5.11

However, the exoplanet's emission (if any) may also consist of relatively short broadband bursts. At full time-frequency resolution, these bursts are below the noise background and will show up only after frequency integration. They should be discriminated from residual broadband RFI, being present in the *On* beam in S_A, P_A and P'_A data recordings, and absent in P_B and P'_B of the *Off* beam as well as from the D_A recordings of the *On* beam. Thus we compared systematically data recordings that should contain the signal from the target with the ones that should not contain it. To visualize these comparisons, we made scatter plots of *On* beam values integrated over frequency versus *Off* beam values corresponding to them. Each point is a normalized intensity (in units of standard deviations) from a time series integrated over frequency for target (abscissae) and reference (ordinates) signals. In this plot, an excess of signal peaks in the target data will be visible on the right edge of the cloud of points. Examples of resulting scatter plots are shown in Fig. 5.12.

In our data, we have noticed a weak excess of high values in the *On* beam, compared to *Off* beam, for certain nights. With different pairs of signals to compare, we obtain different shapes of the cloud of points in the scatter plot.

Comparing S_A to D_A (Fig. 5.12, left panel) one can notice a diagonal feature that indicates correlation between S_A and D_A. It is expected because of the large part of beam that S_A and D_A have in common. The points can reach high values (up to 20-30 σ), but σ is in this case is much smaller than for raw data, due to spectral integration over 12-32 MHz (200 frequency channels). A few values that

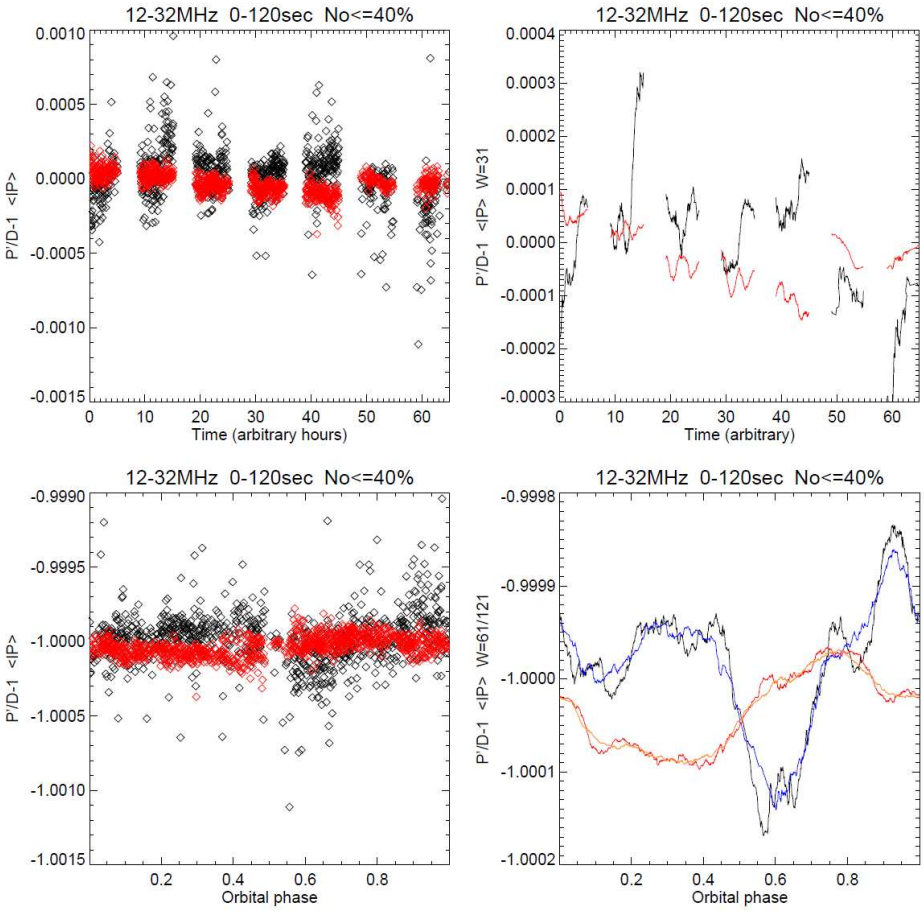

Figure 5.11: Total intensity of 2-minute intervals, weighted by $sin(x)/x$ function (Q_3) of corrected *On* pencil beam P'_A (black and blue) and corrected *Off* pencil beam P'_B (red and orange), represented versus observation time (upper panels, without and with smoothing) and versus orbital period of Corot-7b (lower panels, without and with smoothing).

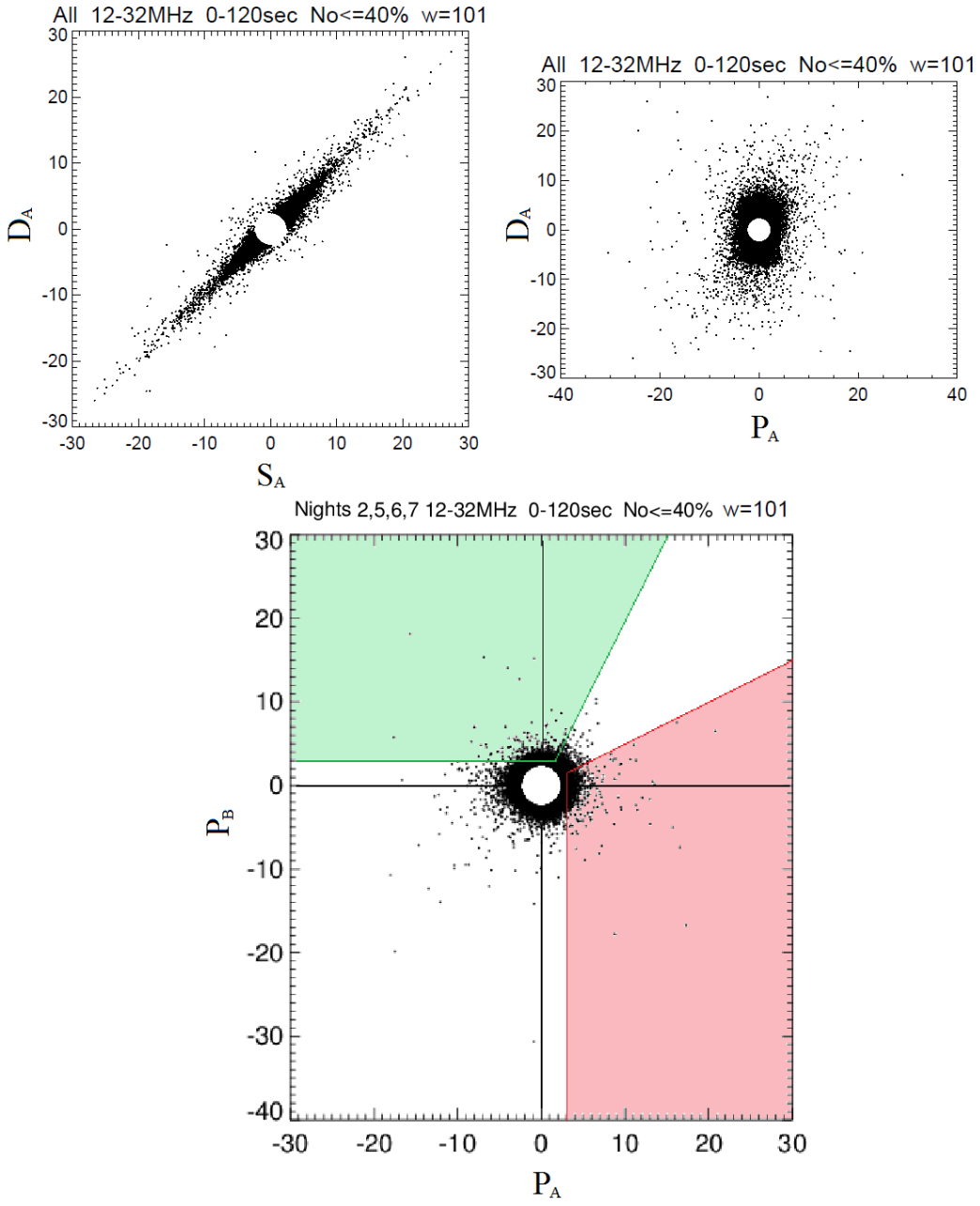

Figure 5.12: Upper left panel: scatter plot (Q_4) of *On* Sum beam S_A versus *On* Difference beam D_A. Upper right panel: scatter plot of *On* Pencil beam P_A versus *On* Difference beam D_A. Lower panel: scatter plot of *On* Pencil beam P_A versus *Off* Pencil beam P_B.

have a clear excess in S_A originate from *night*7 (15 Nov 2009). Various selections do not change this result.

Comparison of P_A and D_A (Fig. 5.12, middle panel) is not conclusive, because the cloud of points is much more elongated in the direction of D_A due to a larger number of residual RFI in the D_A data, captured by a large crosswise beam.

Comparison of P_A and P_B is more representative as the cloud of points is symmetrical and generally does not exceed 10 σ. A slight excess in P_A is observed for *nights* 2, 5, 6 and 7. The cumulated scatter plot of P_A versus P_B for these nights is shown in Fig. 5.12, right panel. The area highlighted with red indicates the values of P_A that exceed 3σ threshold (σ being a standard deviation of the integrated high-pass filtered time-series) and are at least 2 times the corresponding values of P_B. The green area is the equivalent for P_A and P_B exchanged.

Comparison of the corrected pencil beams (P'_A and P'_B) gives consistent results with P_A and P_B.

As the excess of points in the red area is small, we attempted to examine it statistically in order to draw quantitative conclusions. This is the aim of observables Q_5-Q_8.

A set of thresholds for observables Q_5-Q_8 was chosen as $N = 2.5, ..., 5$ with a step 0.5, based on the described scatter plots.

Observables Q_5 and Q_6 are checks of the asymmetry in the signal distributions. They compare number (Q_5) and power (Q_6) of peaks that are above certain threshold τ and below $-\tau$. The evidence of the presence of bursts could be the excess of positive peaks over negative ones. For any τ there seems to be more positive peaks in the *On* beam than in the *Off* beam. But these peaks are present both in S and in D, and reduce considerably in P, which points to residual RFI. The signal distribution becomes symmetrical for the corrected pencil beam (P'). In Fig. 5.13, the number of positive peaks becomes equal to the number of negative ones, and the ratio of positive peaks over negative is flat versus the orbital period. In the *Off* beam the ratio of positive peaks over negative ones is closer to 1 for any recording (S, D, P, P').

A similar behaviour is observed in Q_7 and Q_8 which compare the different pairs of signals, one that may contain a signal and the other not. Q_7 is the number of *On* peaks that are above the threshold τ and are at least twice as intense as the corresponding *Off* values. When comparing the pair of data acquisitions S_A and D_A, the majority of the points are at 0, which means that in each 2-minute interval the values are correlated, and there are no values in S_A that are twice as large as the corresponding values in D_A and vice versa. Remarkably, there are more bursts in S_A detected on nights 2 and 7, which agrees with the scatter plots (Q_4). Night 7 though contains the most RFI of all the 2009 observation session. The pair P_A and D_A is decorrelated, and there are many more peaks in D_A, that also agrees with the scatter plots. A comparison of two pencil beams (P_A and P_B) as well as two corrected pencil beams (P'_A and P'_B) shows almost the identical numbers of peaks in *On* and *Off* beams (Fig. 5.14) with slight excess in the *On*. The observable Q_8 is the sum of power of the peaks mentioned in Q_7. It behaves exactly the same way as

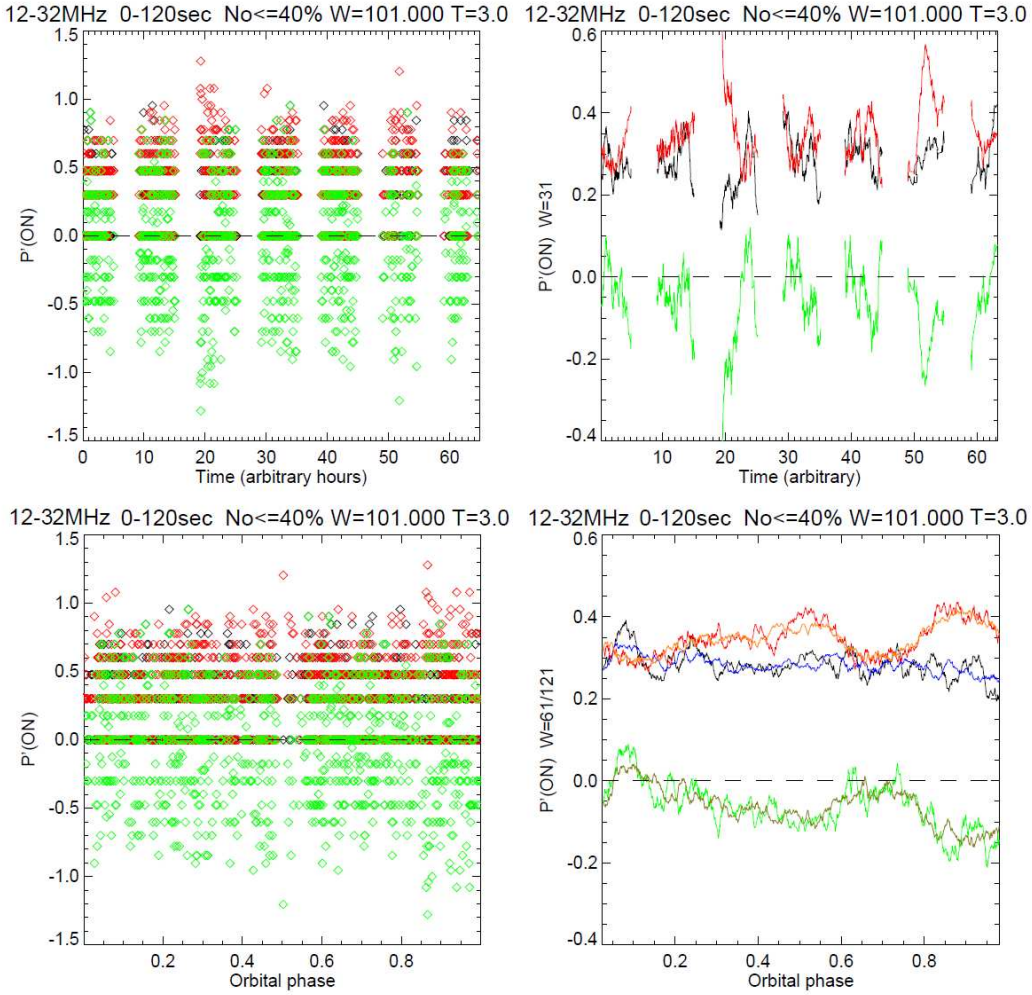

Figure 5.13: Search for distribution asymmetry (Q_5). Logarithm of number of peaks in corrected *On* Pencil beam P'_A that exceed 3σ threshold (black, blue) is compared to the number of negative peaks below -3σ (red, orange) and to logarithm of the ratio between number of positive and negative peaks (green, olive). They are represented versus observation time (upper panels, without and with smoothing) and versus orbital period of Corot-7b (lower panels, without and with smoothing).

Q_7, and can complement Q_7 for a quantitative description of the excess of power in the data recordings that contains the target, compared to those that do not contain it.

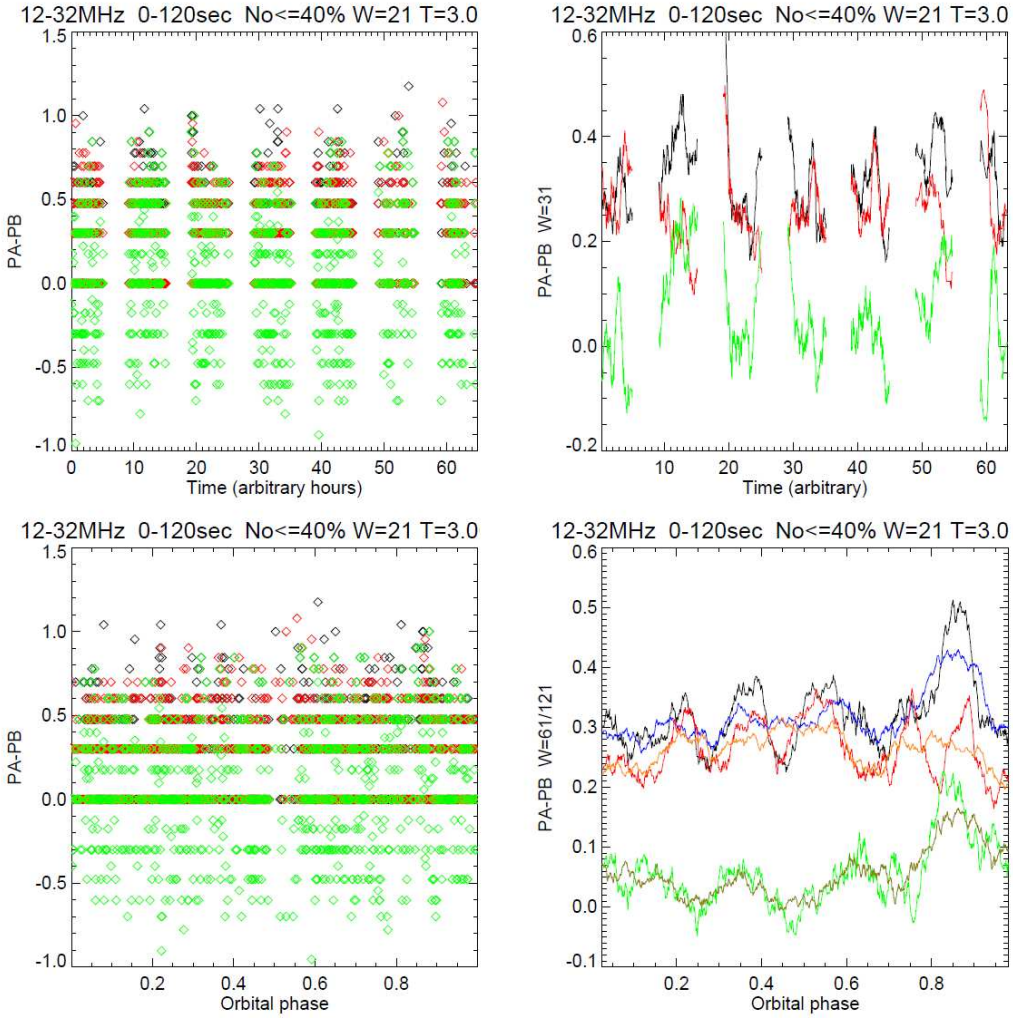

Figure 5.14: Search for broadband bursts (Q_7). Logarithm of number of peaks in *On* Pencil beam P_A that exceed 3σ threshold and are at least twice as intense as corresponding values of *Off* Pencil beam P_B (black, blue), compared to the same for P_A and P_B exchanged (red, orange) and the ratio of former to latter (green, olive). They are represented versus observation time (upper panels, without and with smoothing) and versus orbital period of Corot-7b (lower panels, without and with smoothing).

In summary, although we have obtained hints of confirmation of earlier results on Corot-7b, we think that more work is needed before reaching a definitive conclusion. The 2011 data are very noisy, therefore comparison with the 2009 data requires a

deeper RFI mitigation at pre-processing stage, that will be performed in the near future.

Nevertheless the toolkit, procedures and observables that we have developed behave as expected and this will allow us to apply them easily to further studies. Of particular interest in the complete reprocessing of the 30 Terabytes of observations that have been recorded since 2007 on other exoplanet targets.

Chapter 6

Conclusions and Prospects

Contents

6.1 Pulsars and transients

For the first time in the decameter range we have conducted a pulsar and transient survey of the entire northern sky. An unexpectedly large number of transient candidates (∼450) have been detected in the first 20% of processed survey data. All these transient candidates show a time-frequency dependence complying with dispersion in the interstellar medium ($\sim 1/f^2$). These candidates have a distribution versus the Galactic latitude (b) similar to the one we would expect from real cosmic sources (e.g. neutron stars), with maximum at $b = 0^o$. Their distribution in DM has a similar shape as the distribution of RRATs or pulsars.

Remarkably, LOFAR detected very few transients to date. One reason could be the intrinsic rarity of transients at higher frequencies, and the high sensitivity (large effective area) of UTR-2 at low frequencies. In any case, a thorough study of detected signals is needed, as some of them might as well be RFI (as e.g. perytons [Petroff 2015]) or a new type of radio sources.

The present survey has shown that UTR-2 is very well adapted for detecting transient signals with timescales $\ll$ 2 minutes as well as for or observations in transit mode. UTR-2 has also shown the ability to detect the majority of nearby pulsars. At the preparatory stage of the survey, a census of nearby slow pulsars was made, which resulted in the detection of the decameter emission of 40 known pulsars (see the first paper in Appendix A). Intrinsic broadening of average pulsar profiles has been found in this study, probably linked to the broadening of radio emission beam at lower frequencies, giving motivation to discover pulsars that cannot in principle be observed at higher frequencies. The scattering time was found lower than expected from Kolmogorov's law in this study, which has positive implications for future very-low-frequency observations from the far side of the Moon.

The present pulsar and transient survey is sensitive to low-DM pulses, in contrast with high-frequency surveys [Kondratiev 2009]. This was confirmed by the detection of the low-DM pulsar J0243+6257. Dispersion measure of this pulsar has been refined in the present survey (3.83 instead of 4 pc.cm^{-3} in [Hessels 2008]). Determination of DM is very accurate in the decameter range, and generally low-DM sources are not taken for RFI during data processing. The present survey has thus an ability to uncover the locations of the nearest and therefore most interesting misoriented pulsars, radio loud magnetars, RRATs, XDINSs and other transient sources. They could be subsequently explored in other frequency ranges such as X-rays and gamma rays, enabling evolutionary links between different kinds of neutron stars and constraining the neutron star birthrates. Our Solar System is situated in a "Local Bubble" that has probably been formed by supernova explosions. Nevertheless we don't observe many products of these explosions. Maybe our survey will help to correct this situation. Also it may help in understanding why a large number of neutron stars emit erratically, as this behaviour becomes more emphasized at low frequencies [Ulyanov 2006].

Re-detection of $>$ 20 known pulsars via their individual pulses demonstrates the relatively high survey sensitivity. Survey sensitivity (at 1σ level) was $\sim$16.5 mJy for repetitive pulses, and $\sim$560 mJy for isolated pulses. It was determined on the basis of a calculation in [Zakharenko 2013], taking into account that in the present survey (i) the sources are observed with 5 beams of N-S antenna of UTR-2, which contains 70% of the effective area of the telescope, and (ii) integration time is shorter than in [Zakharenko 2013] (40-60 minutes).

Absence of discovery of new pulsars in the processed fraction of the survey data can mean either that all nearby pulsars producing strong pulses in the processed sky region have already been discovered, or that pulsar radiation becomes very sporadic at low frequencies. Weak nearby pulsars have a chance to be detected in a subsequent search for periodicities (with FFT).

6.2 Exoplanets

The present work focused mainly on the methodology of exoplanet search, and development of automated tools for it, that were then tested on a target of particular interest. Having re-processed the data set of Corot-7b (observations of November 2009), using the developed tools, we have no proof of absence of emission, but neither do we have an unambiguous confirmation of the detection of this exoplanet.

Detection of exoplanets in radio requires thorough understanding of telescope operation as well as control of every data processing step. Nothing should introduce trends or spurious variations. Both telescope beams (*On* and *Off*, with all signal propagation paths through the telescope, all amplifiers and receivers) should be perfectly balanced or otherwise calibrated or accounted for at the post-processing stage. Accurate calibration of the UTR-2 is being made by [Ulyanov 2015] and will soon be available online as a reference table at the Institute of Radio astronomy

website[1]. After this step, it should be easier to conclude about detection or non detection of Corot-7b. In the meantime, I proposed to (and will) analyze existing Corot-7b observations from 2011 in correlation mode, and re-observe it with A and B (*On* and *Off*) receivers switched.

If emission is absent, it can be explained by one of the following reasons: (i) the radio emission, produced in the Corot-7 system is too weak to be detected at the distance of the Earth; (ii) the radio emission is sporadic, and it is 'off' for a significant fraction of the time; (iii) magnetic field of Corot-7b or of its host star is too weak to have the CMI mechanism operating at frequencies above 12 MHz; (iv) a relatively narrow radio emission cone of the cyclotron maser operating in the magnetosphere of Corot-7b is not beamed towards the Earth.

Apart from elimination of possible instrumental and processing effects, a careful selection of targets is needed for a successful detection. New observational data bring new discoveries that are possibly good candidates for radio searches. Currently the exoplanet catalog[2] contains 1958 targets, and this number will increase further with ongoing space missions and large surveys.

The existing theoretical background allows to predict at least an order of magnitude of the radio flux and upper frequency limit for known exoplanets ([Lazio 2004], [Grießmeier 2007], [Grießmeier 2011]). Corot-7b is a super-Earth, and it is not a high-rank candidate in the predictions. Nonetheless it is located very close to its host star, and has a short orbital period of about 20 h. All orbital phases can be easily covered in a few nights of observations. For more promising candidates longer observations may be required. To have a statistically significant variation of the radio emission power with planet's orbital period, coverage of at least a few full orbits is needed. Among the promising targets are hot Jupiters (e.g. τ Bootes), planets around strongly magnetized stars (e.g. HD 189733), planets with high-eccentricity orbits (e.g. HD 80606) and planets with known or suspected star-planet interaction (e.g. HD 179949).

6.3 Data processing

I developed two data processing pipelines: for the pulsar and transients survey and for exoplanet search. The pipelines are flexible and tunable, and can easily be adjusted to observational data of other astrophysical objects or beamformed data of other telescopes. Both pipelines have a significant overlapping part - RFI mitigation.

The RFI mitigation quality of the pulsar/transient survey improved ~ 1.7 times the final sensitivity, as compared to the previous version - used in [Zakharenko 2013]. Nevertheless, periodicity search of weak pulsars in the survey data has shown that RFI mitigation routine is tuned not severely enough, mainly because it was not supposed to remove the possible strong dispersed bursts. After the present RFI mitigation, the residuals on the edges of strong RFI are left in the dynamic spectra.

[1] http://rian.kharkov.ua/decameter/calibration-UTR-2
[2] http://exoplanet.eu/catalog/

They distort the Fourier image of the data and should be removed by means of bad pixel mask expansion or by introducing more severe thresholds. In order to avoid data re-processing, the online RFI mitigation should be done - in the future - with several set-ups in parallel. The more deeply cleaned data will be sent to the periodicity search program, whereas shallow cleaned data will be examined for dispersed pulses.

It appears that many false-positive candidates arise from the relatively narrow band (a few MHz) RFI with linear frequency modulation ('chirp'). In a narrow frequency band this modulation can resemble the quadratic dispersion law. Therefore automated distinction between linear (RFI) and quadratic (dispersed pulses) time-frequency sweeps should be implemented as part of the post-processing. If after the linear frequency sweep compensation the SNR is higher than after dispersion compensation ($\sim 1/f^2$) then the candidate is most likely an RFI.

The last level of candidate selection, similarly to the majority of pulsar surveys, should be done visually. A tool for interactive manual inspection of transient candidates is being created. Candidate's compliance with dispersion law and presence of the signal in several subbands of the main frequency range should be checked. By fine adjustment of smoothing parameters and contrast, the apparent SNR of the signal can be substantially increased.

Search for periodicities in the data should be flexible, with interactive selection of time window and filtering parameters. The known sources of periodic interference should be removed from the search. For this purpose, an RFI database in the (t,f) plane will be created for UTR-2. This will also greatly facilitate the RFI mitigation stage.

For more reliable statistics, we should obtain several snapshots of the sky. The correspondingly large volumes of data could be processed off-line in a short time by the volunteers computing platform. The example of Einstein@home pipeline used for PALFA pulsar survey shows how efficient this way of processing may be.

For the exoplanet data, RFI mitigation is implemented using a figure of merit (see section 3.3.2.3) that increases when a larger part of the data is found to be polluted by RFI. The thresholds applied for RFI elimination can be automatically selected, depending on data time resolution (section 3.3.2.4). For a more thorough RFI mitigation, the use of the phase of antennae cross-correlation might be helpful. It is constant for the signals coming from the common part of antennae ("pencil beam") and rapidly variable with the frequency for the signals from other directions. Generally, the data should be processed with more severe RFI mitigation, in order to remove residual weak RFI. It will be done at the subsequent runs of the pipeline on the data.

The post-processing of exoplanet data seems to account for instrumental effects of UTR-2, such as the offset between *On* and *Off* beams or receivers, and gain variations at the edges of interpointing intervals. The numerous diagnostic plots produced at the post-processing stage, should be further quantified automatically through the definition of higher level observables, in order to avoid tedious visual inspection.

6.4 Observational prospects

Once the present pulsar and transient survey is finished, its obvious continuation will be the on-line transient monitoring program that will use the developed tools for transient detection. There are two major difficulties for this program: data storage and computation power (especially for on-line dedispersion). Ideally, scanning should be done in a wide field of view, processing data on-line, and giving the coordinates, time of occurrence, DM and SNR of the detected transients as an output (possibly as a trigger to other radio telescopes). For this purpose, the raw data should be analyzed on-the-fly, to check for pulses that match any of trial DMs. The data pre-processing in this case should be much faster than the one we applied here to the survey. This speed, without compromising with the quality of the pre-processing, can only be provided by the use of parallel computing on GPUs.

For scanning a wide field of view with simultaneous identification of sources' coordinates with sufficient precision, the principle similar to the UTR-2 heliograph can be used. The heliograph [Stanislavsky 2011] forms a matrix of 5×8 spatially separated beams each $\sim 0.4^o$ size. Another system of 5 beams, described in the Chapter 2, already exists at UTR-2. Minor modification of this beamforming system will allow to obtain wide-field multibeam observations.

The low-frequency radio telescopes that are currently being built (GURT and NenuFAR) can perform joint observations with the UTR-2 in order to better select and identify transient candidates. GURT, being located at the same site as UTR-2, is free from its instrumental effects and can always see the same part of the sky as UTR-2, whereas NenuFAR, located $\sim$ 3000 km away has different ionosphere conditions and a different RFI environment, therefore the coinciding events would likely be of cosmic origin.

GURT has already shown great performance for pulsar detection. With a single section in 2 hours of recording, 5 strong pulsars have been detected. RFI mitigation used was the same as described in Section 3.2. With minor modifications, it will be implemented as a default RFI mitigation pipeline for the majority of GURT observations. When this new telescope has reached its full size it will become an excellent pulsar science tool, capable of studying millisecond pulsars, higher DM pulsars and pulsars with weaker flux density, which are currently unreachable with the UTR-2.

The most reliable detection of exoplanetary radio emission, free of dynamic confusion effect, would be a simultaneous detection with 2+ instruments. UTR-2 is already involved into joint observations with LOFAR on exoplanet detection programs. About two dozen targets have been observed with LOFAR in imaging mode, and 55 Cnc was observed in beam form mode during 32 hours [Zarka 2015] simultaneously with UTR-2. The data is being analyzed, all tools developed in this study are transposed and used for analyzing LOFAR beamformed data.

UTR-2 alone although has a high sensitivity, but measures only one (EW) polarization. This will complicate the discrimination between the stellar and planetary emission if detection occurs. LOFAR has many advantages such as high sensitivity

and spatial resolution, full polarization, digital beamforming and imaging capabilities, but the essential drawback is the limited observational time available for exoplanet search. UTR-2 and LOFAR efforts will soon be complemented by NenuFAR and then by GURT.

GURT and NenuFAR will have a frequency range twice as broad as UTR-2 and ∼2 times more sensitivity than the LOFAR core at low frequency (used for beamformed observations), and they will measure full polarization. This significantly increases their sensitivity to broadband bursts from pulsars, transients and exoplanets. Digital phasing of both arrays will reduce frequency dependent losses in the cables and facilitate telescope calibration. New generation receivers will replace the functions of analogous equipment (such as Sum/Difference couplers) and eliminate their hindering instrumental effects.

Much wider opportunities will be available with SKA-1. SKA-1-Low will be sensitive enough and will operate at appropriate frequencies (down to 50 MHz) to detect even the radio emission of Jupiter-like planets at a distance of $\sim$ 10pc. Direct imaging with 11' spatial resolution will be a fast detection tool, followed by more detailed tied-array observations. Systematic surveys may become a discovery tool, bringing a lot of information about magnetic fields of exoplanets. Comparative magnetospheric physics will then provide statistically significant conclusions on strengths of planetary magnetospheres.

Although SKA is likely to revolutionize the search for exoplanets, there will still be room for UTR-2 and its successors GURT and NenuFAR. Many planets that are close to their stars are expected to show spin-orbit synchronization, hence their magnetic fields might be very low, yielding radio emissions only at the frequencies in the range of UTR-2 [Grießmeier 2007]. And while SKA will cover the southern hemisphere, UTR-2, GURT and NenuFAR will cover the northern hemisphere. Good prospects thus exist for the coming years.

Appendix A

Publications

Publications

Papers:

1. I.Vasylieva, V. Zakharenko, I. Kravtsov, P. Zarka. Decameter pulsar/transient survey of northern sky. Transient candidates and re-detections of known pulsars (in preparation).
2. A. A. Konovalenko, L.G. Sodin, V.V. Zakharenko, P. Zarka , O. M. Ulyanov, M.A. Sidorchuk, S.V. Stepkin, P.A. Tokarsky, V.N. Melnik, M.M. Kalinichenko, A.A. Stanislavsky, V. Koliadin, V. Shepelev, V.V. Dorovsky, A.A. Koval, I. Boobnov, S. Yerin, D.V. Mukha, I. Y. Vasylieva et al. The modern radio astronomy network in Ukraine: UTR-2, URAN and GURT // Experimental Astronomy, 2015 (Submitted)
3. I. Y. Vasylieva, V. V. Zakharenko, A. A. Konovalenko, P. Zarka, O. M. Ulyanov et al. Decameter pulsar/transient survey of northern sky. First results // Radio physics and Radio astronomy, 2014. Volume 19, Issue 3, p. 197-205
4. V.V. Zakharenko, I.Y. Vasylieva, A.A. Konovalenko, O.M. Ulyanov, P. Zarka et al. Detection of decameter wavelength pulse radio emission of 40 known pulsars // Monthly Notices of the Royal Astronomical Society, Volume 431, Issue 4, p.3624-3641 (doi:10.1093/mnras/stt470).
5. V.N. Tkachov, V.V. Zakharenko, I.Y. Vasylieva, Y.A. Tsarin, E.Y. Bannikova et al. Utilization of grid technologies in solving the problems of radio physics and radio astronomy // Radio physics and Radio astronomy, 2013. Volume 18, Issue 2, p. 176-188 (in Russian)
6. I.Y. Vasylieva, V.V. Zakharenko, P. Zarka et al. Data processing pipeline for decameter pulsar/transient survey // Odessa Astronomical publications, V 26, Issue 2, 2013, p. 159-161
7. V.V. Zakharenko, A.V. Markova, I.Y. Vasylieva. «A search of pulsed emission from X-ray dim isolated neutron stars in decameter wavelengths» // Radio physics and Radio astronomy, v.15, N 3, 2010, pp.263-270 (in Russian)
8. V.V. Zakharenko, I.Y. Vasylieva, A. A. Konovalenko, P. Zarka, V.S. Nikolaenko, First results of the decameter survey of the Northern sky. Redetection of known pulsars // Odessa Astronomical publications, V 24, 2011, p.117

Conferences:

1. V.V. Zakharenko, A.A. Konovalenko, P. Zarka, Ya.Yu. Vasylyeva. «A search of pulsed radio emission at decameter wavelengths »: The 10-th International Gamow Summer School «Astronomy and Beyond: Astrophysics, Cosmology and Gravitation, Cosmomicrophysics, Radio-Astronomy and Astrobiology» Aug 2328, Odessa, 2010 (in russian)
2. Ya.Yu. Vasylyeva, V.V. Zakharenko. «Methods of searching for pulsed emission in the observational data»: Integrated computer technologies in engineering industry, Nov 23-26, Kharkiv, KHAI, 2010 (in russian)
3. Ya. Yu. Vasylyeva.The Northern Sky pulsars and transient survey in decameter range. Initial results //VII Conference of Science and Technology «Contemporary Problems of rocket-space equipment and technology», Apr 2011, Kharkiv, Ukraine
4. V.V. Zakharenko, Ya.Yu. Vasylyeva, A.A. Konovalenko, P. Zarka, V.S. Nikolaenko. "First results of the decameter survey of the Northern sky. Redetection of known pulsars": 11-th International Gamow Summer School "Astronomy and Beyond: Astrophysics, Cosmology and Gravitation, Cosmomicrophysics, Radio-Astronomy and Astrobiology" 22-28 August, 2011, Odessa, Ukraine (in russian),
5. I. Y. Vasylieva, V. V. Zakharenko, A. I. Shevtsova. The ongoing survey for sources with short time scales of radiation in the decameter range // XII Kharkiv Young Scientist Conference on Radio physics, Electronics, Photonics and Biophysics, 4 – 7 December 2012.
6. I.Y. Vasylieva. The survey for pulsed and transient sources at decameter wavelengths // Elbereth 2012,

conference of Doctoral School of Astronomy and Astrophysics (ED-127) of Ile-de-France, Institute of Astrophysics, Paris, France, http://elbereth2012.obspm.fr/IMG/pdf/Booklet.pdf (page 15), 11-14 December 2012

7. I.Y Vasylieva, V.V. Zakharenko, P. Zarka, O.M. Ulyanov, A.I. Shevtsova, A.A. Seredkina. Data processing pipeline for decameter pulsar/transient survey // 13-th International Gamow Summer School "Astronomy and Beyond: Astrophysics, Cosmology and Gravitation, Cosmo-microphysics, Radio-Astronomy and Astrobiology" 19-24 August, 2013, Odessa, Ukraine

8. I.Y Vasylieva, V.V. Zakharenko, P. Zarka. Fast data processing pipeline for decameter data processing
(poster) // Astroinformatics 2013 workshop, 9-13 December 2013, Sydney, Australia (Travel grant of CSIRO ATNF)

9. Konovalenko O., Zarka P., Melnyk V., Kalinichenko M., Ulyanov O., Zakharenko V., Sidorchuk M, Bubnov I., Gridin A., Mylostna K., Vasylieva I., Extremely-low-frequency studies of radio emissions from space at UTR-2 and GURT (poster) // Journees Radio SKA-LOFAR 2014, 11-13 February 2014, IAP, Paris, France

10. I. Vasylieva, P. Zarka, S. Zakharenko. Processing the TAB data from UTR-2 in the pipeline mode // NenuFar Workshop: Science with NenuFAR, 13-14 February 2014, Paris, France

11. A. Konovalenko, P. Zarka, V. Zakharenko, O. Ulyanov, M. Sidorchuk, S. Stepkin, P. Tokarsky, A. Stanislavsky, N. Kalinichenko, V. Koliadin, V. Melnik, V. Dorovskyy, V. Shepelev, A. Koval, I. Bubnov, S. Yerin, I. Vasylieva. State-of-the-art of low frequency radio astronomy, relevant antenna systems and international cooperation in Ukraine // ICATT'15, 21-24 Apr 2015, Kharkiv, Ukraine

12. I. Vasylieva, P. Zarka, V. Ryabov, V. Zakharenko. Is there an exoplanet under your noise // Journees de la SF2A 2015, 2-5 June 2015, Toulouse, France

13. Zakharenko V.V., Kravtsov I.P., Vasylieva I.Y., Ulyanov O.M., Shevtsova A.I., Skoryk A.O., Mykhailova S.S., Konovalenko O.O., Zarka P. The first results of transient signal processing in decameter pulsar/transient survey of northern sky // The XV-th G. Gamow's Odessa Astronomical Summer Conference-School, 16-23 August, 2015, Odessa, Ukraine

14. "Fine Structure of the Pulsar Decameter Radiation as the Probe of the Propagation Medium" Anastasiia Skoryk, O. Ulyanov, V. Zakharenko, A. Shevtsova, Y. Vasylieva, I. Kravtsov, M. Plakhov // International Young Scientists Forum on Applied Physics, September 29 – October 2, 2015, Dnipropetrovsk, Ukraine

15. "Decameter Pulsar/Transient Survey of Northern Sky. Multiparametric Pipeline Candidate Selection" Igor Kravtsov, V. Zakharenko, I. Vasylieva, O. Ulyanov, A. Shevtsova, A. Skoryk, O. Konovalenko, S. Mykhailova, P. Zarka // International Young Scientists Forum on Applied Physics, September 29 – October 2, 2015, Dnipropetrovsk, Ukraine

16. "Rotation Measure Calculation Algorithm for Pulse Radiation in Decameter Range" Alisa Shevtsova, O. Ulyanov, A. Skoryk, V. Zakharenko, I. Vasylieva, I. Kravtsov, Institute of Radio Astronomy of NAS of Ukraine, Kharkiv, Ukraine // International Young Scientists Forum on Applied Physics, September 29–October 2, 2015, Dnipropetrovsk, Ukraine

A.1 Selected papers

I include below:

(i) The paper concerning the preparatory stage of the pulsar/transient survey: a census of known pulsars in decameter rande with UTR-2. Title: "Detection of decametre-wavelength pulsed radio emission of 40 known pulsars" ("Monthly Notices of the Royal Astronomical Society" journal)

(ii) Selected pages of a paper "The modern radio astronomy network in Ukraine: UTR-2, URAN and GURT" submitted to the "Experimental Astronomy" journal, showing the performance of our RFI mitigation pipeline.

(iii) The proceedings of the XIII Gamov's international summer conference/school (Odessa, Ukraine) with a description of the data processing pipeline of the pulsar/transient survey.

(iv) The paper Decameter pulsar/transient survey of northern sky. First results. (Ukrainian journal "Radiophysics and Radio astronomy")

Monthly Notices
of the
ROYAL ASTRONOMICAL SOCIETY

MNRAS **431,** 3624–3641 (2013)
Advance Access publication 2013 April 11

doi:10.1093/mnras/stt470

Detection of decametre-wavelength pulsed radio emission of 40 known pulsars

V. V. Zakharenko,[1]⋆ I. Y. Vasylieva,[1] A. A. Konovalenko,[1] O. M. Ulyanov,[1] M. Serylak,[2,3] P. Zarka,[4] J.-M. Grießmeier,[2,3] I. Cognard[2] and V. S. Nikolaenko[1]

[1]*Institute of Radio Astronomy of Nat. Acad. Sci. of Ukraine, Krasnoznamennaya 4, 61022 Kharkiv, Ukraine*
[2]*LPC2E, 3A, Avenue de la Recherche Scientifique, F-45071 Orléans cedex 2, France*
[3]*Station de radioastronomie de Nançay, Observatoire de Paris, CNRS/INSU, F-18330 Nançay, France*
[4]*LESIA, Observatoire de Paris, CNRS, UPMC, Université Paris Diderot, 5 Place Jules Janssen, F-92190 Meudon, France*

Accepted 2013 March 9. Received 2013 March 7; in original form 2012 August 20

ABSTRACT

The study of pulsars at the lowest radio frequencies observable from the ground (10–30 MHz) is complicated by strong interstellar (dispersion, scattering) and ionospheric (scintillation, refraction) propagation effects, as well as intense Galactic background noise and interference. However, it permits us to measure interstellar plasma parameters (the effects of which increase by a power of two to >4 times the wavelength), the spectrum and the pulse profile at low frequencies more accurately. Up to now, only ∼10 pulsars have been successfully detected at these frequencies. The recent upgrade of the receivers at the Ukrainian T-shaped Radio telescope, second modification (UTR-2) has increased its sensitivity and motivated a new search for pulsed radio emissions. In this work we carried out a survey of known pulsars with declination above -10°, period >0.1 s and dispersion measure (DM) < 30 pc cm^{-3}, i.e. a sample of 74 sources. Our goal was either to detect pulsars not recorded before in the decametre range or to identify factors that prevent their detection. As a result, we have detected the radio emission of 40 pulsars, i.e. 55 per cent of the observed sample. For 30 of them, this was a first detection at these frequencies. Parameters of their average profiles have been calculated, including the intrinsic widening of the pulse (not due to interstellar scattering) with decreasing frequency. Furthermore, two pulsars beyond the selected DM (B0138+59 with DM ≈ 35 pc cm^{-3} and B0525+21 with DM ≈51 pc cm^{-3}) were also detected. Our results indicate that there is still room to detect new transient and pulsed sources with low-frequency observations.

Key words: methods: data analysis – pulsars: general – pulsars: individual: PSR B0031−07.

1 INTRODUCTION

After the discovery of pulsars at 81.5 MHz (Hewish et al. 1968), the first pulsar detected at 40 MHz was PSR B1133+16 (Arecibo Observatory, 1968, unpublished). In 1969–1970 the pulsars PSR B1133+16 and B0809+74 were detected at 25 MHz (Bruck 1970). Systematic observations of pulsed radio emission in the decametre wavelength range started in 1972 after the commissioning of the Ukrainian T-shaped Radio telescope, second modification (UTR-2), near Kharkov, Ukraine, with an initial frequency range of 10–25 MHz (Braude, Megn & Sodin 1978). In 1973 the emission of three more pulsars was discovered (Bruck & Ustimenko 1973). Overall, only ∼10 pulsars were detected at low frequencies until the late 1980s (Bruck & Ustimenko 1976; Bruck, Ulyanov & Ustimenko 1986; Phillips & Wolszczan 1989). Large programmes and targeted studies were conducted between 25 and 40 MHz using radio telescopes such as the Arecibo dish (25 MHz, USA: Phillips & Wolszczan 1989), the Gauribidanur T-array (34.5 MHz, India: Deshpande & Radhakrishnan 1992, 1994), the DCR-1000 radio telescope (28–40 MHz, Pushchino, Russia: Izvekova et al. 1981) and Florida University's 640-dipole array (26.3 MHz: Reyes et al. 1981).

Various characteristics of the low-frequency radio emission were investigated, including flux density, spectral index (with respect to higher frequency measurements), mean pulse profile and its variation with frequency (generally an increasing pulse width and subpulse separation with decreasing frequency; see e.g. Bruck 1987; Thorsett 1991). Also, the giant pulses of the Crab pulsar were detected in the decametre range (Popov et al. 2006), individual pulse characteristics and the subpulse structure of some pulsars were investigated (Ulyanov et al. 2007; Ulyanov, Zakharenko & Bruck

⋆ E-mail: zakhar@rian.kharkov.ua

2008; Ulyanov & Zakharenko 2012) and anomalous intensive pulses were discovered (Ulyanov et al. 2006).

Today, the largest metre-wave radio telescope, the Low-Frequency Array (LOFAR), is becoming operational (van Haarlem et al., in preparation) and one of its key science cases is the study of pulsars and transient radio sources (Stappers et al. 2011). The frequency range of the telescope is divided into two bands. The low-band antennae cover the range 10–90 MHz, although they are optimized for frequencies above 30 MHz (Stappers et al. 2011; van Haarlem et al., in preparation). In contrast, UTR-2 can operate in the band 8–40 MHz (it is now the world's largest radio telescope in this range) but it is most sensitive at frequencies below 25 MHz. Therefore joint observations (simultaneous or not) will be highly beneficial, providing a continuous frequency coverage from 8–240 MHz.

At present, only a small number of pulsars have been detected in the decametre wavelength range, which can lead to erroneous conclusions about pulsar properties at low frequencies. In order to improve this situation, we took advantage of the substantial improvement in sensitivity provided by the modernized receiver system at UTR-2 (Ryabov et al. 2010; Konovalenko et al. 2011) in order to increase the sample of low-frequency pulsars. We start with a survey of all known pulsars that are visible from this telescope (located at longitude $= 36^\circ 56' 29''$E, latitude $= +49^\circ 38' 10''$). Where detection fails, we try to identify the factors that prevented detection.

1.1 Challenges and advantages of observing pulsed signals at low frequencies

The lower bound of the radio transparency window of Earth's ionosphere is determined by a critical frequency of about 10 MHz. In the lowest two octaves above this frequency, research into pulsed and transient radio emission is complicated by a number of hindering factors. The most serious obstacle is the growth of the scattering time due to propagation through the interstellar medium (ISM) towards lower frequencies $\propto \nu^{\alpha_{SC}}$, with $\alpha_{SC} = -4.4$ for a Kolmogorov distribution of inhomogeneities and ν the frequency of observation. This leads to an increase of the scattering time between the decametre range ($\nu = 25$ MHz) and the decimetre range ($\nu = 1$ GHz) by a factor $(25/1000)^{-4.4} \approx 10^7$. At low frequencies, the pulses are broadened so much that they start to overlap, washing out the contrast between intensity maxima and minima. This is most striking when the pulse period is short with respect to the scattering time. For example, for the Crab pulsar ($P \approx 0.033$ s) at 25 MHz the scattering time is expected to be about 30 s. Actual measurements of the scattering time of giant pulses (Popov et al. 2006) gave values of about 3 s, still 100 times larger than the pulsar period. Regular pulses of the pulsar were thus not detected. Even the detection of long-period pulsars becomes extremely difficult when they are distant and strongly scattered.

The next serious hindering factor is the growth of Galactic background noise towards lower frequencies $\propto \nu^{-2.5}$ down to $\approx$5 MHz (Ellis 1982), with a brightness temperature reaching 550 000 K at 8 MHz outside the Galactic disc and values several times higher in the Galactic plane (Milogradov-Turin & Smith 1973; Caswell 1976; Roger et al. 1999).

Another difficulty is the scintillation in the ionosphere, quite strong at low frequencies and resulting in undesirable intensity modulations of received radio emission. The combined influence of scintillation and refraction leads to fluctuations of the apparent position of a source even when it is situated near the zenith. For UTR-2, the mean position error is $0.^\circ 1$ and the maximum error is $\geq 0.^\circ 7$ (Braude et al. 2002), larger than the beam width of UTR-2 at 25 MHz ($0.^\circ 5$). In addition, the intrinsic sporadicity of pulsar radiation appears to increase towards lower frequencies (Ulyanov et al. 2006). Therefore, obtaining a stable shape of the average pulse profile requires observations of longer duration.

An instrumental factor that limits the sensitivity reachable in the range 10–30 MHz is the small absolute observation bandwidth. The sensitivity is proportional to the square root of the frequency bandwidth but, due to the frequency dependence of the pulsar emission and of the noise parameters, integration over a broad frequency band should be avoided in this range.

Let us estimate the signal-to-noise ratio (S/N) deterioration for two frequencies 25 and 100 MHz, separated only by two octaves. It is well known that the majority of pulsars have a turnover in their spectrum at metre wavelengths. At lower frequencies, the flux density falls off with spectral index α varying within wide limits 0–4; see e.g. Malofeev, Malov & Shchegoleva (2000) and Maron et al. (2000). Thus, pulsar fluxes for the aforementioned frequencies and a moderate value of $\alpha = 1$ will differ by a factor of 4. Moreover, due to the increase of Galactic background noise by a factor $(25/100)^{-2.5} = 32$, the resulting S/N is reduced by more than two orders of magnitude.

Finally, interference from broadcast radio stations may exceed astronomical signals by up to 70–80 dB (especially during the daytime) and propagation through the ionosphere can further reduce the S/N by a small factor. Taken together, these reasons explain why only a relatively small number of pulsars has been detected at the lowest frequencies so far.

Despite all these difficulties, the decametre range remains quite attractive, especially due to the above pulse profile broadening, which leads to a significant increase of the beaming fraction in the 10–30 MHz range in comparison with 1.4-GHz surveys. There are also indications for some pulsars of the presence in the decametre wavelength range of a wide, low-intensity 'plateau' in addition to the pulse (see e.g. Phillips & Wolszczan 1989).

Another factor is that some pulsars such as PSR B0943+10 are characterized by a steep spectral index, i.e. a flux density strongly increasing at low frequencies. This increases the probability of discovering new sources at very low frequencies.

The aforementioned strong frequency dependence of parameters such as the dispersion and the rotation measure allows us to determine them very accurately in the decametre range. The dispersion delay is given by (Backer et al. 1993)

$$\Delta t = 10^{16}\mathrm{DM}/2.410331(\nu_{\min}^{-2} - \nu_{\max}^{-2}). \quad (1)$$

This quadratic dependence on wavelength permits us to measure the dispersion measure (DM) very accurately. It also allows us to distinguish clearly between single pulses, even from the closest sources, and broad-band terrestrial interference. Indeed, a very small DM of 0.1 pc cm^{-3} gives a signal propagation delay of about 1.14 s between frequencies of 16.5 and 33.0 MHz. This exceeds the pulse width of all known pulsars. For high-frequency observations, the distinction between a truly zero DM and a DM of a few pc cm^{-3} is a significant problem (see e.g. Kondratiev et al. 2009). The presence of dispersion in the signal can be especially valuable for the detection of signals from nearby transient radio sources, because frequency-dependent dispersion is one of the main characteristics allowing us to distinguish them from broad-band interference of terrestrial origin.

Similarly, magnetic field variations along the line of sight will be easier to detect at low frequencies because of the quadratic dependence of Faraday rotation on wavelength.

Irregular low scattering with an exponent $\alpha_{SC} < 4$, observed for giant pulses of the Crab pulsar, was confirmed in Bhat et al. (2007) as an exceptional event. The results of Popov et al. (2006) show that at very low frequencies, thanks to this irregular low scattering, not only close transient signals but also sources with DM up to 60 pc cm^{-3} can be detected.

Using the model of galactic electron concentration by Cordes & Lazio (2002), this maximum DM translates into a maximum distance $\geq$2 kpc in the Galactic plane and up to the borders of the Galactic disc in the direction of the poles. This restriction to relatively close sources makes the limitation in S/N imposed by intense low-frequency Galactic background noise less constraining.

This is why the decametre range can be very favourable for the study of transient phenomena and can help to provide answers to important open questions, for example

(i) an explanation of the discrepancy between supernova explosion rates measured by gamma-ray emission of radioactive aluminium (^{26}Al) of the Galaxy (Diehl et al. 2006) and the number of various remnants of these explosions (Keane & Kramer 2008); the latter can be significantly increased by the recently discovered Rotating RAdio Transients (RRATs) (McLaughlin et al. 2006);

(ii) verification of contradictory data regarding the existence of radio emission from X-ray Dim Isolated Neutron Stars (XDINS) (Malofeev, Malov & Teplykh 2005; Kondratiev et al. 2009; Zakharenko, Markova & Vasylieva 2011);

(iii) better constraints for the neutron-star radio-emission mechanism.

1.2 Maximizing the sensitivity of the pulsar search at the radio telescope UTR-2

Since the upgrade of the preamplification system (Abranin et al. 2001), receiver noise is negligible in comparison with the above values of the sky temperatures. Evolution of backends towards digital receivers (Lecacheux et al. 1998; Zakharenko et al. 2007) led after 2006 to a new generation of digital receivers (hereafter DSPZ), the characteristics of which are described in (Kozhin, Vynogradov & Vavriv 2007; Ryabov et al. 2010; Konovalenko et al. 2011). DSPZ receivers can record the entire band of the radio telescope at once. Thus, we can compute the maximum sensitivity S achieved for a given collecting area. We have chosen the 4σ level (here, σ is standard deviation) as the maximum intensity radiated by non-detected sources (as in Kondratiev et al. 2009; Zakharenko et al. 2011). This level is given by the formula

$$S = \frac{4 \times (2kT)}{A_e(z)\sqrt{\Delta\nu \Delta t (t_i/P)}}, \quad (2)$$

with k the Boltzmann constant, T the galactic background temperature, A_e(z) the collecting area of the telescope (150 000 m^2 in the zenith direction), $\Delta\nu$ the frequency band of observations, Δt the integration time and (t_i/P) the fraction of time occupied by the pulse itself, which is of duration t_i, relative to the pulsar period P. Assuming $T \approx 20\,000$ K, $A_e \approx 100\,000$ m^2 (taking into account the geometrical factor for off-zenith sources), $\Delta\nu = 16.5$ MHz, $\Delta t = 5400$ s and $(t_i/P) = 0.05$, the resulting sensitivity is about 33 mJy. Actually, due to scintillations in the ionosphere, the effect of nulling and the more sporadic nature of pulsar emission at low frequencies compared with higher ones, this estimate of the sensitivity should be considered as an optimistic one. If we consider the possibility of individual pulse detection, the product $\Delta t\ (t_i/P)$ in expression (2) must be replaced by $\Delta t = 0.1$ s, the pulse width expected for RRATs or giant pulses of pulsars. Then the detection limit is approximately 1.6 Jy. This can be regarded conversely as a pessimistic estimate, since for a large fraction of RRATs or giant pulses we can expect a few pulses per observational period.

In searches for decametre radio emission from XDINSs (Zakharenko et al. 2011), sensitivities of a few mJy were achieved. This make us hope that the improved instrumentation capabilities will give us a better chance of detecting pulse radiation from objects that have not been detected previously. However, the total number of detected pulsars in the decametre range will depend on the extent to which they are affected by the limiting factors discussed in Section 1.1.

Therefore, the motivation for the observations presented here is to answer the question: how many known pulsars can be detected in the decametre range in comparison with higher frequency observations? In addition, we tried to identify factors that prevent us from detecting a pulsar and find ways to reduce their impact.

The structure of this article is as follows. Section 2 describes the instrumentation and method of observation. Section 3 presents the results of the observations, which are discussed in Section 4. Section 5 presents our conclusions.

2 INSTRUMENTATION AND OBSERVATIONS

The good interference immunity of UTR-2 enables round-the-clock observations even in a polluted situation. To have good sensitivity, the effective area of the telescope must be sufficiently high, so we chose sources with declination $\delta > -10^\circ$, such that the decrease of A_e due to geometrical projection is less than a factor of two (the latitude of UTR-2; see Section 1). In the numerical application of equation (2) above, we used the average $A_e(z)$ for the current survey. Another important parameter is the time resolution. Its selection (8 ms) supposes that only a few of the known nearby pulsars (B0950+08, B0809+74) have a lower scattering time at decametre wavelengths. Taking into account this fact and the known scattering time constants for other pulsars, we fixed a minimum period of 100 ms for the observed pulsars. For the survey we chose bounds of DM = 0–30 pc cm^{-3}.

In 2010 October, the Australia Telescope National Facility (ATNF) pulsar data base (Manchester et al. 2005) contained 74 pulsars satisfying these criteria.

It is well known that high DM accuracy is a crucial factor to determine the shape of the average profile and to calculate several physical parameters of the pulsar's radio emission. The trial DM step has to be chosen such that the intensity decrease between an analysis with the best trial DM and with the precise value of the DM remains low. According to expression (12) of Cordes & McLaughlin (2003), the ratio of fluxes at inexact DM ($F_{\delta DM}$) and at the true DM (F) can be written as

$$\frac{F_{\delta DM}}{F} = \frac{\sqrt{\pi}}{2}\zeta^{-1}\ \mathrm{erf}\ \zeta, \quad (3)$$

where $\zeta = 6.91 \times 10^{-3}\delta\mathrm{DM}\ (\Delta\nu_{\mathrm{MHz}})/(W_{\mathrm{ms}}\nu^3_{\mathrm{GHz}})$, with ν the central frequency of observation, $\Delta\nu$ the bandwidth and W_{ms} the pulse width. In order to keep this ratio below 5 per cent for $\Delta\nu = 16.5$ MHz, $\nu = 0.024$ GHz and $W = 100$ ms, a maximum error $\delta\mathrm{DM} = 0.005$ pc cm^{-3} can be tolerated.

To determine the DM with the highest possible accuracy, the trial DM step should be chosen to be as small as possible. For our data, its

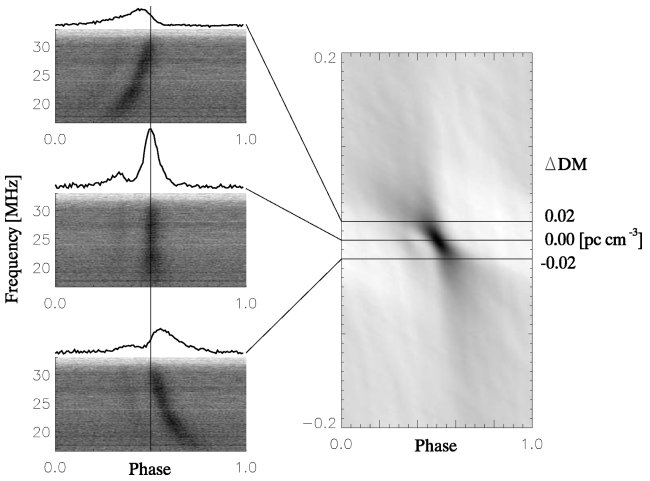

Figure 1. An example of determination of the DM in the band 16.5–33.0 MHz for the pulsar PSR B0031−07. The grey-scale image to the right represents the average pulse profile versus rotational phase and dispersion measure. The slope of the region of maximum intensity is induced by the fact that the compensation of dispersion delay is related to the upper frequency of the range. 'Undercompensation' (ΔDM < 0) shifts the average profile to a later phase of the pulsar rotation period, while 'overcompensation' (ΔDM > 0) shifts it to an earlier phase (left panels).

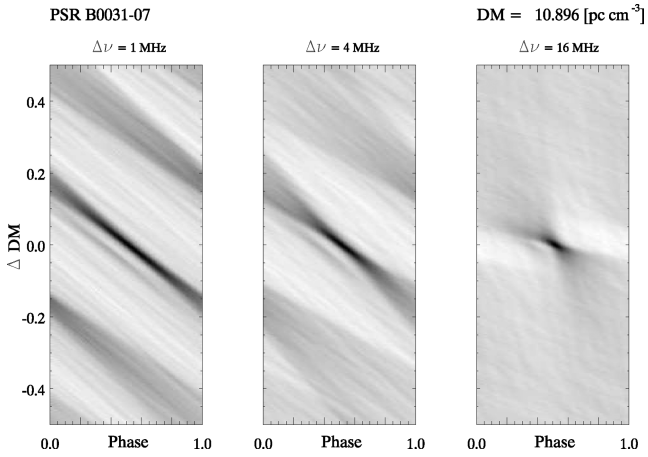

Figure 2. 'Rotational phase–dispersion measure' plane with integration over frequency ranges $\Delta\nu$ of 1 MHz (left panel), 4 MHz (middle panel) and 16 MHz (right panel). The size of the maximum intensity region increases when the bandwidth decreases, allowing us to detect a pulsar with larger deviations of DM from the optimum value but leading to a DM measurement with less accuracy.

value has a lower threshold related to the available time resolution: adjacent trial DMs should correspond to a relative time delay at the lowest frequencies of at least one time bin (8 ms). We used a step width of $\Delta\mathrm{DM} = 0.002\,\mathrm{pc\,cm^{-3}}$ (corresponding to a shift of 2.5 time bins at the lowest frequencies).

To illustrate the search for a refined DM, we show intermediate and final data for PSR B0031−07. Fig. 1 shows the results of compensation of dispersive propagation delay with different values of the trial DM. The left panel shows interference-free and accumulated dynamic spectra over 5700 periods of the pulsar, in the frequency range 16.5–33.0 MHz. On the top of each of the three panels the averaged and frequency-integrated pulse profile of the pulsar is shown. Each profile corresponds to a horizontal cut of the grey-scale image in the right panel (at a specific value of the trial DM). Profiles are shown with a pitch of $0.02\,\mathrm{pc\,cm^{-3}}$. The pulse profile with the maximum S/N, which occurs for a good vertical alignment of pulse components at all frequencies of the dynamic spectrum, corresponds to the best compensation of the dispersion delay.

In our algorithm, the compensation of the dispersion delay is calculated with respect to the highest frequency channel. This defines the slope of the region of maximum intensity in the 'rotational phase–dispersion measure' plane (right side panel of Fig. 1). When deviating from the optimal DM towards negative ΔDM ('undercompensation'), the maximum of the average profile decreases and shifts to a later phase of the period (Fig. 1, left lower panel), while an 'overcompensation' ($\Delta\mathrm{DM} > 0$) causes a shift to an earlier phase (Fig. 1, left upper panel).

The lower the frequency and the broader the measurement bandwidth, the more accurate is the determination of the DM, as follows from equation (3). Fig. 2 shows three images of the 'rotational phase–dispersion measure' plane for PSR B0031−07, with integration over different frequency ranges (from left to right: $\Delta\nu = 1$, 4 and 16 MHz) around the same centre frequency of 25 MHz. One can see that the size of the high-intensity region increases for a narrower bandwidth of observations. At the same time, the maximum deviation from the optimal DM that allows us to detect a pulsar also increases. Maximizing the observational bandwidth thus leads to better accuracy in determining the DM, but its inaccurate choice will not allow us to detect a pulsar (if the high-intensity region falls outside the explored DM range). However, if too wide a bandwidth is taken then the frequency evolution of the pulse profile can affect the DM value (Hassall et al. 2012).

The choice of frequency band is related to the transparency of the ionosphere and to the interference situation. In the morning, afternoon and evening, the conditions are acceptable only for observations at frequencies above 14–16 MHz. At night, observations down to 8 MHz can be conducted, because the interference level is low. Due to round-the-clock observations, the frequency range for our survey was chosen between 16.5 and 33.0 MHz. In spectral mode, the DSPZ receiver has 4096 frequency channels in this range, each of approximately 4 kHz width. Each pulsar was observed for 90 min. During this interval, 1800–25 000 periods have been accumulated, depending on the pulsar period (see Table 1). We used incoherent dedispersion, i.e. in the time–frequency plane after detection, which broadens the signal by no more than 100 ms for $\mathrm{DM} = 30\,\mathrm{pc\,cm^{-3}}$ even in the lowest frequency channel, where the majority of pulsars have negligibly low radiation.

The depth of radio frequency interference (RFI) cleaning can be varied in our interference-removal algorithm, depending on interference conditions. Masking affected frequency channels and/or time intervals leads to an unavoidable loss of samples where pulsar radiation is present. Therefore, we applied less deep cleaning for night-time observations. For the data obtained during the daytime (Fig. 3), when the interference levels exceeded the levels of unaffected channels by tens of dB a deeper cleaning was applied.

The cleaning procedure consists of several stages. First, in the narrow-band (4 kHz) spectral channels the standard deviation (σ_{ch}) is calculated iteratively by discarding the values exceeding $3\sigma_{\mathrm{ch}}$ at each step (with a stop criterion corresponding to consecutive values of σ_{ch} differing by no more than 10^{-5}). The resulting value is used to determine two thresholds of cleaning. The first one (usually between 4–$6\sigma_{\mathrm{ch}}$) is the clipping level. This mode is useful when a relatively strong pulsar signal overlaps with low-intensity interference or a background-noise peak due to the scintillations of a nearby point source (this situation occurs quite often because of the relatively

Table 1. DM values given in the catalogue of Manchester et al. (2005) and obtained during the present work at UTR-2 for the 40 detected pulsars.

No	Name	DM* (pc cm^{-3})	DM (UTR-2) (pc cm^{-3})	P (s)	Number of P
1	B0031−07	11.38(8)	10.896(4)	0.943	5726
2	J0051+0423	13.9(1)	13.936(3)	0.355	15 211
3	B0053+47	18.09(4)	18.144(8)	0.472	11 440
4	B0148−06	25.66(3)	25.661(12)	1.465	3686
5	B0320+39	26.01(3)	26.162(11)	3.032	1781
6	B0329+54	25.66(3)	25.661(11)	0.714	7563
7	B0450+55	14.495(7)	14.602(5)	0.341	15 835
8	B0809+74	6.116(18)	5.755(3)	1.292	4179
9	B0823+26	19.454(4)	19.484(6)	0.531	10 169
10	B0834+06	12.889(6)	12.872(4)	1.274	4238
11	B0919+06	27.271(6)	27.316(6)	0.431	12 529
12	J0927+23	23(2)	24.032(10)	0.762	7086
13	B0940+16	20.32(5)	20.354(8)	1.087	4967
14	B0943+10	15.4(5)	15.339(4)	1.098	4918
15	B0950+08	2.958(3)	2.972(2)	0.253	21 343
16	B1112+50	9.195(8)	9.185(4)	1.656	3260
17	B1133+16	4.864(5)	4.846(2)	1.188	4545
18	J1238+21	17.5(1.2)	17.968(5)	1.119	4825
19	B1237+25	9.242(6)	9.268(2)	1.382	3907
20	B1322+83	13.312(18)	13.312(4)	0.670	8059
21	B1508+55	19.613(20)	19.622(9)	0.740	7297
22	B1530+27	14.698(18)	14.706(3)	1.125	4800
23	B1540−06	18.403(4)	18.334(100)	0.709	7616
24	B1604−00	10.682(5)	10.688(2)	0.422	12 796
25	B1612+07	21.39(3)	21.402(14)	1.207	4473
26	B1633+24	24.32(4)	24.540(8)	0.491	10 997
27	J1741+2758	29.3(6)	29.146(18)	1.361	3967
28	B1822−09	19.38(4)	19.408(21)	0.769	7022
29	B1839+56	26.698(11)	26.804(6)	1.653	3266
30	J1851−0053	24(4)	24.556(37)	1.409	3832
31	J1908+0734	11.104(11)	11.234(50)	0.212	25 471
32	B1919+21	12.455(6)	12.435(4)	1.337	4038
33	B1929+10	3.180(4)	3.180(2)	0.227	23 788
34	B1944+17	16.220(16)	15.720(4)	0.441	12 244
35	B1952+29	7.932(7)	7.870(5)	0.427	12 646
36	B2016+28	14.172(4)	14.200(7)	0.558	9677
37	B2110+27	25.113(4)	25.114(18)	1.203	4488
38	J2307+2225	7.08(3)	6.842(12)	0.536	10 074
39	B2310+42	17.2758(13)	17.256(15)	0.349	15 472
40	B2315+21	20.906(7)	20.904(13)	1.445	3737

*Manchester et al. (2005).

wide antenna pattern). Moreover, such scintillations usually amplify not only the signal of the point source but also the pulsar signal. In order not to discard the corresponding measurements, we clip the signal level but retain it in subsequent analysis). However, if a signal is extremely strong in a single DSPZ channel, it is almost certainly interference. Therefore, the second threshold (usually at 6–10σ_{ch}) corresponds to the elimination of high-intensity signals. This step actually removes efficiently intense broad-band interference. In summary, values below the first threshold are left unaltered, values between the first and the second threshold are clipped and values above the second threshold are removed (blanked).

During the daytime we need to eliminate more frequency channels affected by interference from broadcast and specialized radio stations. For that purpose, we compare the average power in each channel with that in adjacent channels. Using the same iterative algorithm as above, the standard deviation σ_{sp} of unpolluted frequency channels (averaged during ≈10 s) is calculated. Then, all

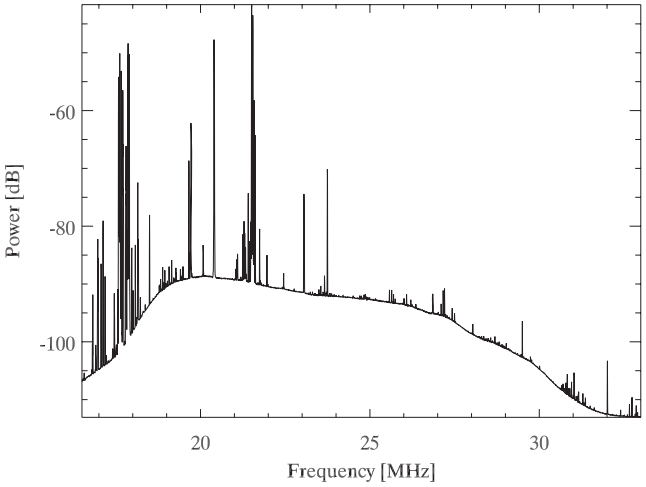

Figure 3. Example of spectrum received by UTR-2 during the daytime, affected by strong interference.

channels with average level exceeding a given threshold (usually $4\sigma_{sp}$) are excluded from the analysis.

Furthermore, low-intensity broad-band interference often occurs in the range 27–33 MHz during the daytime. To eliminate this, another specific cleaning stage is applied. The previously cleaned dynamic spectra are integrated versus frequency and the σ_{sum} of the resulting time series is calculated. Time intervals with intensity exceeding $4\sigma_{sum}$ are also excluded. When calculating pulsar fluxes, the information on the number of retained frequency channels and time intervals is taken into account.

We conducted three sessions of observations (2010 October 11–18, 2011 January 17–24 and 2011 March 21–28). During the first session, all 74 pulsars were observed. During the second and the third sessions, those sources that were not detected in the previous session were reobserved. The third session was also used to observe some pulsars with DM $\geq$ 30 pc cm^{-3}.

3 RESULTS

For the first time, 40 pulsars known from higher frequency observations have been detected in the decametre wavelength range. For only 10 of these have decametre data previously been published. After determining accurately each pulsar's DM and average flux density, its spectral index was computed from the pulsar's known spectral maximum in flux density and our decametre-wavelength measurements. Also, the widths of the average pulse profiles at 50 per cent and 10 per cent levels relative to its maximum intensity and the scattering time constant at 25 MHz have been determined. Power-law indices for the scattering time constant have been calculated with respect to the catalogue data at 1 GHz. For the 34 non-detected pulsars (out of our sample of 74), upper limits on the flux density corresponding to the 4σ level have been obtained.

3.1 Refining the dispersion measure

Figs A1 and A2 in the Appendix show average profiles and grey-scale images of the 'rotational phase–dispersion measure' plane for all detected pulsars. Fig. A1 shows the average profiles of 15 pulsars with high S/N at 25 MHz (over the band 23–27 MHz, bold curve) and at 20 MHz (over the band 18–22 MHz, thin curve). We chose to restrict our focus to 4-MHz bandwidths whenever permitted by the S/N in order to avoid smearing due to the intrinsic variation

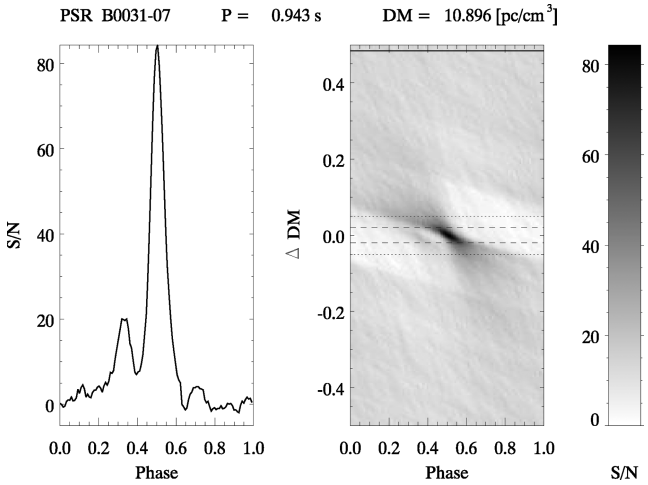

Figure 4. Average profile corresponding to the optimal DM for PSR B0031−07, after integration over the frequency range 23–27 MHz (left panel). The grey-scale image displays the profiles obtained for different DMs, over the band 16.5–33 MHz (right panel). The S/N decreases by a factor of 2 and by a factor of 10 within ±0.02 (dashed line) and ±0.05 (dotted line) pc cm^{-3} of the optimal DM, respectively. The bold line indicates the DM value from the catalogue of Manchester et al. (2005). It is impossible to detect a pulsar with such a DM value in broad-band low-frequency observations.

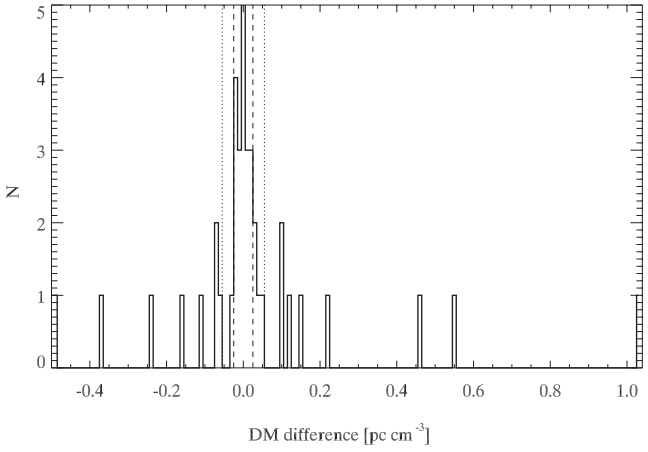

Figure 5. Histogram of DM differences between UTR-2 measurements and those of Manchester et al. (2005), along with the limits at ±0.02 and ±0.05 pc cm^{-3}.

of the average pulse profile with frequency. For the 25 pulsars depicted in Fig. A2, the S/N in a band of 4 MHz was too low and therefore the average profile is obtained over the band 20–32 MHz (or 16.5–33.0 MHz for PSRs B0148−06, J1238+21, B0940+16 and B1822−09).

Let us consider the case of PSR B0031−07 shown in Fig. 4 as an example. The left panel shows the average pulse profile, obtained by stacking of all pulses during 90 min of observation integrated over the band 25 ± 2 MHz. The right panel shows the grey-scale intensity image of the accumulated signal of the pulsar as a function of the DM. To improve the accuracy of the DM determination for all pulsars, the full observational band (16.5–33 MHz) has been used. We evaluated error bars for DM as the intervals in which the S/N decreases by 5 per cent, by a factor of 2 and by a factor of 10, respectively. The size of these intervals for each pulsar depends on several factors, including the average profile shape, the pulse width, the noise level in the off-pulse area, etc. For the case of PSR B0031−07, the latter two intervals are about ±0.02 and ±0.05 pc cm^{-3}. In Fig. 4 they are marked by dashed and dotted lines respectively. The DM value for this pulsar (11.38 pc cm^{-3}) specified in the catalogue (Manchester et al. 2005) is marked in Fig. 4 with a bold line. It is obviously not appropriate for our low-frequency broad-band measurements. At this DM value, the decametre pulsar signal is smeared and weakened to such an extent that it becomes impossible to distinguish the pulse component from the off-pulse area. Our measurements (10.896 ± 0.004 pc cm^{-3}) confirm the conclusion of Karuppusamy, Stappers & Serylak (2011) that for PSR B0031−07 the DM value and the rate of DM change given by Hobbs et al. (2004) and Manchester et al. (2005) are likely to be incorrect. Also, for PSR B0809+74, regularly observed at UTR-2, DM = 6.116 ± 0.018 pc cm^{-3} in (Hobbs et al. 2004) is not consistent with our measurements. For some of the pulsars the error bars given in the catalogue are quite large (for example, for PSR J0927+23). Therefore, we used the data from Manchester et al. (2005) as a starting value and searched in a DM interval of ±10 per cent around the specified value. This range is wide enough and may include even the largest time variations of the DM (Phillips & Wolszczan 1992; Hobbs et al. 2004; Karuppusamy et al. 2011).

The DMs that we have determined at UTR-2 are listed in Table 1 and compared with the values from the catalogue of Manchester et al. (2005). The errors in our DM values were estimated as the interval over which the S/N ratio drops by 5 per cent.

We have analysed the differences in DMs between our results and catalogue values. The results are shown in Fig. 5, as a histogram of the number of pulsars versus the DM differences. ΔDM lies within ±0.02 pc cm^{-3} for 14 pulsars, within ±0.05 pc cm^{-3} for 24 pulsars and above ±0.05 pc cm^{-3} for 16 pulsars.

While our average DM values agree well with those listed in the catalogue Manchester et al. (2005), the standard deviations of the DM differences of Fig. 5 notably exceed our error bars for DM determination from decametre measurements. For example, the average value of the DM differences in Fig. 5 is 0.025, whereas the standard deviation is 0.248 pc cm^{-3}. If we exclude the pulsars with the largest errors in Manchester et al. (2005) (PSR J0927+23 and PSR J1851−0053; see Table 1), as well as PSR B0809+74, for which the DM in other catalogues (Taylor, Manchester & Lyne 1993) is closer to our value than that of Manchester et al. (2005), the average value is −0.006 and the standard deviation is 0.154 pc cm^{-3}. In both cases, the standard deviation of ΔDM is several times larger that the error in our measurements.

This illustrates the importance of low-frequency measurements for future redetection or new searches of pulsars, to determine accurately DMs as well as rotation measures, average pulse width and other related characteristics (DM change rate, etc.). Based on the above refined DMs, we can now estimate the S/N, flux densities and spectral indices of the 40 detected pulsars.

3.2 Flux densities and spectral indices

Flux densities of detected pulsars and upper detection limits for non-detected ones have been determined on the basis of equation (2), taking into account the following considerations: in a band of one octave, the values of the background temperature, telescope effective area or pulsar flux density cannot be regarded as constants. However, without integration in frequency it is impossible to achieve the required sensitivity. We have therefore chosen a compromise:

Table 2. Flux density of strong pulsars detected at two frequencies and spectral indices α_{20-25} and $\alpha_{25-\nu_{max}}$. The maximum error in spectral indices is $\sim\pm1.8$.

N	Pulsar	Flux (mJy) (20 MHz)	Flux (mJy) (25 MHz)	α_{20-25}	Flux (mJy) (ν_{max})	$\alpha_{25-\nu_{max}}$
1	B0031−07	353 ±106	345 ±104	−0.1	560 ± 310* (102.5 MHz)	0.34
2	B0053+47	34 ±11	100 ±30	4.83	80 ± 26* (102.5 MHz)	−0.16
3	B0809+74	1300 ±390	1190 ±360	−0.4	1870 ± 350** (61 MHz)	0.51
4	B0823+26	186 ±56	203 ±61	0.39	1070 ± 560** (85 MHz)	1.36
5	B0834+06	291 ±88	329 ±99	0.55	2090 ± 420** (61 MHz)	2.07
6	B0919+06	238 ±72	570 ±171	3.91	770 ± 160** (85 MHz)	0.25
7	B0943+10	133 ±40	198 ±60	1.78	1290 ± 350** (61 MHz)	2.1
8	B0950+08	122 ±37	284 ±86	3.79	2330 ± 1620** (102.5 MHz)	1.49
9	B1112+50	19 ±6	25 ±8	1.23	60 ± 14* (102.5 MHz)	0.62
10	B1133+16	105 ±32	283 ±86	4.44	1280 ± 550* (102.5 MHz)	1.07
11	B1237+25	16 ±5	33 ±10	3.24	530 ± 100** (102.5 MHz)	1.97
12	B1508+55	35 ±11	96 ±29	4.52	1280 ± 500* (102.5 MHz)	1.84
13	B1839+56	32 ±10	89 ±27	4.58	120 ± 50** (102.5 MHz)	0.21
14	B1919+21	240 ±73	490 ±148	3.2	2100 ± 430** (61 MHz)	1.63
15	B1929+10	50 ±16	83 ±25	2.27	950 ± 660* (102.5 MHz)	1.73
				$m = 2.55$ $\sigma = 1.85$		$m = 1.14$ $\sigma = 0.77$

*Malofeev et al. (2000).
**Izvekova et al. (1981).

if the S/N allows reliable measurement of the pulsar radiation in a band of 4 MHz, then the pulsar radio emission parameters are determined in the bands 23–27 and 18–22 MHz, which correspond to central frequencies of 25 and 20 MHz, respectively.

Errors in the flux measurements performed with large phased arrays such as UTR-2 include the following: (i) errors introduced by the electronic path between the antennas and the receivers, which can be estimated using an internal calibration system (including a reference noise generator), (ii) errors in dipole antenna responses (not covered by the calibration) and (iii) flux reflected and absorbed by the ground. The first error is no more than 1–2 per cent, thanks to the internal calibration. Imperfect knowledge of dipole parameters leads to an error of up to 10 per cent in flux measurements. The largest contribution is caused by our inaccurate knowledge of the conductivity of the soil. Despite monitoring of the ground conductivity and correcting our measurements for this parameter, this error may reach 15 per cent. The overall error in our flux density measurements thus does not exceed 30 per cent. The maximum error in spectral indices in Table 2, related to the quadratic combination of the above maximum error ~30 per cent in flux densities, is typically ±1.8.

For those pulsars that have an insufficient S/N in a bandwidth of 4 MHz, we have integrated the signal over the range 20–32 MHz (centre frequency of $\sqrt{20 \times 32} \sim 25.3$ MHz). In that case, errors (ii) and (iii) as well as the unknown pulsar flux-density spectrum lead to an estimated error of 50 per cent.

Flux densities of strong pulsars detected at two frequencies are shown in Table 2. The table also contains the spectral indices α_{20-25} (between frequencies 20 and 25 MHz) and $\alpha_{25-\nu_{max}}$ (between 25 MHz and the frequency ν_{max} at which the maximum flux density was measured) for those pulsars for which these data are known from the literature (Izvekova et al. 1981; Malofeev et al. 2000). ν_{max} is given in the second row of the sixth column.

In Table 3, results on pulsars detected with a low S/N are given. Here, we integrate over the 20–32 MHz range and indicate the flux as well as the spectral index $\alpha_{25-\nu_{max}}$.

Taking into account the small frequency spacing between 20 and 25 MHz and the above errors in measuring flux densities, the spectral index α_{20-25} should be considered with caution. However, even with this limited accuracy, one can note that the average value of the low-frequency spectral index of the 15 pulsars in Table 2 ($\langle\alpha_{20-25}\rangle = 2.55$) significantly exceeds the average value of the spectral index between decametre and metre waves ($\langle\alpha_{25-\nu_{max}}\rangle \approx 1.1$). This may reveal the steepening of the spectral index in the decametre range, provided that measurements at ν_{max} (especially the position of the maximum flux density) are reliable. Further studies with UTR-2 and LOFAR will help to clarify this issue. The average spectral index of strong pulsars in Table 2 ($\langle\alpha_{25-\nu_{max}}\rangle \approx 1.1$) is smaller than that of weaker pulsars (≈1.4, Table 3). i.e. the latter ones have a steeper spectrum from metre to decametre wavelengths, which naturally explains their smaller flux density at low frequencies.

Table 4 shows the upper limit of detection at 4σ for non-detected pulsars, with parameters $\Delta\nu = 4$ MHz, $\Delta t = 5400$ s, $(t_i/P) = 0.1$. In Section 4 we discuss the possibility of detecting the remaining pulsars from our sample.

3.3 Pulse width at the 50 per cent and 10 per cent levels and scattering time constant

On the basis of the accurate DM values in Table 1, we obtained average pulse shapes from which pulse widths at 50 per cent level (FWHM) and, whenever possible, at 10 per cent of the maximum intensity were determined (Table 5). Also, the scattering time constant at 25 MHz and the power-law exponent of the scattering variations between 25 and 1000 MHz (Manchester et al. 2005) were calculated. In the decametre range, the scattering time can be comparable to or even greater than the pulse width, even for nearby pulsars. Obviously, in this case it is difficult to separate the effects of scattering and intrinsic profile broadening versus frequency. The separation of these effects requires a specific approach as in Hassall et al. (2012), which is beyond the scope of this paper. In Table 5 we indicate the values of the pulse width at 50 per cent ($W_{0.5}$) and 10 per cent ($W_{0.1}$) levels, the scattering time constant at 25 MHz τ_{SC25} and the value of the power-law index $\alpha_{SC25-1000}$ obtained from the plots shown in Figs A1 and A2 and in the literature. These latter values are upper bounds because τ_{SC25} was determined by fitting the intensity decrease versus time in the pulse tail by a law $\propto e^{-t/\tau_{SC25}}$, assuming a rectangular shape for the pulse in emission. More precise values, taking into account a realistic pulse shape, will be obtained in the future (in preparation). Values of τ_{SC25} for four pulsars denoted by an asterisk in Table 5 were taken from Ulyanov & Zakharenko (2012), where this parameter was defined on the basis of records of

Table 3. Parameters of those pulsars detected with a low S/N; flux at 25 MHz and spectral indices $\alpha_{25-\mathrm{MW}}$ for those pulsars for which these data are known from the literature.

N	Pulsar	Flux (mJy) (25 MHz)	Flux (mJy) ($\nu_{\max}$)	$\alpha_{25-\nu_{\max}}$
1	J0051+0423	32 ± 16	–	–
2	B0148−06	1.4 ± 1	109 ± 55* (102.5 MHz)	3.09
3	B0320+39	29 ± 15	230 ± 70* (102.5 MHz)	1.47
4	B0329+54	140 ± 71	1050 ± 210** (102.5 MHz)	1.43
5	B0450+55	37 ± 19	150 ± 60* (102.5 MHz)	0.99
6	J0927+23	8.5 ± 5	30 ± 13* (102.5 MHz)	0.89
7	B0940+16	7.3 ± 4	190 ± 120** (102.5 MHz)	2.31
8	J1238+21	19 ± 10	60 ± 22* (102.5 MHz)	0.81
9	B1322+83	5.8 ± 3	36 ± 12* (102.5 MHz)	1.29
10	B1530+27	19 ± 10	94 ± 44* (102.5 MHz)	1.13
11	B1540−06	5.2 ± 3	130 ± 30* (102.5 MHz)	2.28
12	B1604−00	5.0 ± 3	330 ± 70** (102.5 MHz)	2.97
13	B1612+07	33 ± 17	100 ± 40* (102.5 MHz)	0.79
14	B1633+24	25 ± 13	50 ± 15* (102.5 MHz)	0.49
15	J1741+2758	14 ± 8	30 ± 10* (102.5 MHz)	0.54
16	B1822−09	47 ± 24	790 ± 160** (61 MHz)	3.16
17	J1851−0053	7.0 ± 4	–	–
18	J1908+0734	6.4 ± 4	–	–
19	B1944+17	27 ± 14	150 ± 90** (102.5 MHz)	1.22
20	B1952+29	15 ± 8	–	–
21	B2016+28	71 ± 36	260 ± 100* (102.5 MHz)	0.92
22	B2110+27	105 ± 53	130 ± 30* (102.5 MHz)	0.15
23	J2307+2225	2.7 ± 2	30 ± 13* (102.5 MHz)	1.71
24	B2310+42	21 ± 11	110 ± 90* (102.5 MHz)	1.17
25	B2315+21	27 ± 14	100 ± 30* (102.5 MHz)	0.93
				$m = 1.42$ $\sigma = 0.87$

*Malofeev et al. (2000).
**Izvekova et al. (1981).

Table 4. Upper limits (at 4σ) of flux densities of non-detected pulsars.

N	Pulsar	Flux (mJy) (25 MHz)	*N*	Pulsar	Flux (mJy) (25 MHz)
1	J0006+1834	≤75	18	J1549+2113	≤90
2	J0137+1654	≤68	19	J1740+1000	≤130
3	J0152+0948	≤74	20	J1817−0743	≤210
4	B0301+19	≤66	21	J1832+0029	≤240
5	B0410+69	≤92	22	J1848+0647	≤210
6	J0459−0210	≤83	23	J1917+0834	≤180
7	B0609+37	≤81	24	B1916+14	≤160
8	B0656+14	≤85	25	J1918+1541	≤150
9	B0655+64	≤69	26	B1918+26	≤120
10	B0820+02	≤69	27	J2015+2524	≤120
11	B0917+63	≤59	28	B2020+28	≤125
12	J0943+22	≤44	29	B2021+51	≤106
13	J0947+27	≤43	30	J2151+2315	≤83
14	J1046+0304	≤78	31	J2215+1538	≤82
15	J1246+22	≤58	32	J2248−0101	≤81
16	J1313+0931	≤100	33	J2253+1516	≤78
17	J1503+2111	≤87	34	J2346−0609	≤95

individual pulses with high time resolution. They were not considered in the calculation of the mean value of $\alpha_{\mathrm{SC25-1000}}$.

The obtained average value of $\alpha_{\mathrm{SC25-1000}}$ (4.01) and its standard deviation (0.24) are close to those obtained by Kuzmin, Losovskii & Lapaev (2007) (4.1 ± 0.3). However, estimates of the power-law index $\alpha_{\mathrm{SC25-1000}}$ for many pulsars in Table 5 appear to be significantly lower than the index corresponding to a Kolmogorov distribution (4.4).

4 DISCUSSION

Not only the number of detected pulsars but also their observed peak S/N values (after accurate DM determination) show promising prospects in searching for pulsed and transient sources in the decametre range. Thus, we hope to discover periodic radio sources as well as aperiodic radio emissions.

4.1 Fraction of pulsars available for detection in the decametre range

The efficiency of the decametre survey of pulsed sources at UTR-2 depends directly on the relative fraction of pulsars available for observations at low frequencies.

The sensitivity of the survey is not the same for different sky regions. It depends first on the zenith angle of the source, and thus on the effective area of the telescope, and secondly on the Galactic background in the selected direction. Fig. 6 shows the 4σ upper limits (see Table 4) corresponding to non-detected pulsars as a function of hour angle (upper panel) and declination (right panel). The area close to the Galactic Centre (RA=17h45m) is clearly distinguishable. Here, both the effect of high temperature of the Galactic background and low δ of sources reduce the sensitivity simultaneously. In the anticentre direction, the impact of intense galactic noise is partially compensated for by the small zenith angles of the pulsars in that area observed from UTR-2. Fig. 6 also gives the ratio $A_{\mathrm{e}}/A_{\mathrm{e\,max}}$. The number of non-detected pulsars does not depend strictly on the zenith angle. The left lower panel shows the comparison between the coordinates of the detected (crosses) and non-detected pulsars (diamonds with normalized values of the

Table 5. Pulse width $W_{0.5}$, $W_{0.1}$ at the level of 0.5 and 0.1 of the maximum intensity at frequencies of 20 and 25 MHz, with the characteristic scattering time in the decametre range τ_{SC25} and the power-law index of the scattering parameters at these frequencies $\alpha_{SC25-1000}$.

N	Pulsar	$\nu = 25$ MHz		$\nu = 20$ MHz		τ_{SC}	α_{SC}
		$W_{0.5}$	$W_{0.1}$	$W_{0.5}$	$W_{0.1}$	(25 MHz)	(25–1000 MHz)
		(ms)	(ms)	(ms)	(ms)	(ms)	
1	B0031−07	79(10)	175(20)	103(10)	222(20)	44(10)	4.3
2	0051+0423	99(20)	191(40)	87(20)	127(40)	48(20)	–
3	B0053+47	111(10)	211(20)	115(10)	290(20)	55(10)	–
4	B0148−06	–	–	–	–	–	–
5	B0320+39	393(20)	703(40)	–	–	200(20)	3.91
6	B0329+54	246(20)	470(40)	–	–	145(20)	3.97
7	B0450+55	87(20)	195(40)	–	–	52(20)	3.93
8	B0809+74	70	151	75	151	2.5(5)*	–
9	B0823+26	97(10)	146(20)	–	–	37(10)	3.84
10	B0834+06	80(10)	180(20)	122(10)	246(20)	60(10)	4.25
11	B0919+06	151(10)	286(20)	183(10)	266(20)	60(10)	3.56
12	J0927+23	234(20)	532(40)	342(20)	592(40)	150(20)	–
13	B0940+16	258(20)	377(40)	191(20)	437(40)	60(20)	–
14	B0943+10	71	153	112	226	12(2)*	–
15	B0950+08	39	67	44	75	1(0.05)*	–
16	B1112+50	131(10)	246(20)	179(10)	457(20)	65(10)	4.18
17	B1133+16	81	157	96	181	6.5(5)*	–
18	J1238+21	147(20)	342(40)	222(20)	449(40)	72(20)	–
19	B1237+25	49(10)	159(20)	62(10)	192(20)	14(10)	4.0
20	B1322+83	36(20)	76(40)	–	–	15(10)	–
21	B1508+55	142(10)	338(20)	203(20)	280(20)	125(10)	3.79
22	B1530+27	135(20)	203(40)	–	–	20(10)	4.05
23	B1540−06	75(20)	132(40)	–	–	30(20)	4.06
24	B1604−00	61(20)	126(40)	100(20)	172(40)	56(20)	4.41
25	B1612+07	361(20)	616(40)	–	–	180(20)	4.38
26	B1633+24	132(20)	–	168(20)	323(40)	68(20)	–
27	J1741+2758	–	–	–	–	–	–
28	B1822−09	–	–	–	–	–	–
29	B1839+56	196(10)	409(20)	356(10)	516(20)	110(10)	3.76
30	J1851−0053	–	–	–	–	–	–
31	J1908+0734	52(20)	155(40)	–	–	30(20)	–
32	B1919+21	54(10)	107(20)	84(10)	156(20)	22(10)	3.95
33	B1929+10	31(10)	60(20)	37(10)	60(20)	–	–
34	B1944+17	73(20)	105(40)	–	–	20(10)	3.51
35	B1952+29	15(10)	–	–	–	–	–
36	B2016+28	99(20)	254(40)	–	–	70(20)	3.9
37	B2110+27	265(20)	354(40)	249(20)	452(40)	52(20)	3.92
38	J2307+2225	–	–	–	–	26(20)	–
39	B2310+42	95(20)	196(40)	–	–	40(20)	–
40	B2315+21	130(20)	294(40)	–	–	72(20)	4.18
							$m = 4.01$
							$\sigma = 0.24$

*Ulyanov & Zakharenko (2012).

upper limit of detection, as also plotted in the upper panel). Values in Fig. 6 were normalized by the 4σ level for PSR B0809+74 (dashed line). Fig. 6 shows that the sensitivity achieved by the observations for almost all non-detected pulsars is lower than that for PSR B0809+74 by 1.4–4.5 times. An increase in sensitivity can be achieved by increasing the integration time (currently 90 min to 6–8 h), which will allow us to reduce the detection threshold for sources of periodic pulsed radiation by a factor of 1.5–2.5. In this case, the sensitivity for more than 25 pulsars of our sample would be better than the sensitivity reached for PSR B0809+74 after 90 min integration.

To analyse the possibility of detecting more pulsars by increasing the sensitivity, we have plotted a histogram (Fig. 7) of the 400-MHz fluxes (taken from Manchester et al. 2005) of the pulsars that we detected. The number of pulsars detected in the decametre range (solid line) and all pulsars from the sample (dash–dotted line) are displayed on a linear scale in the left panel of Fig. 7 and on a logarithmic scale in the right panel.

Of course, the flux at 400 MHz cannot be directly related to the flux at 25 MHz because of different spectral indices and propagation effects in the interstellar medium. This is illustrated by the non-detection of the pulsar B2021+51, which nevertheless has a high flux density at 400 MHz (77 mJy). In spite of these particular cases, there is a clear relation between the fraction of detected pulsars and their flux (lower panel of Fig. 7). A sensitivity increase by one step of the histogram ($10^{0.5}$ times) approximately doubles the number of detected pulsars at low flux densities. Thus our expected sensitivity increase by a factor of 1.5–2.5 should allow us to detect about 10–15 pulsars from the remaining 34 non-detected targets of our initial sample.

The second factor that significantly reduces the amount of detected pulsars is interference. Numerous occurrences of low-intensity broad-band and narrow-band RFI are visible in the 'rotational phase–dispersion measure' plane, after dedispersion, pulse accumulation and integration in frequency, as lines with various slopes and intensities. Fig. 8 illustrates the impact of interference on the attempt to detect PSR J2215+1538. An increase in intensity is visible both at a DM close to that given in Manchester et al. (2005) and at a DM lower by 0.3 pc cm^{-3}. Moreover, the region of maximum intensity at higher DMs is non-homogeneous. This may be explained by the influence of weak broad-band interference, which has not been well removed by our cleaning procedures. Usually, when searching for the true DM of a pulsar observed in polluted conditions, we split the spectrum into different frequency bands. If the DM found in different bands (as in Fig. 3) is the same for all data sets, we regard it as certain (as it is the case, for example, for PSRs B1540−06, J1908+0734 and B1944+17 in Fig. 2a). For PSR J2215+1538, as well as a dozen other pulsars, there are two or more intensity maxima in the 'rotational phase–dispersion measure' plane for different frequency bands. We cannot decide between these various maxima from the presently available data. We therefore cannot conclude a reliable detection of these pulsars in the absence of additional measurements. Observations in more favourable interference conditions (the current observations were partially taken in the daytime, under non-optimal interference conditions) will probably allow us to detect a few more pulsars from our sample.

At a result of the present study, the fraction of pulsars with DM < 30 pc cm^{-3} detected in the decametre range is ≈55 per cent. With increased observing time and/or improved interference elimination, this value should rise up to 60–80 per cent.

Besides observing all sources in our sample, we have conducted several observations of pulsars with DM > 30 pc cm^{-3}. Fig. 9 shows the successful detection of PSR B0525+21 with a DM ≈50.9 pc cm^{-3}. The pulsar was observed during the daytime (local time in the range 16:50–18:20) and the observation was affected by powerful interference (cf. Fig. 3). The upper panel of Fig. 9 shows the normalized dynamic spectrum of the observation. The data contain a strong signal from the Crab nebula, entering through the telescope's side lobes.

Further processing was complicated not only by scintillation but also by the presence of broad-band noise in the range 27.5–30.5 MHz. However, in spite of the interference and the high temperature of the Galactic background in that field, the dual-peak profile of PSR B0525+21 can be recognized both in the average profile (lower left panel) and in the grey-scale 'rotational phase–dispersion measure' image (lower right panel). Obviously, the normalization by off-pulse radiation, which is heavily affected by the interference

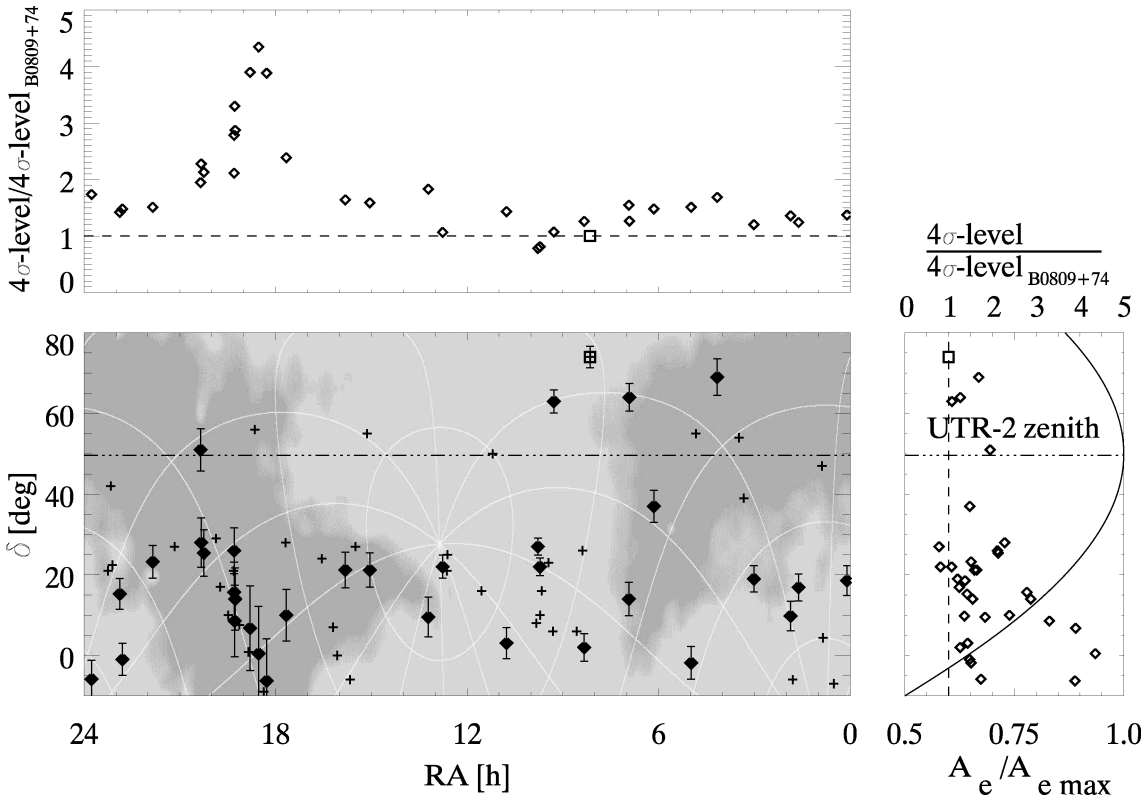

Figure 6. Upper limit on the flux density of non-detected pulsars (duty cycle 0.1, $\Delta\nu = 4$ MHz) as a function of hour angle (upper panel) and declination (right panel). The left lower panel shows, for comparison, the coordinates of the detected (crosses) and non-detected pulsars (diamonds with normalized values of the 4σ detection limit). Positions of the pulsars are overlapped on the northern sky map at 20 MHz (Sidorchuk et al. 2008). The peak in the upper panel corresponds approximately to the direction of the Galactic Centre. Detection limits were normalized by the 4σ level for PSR B0809+74 (open square and dashed line).

and probably by scintillations, gives an underestimated S/N value in this case. Flux estimates obtained with formula (2) are significantly underestimated as well. The same can be said about a few other pulsars, for which the off-pulse part of the period is also distorted by the influence of low-intensity RFI (Fig. 2a). In addition, due to the impact of interference, the fraction of excluded samples (narrow-band frequency channels and/or selected time intervals) was about 50 per cent for the case of PSR B0525+21. For this reason, the accuracy in the DM was much lower than for other pulsars (± 0.1 pc cm^{-3}). Moreover, the observational parameters ($\Delta t =$ 8 ms, $\Delta\nu = 4$ kHz) and the incoherent method of dispersion compensation resulted in a significant 'smearing' of the signal in the low-frequency channels (up to 170 ms, which is comparable to the broadening due to scattering). However, for the observation of more distant sources, observation parameters and methods of dispersion compensation can be optimized. The usage of the upper part of the operating frequency range, where the dispersion delay is smaller, makes it possible to detect more distant pulsars with only a small loss in sensitivity.

The detection of PSR B0525+21 indicates the high potential of the telescope and our processing algorithms, which can recover weak signals in the strong interference background of daytime observations. The estimation of the distance of PSR B0525+21 (Cordes & Lazio 2002) is ≈1.6 kpc and that of PSR B0138+59 (which we detected with a DM of 34.98 ± 0.02 pc cm^{-3}) is ≈2.2 kpc, PSR J1238+21 ≈2.2 kpc, PSR J1741+2758 ≈1.7 kpc, PSR B1839+56 ≈1.7 kpc and PSR B2110+27 ≈2.0 kpc. For this reason, we believe that, even though the fraction of detectable pulsars decreases at low frequencies, the detection volume for pulsars can still be important in the decametre wavelength range.

4.2 Impact of scattering in the ISM on the number of detected sources of pulsed radiation at low frequencies

Analysis of the data in the catalogue (Manchester et al. 2005) shows that, up to values of DM 60–70 pc cm^{-3}, pulsars have a scattering time constant that still allows their detection at low frequencies. For those pulsars, Fig. 10 shows the scattering time constant values normalized by the pulse period as a function of the DM. The rectangle on the picture denotes PSR B1822−09, successfully detected during our observations. We see that only 15–20 per cent of all pulsars with DM 0–70 pc cm^{-3} have a scattering time constant that is noticeably higher than that of PSR B1822−09.

In addition, our measurements (see Section 3), even if we consider them upper estimates, show that for a significant number of pulsars the exponent that describes the increase of characteristic scattering time is somewhat less than 4.4. This will hopefully allow us to detect more pulsars and transient sources in the decametre range. For a more accurate separation of the effects of pulse broadening and scattering, joint observations of LOFAR and UTR-2 covering the range 10–90 MHz are required.

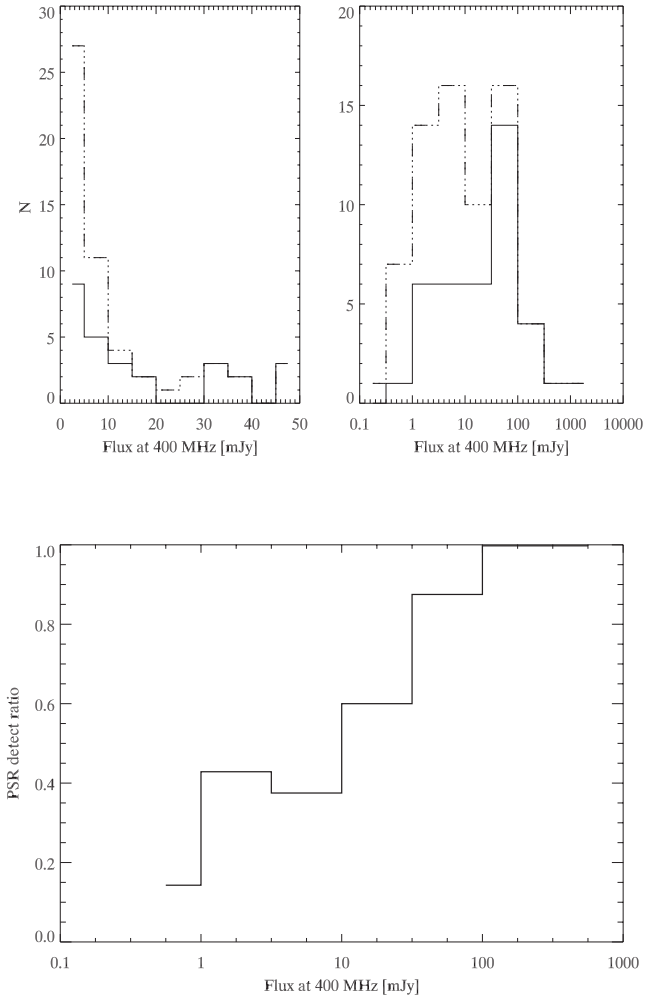

Figure 7. Distribution histograms of detected pulsars (solid line) and of the full sample (dashed line) on a linear scale (left panel) and a logarithmic one (right panel). The bottom panel shows the ratio of the detected pulsars to the entire number in the sample.

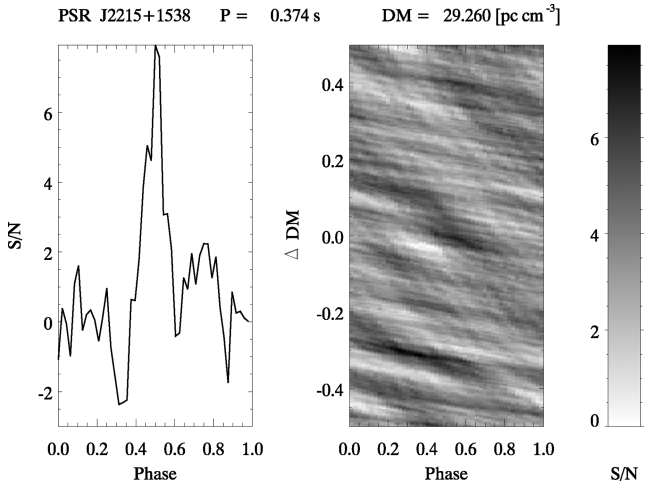

Figure 8. Impact of interference while attempting to detect the pulsar J2215+1538. Characteristic intensity increases are seen for both a DM close to the one given in Manchester et al. (2005) and a DM lower by 0.3 pc cm^{-3}.

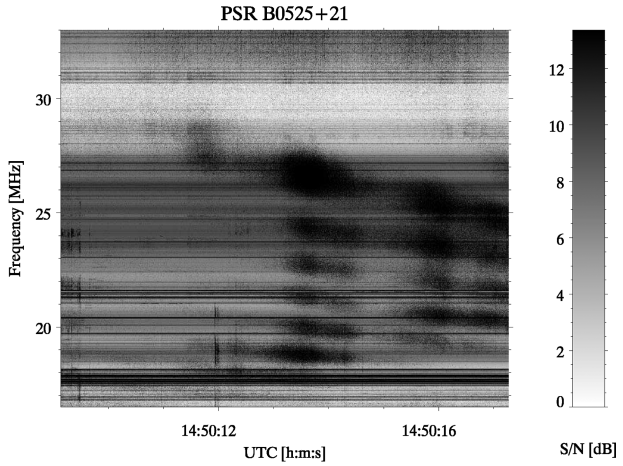

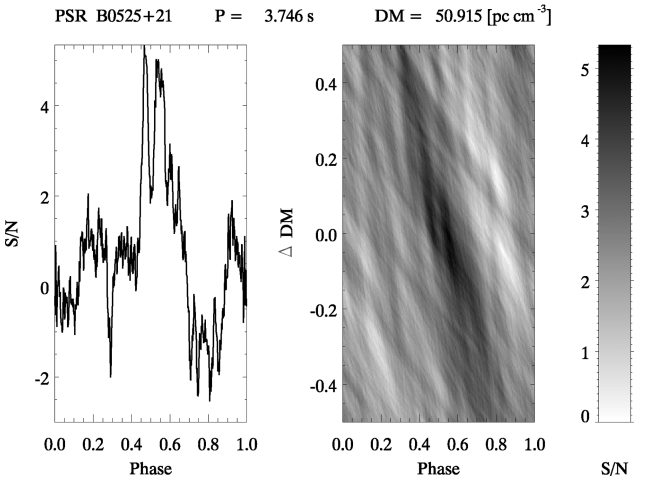

Figure 9. Normalized dynamic spectrum of the observation of PSR B0525+21 (upper panel). The data contain a strong signal from the Crab nebula, entering through the telescope's side lobes. The lower panel shows the result of the successful detection of the pulsar at DM ≈50.9 pc cm^{-3}.

4.3 On the possibility of detecting new sources due to growth of the beaming fraction

The main factor that could lead to an increase in the number of detected pulsars in the decametre range is the intrinsic widening of the pulse profile (Cordes 1978; Thorsett 1991). As mentioned above, Cordes (1978) found a pulse width $\propto \nu^{-0.25}$. A similar relation for pulse component separation was obtained in Thorsett (1991). The distance between the components Θ is described by the formula

$$\Theta = Af^{-\alpha_c} + \Theta_0, \quad (4)$$

where A, α_c and Θ_0 are parameters specific for each pulsar. For pulsars listed by Thorsett (1991), the exponent in this equation is $0.34 \leq \alpha_c \leq 1.08$.

Intrinsic pulse widening was extrapolated for frequencies of 25 and 100 MHz using both the parameters and pulsars from Thorsett (1991). In Fig. 11 these data are indicated by bold crosses. We calculated that the relative pulse widening between 25 and 100 MHz is in the range 1.3–2.6.

Using the data from Table 5, we calculated the values of pulse widening for pulsars detected with a sufficient S/N (Table 2) for

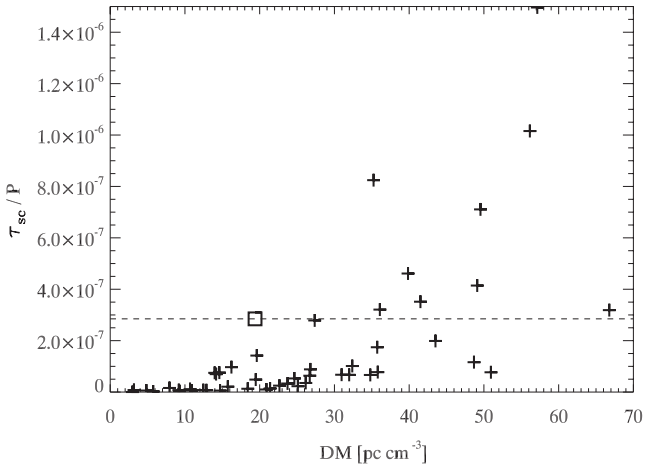

Figure 10. Scattering time constant values at 1 GHz (Manchester et al. 2005) normalized by the period of each pulsar as a function of the DM. The rectangle denotes the pulsar B1822−09, successfully detected during our observations. Only 15–20 per cent of all pulsars have a scattering time constant high enough potentially to hinder their detection at low frequencies.

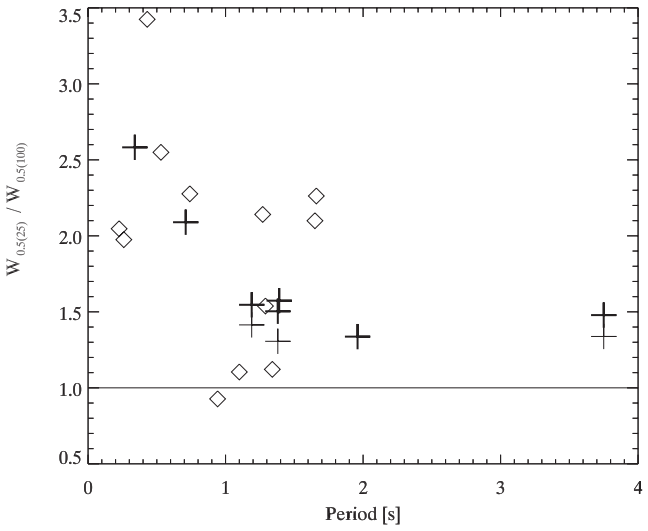

Figure 11. Relative expansion of the FWHM profile between frequencies 25 and 100 MHz as a function of period. Bold crosses are extrapolated from the parameters obtained in Thorsett (1991) for pulsars B0301+19, B0329+54, B0525+21, B1133+16, B1237+25, B2020+28 and B2045−16. Thin crosses correspond to pulsars in common in Thorsett (1991) and in the present study (B0525+21, B1133+16, B1237+25), while diamonds denote the other pulsars from our study.

the same frequencies 25 and 100 MHz. To do this, we estimated and subtracted the broadening due to scattering in the ISM from the $W_{0.5}$ width. As we consider that upper estimates were obtained for τ_{SC}, the corrected values of $W_{0.5}$ might be underestimated. In Fig. 11 these estimates from UTR-2 measurements only are denoted by diamonds and thin crosses. The latter correspond to pulsars also listed in Thorsett (1991) (PSRs B0525+21, B1133+16 and B1237+25), whereas diamonds denote the other pulsars from our study. Our estimates for the three coincident pulsars are somewhat lower (by 5–15 per cent) than the relative width obtained in Thorsett (1991), consistent with our assumptions about underestimating the corrected pulse width at low frequencies. However, for almost all pulsars we obtain a substantial pulse widening (on average a factor of 1.8, with a standard deviation of 0.7).

Except for a few rare cases, for which the pulse profile becomes narrower towards low frequencies (see Fig. 11), most profiles broaden towards low frequencies, which suggests that the number of visible pulsed and transient sources should increase at low frequencies. In the present study, 40 pulsars with DM 0–30 pc cm^{-3}, $\delta = -10$–90° and period >0.1 s were detected. We confirmed that the beaming fraction increases at low frequencies (Fig. 11), so at lower frequencies the pulsar beam will more likely cross Earth. If we estimate that fraction as 1.5 (the beam at 25 MHz is 50 per cent wider than at 100 MHz), we can expect the detection of nearly 20 new pulsed sources that are not visible at higher frequencies.

5 CONCLUSIONS

From the full sample of sources with declination above -10°, period longer than 0.1 s and DM less than 30 pc cm^{-3}, we have detected at UTR-2 the radio emission of 40 pulsars, of which 30 have never been detected in the decametre range previously. For most of the detected pulsars, the DM values have been considerably refined and the values of the flux density at 25 ± 2 and 20 ± 2 MHz (or in the band 20–32 MHz) have been obtained for the first time. Spectral indices α_{20-25} and $\alpha_{25-\nu_{max}}$ have been calculated for those pulsars, for which the flux data at metre wavelengths are taken from the literature. The pulse width at 50 per cent and 10 per cent levels relative to the maximum intensity has been measured. We have estimated for the first time the high detection fraction in the decametre range (∼55 per cent) and we have demonstrated that the characteristics of pulsar radio emission can be determined with high accuracy. On average, the values of $\alpha_{SC25-1000}$ are smaller than 4.4, which favours the discovery of pulsars with DMs up to 70 pc cm^{-3}. As a confirmation, the pulsars B0138+59 and B0525+21 have been detected with DM ≈ 34.9 pc cm^{-3} and ≈50.9 pc cm^{-3}, respectively. An upper limit for $\alpha_{SC25-1000}$ (the spectral index of the scattering time-scale τ_{SC25}) has been obtained. Values of the intrinsic widening of the pulsar profiles at low frequencies have been estimated, which agree well with the few known from the literature. This widening of the average pulse profile of most pulsars at low frequencies provides unique information about the nearest sources of repeating and, in particular, transient radiation (RRAT, giant pulses of pulsars). The present work has shown for the first time that in the decametre range the detection and study of the majority of nearby slow pulsars is possible and that we can expect the detection of new sources of transient and pulsed radiation, most of which cannot be observed at higher frequencies. We take this as motivation to conduct a full survey of the northern sky at low frequencies, aimed at searching for pulsars and transient sources in the Galactic neighbourhood. Such a survey is both useful, required and achievable.

ACKNOWLEDGEMENTS

This work was partly supported by ANR programme NT05-1-42530 'Radio-Exopla' and pursued in the frame of the NASU-CNRS PICS program 'Development of LF radioastronomy with ultrahigh sensitivity and resolution' (Grant 1.33.11). This work is also supported by the National Academy of Sciences of Ukraine and the Russian Foundation for Basic Research (Ukrainian–Russian Project 2012). We thank the authors of the ATNF Pulsar Catalogue (http://www.atnf.csiro.au/people/pulsar/psrcat/: Manchester et al. 2005). We thank the referee for some very useful comments.

REFERENCES

Abranin E. P., Bruck Yu. M., Zakharenko V. V., Konovalenko A. A., 2001, Experimental Astron., 11, 85
Backer D. C., Hama S., Hook S. V., Foster R. S., 1993, ApJ, 404, 636
Bhat R. N. D. et al., 2007, ApJ, 665, 618
Braude S. Ya., Megn A. V., Sodin L. G., 1978, Antennas, Vol. 26. Sviaz', Moscow, p. 3
Braude S. Ya., Rashkovsky S. L., Sidorchuk K. M., Sidorchuk M. A., Sokolov K. P., Sharykin N. K., Zakharenko S. M., 2002, Ap&SS, 280, 235
Bruck Yu., 1970, Izv. Vuzov Radiophysica, 13, 1814
Bruck Yu., 1987, Aust. J. Phys., 40, 861
Bruck Yu., Ustimenko B., 1973, Nat, 242, 58
Bruck Yu., Ustimenko B., 1976, Nat, 260, 766
Bruck Yu., Ulyanov O., Ustimenko B., 1986, Sov. Astron. J., 63, 970
Caswell J. L., 1976, MNRAS, 177, 601
Cordes J. M., 1978, ApJ, 222, 1006
Cordes J. M., Lazio T. J. W., 2002, preprint (astro-ph/0207156)
Cordes J. M., McLaughlin M. A., 2003, ApJ, 596, 1142
Deshpande A., Radhakrishnan V., 1992, JA&A, 13, 151
Deshpande A. A., Radhakrishnan V., 1994, JA&A, 15, 329
Diehl R. et al., 2006, Nat, 439, 45
Ellis G. R. A., 1982, Aust. J. Phys., 35, 91
Hassall T. E. et al., 2012, A&A, 543, A66
Hewish A., Bell S. J., Pilkington J. D. H., Scott P. F., Collins R. A., 1968, Nat, 217, 709
Hobbs G., Lyne A. G., Kramer M., Martin C. E., Jordan C., 2004, MNRAS, 353, 1311
Izvekova V. A., Kuzmin A. D., Malofeev V. M., Shitov Iu. P., 1981, Ap&SS, 78, 45
Karuppusamy R., Stappers B. W., Serylak M., 2011, A&A, 525, A55
Keane E. F., Kramer M., 2008, MNRAS, 391, 2009
Kondratiev V. I., McLaughlin M. A., Lorimer D. R., Burgay M., Possenti A., Turolla R., Popov S. B., Zane S., 2009, ApJ, 702, 692
Konovalenko A. A. et al., 2011, in Rucker H. O., Kurth W. S., Louarn P., Fischer G., eds, Planetary Radio Emissions VII. Austrian Academy of Sciences Press, Vienna, p. 521
Kozhin R., Vynogradov V., Vavriv D., 2007, in Kostenko A., Nosich A., Yakovenko V., eds, The Sixth International Kharkov Symposium on Physics and Engineering of Microwaves, Millimeter and Submillimeter Waves and Workshop on Terahertz Technologies, MSMW'07, Kharkiv, Ukraine, p. 736
Kuzmin A. D., Losovskii B. Ya., Lapaev K. A., 2007, Astron. Rep., 51, 615
Lecacheux A., Rosolen C., Clerc V., Kleewein P., Rucker H. O., Boudjada M., van Driel W., 1998, in Phillips T. G., ed., Proc. SPIE Vol. 3357, Advanced Technology MMW, Radio, and Terahertz Telescopes. SPIE, Bellingham, p. 533
Malofeev V. M., Malov O. I., Shchegoleva N. V., 2000, Astron. Rep., 44, 436
Malofeev V. M., Malov O. I., Teplykh D. A., 2005, Ap&SS, 308, 211
Manchester R. N., Hobbs G. B., Teoh A., Hobbs M., 2005, AJ, 129, 1993
Maron O., Kijak J., Kramer M., Wielebinski R., 2000, A&AS, 147, 195
McLaughlin M. A. et al., 2006, Nat, 439, 817
Milogradov-Turin J., Smith F. G., 1973, MNRAS, 161, 269
Phillips J. A., Wolszczan A., 1989, ApJ, 344, L69
Phillips J. A., Wolszczan A., 1992, ApJ, 385, 273
Popov M. V. et al., 2006, Astron. Rep., 50, 562
Reyes F., Carr T. D., Oliver J. P., May J., Bitran M., Aparici J., 1981, Rev. Mex. Astron. Astrofis., 6, 219
Roger R. S., Costain C. H., Landecker T. L., Swerdlyk C. M., 1999, A&AS, 137, 7
Ryabov V. B., Vavriv D. M., Zarka P., Ryabov B. P., Kozhin R., Vinogradov V. V., Denis L., 2010, A&A, 510, A16
Sidorchuk M. A., Ulyanov O. M., Shepelev V. A., Mukha D. V., Brazhenko A. I., Vashchishin R. V., Frantzusenko A. V., 2008, Scientific Workshop – Astrophysics with E-LOFAR, available at: http://www.hs.uni-hamburg.de/DE/Ins/Lofar/lofar_workshop/poster_abstracts.html
Stappers B. W. et al., 2011, A&A, 530, 80
Taylor J. H., Manchester R. N., Lyne A. G., 1993, ApJS, 88, 529
Thorsett S., 1991, ApJ, 377, 263
Ulyanov O., Zakharenko V., 2012, Astron. Rep., 56, 417
Ulyanov O. M., Zakharenko V. V., Konovalenko A. A., Lecacheux A., Rosole C., Rucker H. O., 2006, Radiofizika and Radioastronomia, 11, 113
Ulyanov O. M., Deshpande A., Zakharenko V. V., Asgekar A., Shankar U., 2007, Radiofizika and Radioastronomia, 12, 5
Ulyanov O., Zakharenko V., Bruck Yu., 2008, AZh, 85, 1
Zakharenko V. V., Nikolaenko V. S., Ulyanov O. M., Motiyenko R. A., 2007, 12, 233
Zakharenko V., Markova A., Vasylieva I., 2011, Radio Phys. Radio Astron., 2, 15

APPENDIX A: PULSAR PROFILES

Average profiles of 15 pulsars with high S/N (Fig. A1) over bands 23–27 MHz (bold curve) and 18–22 MHz (thin curve) and average profiles of 25 pulsars with low S/N (Fig. A2) over the band 20–32 MHz (or 16.5–33.0 MHz for PSRs B0148−06, J1238+21, B0940+16 and B1822−09), along with grey-scale images of the 'rotational phase–dispersion measure' plane for each pulsar over the band 16.5–33.0 MHz (both Figs A1 and A2).

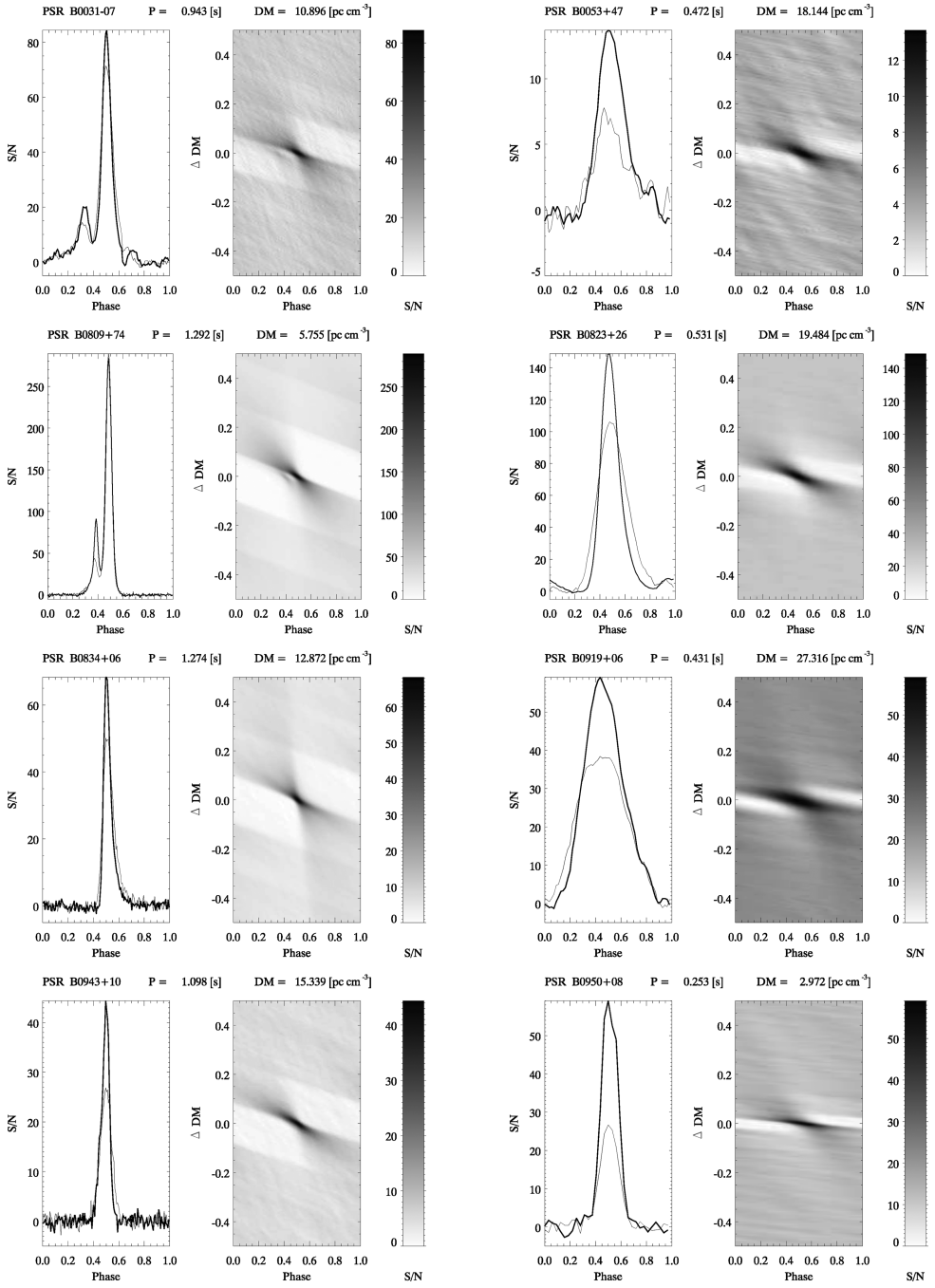

Figure A1. Average profiles of 15 pulsars with high S/N over the bands 23–27 MHz (bold curve) and 18–22 MHz (thin curve).

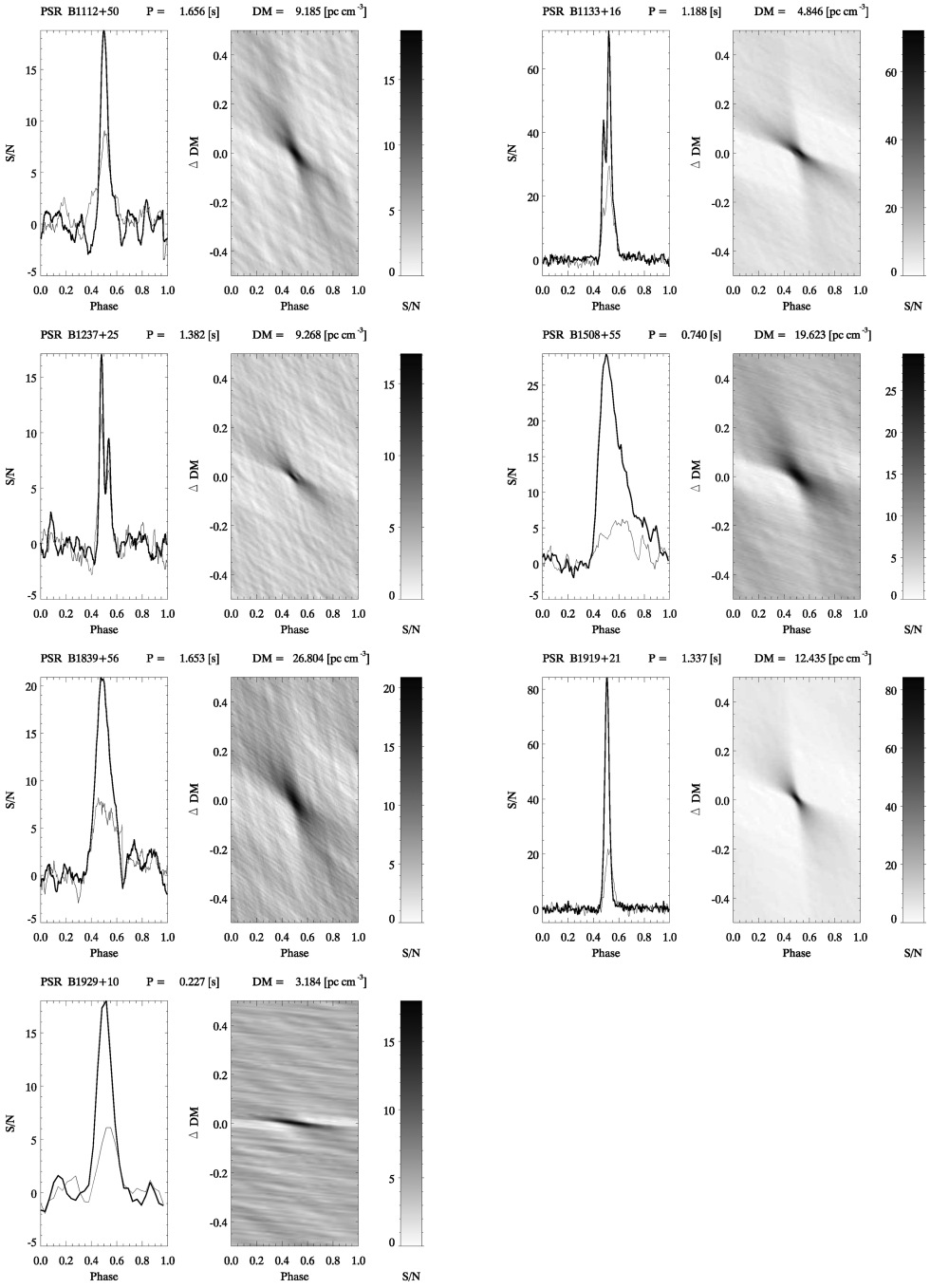

Figure A1 – *continued*

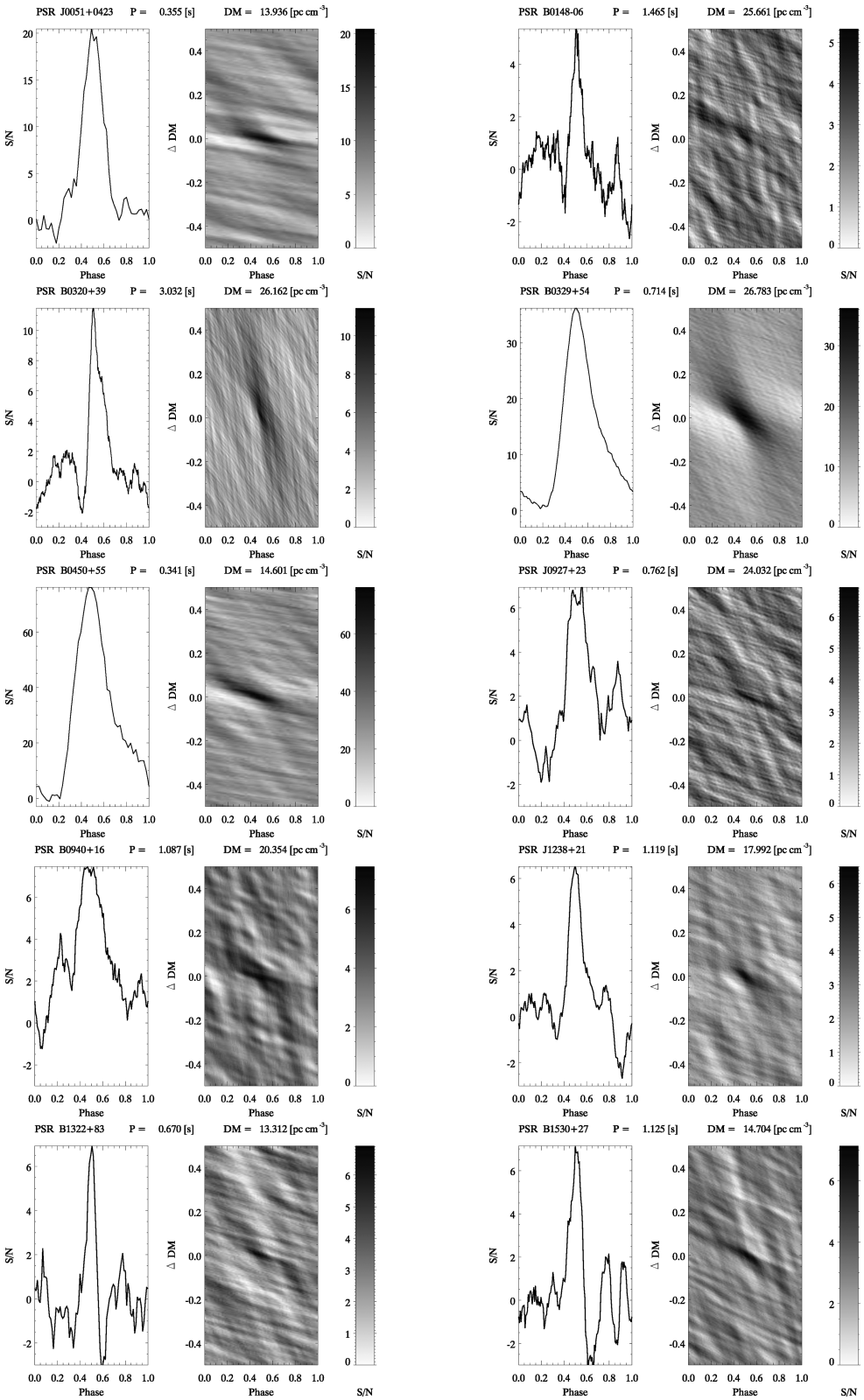

Figure A2. Average profiles of 25 pulsars with low S/N over the band 20–32 MHz (or 16.5–33.0 MHz for PSRs B0148−06, J1238+21, B0940+16 and B1822−09).

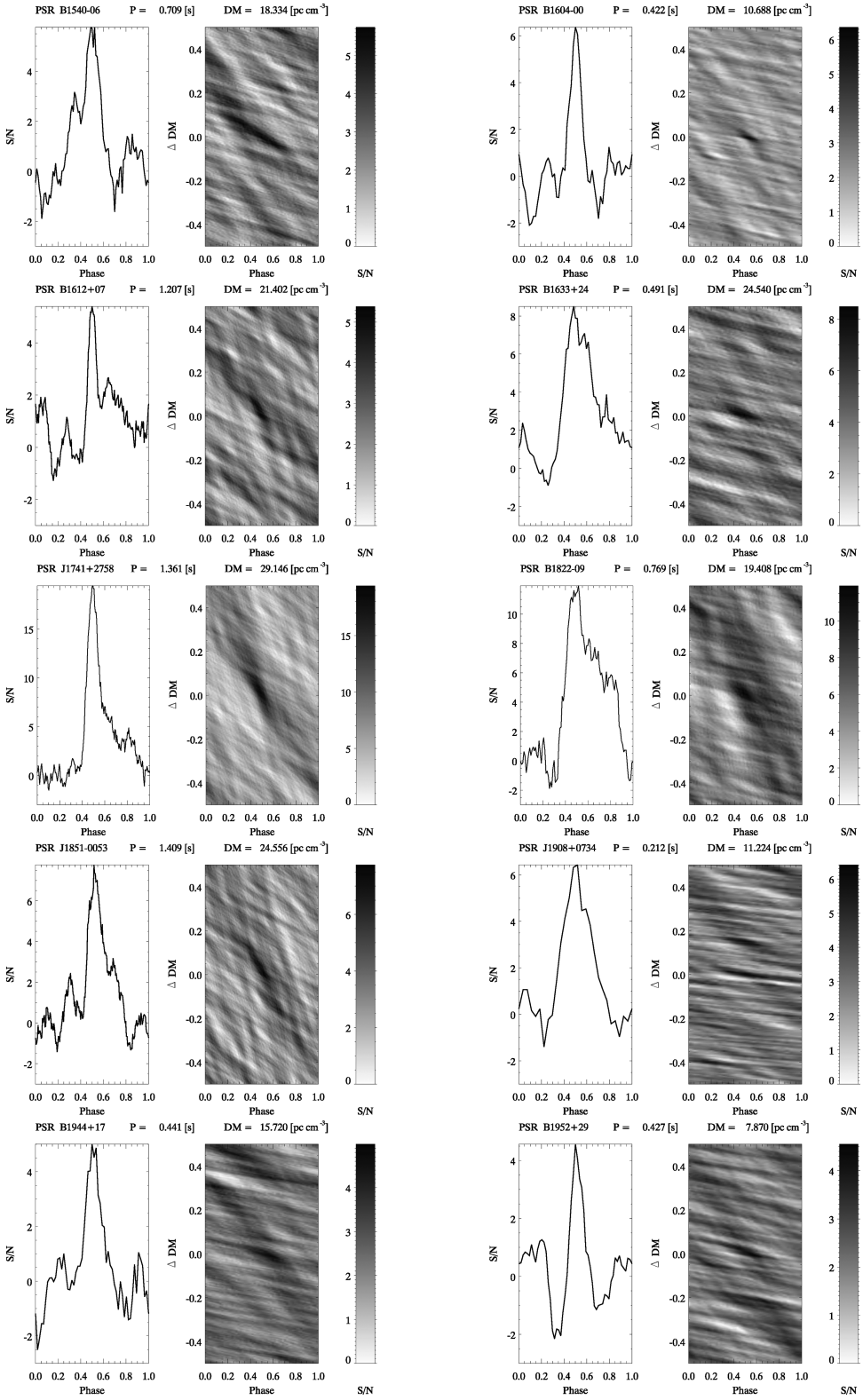

Figure A2 – *continued*

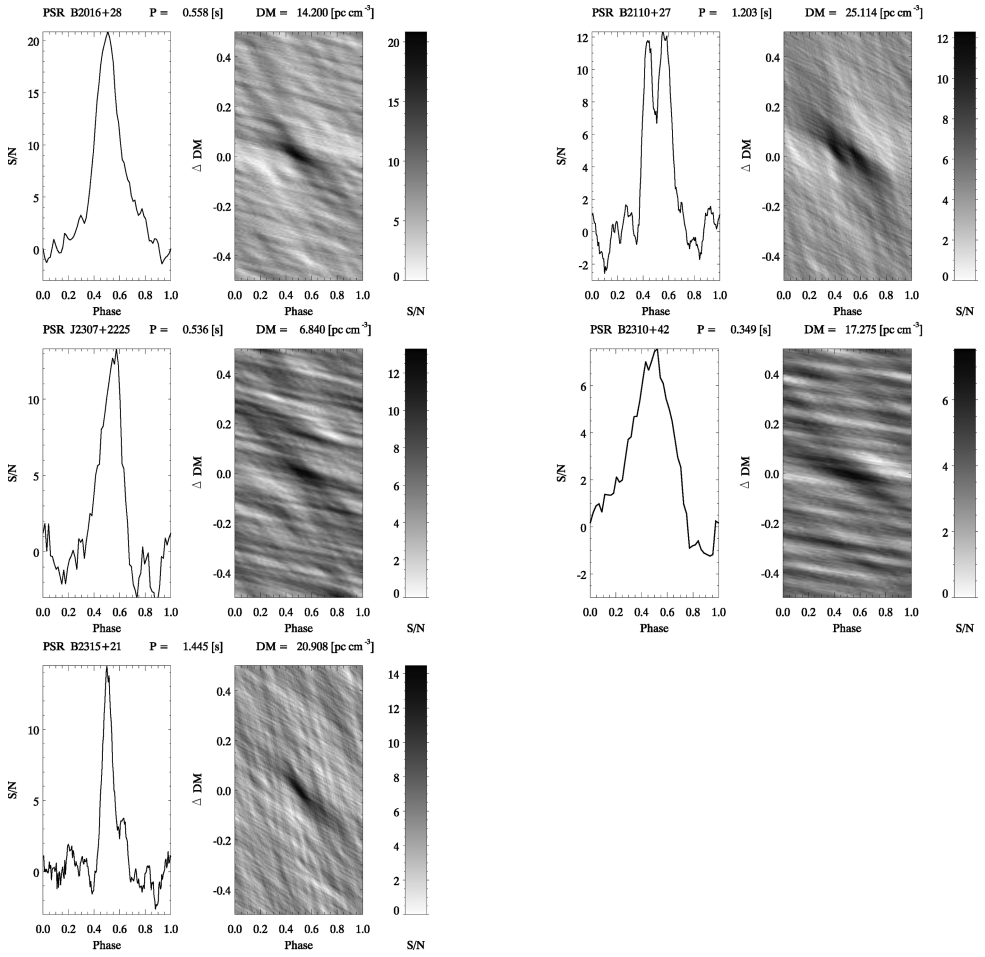

Figure A2 – *continued*

This paper has been typeset from a TEX/LATEX file prepared by the author.

The modern radio astronomy network in Ukraine: UTR-2, URAN and GURT

A. Konovalenko[1], L. Sodin[1], V. Zakharenko[1], P. Zarka[2], O. Ulyanov[1], M. Sidorchuk[1], S. Stepkin[1], P. Tokarsky[1], V. Melnik[1], N. Kalinichenko[1], A. Stanislavsky[1], V. Koliadin[1], V. Shepelev[1], V. Dorovskyy[1], V. Ryabov[3], A. Koval[1], I. Bubnov[1], S. Yerin[1], A. Gridin[1], V. Kulishenko[1], A. Reznichenko[1], V. Bortsov[1], V. Lisachenko[1], A. Reznik[1], G. Kvasov[1], D. Mukha[1], G. Litvinenko[1], A. Khristenko[1], V.V. Shevchenko[1], V.A. Shevchenko[1], A. Belov[1], E. Rudavin[1], I. Vasylieva[1], A. Miroshnichenko[1], N. Vasilenko[1], M. Olyak[1], K. Mylostna[1], A. Skoryk[1], A. Shevtsova[1], M. Plakhov[1], I. Kravtsov[1], Y. Volvach[1], O. Lytvinenko[1], N. Shevchuk[1], I. Zhouk[1],V. Bovkun[1], A. Antonov[1], D. Vavriv[1], V. Vinogradov[1], R. Kozhin[1], A. Kravtsov[1], E. Bulakh[1], A. Kuzin[1], A. Vasilyev[1], A. Brazhenko[4], R. Vashchishin[4], O. Pylaev[4], V. Koshovyy[5], A. Lozinsky[5], O. Ivantyshin[5], H.O. Rucker[6], M. Panchenko[6], G. Fischer[6], A. Lecacheux[2], L. Denis[7], A. Coffre[7], J.-M. Grieβmeier[8], M. Tagger[9], J. Girard[9], D. Charrier[10], C. Briand[2], G. Mann[11]

[1] Institute of Radio Astronomy, National Academy of Sciences of Ukraine, Kharkiv, Ukraine
[2] LESIA, Observatoire de Paris, CNRS, France
[3] Future University-Hakodate, 116-2 Kamedanakano-cho, Hakodate 041-8655, Japan
[4] Poltava gravimetrical observatory of Institute of geophysics, National Academy of Sciences of Ukraine, Poltava, Ukraine
[5] Karpenko Physiko-Mechanical Institute, National Academy of Sciences of Ukraine, Lviv, Ukraine
[6] Space Research Institute, Austrian Academy of Sciences, Graz, Austria
[7] USN, Nançay, France
[8] LPC2E, Orléans, France
[9] CEA/AIM, Saclay, France
[10] Subatech, Nantes, France
[11] Leibniz-Institut für Astrophysik Potsdam, Potsdam, Germany

Corresponding authors: yerin.serge@gmail.com phone +380 97 368 21 29, fax +380 57 706 14 15
akonov@rian.kharkov.ua, +38 057 706 14 12

Abstract

The current status of the large decameter wavelength radio telescope UTR-2 (Ukrainian T-shaped Radio telescope) together with its VLBI system called URAN are described in detail. By multi-faceted modernization of these instruments through the implementation of new information technologies based on novel analog and digital devices, the UTR-2 observational capabilities have been substantially enhanced by introducing new techniques. The total effective area of UTR-2 with URAN arrays achieves 200 000 sq. m, with the observational bandwidth of 24 MHz (within the frequency range 8 – 32 MHz) and frequency-time resolutions down to 4 kHz and 0.5 msec, respectively. Depending on the time-frequency resolution and confusion effects, the UTR-2 sensitivity varies from a few Jy to several mJy, and the angular resolution lies in the range between ~ 30 angular minutes (within the single antenna array) to several microseconds (in the VLBI mode). In the framework of national and international research projects run in recent years many new astonishing results in the study of Solar system objects, Galaxy and Metagalaxy have been obtained. In order to extend the frequency range of observations to 8 – 80 MHz and enlarge the dimensions of the UTR-2 array, the new sub-array system GURT (Giant Ukrainian Radio Telescope) is now under construction. The new radio telescope systems described herein can be used in a synergy with other existing low-frequency arrays such as LOFAR, LWA, NenuFAR as well as a part of ground-based support for space-based instruments.

Key words: ***radio astronomy, radio telescope, antenna arrays, space research.***

Acknowledgements

The authors are thankful to their numerous colleagues for participation in instruments development and observations. All investigations have been carried out with maximum and thorough support from a number of national and international programs and foundations, especially National Academy of Sciences of Ukraine, CNRS (Centre national de la recherche scientifique), France, Austrian Academy of Sciences (OAW) and others.

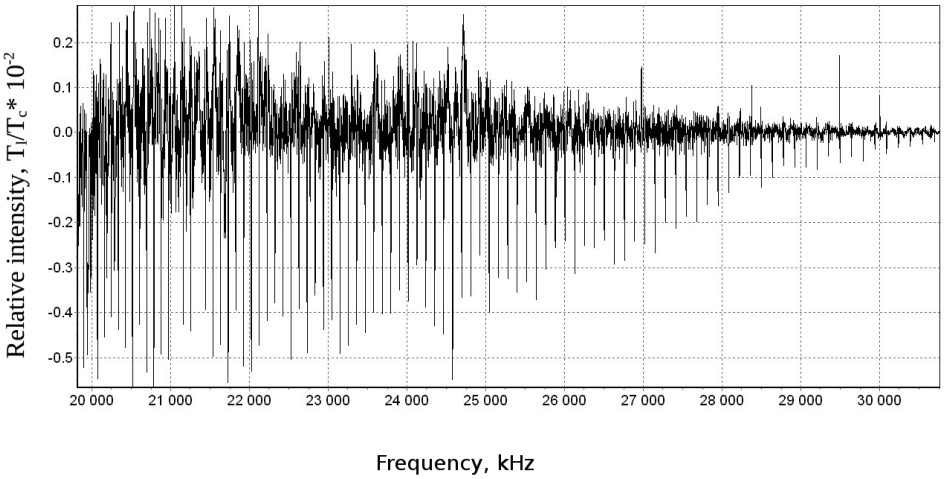

Fig. 14 Carbon RRLs towards Cas A, measured with the West arm of the UTR-2 array.

3.6 Detection of individual pulses from pulsars and their fine time structure at decameter waves

The discovery of pulsars, one of the brightest objects in radio astronomy in the last 50 years, coincided with the final stage of constructing the UTR-2 (West arm). The significance of the discovery as well as availability of the high-level telescope system motivated the initiation of the research program that has progressively been covering larger and larger diversity of objects, emitting the short-duration signals. The first low frequency detection of regular (Bruck and Ustimenko 1973, Bruck and Ustimenko 1976) and giant (Popov et al. 2006) pulses from pulsars as well as the discovery of anomalously intense pulses (Ulyanov et al. 2006) occurred at UTR-2 at the end of 90-s. A pulsar census in the 16.5 – 33.0 MHz frequency band has been carried out on UTR-2, leading to re-detection of 40 known pulsars with DM < 30 pc·cm^{-3} (Zakharenko et al. 2013).

Figure 15 shows the average pulse profile (two periods) of the pulsar PSR B0809+74, averaged over 1.5 hours of observational time. The Signal-to-Noise ratio (SNR) reaches the value about 350 at the time resolution of 8 msec in the 16.5 – 33.0 MHz band. Below the average pulse profile in Fig. 15 we plot the average intensity versus frequency. Very long dispersion delays even for the nearest pulsars (hundreds and thousands of seconds between the frequencies separated by several MHz in the band between 8 and 33 MHz) illustrated by the dynamic spectrum shown in the top right panel require the accurate compensation, and hence, precise knowledge of the dispersion measure value. It can be determined in the decameter range with the highest possible precision, since the peak position in the average pulse profile is very sensitive even to the slightest variation in the dispersion measure value.

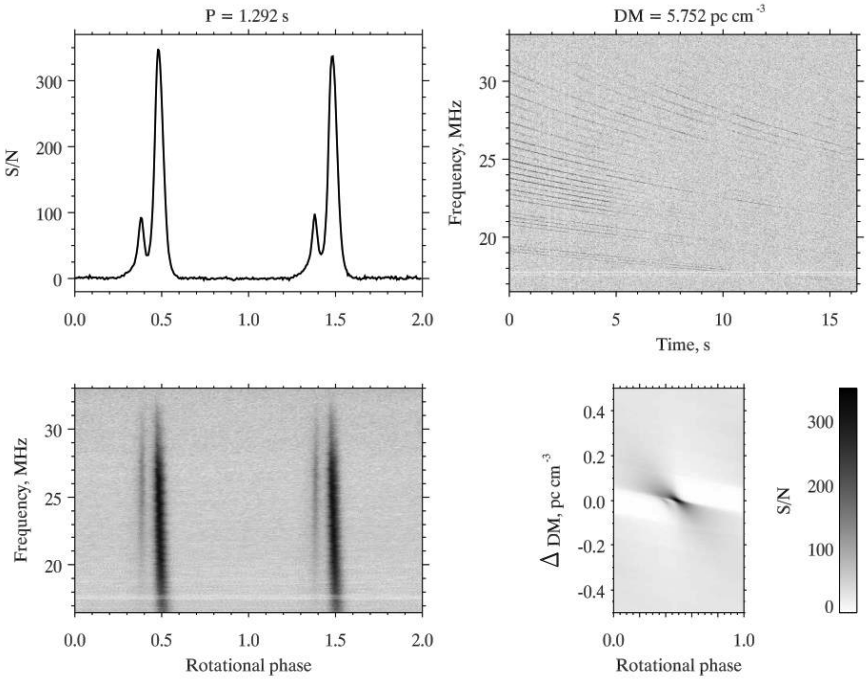

Fig. 15 Observations of pulsar B0809+74. The left sub-panels show an average pulsar profile (upper) and its frequency dependence (lower). Upper right panel: the normalized dynamic spectrum with individual pulses (after interference mitigation). Lower right panel: intensity of average pulse profile versus deviation in dispersion measure from the correct value.

3.7 Observations of polarization effects in low-frequency pulsar radio emission

The rotation of the emission polarization plane caused by Faraday effect is detected in the high frequency part of the observational bandwidth for the pulsar PSR J0243+6257. This is illustrated in the top panel of Figure 16 for a single pulse dynamic spectrum. The same effect was also detected for the pulsar PSR J0950+08 in the middle and low frequency part of the dynamic spectrum calculated for a single pulse (see Figure 16 bottom panel). This effect appears as frequency dependent intensity modulation in a dynamic spectrum (striped structure of spectrum) and it is due to the rotation of the emission polarization plane during propagation of the elliptically polarized wave through weakly anisotropic interstellar plasma (Zheleznyakov 1997, Ulyanov et al. 2013, Ulyanov et al. 2014, Ulyanov et al. 2013). Comparison of the individual pulse profiles obtained in different frequency ranges reveals another effect of propagation. It is scattering of radio emission by the electron density inhomogeneities in the medium. The interstellar medium thus contributes the main part to this effect. Scattering leads to the pulse broadening and appearance of the "tail", which increases with a decrease in frequency. More evidently this effect is visible for the individual pulses of the pulsar PSR J0243+6257 within four different frequency sub-bands (see Figure 16 top panel, right). The scattering time constant which is defined as the width of the "tail" at the 25% level from the maximum intensity is inversely proportional to the frequency raised into power of four.

These properties of the pulsar radio emission become more evident (with maximal contrast) in the decameter range compared to higher observational frequencies. This makes our observations an ideal probe of the interstellar medium, in particular for identifying most important phenomena in such areas of high interest as pulsar magnetospheres and fast pulsar plasma.

DATA PROCESSING PIPELINE FOR DECAMETER PULSAR/TRANSIENT SURVEY

Vasylieva I.Y.[1,2], Zakharenko V.V.[1], Zarka P.[2], Ulyanov O.M.[1], Shevtsova A.I.[1], Seredkina A.A.[1]

[1] Institute of radio astronomy of NAS of Ukraine
Kharkiv, Ukraine
[2] LESIA, Observatory of Paris of CNRS of France
Meudon, France
iaroslavna.vasylieva@gmail.com

ABSTRACT. The study of the low-frequency radio sky at short time scales provides the insights into the nature of transient radio sources as well as gives a sensitive tool for interstellar medium sensing. The decameter survey of the northern sky is aimed to discover new sources of transient and repetitive emission within more than 100 Tb of the high time resolution data. The efficient pipeline of data cleaning and processing is developed and successfully tested.

Key words: transient emission, pulsars, cleaning procedure

1. Introduction

The sources of rapidly varying pulsed radio emission (pulsars) have been investigated in the decameter range for more than 40 years. It was revealed that this range is very promising in terms of detecting new phenomena in their behavior. For example, the phenomenon of the anomalously intense pulses was discovered in the decameter range [1]. The sporadic behavior of certain pulsars is more noticeable at low frequencies [2]. The precision of interstellar medium sensing is highest in decameter range, as the dispersion measure and rotation measure increase as a square of frequency. Transient radio emission which can also be generated by neutron stars may also exhibit many interesting peculiarities at low frequencies.

The study of transient sources of radio emission is one of the key projects for the new generation of radio telescopes such as LOFAR and SKA [3,4]. The SKA mainly explores the higher band of radio spectrum, whereas LOFAR has the operating frequency range 10-240 MHz but is still optimized to work above 30MHz. Therefore the lowest part of radio spectrum, observable from the ground (10-30 MHz), will not be covered enough by investigation of transient radio sources.

The most sensitive radio telescope in this frequency range is still the UTR-2 (Ukrainian T-shaped Radio telescope, 2nd modification). It has shown the significant success in the detection of pulsed and transient radio emission [5,6]. Until recent time the sensitivity of the telescope was restricted by the receiving system, and the limited capacity of data storage prevented the massive study of all pulsar sample. Now, with the introduction of digital backend it became possible to measure the pulsar characteristics precisely and to draw statistical conclusions from the large sample of observed pulsars [5].

The low-frequency range provides special benefits for the study of neutron stars which are known to be sources of pulsed and transient emission. These benefits are connected with expansion of their beaming fraction at lowest frequencies [5], and they allow discovering new sources which are not reachable for higher-frequency observations. This fact and the statistics of the pulsar behavior at decameter wavelengths have revealed the possibility to detect up to 100 new pulsars and/or transients in the decameter range. This was the motivation to commence a new survey of northern sky with relatively high time resolution (8 ms). In this survey we expect to discover nearby slow pulsars which haven't been detected so far due to the orientation of their narrow radiation cones, which get broader at low frequencies as well as the bursts from RRAT-like sources and other transients.

2. The data cleaning and processing pipeline

The survey strategy is related to the peculiarities of UTR-2 and is a compromise between the integration time for each source (which must be large) and the total observation time (must be the least possible). This contradiction was resolved in the technique using the Earth's rotation and the wide beam pattern of antenna. Thus, the entire northern sky can be surveyed in 40 days, implying the storage and processing of ~100 terabytes of the data. To confirm the detections, the re-observations of candidate-sources will be needed, and to detect more transients, the multiple records of the sky are essential. It will lead even to larger data amounts to be processed. The fast an efficient data processing pipeline is therefore needed to deal with all the observational data in the automatic mode.

The processing of survey data includes the following stages: (i) the interference excision, (ii) procedure of dispersive delay compensation with different trial values of dispersion measure (DM) constant (hereafter, dedispersion), (iii) search for individual dispersed pulses and (iv) search for periodicity in the processed data.

2.1. The interference excision

The most tricky and important task, the data cleaning procedure, is needed for both pulsar and transient pipelines. Due to the large area, occupied by the beam on the sky, there are much terrestrial interference and signals from other cosmic sources captured by the beam. All these artificial or natural signals may show up as the false-positive detection of the spurious sources, giving certain

periodicities in the Fourier domain or bright spots on the individual bursts search diagrams.

The level of the interference varies from time to time, depending on the time of the day, season etc. Therefore the different depth of cleaning should be used during the processing. In our case the most reasonable way is to perform an adaptive procedure, consisting of several stages, which adds or removes the additional stages depending on the percentage of data samples, contaminated by the interference. The thresholds used in the cleaning should be more severe when searching for periodic weak pulsar signals, which are normally under the noise level, and less severe when identifying the transient signals, which are supposed to be rather strong.

The implementation, best fitting to the criteria above, is made up of several stages of cleaning in the time and frequency direction.

Initially we calculate iteratively the mean and standard deviation (σ) in each frequency channel, clipping the values above 3 σ at each iteration. Then we normalize the data, to eliminate the amplitude-frequency characteristic unevenness of the telescope and to make data zero-mean. The normalized data are shown in Fig. 1, a). The intense (black) features are all from terrestrial origin, and are the interference.

After that we make two stages of cleaning the 'bad' (interference) samples. Fig 1 shows the cleaning stages in the same order as in the pipeline. The underlying principle of first stage is described in [7], in section 'The SumThreshold method', and adapted to UTR-2 data. The main point is that the different thresholds are applied to the data, and the connected shapes of samples exceeding each threshold are found. A combination of N samples (either in time or in frequency direction) is flagged as interference if its average exceeds the threshold T_N (given in the absolute value or relative to the standard deviation σ). The sliding window size N is increased from iteration to iteration, and the larger is N, the lower is the threshold, applied to the average of the samples. The values that have been flagged in the previous iteration are not taken into account in the subsequent one. For UTR-2 data after normalization (zero-mean), the sizes of N and the corresponding thresholds differ for the time and frequency direction. They are listed in the table 1.

Table 1

Time direction:					
N	2	8	16	128	256
T_N	6.67·σ	2.96·σ	1.97·σ	0.58·σ	0.4·σ
Frequency direction:					
N	1	2	4	8	64
T_N	10·σ	6.67·σ	4.44·σ	2.96·σ	0.88·σ

The result of the performance of the described can be seen in Fig. 1, b).

The last stage is the modified version of cleaning procedure, described in [5], without examining of single samples (it is moved to the 1st stage). To eliminate the low-level wideband and narrowband interference, we accumulate the data by frequency or time, correspondingly. After that the σ of integrated time series (or of average spectrum) is re-calculated and the spikes exceeding the 4σ-level are flagged (Fig. 1, c)).

All the flagged samples are stored in binary 'bad samples map' (Fig. 1, d)), where 1 is a good sample, 0 is a bad one. They are replaced by the median, calculated over all 'good' samples of the dynamic spectrum.

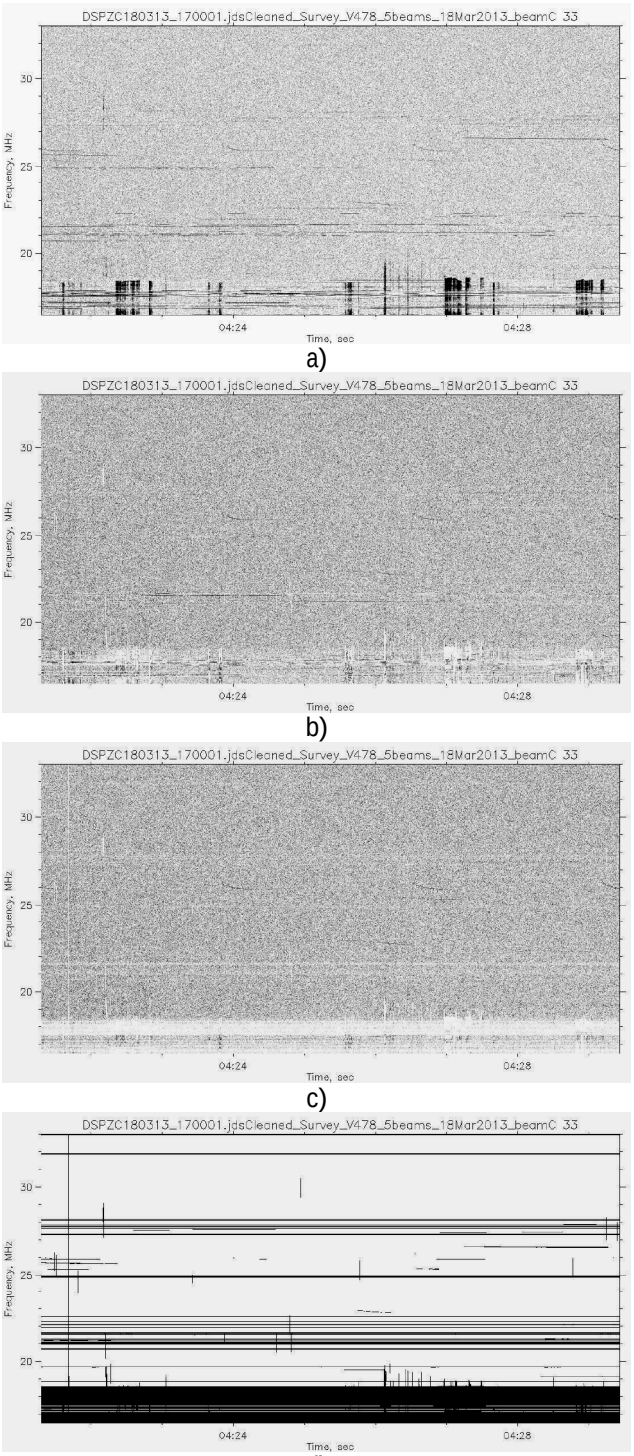

Figure 1: The successive stages of data cleaning procedure

When the data are rather clean, only with short features along the time or frequency direction, the first stage of the cleaning algorithm is applied. If the data contains numerous

wideband interference or continuously broadcasting radio stations' signals, we add the remaining two stages of the cleaning to the pipeline. At this step, the whole frequency channels or time intervals are removed from the data.

This sophisticated algorithm shows sufficient performance visible by naked eye and is well adapted to UTR-2 data. The average value of data, lost due to interference during one observational night, is about 4%. Mostly it is the data of the first and the last hours of observations, whereas the middle of the night tends to be almost interference-free.

2.2. Dispersive delay compensation

The clean data are then dedispersed with different dispersion measure (DM) trials. Initially we restrict the upper value of DM as 30 pc·cm^{-3}, but later this value will be raised to 60 pc·cm^{-3} for pulsars, and 100 pc·cm^{-3} for transients. We have chosen the step of trial DMs to be 0.01 pc·cm^{-3}. The precision could be higher, but we have selected this value as an optimum between the precision and the processing time. The precision reached in the higher-frequency surveys is less, because the propagation effects are not so influential there. Due to this, the decameter range is the unique probe of the interstellar medium via its dispersion, scattering and the Faraday effect.

2.3. Search for individual dispersed pulses

The further step of the pipeline is a search for individual transient events, which implies examining the data for dispersed pulses, exceeding certain threshold. At this stage we potentially can detect the giant pulses or anomalously intense pulses of pulsars, RRAT-like signals etc. The nearby pulsar will show up as a series of the intense pulses at the same dispersion measure trial value. To reduce the fluctuations of the background noise and to distinguish the useful signal, we normally apply the filtering of the low-frequency components of the data with a cut-off frequency of high-pass filter about 0.2 Hz. To increase the sensitivity, we also use the integration of 4 time samples into 1 (32 ms).

The detection algorithm denotes the suspected transient events by the circles, with the diameter proportional to the signal-to-noise ratio of the event. To reject the spurious events, we return to previous stages of processing and check the event visually. We check whether the cleaning has removed only obstructive signals, whether after dedispersion with the corresponding trial DM the signal is aligned into a straight vertical line on the dynamic spectrum and whether there are several events at the same dispersion measure (then we assume the detection of a pulsar). Fig. 2 shows the result of algorithm performance at the strong pulsar B0809+74 with the dispersion measure 5.755 pc·cm^{-3}. We see the repetitive events of different intensity, with intervals multiple of pulsar period.

2.4. Search for periodicity

The search for weak pulsar signals is possible due to their periodicity. We make the Fourier analysis and fold the integrated time series with the trial periods of pulsar. As we restrict the lower value of pulsar periods in the survey down to 0.1 s, we should consider the harmonics less than 10 Hz in the Fourier domain. The higher harmonics are filtered out. The Fourier transform is applied to each integrated time series, obtained by summing the shifted frequency channels with respect to one another according to the DM trial value. To increase the signal-to noise, we sum several FFT outputs of neighboring DM trials. To increase the power of the first harmonic, we add the 2, 4, 8 and 16 harmonics to it. The result is the peaks of certain shape, outstanding above the noise. Each of these peaks corresponds to 1/trial period, which we will depict on the period-dispersion measure plane, looking for characteristic shape of average dispersed pulses.

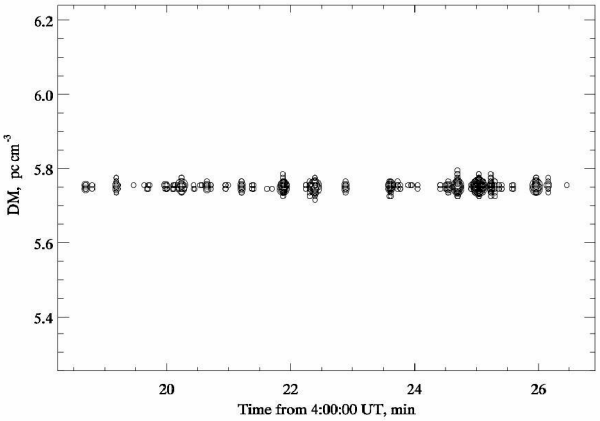

Figure 2: The result of individual pulses search algorithm with pulsar B0809+74

3. Results and perspectives

Up to now, by means of the described pipeline we have processed about 25% of survey data. A large number of transient-candidates are obtained, and we are excluding the spurious events from them.

The upper value of DM=100 pc·cm^{-3} will lead into 10 000 different shifts to be made between the frequency channels in the data. For 100 Tb of data, this will take a lot of processing time. To accelerate the data processing, we are introducing the techniques of parallel and distributed computing to the pipeline. The GPU-based dedispersion and processing of the different data fragments at the available nodes of Ukrainian Academical Grid will speed-up the processing up to 200 times. Another alternative is the usage of volunteer distributed computing system BOINC [8]. The Einstein@Home project, powered by BOINC, was used to discover 24 new pulsars in Parkes Multibeam Pulsar Survey data [9].

References

1. Ulyanov O. et al.: 2006, *Radiofizika and Radioastronomia*, **11**, 113.
2. Ulyanov O., Zakharenko V.: 2012, *Astron. Rep.*, **56**, 417.
3. Stappers B.W. et al.: 2011, *A&A*, **530**, id.A80.
4. Colegate T.M., Clarke N.: *PASA*, **28**, 4, 299.
5. Zakharenko V. et al.: *MNRAS*, **431**, 4, 3624.
6. Popov M. V. et al.: 2006, *Astron. Rep.*, **50**, 562.
7. Offringa A.R.: 2012, University of Groningen, *diss.*
8. *http://boinc.berkeley.edu/*
9. Knispel B. et al.: 2013, *ApJ*, **774**, 93.

Радиофизика и радиоастрономия. 2014, Т. 19, № 3, с. 197–205

РАДИОАСТРОНОМИЯ И АСТРОФИЗИКА

I. Y. VASYLIEVA [1], V. V. ZAKHARENKO [1], A. A. KONOVALENKO [1], P. ZARKA [2], O. M. ULYANOV [1], A. I. SHEVTSOVA [1], AND A. O. SKORYK [1]

[1] Institute of Radio Astronomy, National Academy of Sciences of Ukraine, 4, Chervonopraporna St., Kharkiv, 61002, Ukraine
E-mail: zakhar@rian.kharkov.ua

[2] LESIA, Observatoire de Paris, CNRS, UPMC, 5, Place Jules Janssen, Meudon, 92190, France

DECAMETER PULSAR/TRANSIENT SURVEY OF NORTHEN SKY. FIRST RESULTS

The decameter pulsar/transient survey is now being made using the UTR-2 radio telescope. The survey strategy and parameters, equipment characteristics, data processing algorithms as well as preliminary results are described. The very first result was the discovery of decameter emission of the pulsar J0240+62. Test measurements have shown the sensitivity, reached in the present survey, being 5 Jy for the transient signals, and several mJy – for the periodic pulsar emission.

Key words: survey, decameter range, pulsar, transient

1. Introduction

The discovery of pulsars [1] has had an enormous importance for astronomy and astrophysics. In addition to studying this new class of objects directly (their internal structure, main characteristics and radiation models), pulsar science has built connections to various problems in other fields of astrophysics. Pulsar timing, especially the study of the Hulse–Taylor pulsar [2] and the binary pulsar J0737-3039(A/B) [3], established the most strict tests of the relativity theory. A precise measurement of period of the pulsar B1257+12 [4] has led to the discovery of a planetary system around a pulsar. Study of repetitive and sporadic emission of neutron stars has revealed new branches of their evolution: magnetars [5], XDINSs [6], RRATs [7], intermittent pulsars [8] and X-ray link to radio pulsars [9]. Powerful pulsed emission of neutron stars can be used as a probe of electron density in the Galaxy [10]. Timing of millisecond pulsars is an attempt to detect gravitational waves [11]. There is no doubt that future theoretical and experimental studies of neutron stars will bring more and more new discoveries.

Ultra-broadband emission (from low-frequency radio waves to highest energy gamma range) makes neutron stars unique objects of studying, within all electromagnetic spectrum. Dozens of surveys have been made [12–15] in various wavelength ranges – from meter waves to gamma range, in order to find new targets for studies. Nevertheless, the relevance of new surveys does not diminish. Whereas the high-frequency range is well suited for studies of distant neutron stars in the Galaxy, and the extragalactic transient events, the most low-frequency region of the electromagnetic spectrum, on the contrary, carries the information about the closest pulsars and transient sources of radio emission. The discovery of new neutron stars in our neighborhood, which were left out in the high-frequency surveys, is possible due to the expansion of their emitting cone and increase in the beaming fraction, as compared to higher frequencies. Thus, one of the most relevant tasks for the lowest end of electromagnetic spectrum (decameter wave range) is a survey of the pulsed and transient emission sources, accessible in this range. It is especially important, because such a survey has never been made at these frequencies before. Formerly, this task could hardly be considered feasible, but at present, due to improvement of telescopes,

receiving equipment, computer hardware and methods of search, such a survey has become possible. After a successful re-detection of 40 known pulsars at decameter wavelengths [16], which has demonstrated the potential of the decameter wavelength range, we commenced a survey of the entire Northern sky at the most sensitive UTR-2 decameter wave radio telescope.

Present work describes the survey concept, equipment and software used, and the very first results. Section 2 summarizes information about instrumentation and parameters of the survey. Section 3 describes the main stages of data processing pipeline and the corresponding software. Section 4 demonstrates (as a testing result) the detection of known pulsars in survey data, in a form of summary plots produced by data processing routines. Section 5 presents the analysis of detected transient signals, in particular, the detection of decameter emission of recently discovered [12] nearby pulsar J0240+62. The last Section provides the conclusions and prospects.

2. Instrumentation and Survey Parameters

The largest decameter wavelength radio telescope UTR-2 [17], equipped with a broadband preamplification system [18] and a set of digital receiving equipment [19], can operate in a five-beam mode, with the width of each beam $\sim 24'$ at 25 MHz, and the angular distance between the beams $\sim 23'$. In this case, five beams, directed along the meridian, capture the angle range of about $2.5°$ by declination. A drift-scan survey (driven by the Earth's rotation), allows to cover the whole northern celestial hemisphere during 80 nights of observations.

Concept of the survey is designed to gain the maximum use of the UTR-2 advantages. It necessitates making a compromise between the integration time for each source (which should be as longer as possible) and the total observation time (which is restricted). A broad directional pattern of "North–South" antenna allows keeping sources within the beam for 40–60 min. Sum, Difference and Product of directional patterns of the two antennae ("North–South" and "East–West") can be used, ensuring the flexibility of data analysis.

Here are some considerations that we have followed, choosing the survey parameters. In order to have a high sensitivity, the effective area of the telescope (A_E) must be large. But it decreases with growth of zenith angle (z). Therefore we have limited the declination (δ) of surveyed parts of the sky from $-10°$ to $+90°$ (coordinates of UTR-2: $49°38'10''$ N, $36°56'29''$ E). Decrease in the effective area at $\delta = -10°$ in this case does not exceed 2 times, compared to zenith direction. Choice of the time resolution ($\Delta t = 8$ ms), is based on measurements of the scattering time constant (τ_{SC}) of nearby pulsars, only two of which (B0950+08 and B0809+74), have the τ_{SC} less than the selected Δt at decameter wavelengths. Another key parameter is the highest accessible dispersion measure (DM), which we take into account while processing the data. As an integral of the electron density along the line of sight, it is directly related to the distance from the Earth, at which we search for the source of pulsed signals. We chose it the same as in [16]: 30 $\mathrm{pc \cdot cm^{-3}}$ (which corresponds to $1-2$ kpc maximum distances to the sources with low galactic latitudes $|b| < 5°$). It is related to a very time-consuming and computationally expensive nature of dedispersion procedure. In the near future (having larger computing capabilities), the raw data can be reprocessed with increased maximum DM up to $60-100$ $\mathrm{pc \cdot cm^{-3}}$, in order to search for more distant sources of pulsed signals. The selected frequency range is $16.5-33.0$ MHz. It is divided into 4096 partial frequency channels. This part of the UTR-2 frequency range is least affected by interference.

3. Data Processing Pipeline

The total amount of raw survey data will be about 100 terabytes. In addition, all the events that resemble signatures of pulsar or transient emission (we call them "candidates" hereafter), must be re-observed, in order to confirm or refute the detection. This will result in even larger data sets to be processed. Therefore, fast and efficient data processing techniques should be used.

The data processing pipeline includes 3 main stages:

– interference mitigation (including normalizing and calibration),

– compensation for dispersion delays between frequency channels, and further integration over the frequency band,

– search for sources of repetitive and transient emission.

The last step is flexible. It implies having a toolkit with several processing procedures, which can be adjusted to the specific multi-parametric search. Due

to a fragmented structure of raw data, we can start processing almost on the fly – immediately after the recording of the first file (about 9 min after the start of observation). For the alignment of processing time between all the steps, parallelization can be used.

3.1. Interference Mitigation

Decameter range is extremely polluted with the radio frequency interference (RFI) of natural and artificial origin. Their signatures in the data can result in a false-positive detection of spurious signals in both the time domain and the Fourier image domain.

The RFI level depends on time of the day, season, etc. Therefore the processing algorithms with different depth of RFI mitigation should be used. At this stage, the calibration is taken into account. The applied RFI mitigation algorithm is described in more detail in work [20]. The plots of raw and cleaned dynamic spectra, as well as the map of contaminated pixels are kept to check the following stages of processing.

3.2 Dedispersion

According to the dispersion equation of electromagnetic wave propagation in cold plasma, the ΔT delay of signal at a certain frequency f with respect to infinitely high frequency is:

$$\Delta T = 10^{16} \frac{\mathrm{DM}}{2.410331} f^{-2}. \quad (1)$$

In this case, we compensate for a propagation delay between the upper (33 MHz) and the current frequency of the spectrogram and then integrate over all frequency channels. The data is processed by looking through a "trial" DM within 0 to 30 $\mathrm{pc}\cdot\mathrm{cm}^{-3}$ with a step $0.01\ \mathrm{pc}\cdot\mathrm{cm}^{-3}$. A step between adjacent DM trials has been chosen as a compromise between the accuracy of dispersion compensation and the processing time. Nevertheless, under these conditions, the processing time on a personal computer still exceeds the observation time by a factor of 100.

We have developed the programs which parallelize calculations, and thus increase 50-fold the processing speed (on a computer with the Intel Core i7 CPU and 32GB RAM, it takes approximately 23 hours to process a 12-hour observation). Given that the telescope works in a five-beam mode, this step requires further increase in productivity, use of parallelism and processing power of GPUs. For efficient pipelining we still need acceleration of about 10 times compared to the results already achieved.

3.3.1 Search for Individual Transient Signals

The next step of the pipeline is a search for transient signals in the "time – dispersion measure" plane. Here we examine each of 3000 time series, integrated over frequency, whether they exceed a certain threshold. At this stage, we can potentially find giant or anomalously intense pulses of pulsars, RRAT-like signals, etc. Radio emission of strong pulsars will be displayed as a series of consecutive pulses at the same trial value of DM.

In order to suppress the background noise fluctuations and highlight the useful signal, we filtered out low frequency components, lower than a cutoff frequency of the high pass filter, i.e. 0.2 Hz. To increase sensitivity, we also use integration of 4 adjacent time samples (i.e. the effective time resolution becomes 32 ms). The samples that exceed the threshold ($5.5\sigma_{\mathrm{DM}}$ – a standard deviation, calculated for each integrated time series with corresponding trial DM), are put down to the database, indicating their DM, S/N ratio of the event and the time elapsed from the beginning of the file. They are marked on the "time – dispersion measure" plane by circles, with radii proportional to the S/N value of the event. To check for false-positive detections, the pre-processed data are examined in different ways, introducing different input parameter values (e.g. checking in different frequency bands) and also are checked visually. Fig. 1 shows the example of false-positive detection. The dynamic spectrum (after the dispersion delay compensation) shows the frequency sweep of the signal, different from the dispersion relation (1).

3.3.2 Periodicity Search

As mentioned above, the search for weak pulsar signals is possible due to their periodic nature and the accumulation of the source through signal within a wide "North–South" antenna pattern, during $40-60$ min. We make the Fourier transform of the data for this time window, i.e. $40-60$ min. In the same way as when searching for transient signals, for each value of trial DM, we calculate the standard deviation (σ_{FFT}). Values, exceeding a certain threshold ($6\sigma_{\mathrm{FFT}} - 10\sigma_{\mathrm{FFT}}$), are also put down in the output file and marked with circles on the "frequency – dispersion measure" plane. The radii of the circles are in

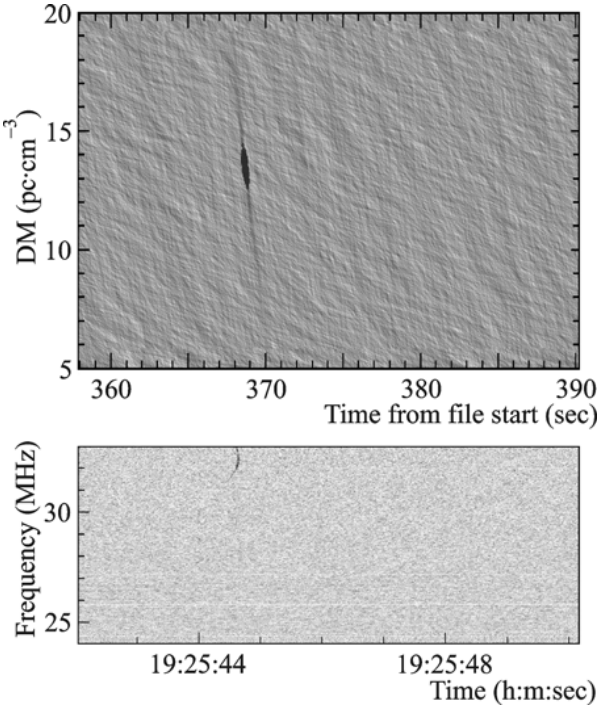

Fig. 1. False-positive detection in the "time – dispersion measure" plane (upper panel). The test has shown the presence of a signal (lower panel) with time-frequency dependence different from the dispersion law (1)

this case proportional to the S/N ratio logarithm. Thus we can detect a wide range of variations of harmonic intensity values for the weak and strong pulsars.

4. Methodology of Pulsar and Transient Search

By the beginning of 2014, the initial observations, which began in April 2010, were almost completed. We have obtained the records of more than 90 % of the Northern sky. For the remaining areas (gaps between the strips, which were recorded with a six-month shift, and the circumpolar regions), one more short-term observational session is required. Fig. 2 shows the map of surveyed sky regions.

The survey database includes:

– raw data,

– normalized data after RFI mitigation,

– intermediate files with compensated dispersion delay,

– outputs of repetitive and transient search routines.

Preprocessing (steps 1 and 2 of the pipeline) is now completed for a half of the raw data. Using the aforesaid search routines, we have processed the

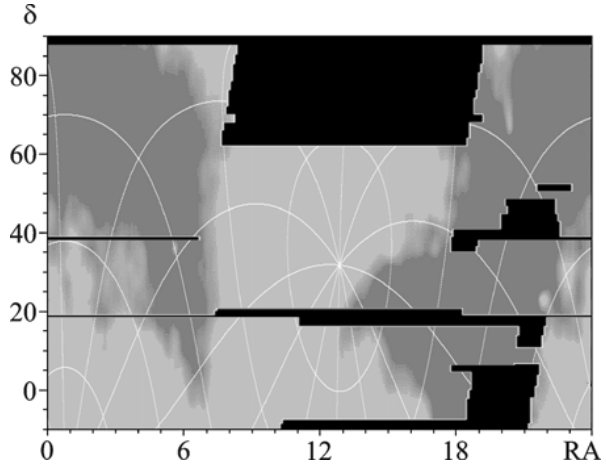

Fig. 2. Surveyed sky region in the RA–δ coordinates

survey data that contain recordings of radio emission of known pulsars, such as PSR B0809+74, B0834+06, B0950+08.

To clearly represent the transient events that occurred during the night of observations, the data might be depicted as shown in Fig. 3. The upper panel of the Figure shows in the "dispersion measure – signal-to-noise ratio" coordinates the data points, exceeding the selected threshold $5.5\sigma_{DM}$ (≈ 5 Jy, under the selected observational parameters). The peak corresponds to the DM of 12.88 $pc \cdot cm^{-3}$ (pulsar B0834+06). The bottom panel "time (in hours from the start of recording) – dispersion measure" serves to determine the time of signal maximum. Also, both panels show clearly the interference, left out during the cleaning procedure, which are noticeable at low values of DM.

As aforesaid, another processing step is a search for repetitive pulses. Example of processing of 1-hour records of pulsar B0809+74 in the survey mode is shown in Fig. 4.

The upper panel shows the variations of individual pulse intensity (with respect to the noise) integrated over the entire frequency range 16.5 – 33.0 MHz, in 6 consecutive 520-sec files. Individual pulses, with respect to pulsar rotational phase, are shown in the second panel, where each vertical line is one period of neutron star rotation. The dark "corridor" in the middle is the beaming fraction of the pulsar. The third panel shows the S/N ratio of the first harmonic of the pulsar signal being inverse to its rotational period. The fourth panel shows the normalized directional pattern of the sum of the UTR-2 "North–South" and "East–West" antennae towards the pulsar.

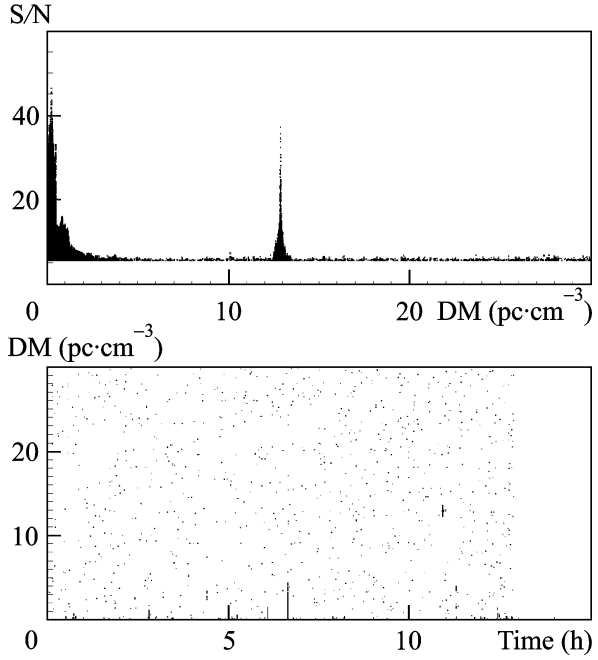

Fig. 3. Principal output of the transient search program. The lower panel shows all the events during one night of observations which exceed a 5.5 σ_{DM} level (dots). The upper panel represents the same events, sorted by DM, in the coordinates "signal-to-noise ratio versus dispersion measure"

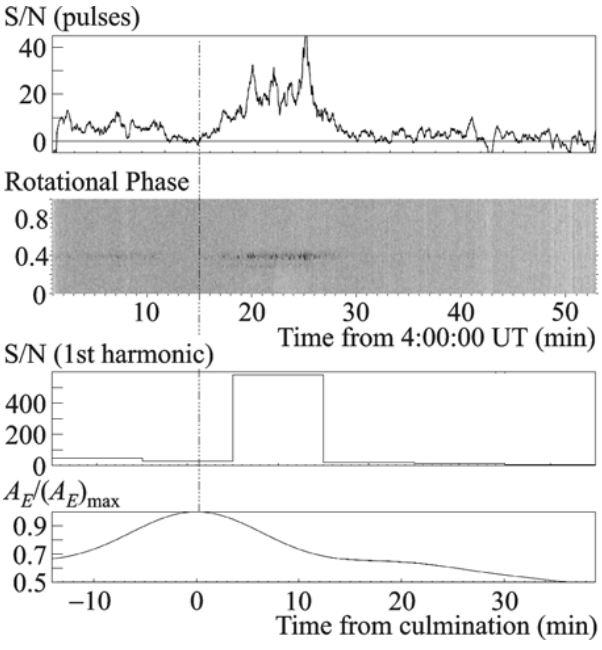

Fig. 4. An example of detection of pulsar B0809+74 in surveyed data. The panels from top to bottom: power of individual pulses integrated over entire frequency range, dependence of intensity on the rotational phase of pulsar, S/N of the first harmonic in the 6 consecutive 520-sec files, normalized directional pattern of the sum of the UTR-2 "North–South" and "East–West" antennae towards the pulsar

The Figure helps understand that the time of maximum intensity of the pulsar radio emission does not coincide with culmination time (maximum of the antenna pattern and a dash-dot line). Only the use of the sum (not multiplication) of two antennae could result in capture and integrating the first harmonic of the pulsar radio emission up to the impressive value of S/N ratio ~ 600. Further processing is also aimed at S/N increasing. Fig. 5 shows first 17 harmonics of the pulsar: at the top – S/N of harmonics at the trial DM value of 5.75 pc $\cdot$ cm^{-3}, in the middle – the layout of harmonics in several adjacent values of trial DM. It is evident from this panel, that there is an additional resource to accumulate the pulsar power, which can be vital for detection of weak periodic sources.

Summing of 100 adjacent values of DM (lower panel, left), we can raise the S/N up to 2000 (lower panel, right – the value of the first harmonic is highlighted by the solid line). Adding of all higher harmonics' power to the first harmonic value (dotted line) gives about a twofold S/N increase for this pulsar. Note that during the transition of a pulsar across the directional pattern (up to 60 min), if its emission is constantly present in the beam, the S/N ratio might be additionally two-fold higher than the obtained one.

Thus, the way the data are recorded in the survey, provides a high sensitivity to the periodic emission of weak radio sources. Flux density of the aforesaid pulsar is about 1.2 Jy. A reserve in the S/N ratio gives hope for detection of repetitive radio emission sources at the level of several mJy.

5. Detected Transient Signals. Decameter Radio Emission of Pulsar J0240+62

To date, by means of the transient signal search program, we have processed 30 % of records of the Northern sky. We have found about 70 events with S/N ratio above 6.5 σ_{DM}, more than 60 of which have a DM value that does not coincide with DM of any known pulsar. Their time-frequency behavior obeys the dispersion law (1), which is a strong argument to put them into the "candidates" list. At the next step of the search we will run the follow-up observations, targeted at these "candidates".

By now, the most important result has become a detection of decameter emission of the recently discovered pulsar J0240+62 [12]. Fig. 6 shows results of the transient search program: DM = 3.83 ± 0.01 pc $\cdot$ cm^{-3},

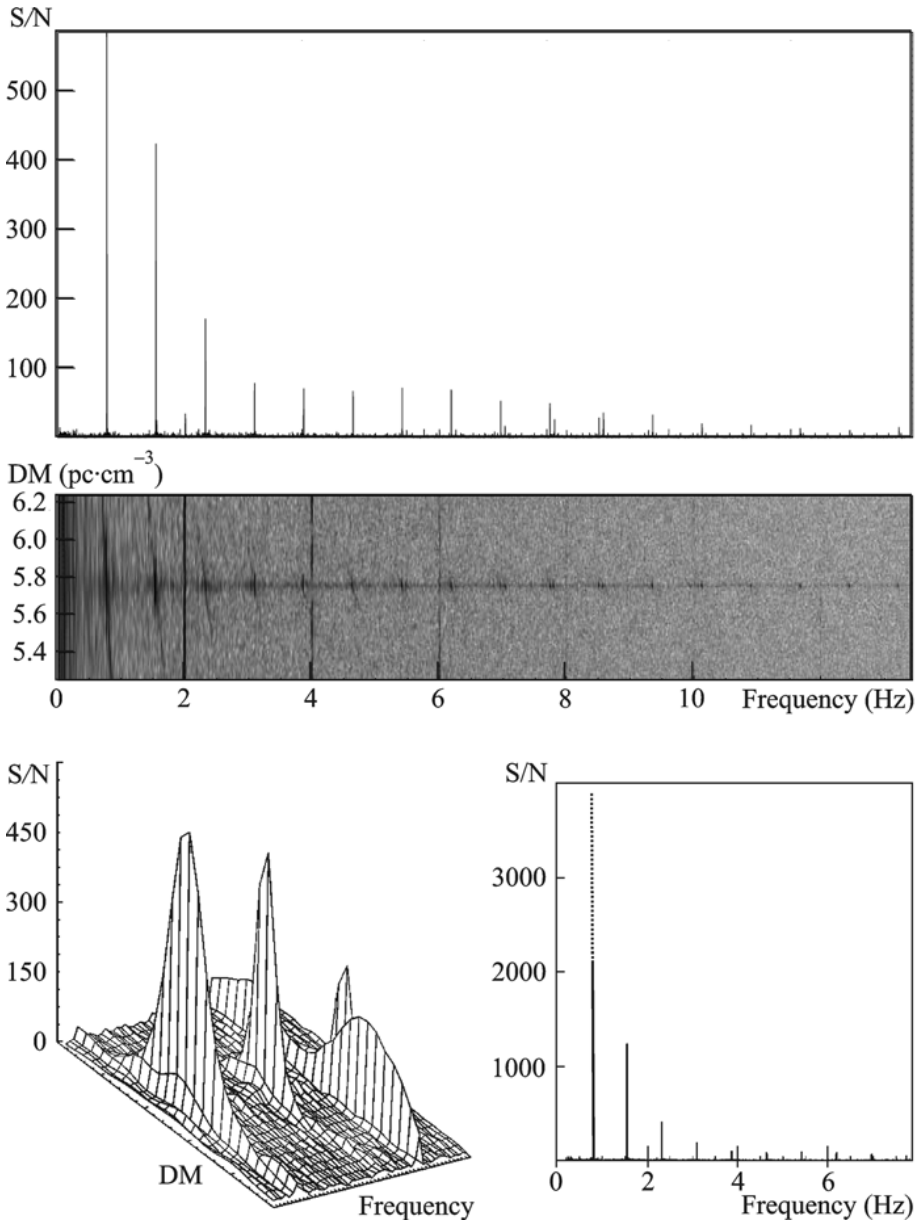

Fig. 5. Power of harmonics of PSR B0809+74 radio emission versus DM. The upper panel: intensity of first 17 harmonics at the true value of pulsar DM (which is known). The middle panel: the harmonic power at several adjacent DM values. The lower panel, left, shows how the harmonic power decreases as the trial DM value shifts away from the true value (5.75 pc · cm^{-3}). The lower panel, right, shows the result of averaging of 100 adjacent DM values (dash-dot line – the result of addition of the higher harmonics power to the first harmonic value)

$S/N = 21.9$. Given that the maximum was detected at 2 h and 7 min of local time on October 8, 2013, the Right Ascension (RA) of the source was 2 h and 41 min (total time, when the pulsed emission at this DM is present in beam C of the UTR-2 makes more than one hour).

Declination, corresponding to the center of beam C was $\delta = 63.14°$. Having determined the approximate values of RA, δ and DM, we had no doubt that it was a record of the decameter radio emission of the aforementioned pulsar. In adjacent beams (B, D, and E) the emission was also present, but only within the time interval of 2 h 7 min to 2 h 11 min. This effect can be explained as follows. The directional pattern of the sum of antennas "North–South" and "East–West" has a crosswise form. "Knife-like" patterns of antenna "North–South" in a five-beam mode are separated, as aforesaid, by 23′. But a "knife-like"

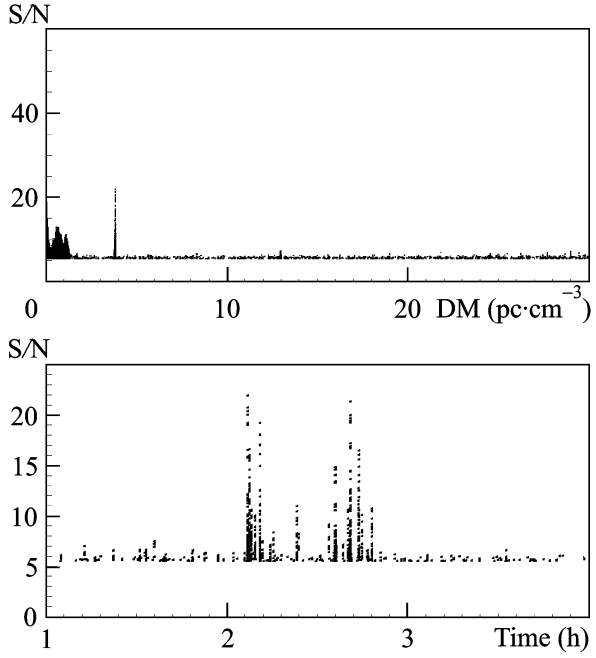

Fig. 6. Detection of pulsar J0240+62. The upper panel shows S/N ratio with respect to DM with a maximum at $\mathrm{DM} = 3.83\ \mathrm{pc}\cdot\mathrm{cm}^{-3}$. The lower panel shows pulsar's pulses within the DM range of $3.83 \pm 0.05\ \mathrm{pc}\cdot\mathrm{cm}^{-3}$ in the C beam versus local time

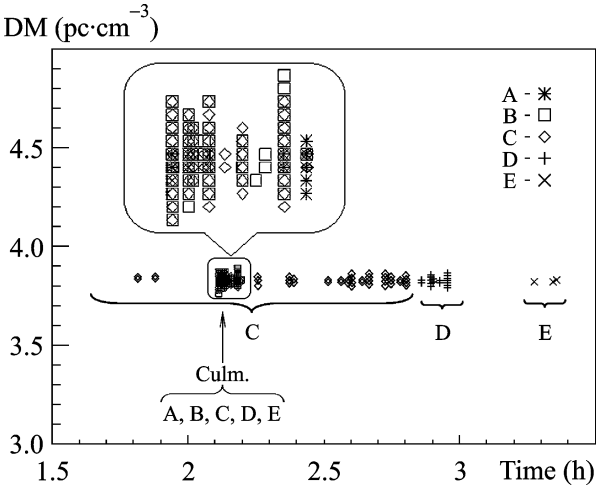

Fig. 7. Upper panel: track of a simulated source through the beams of UTR-2. Lower panel: pulsar detection in all beams of the telescope (A–E). The most intense pulses take place in the B and C beams. At the expected culmination time of PSR J0240+62, its emission was present in all beams of UTR-2

pattern of "East–West" antenna, with a width of 1°, is common. The transition of the source over the "East–West" antenna had to occur exactly between 2 h 7 min through 2 h 11 min.

Fig. 7 shows a simulated source transit, having $\delta = 60°$ through the center of beam C in the coordinates "hour angle (in minutes from culmination) – Code V (directional cosine of UTR-2 pointing)". Calculation shows that far from the culmination, the source will cross the center of beam D (40 min before and after the culmination) and the center of beam E (60 min before and after the culmination). Antenna gain will be less than $0.5(A_E)_{\max}$, but still non-zero. And as is seen above, the most intense pulses can occur apart from the source's culmination. The lower part of the figure shows how the detected pulses are allocated in all five beams. In each beam, pulses have been detected with the S/N ratio of more than $8\sigma_{\mathrm{DM}}$.

6. Discussion and Prospects

Thus, we can claim about a high detection efficiency of individual pulses as well as their repetitive sequences. The large relative bandwidth $(f_{\mathrm{up}}/f_{\mathrm{low}})$ enables high precision distinguishing between the dispersion law, inherent in cold interstellar plasma from other time–frequency dependences, such as man-made interference. Whereas, for the high-frequency surveys the preliminary determination of RA an δ of a source is accurate, and the third coordinate – the distance to the source defined by the dispersion delay in the interstellar medium – is determined poorly, then at low frequencies, the situation is just the opposite. Surely, during the follow-up observations all these three parameters will be essentially refined.

Developed preprocessing routines and automatic transient signal search pipeline can successfully carry out a blind search for individual and repetitive pulses. Preprocessing has already been done on approximately 50 % of data. The number of "candidates" is already quite large (dozens with a flux density of 5 Jy and higher).

For multiparameter checks of "candidates", an online access to the intermediate processing results is needed. This requires enhancement of the processing cluster(s) (currently, these are the Institute of Radio Astronomy and UTR-2 clusters) and increasing the disk space available.

High sensitivity to repetitive pulse sequences allows detection of sources with a flux density ranging from a few mJy to a few Jy. This sensitivity is very high for the decameter wavelength range. If we take into account that along with increasing beaming fraction at lower frequencies some pulsars might have a broad "plateau" with intensity of a

few percent of the main pulse, then the ability to detect such pulsars oriented past the Earth with their narrow main pulse is much higher in the decameter wavelength range.

Acknowledgements

This work has been supported by Projects "Development of the UTR-2 radio telescope cluster for the UTR and GURT data processing" in the framework of NASU Program "Informatization for 2014", and "Coordinated simultaneous studies of the solar system objects by means of the methods of ground- and space-based low-frequency radio astronomy" within the NASU Program "Scientific Space Research for 2012-2016".

REFERENCES

1. *Hewish A., Bell S. J., Pilkington J. D. H., Scott P. F., and Collins R. A.* Observation of a Rapidly Pulsating Radio Source // Nature. – 1968. – Vol. 217. – P. 709–713.
2. *Hulse R. A. and Taylor J. H.* Discovery of a pulsar in a binary system // Asnrophys J. – 1975. – Vol. 195. – P. L51–L53.
3. *Kramer M., Stairs I. H., Manchester R. N., McLaughlin M. A., Lyne A. G., Ferdman R. D., Burgay M., Lorimer D. R., Possenti A., D'Amico N., Sarkissian J. M., Hobbs G. B., Reynolds J. E., Freire P. C. C., and Camilo F.* Tests of General Relativity from Timing the Double Pulsar // Science. – 2006. – Vol. 314, Is. 5796. – P. 97–102.
4. *Wolszczan A. and Frail D.* A planetary system around the millisecond pulsar PSR1257+12 // Nature. – 1992. – Vol. 355, No. 6356. – P. 145–147.
5. *Camilo F., Ransom S. M., Halpern J. P., Reynolds J., Helfand D. J., Zimmerman N., and Sarkissian J.* Transient pulsed radio emission from a magnetar // Nature. – 2006 – Vol. 442, No. 7105. – P. 892–895.
6. *Voges W., Aschenbach B., Boller Th., Bräuninger H., Briel U., Burkert W., Dennerl K., Englhauser J., Gruber R., Haberl F., Hartner G., Hasinger G., Kürster M., Pfeffermann E., Pietsch W., Predehl P., Rosso C., Schmitt J. H. M. M., Trümper J., and Zimmermann H. U.* The ROSAT all-sky survey bright source catalogue // Astron. Astrophys. – 1999. – Vol. 349, No. 1. – P. 389–405.
7. *McLaughlin M. A., Lyne A. G., Lorimer D. R., Kramer M., Faulkner A. J., Manchester R. N., Cordes J. M., Camilo F., Possenti A., Stairs I. H., Hobbs G., D'Amico N., Burgay M., and O'Brien J. T.* Transient radio bursts from rotating neutron stars // Nature. – 2006. – Vol. 439, No. 7078. – P. 817–820.
8. *Rea N., Kramer M., Stella L., Jonker P. G., Bassa C. G., Groot P. J., Israel G. L., Méndez M., Possenti A.,* and *Lyne A.* On the nature of the intermittent pulsar PSR B1931+24 // Mon. Not. R. Astron. Soc. – 2008. – Vol. 391, No. 2. – P. 663–667.
9. *Archibald A. M., Stairs I. H., Ransom S. M., Kaspi V. M., Kondratiev V. I., Lorimer D. R., McLaughlin M. A., Boyles J., Hessels J. W. T., Lynch R., Leeuwen J., Roberts M. S. E., Jenet F., Champion D. J., Rosen R., Barlow B. N., Dunlap B. H.,* and *Remillard R. A.* A Radio Pulsar/X-ray Binary Link // Science. – 2009. – Vol. 324, No. 5933. – P. 1411–1414.
10. *Cordes J. M.* and *Lazio T. J. W.* NE2001. I. A new model for the galactic distribution of free electrons and its fluctuations // astro-ph/0207156 – 2002.
11. *Manchester R. N., Hobbs G., Bailes M., Coles W. A., van Straten W., Keith M. J., Shannon R. M., Bhat N. D. R., Brown A., Burke-Spolaor S. G., Champion D. J., Chaudhary A., Edwards R. T., Hampson G., Hotan A. W., Jameson A., Jenet F. A., Kesteven M. J., Khoo J., Kocz J., Maciesiak K., Oslowski S., Ravi V., Reynolds J. R., Sarkissian J. M., Verbiest J. P. W., Wen Z. L., Wilson W. E., Yardley D., Yan W. M., and You X. P.* The Parkes Pulsar Timing Array Project // Publ. Astron. Soc. Aust. – 2013. – Vol. 30. – id. e017.
12. *Manchester R. N., Hobbs G. B., Teoh A., and Hobbs M.* The Australia Telescope National Facility Pulsar. Catalogue // Astron. J. – 2005. – Vol. 129, No. 4. – P. 1993–2006.
13. *Manchester R. N., Lyne A. G., D'Amico N., Bailes M., Johnston S., Lorimer D. R., Harrison P. A., Nicastro L., and Bell J. F.* The Parkes Southern Pulsar Survey. I. Observing and data analysis systems and initial results // Mon. Not. R. Astron. Soc. – 1996. – Vol. 279, No. 1. – P. 1235–1250.
14. *Cordes J. M., Freire P. C. C., Lorimer D. R., Camilo F., Champion D. J., Nice D. J., Ramachandran R., Hessels J. W. T., Vlemmings W., van Leeuwen J., Ransom S. M., Bhat N. D. R., Arzoumanian Z., McLaughlin M. A., Kaspi V. M., Kasian L., Deneva J. S., Reid B., Chatterjee S., Han J. L., Backer D. C., Stairs I. H., Deshpande A. A., and Faucher-Giguère C.-A.* Arecibo Pulsar Survey Using ALFA. I. Survey Strategy and First Discoveries // Astrophys. J. – 2006. – Vol. 637, No. 1. – P. 446–455.
15. 350-MHz Drift Scan Pulsar Survey. Available from: http://astro.phys.wvu.edu/GBTdrift350/.
16. *Zakharenko V., Vasylieva I., Konovalenko A., Ulyanov O., Zarka P., Grießmeier J.-M., Cognard I., Nikolaenko V., and Serylak M.* Detection of decameter wavelength pulsed radio emission of 40 known pulsars // Mon. Not. R. Astron. Soc. – 2013. – Vol. 431. – P. 3624–3641.
17. *Braude S. Y., Megn A. V., and Sodin L. G.* UTR-2 Decameter Wavelength Radio Telescope // Antennas. – Moscow: Svyaz. –1978.– No. 26. – P. 3–14, (in Russian).
18. *Abranin E. P., Bruck Yu. M., Zakharenko V. V.,* and *Konovalenko A. A.* The New Preamplification System for the UTR-2 Radio Telescope. Part 1: Circuit Analysis and Design. Part 2. Implementation and Test Operation // Exp. Astron. – 2001. – Vol. 11, No. 2. – P.85–112.
19. *Kozhin R. V., Vynogradov V. V.,* and *Vavriv D. M.* Low-noise, high dynamic range digital receiver/spectrometer for radio astronomy applications // MSMW'07 Symposium Proc. – Kharkiv (Ukraine). – 2007. – P. 736–738.
20. *Vasylieva I. Y., Zakharenko V. V., Zarka P., Ulyanov O.M., Shevtsova A. I.,* and *Seredkina A. O.* Data processing pipeline for decameter pulsar/transient survey // Odessa astronomy publications. – 2013. – Vol. 26, No. 2. – P. 159–161.

Я. Ю. Васильєва [1], В. В. Захаренко [1], А. А. Коноваленко [1], Ф. Зарка [2], О. М. Ульянов [1], А. І. Шевцова [1], А. О. Скорик [1]

[1] Радіоастрономічний інститут НАН України, вул. Червонопрапорна, 4, м. Харків, 61002, Україна

[2] LESIA, Паризька обсерваторія, CNRS, UPMC, пл. Ж. Жансена, 5, м. Медон, 92190, Франція

ДЕКАМЕТРОВИЙ ОГЛЯД ПІВНІЧНОГО НЕБА З МЕТОЮ ПОШУКУ ПУЛЬСАРІВ І ДЖЕРЕЛ ТРАНЗІЄНТНОГО ВИПРОМІНЮВАННЯ. ПЕРШІ РЕЗУЛЬТАТИ

Наразі на радіотелескопі УТР-2 здійснюється декаметровий огляд пульсарів і джерел транзієнтного випромінювання. Описано стратегію та параметри огляду, характеристики обладнання, алгоритми обробки даних, а також попередні результати дослідження. Першим важливим результатом стало відкриття декаметрового випромінювання пульсара J0240+62. Тестові вимірювання показали, що чутливість, досяжна в цьому дослідженні, становить 5 Ян для транзієнтних сигналів та кілька міліянських для періодичного пульсарного випромінювання.

Я. Ю. Васильева [1], В. В. Захаренко [1], А. А. Коноваленко [1], Ф. Зарка [2], О. М. Ульянов [1], А. И. Шевцова [1], А. А. Скорик [1]

[1] Радиоастрономический институт НАН Украины, ул. Краснознаменная, 4, г. Харьков, 61002, Украина

[2] LESIA, Парижская обсерватория, CNRS, UPMC, пл. Ж. Жансена, 5, г. Медон, 92190, Франція

ДЕКАМЕТРОВЫЙ ОБЗОР СЕВЕРНОГО НЕБА С ЦЕЛЬЮ ПОИСКА ПУЛЬСАРОВ И ИСТОЧНИКОВ ТРАНЗИЕНТНОГО ИЗЛУЧЕНИЯ. ПЕРВЫЕ РЕЗУЛЬТАТЫ

В настоящее время на радиотелескопе УТР-2 проводится декаметровый обзор пульсаров и источников транзиентного излучения. Описана стратегия и параметры обзора, характеристики оборудования, алгоритмы обработки данных, а также предварительные результаты исследования. Первым важным результатом стало открытие декаметрового излучения пульсара J0240+62. Тестовые измерения показали, что чувствительность, достигаемая в настоящем исследовании, составляет 5 Ян для транзиентных сигналов и несколько миллиянских для периодического пульсарного излучения.

Submitted 15.05.2014

Bibliography

[Ables 1970] J. G. Ables, M. M. Komesaroff and P. A. Hamilton. *Pulse Broadening of PSR 0833-45 by Interstellar Scattering.* Astrophysical Letters, vol. 6, page 147, July 1970. (Cited on page 12.)

[Abranin 2001] E. P. Abranin, Y. M. Bruck, V. V. Zakharenko and A. A. Konovalenko. *The New Preamplification System for the UTR-2 Radio Telescope.* Experimental Astronomy, vol. 11, pages 85–112, 2001. (Cited on pages 24 and 46.)

[Allen 2013] B. Allen, B. Knispel, J. M. Cordes, J. S. Deneva, J. W. T. Hessels, D. Anderson, C. Aulbert, O. Bock, A. Brazier, S. Chatterjee, P. B. Demorest, H. B. Eggenstein, H. Fehrmann, E. V. Gotthelf, D. Hammer, V. M. Kaspi, M. Kramer, A. G. Lyne, B. Machenschalk, M. A. McLaughlin, C. Messenger, H. J. Pletsch, S. M. Ransom, I. H. Stairs, B. W. Stappers, N. D. R. Bhat, S. Bogdanov, F. Camilo, D. J. Champion, F. Crawford, G. Desvignes, P. C. C. Freire, G. Heald, F. A. Jenet, P. Lazarus, K. J. Lee, J. van Leeuwen, R. Lynch, M. A. Papa, R. Prix, R. Rosen, P. Scholz, X. Siemens, K. Stovall, A. Venkataraman and W. Zhu. *The Einstein@Home Search for Radio Pulsars and PSR J2007+2722 Discovery.* The Astrophysical Journal, vol. 773, page 91, August 2013. (Cited on page 13.)

[Aller 1985] H. D. Aller, M. F. Aller, G. E. Latimer and P. E. Hodge. *Spectra and linear polarizations of extragalactic variable sources at centimeter wavelengths.* Astrophysical Journal Supplement Series, vol. 59, pages 513–768, December 1985. (Cited on page 4.)

[Antoniadis 2013] J. Antoniadis, P. C. C. Freire, N. Wex, T. M. Tauris, R. S. Lynch, M. H. van Kerkwijk, M. Kramer, C. Bassa, V. S. Dhillon, T. Driebe, J. W. T. Hessels, V. M. Kaspi, V. I. Kondratiev, N. Langer, T. R. Marsh, M. A. McLaughlin, T. T. Pennucci, S. M. Ransom, I. H. Stairs, J. van Leeuwen, J. P. W. Verbiest and D. G. Whelan. *A Massive Pulsar in a Compact Relativistic Binary.* Science, vol. 340, page 448, April 2013. (Cited on page 9.)

[Arzoumanian 2002] Z. Arzoumanian, D. F. Chernoff and J. M. Cordes. *The Velocity Distribution of Isolated Radio Pulsars.* The Astrophysical Journal, vol. 568, pages 289–301, March 2002. (Cited on page 10.)

[Backer 1970] D. C. Backer. *Pulsar Nulling Phenomena.* Nature, vol. 228, pages 42–43, October 1970. (Cited on page 8.)

[Backer 1993] D. C. Backer, S. Hama, S. V. Hook and R. S. Foster. *Temporal variations of pulsar dispersion measures.* ApJ, vol. 404, no. 1, page 636, 1993. (Cited on page 54.)

[Barr 2013] E. D. Barr, D. J. Champion, M. Kramer, R. P. Eatough, P. C. C. Freire, R. Karuppusamy, K. J. Lee, J. P. W. Verbiest, C. G. Bassa, A. G. Lyne, B. Stappers, D. R. Lorimer and B. Klein. *The Northern High Time Resolution Universe pulsar survey - I. Setup and initial discoveries.* Monthly Notices of the Royal Astronomical Society, vol. 435, pages 2234–2245, November 2013. (Cited on page 12.)

[Basseville 1993] M. Basseville and I. Nikiforov. Detection of Abrupt Changes - Theory and Application, pages 1–469. April 1993. (Cited on page 49.)

[Bastian 2000] T. S. Bastian, G. A. Dulk and Y. Leblanc. *A Search for Radio Emission from Extrasolar Planets.* The Astrophysical Journal, vol. 545, pages 1058–1063, December 2000. (Cited on page 19.)

[Bates 2011] S. D. Bates, M. Bailes, N. D. R. Bhat, M. Burgay, S. Burke-Spolaor, N. D'Amico, A. Jameson, S. Johnston, M. J. Keith, M. Kramer, L. Levin, A. Lyne, S. Milia, A. Possenti, B. Stappers and W. van Straten. *The High Time Resolution Universe Pulsar Survey - II. Discovery of five millisecond pulsars.* Monthly Notices of the Royal Astronomical Society, vol. 416, pages 2455–2464, October 2011. (Cited on page 12.)

[Bates 2015] S. D. Bates, D. Thornton, M. Bailes, E. Barr, C. G. Bassa, N. D. R. Bhat, M. Burgay, S. Burke-Spolaor, D. J. Champion, C. M. L. Flynn, A. Jameson, S. Johnston, M. J. Keith, M. Kramer, L. Levin, A. Lyne, S. Milia, C. Ng, E. Petroff, A. Possenti, B. W. Stappers, W. van Straten and C. Tiburzi. *The High Time Resolution Universe survey - XI. Discovery of five recycled pulsars and the optical detectability of survey white dwarf companions.* Monthly Notices of the Royal Astronomical Society, vol. 446, pages 4019–4028, February 2015. (Cited on page 12.)

[Bilous 2015] A. Bilous, V. Kondratiev, M. Kramer, E. Keane, J. Hessels, B. Stappers, V. Malofeev, C. Sobey, R. Breton, S. Cooper, H. Falcke and A. Karastergiou. *A LOFAR census of non-recycled pulsars: average profiles, dispersion measures, flux densities, and spectra.* ArXiv e-prints, November 2015. (Cited on pages vi, 83 and 85.)

[Boyles 2013] J. Boyles, R. S. Lynch, S. M. Ransom, I. H. Stairs, D. R. Lorimer, M. A. McLaughlin, J. W. T. Hessels, V. M. Kaspi, V. I. Kondratiev, A. Archibald, A. Berndsen, R. F. Cardoso, A. Cherry, C. R. Epstein, C. Karako-Argaman, C. A. McPhee, T. Pennucci, M. S. E. Roberts, K. Stovall and J. van Leeuwen. *The Green Bank Telescope 350 MHz Drift-scan survey. I. Survey Observations and the Discovery of 13 Pulsars.* The Astrophysical Journal, vol. 763, page 80, February 2013. (Cited on page 13.)

[Braude 1978a] S. I. Braude, A. V. Megn, B. P. Riabov, N. K. Sharykin and I. N. Zhuk. *Decametric survey of discrete sources in the Northern sky. I - The*

UTR-2 radio telescope: Experimental techniques and data processing. Astrophysics and space science, vol. 54, pages 3–36, March 1978. (Cited on page 38.)

[Braude 1978b] S.Ya. Braude, A.V. Megn and L.G. Sodin. *Decameter wavelength radio telescope UTR-2 (in Russian).* Antennae, no. 26, pages 3–15, 1978. (Cited on page 24.)

[Braude 2002] S. Y. Braude, S. L. Rashkovsky, K. M. Sidorchuk, M. A. Sidorchuk, K. P. Sokolov, N. K. Sharykin and S. M. Zakharenko. *Decametric survey of discrete sources in the northern sky.* Astrophysics and space science, vol. 280, pages 235–300, May 2002. (Cited on page 38.)

[Bruk 1976] I. M. Bruk and B. I. Ustimenko. *Decametric radio emission from four pulsars.* Nature, vol. 260, page 766, April 1976. (Cited on page 5.)

[Bruk 1977] Iu. M. Bruk and B. Iu. Ustimenko. *Some features of the pulsed radiation from the pulsar 1919+21 at 16.7, 20 and 25 MHz.* Astrophysics and Space Science, 1977. (Cited on page 5.)

[Budding 1998] E. Budding, O. B. Slee and K. Jones. *Further Discussion of Binary Star Radio Survey Data.* Publications of the Astronomical Society of Australia, vol. 15, pages 183–188, July 1998. (Cited on page 16.)

[Burgay 2003] M. Burgay, N. D'Amico, A. Possenti, R. N. Manchester, A. G. Lyne, B. C. Joshi, M. A. McLaughlin, M. Kramer, J. M. Sarkissian, F. Camilo, V. Kalogera, C. Kim and D. R. Lorimer. *An increased estimate of the merger rate of double neutron stars from observations of a highly relativistic system.* Nature, vol. 426, pages 531–533, December 2003. (Cited on page 9.)

[Burgay 2013] M. Burgay, M. Bailes, S. D. Bates, N. D. R. Bhat, S. Burke-Spolaor, D. J. Champion, P. Coster, N. D'Amico, S. Johnston, M. J. Keith, M. Kramer, L. Levin, A. G. Lyne, S. Milia, C. Ng, A. Possenti, B. W. Stappers, D. Thornton, C. Tiburzi, W. van Straten and C. G. Bassa. *The High Time Resolution Universe Pulsar Survey - VII. Discovery of five millisecond pulsars and the different luminosity properties of binary and isolated recycled pulsars.* Monthly Notices of the Royal Astronomical Society, vol. 433, pages 259–269, July 2013. (Cited on page 12.)

[Burke 1955] B. F. Burke and K. L. Franklin. *Observations of a Variable Radio Source Associated with the Planet Jupiter.* Journal of Geophysical Research, vol. 60, pages 213–217, June 1955. (Cited on page 14.)

[Camilo 2003] F. Camilo. *Deep Searches for Young Pulsars.* In M. Bailes, D. J. Nice and S. E. Thorsett, editeurs, Radio Pulsars, volume 302 of *Astronomical Society of the Pacific Conference Series*, page 145, 2003. (Cited on page 10.)

[Clifton 1992] T. R. Clifton, A. G. Lyne, A. W. Jones, J. McKenna and M. Ashworth. *A high-frequency survey of the galactic plane for young and distant pulsars.* Monthly Notices of the Royal Astronomical Society, vol. 254, pages 177–184, January 1992. (Cited on page 12.)

[Coenen 2014] T. Coenen, J. van Leeuwen, J. W. T. Hessels, B. W. Stappers, V. I. Kondratiev, A. Alexov, R. P. Breton, A. Bilous, S. Cooper, H. Falcke, R. A. Fallows, V. Gajjar, J.-M. Grießmeier, T. E. Hassall, A. Karastergiou, E. F. Keane, M. Kramer, M. Kuniyoshi, A. Noutsos, S. Osłowski, M. Pilia, M. Serylak, C. Schrijvers, C. Sobey, S. ter Veen, J. Verbiest, P. Weltevrede, S. Wijnholds, K. Zagkouris, A. S. van Amesfoort, J. Anderson, A. Asgekar, I. M. Avruch, M. E. Bell, M. J. Bentum, G. Bernardi, P. Best, A. Bonafede, F. Breitling, J. Broderick, M. Brüggen, H. R. Butcher, B. Ciardi, A. Corstanje, A. Deller, S. Duscha, J. Eislöffel, R. Fender, C. Ferrari, W. Frieswijk, M. A. Garrett, F. de Gasperin, E. de Geus, A. W. Gunst, J. P. Hamaker, G. Heald, M. Hoeft, A. van der Horst, E. Juette, G. Kuper, C. Law, G. Mann, R. McFadden, D. McKay-Bukowski, J. P. McKean, H. Munk, E. Orru, H. Paas, M. Pandey-Pommier, A. G. Polatidis, W. Reich, A. Renting, H. Röttgering, A. Rowlinson, A. M. M. Scaife, D. Schwarz, J. Sluman, O. Smirnov, J. Swinbank, M. Tagger, Y. Tang, C. Tasse, S. Thoudam, C. Toribio, R. Vermeulen, C. Vocks, R. J. van Weeren, O. Wucknitz, P. Zarka and A. Zensus. *The LOFAR pilot surveys for pulsars and fast radio transients.* Astronomy and Astrophysics, vol. 570, page A60, October 2014. (Cited on page 14.)

[Cognard 1996] I. Cognard, J. A. Shrauner, J. H. Taylor and S. E. Thorsett. *Giant Radio Pulses from a Millisecond Pulsar.* Astrophysical Journal Letters, vol. 457, page L81, February 1996. (Cited on pages iii, 4 and 9.)

[Colgate 1971] S. A. Colgate and P. D. Noerdlinger. *Coherent Emission from Expanding Supernova Shells.* Astrophysical Journal, vol. 165, page 509, May 1971. (Cited on page 4.)

[Cordes 2002] J. M. Cordes and T. J. W. Lazio. *NE2001.I. A New Model for the Galactic Distribution of Free Electrons and its Fluctuations.* ArXiv Astrophysics e-prints, July 2002. (Cited on page 9.)

[Cordes 2004] J. M. Cordes and T. J. W. Lazio. *NE2001: A New Model for the Galactic Distribution of Free Electrons and its Fluctuations.* In Milky Way Surveys: The Structure and Evolution of our Galaxy, Proceedings of ASP Conference, volume 317, page 211, 2004. (Cited on page 60.)

[Cordes 2008] J. M. Cordes. *Arecibo Pulsar and Transient Surveys Using ALFA.* In C. Bassa, Z. Wang, A. Cumming and V. M. Kaspi, editeurs, 40 Years of Pulsars: Millisecond Pulsars, Magnetars and More, volume 983 of *American Institute of Physics Conference Series*, pages 567–575, February 2008. (Cited on page 12.)

[Davies 1970] J. G. Davies and M. I. Large. *A single-pulse search for pulsars.* Monthly Notices of the Royal Astronomical Society, vol. 149, page 301, 1970. (Cited on page 11.)

[Davies 1972] J. G. Davies, A. G. Lyne and J. H. Seiradakis. *Pulsar Associated with the Supernova Remnant IC 443.* Nature, vol. 240, pages 229–230, November 1972. (Cited on page 11.)

[Davies 1973] J. G. Davies, A. G. Lyne and J. H. Seiradakis. *Thirteen New Pulsars.* Nature Physical Science, vol. 244, pages 84–85, August 1973. (Cited on page 11.)

[Demorest 2010] P. B. Demorest, T. Pennucci, S. M. Ransom, M. S. E. Roberts and J. W. T. Hessels. *A two-solar-mass neutron star measured using Shapiro delay.* Nature, vol. 467, pages 1081–1083, October 2010. (Cited on page 9.)

[Deneva 2009] J. S. Deneva, J. M. Cordes, M. A. McLaughlin, D. J. Nice, D. R. Lorimer, F. Crawford, N. D. R. Bhat, F. Camilo, D. J. Champion, P. C. C. Freire, S. Edel, V. I. Kondratiev, J. W. T. Hessels, F. A. Jenet, L. Kasian, V. M. Kaspi, M. Kramer, P. Lazarus, S. M. Ransom, I. H. Stairs, B. W. Stappers, J. van Leeuwen, A. Brazier, A. Venkataraman, J. A. Zollweg and S. Bogdanov. *Arecibo Pulsar Survey Using ALFA: Probing Radio Pulsar Intermittency And Transients.* The Astrophysical Journal, vol. 703, no. 2, page 2259, 2009. (Cited on page 13.)

[Desch 1984] M. D. Desch and M. L. Kaiser. *Predictions for Uranus from a radiometric Bode's law.* Nature, vol. 310, pages 755–757, August 1984. (Cited on page 15.)

[Drake 1968] F. D. Drake and H. D. Craft. *Second Periodic Pulsation in Pulsars.* Nature, vol. 220, pages 231–235, October 1968. (Cited on page 83.)

[Dyks 2005] J. Dyks, B. Zhang and J. Gil. *Reversals of Radio Emission Direction in PSR B1822-09.* Astrophysical Journal Letters, vol. 626, pages L45–L47, June 2005. (Cited on page 83.)

[Edwards 2001] R. T. Edwards, M. Bailes, W. van Straten and M. C. Britton. *The Swinburne intermediate-latitude pulsar survey.* Monthly Notices of the Royal Astronomical Society, vol. 326, pages 358–374, September 2001. (Cited on page 12.)

[Falcke 2003] Heino Falcke and Peter Gorham. *Detecting radio emission from cosmic ray air showers and neutrinos with a digital radio telescope.* Astroparticle Physics, vol. 19, no. 4, pages 477 – 494, 2003. (Cited on page 3.)

[Fares 2010] R. Fares, J.-F. Donati, C. Moutou, M. M. Jardine, J.-M. Grießmeier, P. Zarka, E. L. Shkolnik, D. Bohlender, C. Catala and A. Collier Cameron. *Searching for star-planet interactions within the magnetosphere*

of HD189733. Monthly Notices of the Royal Astronomical Society, vol. 406, pages 409–419, July 2010. (Cited on page 18.)

[Farrell 1999] W. M. Farrell, M. D. Desch and P. Zarka. *On the possibility of coherent cyclotron emission from extrasolar planets*. Journal of Geophysical Research, vol. 104, pages 14025–14032, June 1999. (Cited on page 3.)

[Farrell 2003] W. M. Farrell, M. D. Desch, T. J. Lazio, T. Bastian and P. Zarka. *Limits on the Magnetosphere/Stellar Wind Interactions for the Extrasolar Planet about Tau Bootis*. In D. Deming and S. Seager, editeurs, Scientific Frontiers in Research on Extrasolar Planets, volume 294 of *Astronomical Society of the Pacific Conference Series*, pages 151–156, 2003. (Cited on page 19.)

[Farrell 2004] W. M. Farrell, T. J. W. Lazio, M. D. Desch, T. S. Bastian and P. Zarka. *Radio Emission from Extrasolar Planets*. In R. Norris and F. Stootman, editeurs, Bioastronomy 2002: Life Among the Stars, volume 213 of *IAU Symposium*, page 73, June 2004. (Cited on page 19.)

[Faucher-Giguère 2006] C.-A. Faucher-Giguère and V. M. Kaspi. *Birth and Evolution of Isolated Radio Pulsars*. The Astrophysical Journal, vol. 643, pages 332–355, May 2006. (Cited on pages 6 and 10.)

[Fomalont 2002] E. B. Fomalont and K. I. Kellermann. *THE MICROJANSKY SKY AT 8.4 GHz*. The Astronomical Journal, vol. 123, no. 1, pages 2402–2416, 2002. (Cited on page 46.)

[Fridman 2001] P. A. Fridman and W. A. Baan. *RFI mitigation methods in radio astronomy*. Astronomy and Astrophysics, vol. 378, no. 1, pages 327–344, 2001. (Cited on page 47.)

[Fruchter 1988] A. S. Fruchter, D. R. Stinebring and J. H. Taylor. *A millisecond pulsar in an eclipsing binary*. Nature, vol. 333, pages 237–239, May 1988. (Cited on page 9.)

[Gavriil 2008] F. P. Gavriil, M. E. Gonzalez, E. V. Gotthelf, V. M. Kaspi, M. A. Livingstone and P. M. Woods. *Magnetar-Like Emission from the Young Pulsar in Kes 75*. Science, vol. 319, pages 1802–, March 2008. (Cited on page 9.)

[George 2007] S. J. George and I. R. Stevens. *Giant Metrewave Radio Telescope low-frequency observations of extrasolar planetary systems*. Monthly Notices of the Royal Astronomical Society, vol. 382, pages 455–460, November 2007. (Cited on page 19.)

[George 2008] S. J. George and I. R. Stevens. *A deep 150MHz Giant Metrewave Radio Telescope survey in Eridanus*. Monthly Notices of the Royal Astronomical Society, vol. 390, pages 741–751, October 2008. (Cited on page 19.)

[Gil 1994] J. A. Gil, A. Jessner, J. Kijak, M. Kramer, V. Malofeev, I. Malov, J. H. Seiradakis, W. Sieber and R. Wielebinski. *Multifrequency study of PSR 1822-09.* Astronomy and Astrophysics, vol. 282, pages 45–53, February 1994. (Cited on page 83.)

[Grießmeier 2004] J.-M. Grießmeier, A. Stadelmann, T. Penz, H. Lammer, F. Selsis, I. Ribas, E. F. Guinan, U. Motschmann, H. K. Biernat and W. W. Weiss. *The effect of tidal locking on the magnetospheric and atmospheric evolution of "Hot Jupiters".* Astronomy and Astrophysics, vol. 425, pages 753–762, October 2004. (Cited on page 19.)

[Grießmeier 2007] J.-M. Grießmeier, P. Zarka and H. Spreeuw. *Predicting low-frequency radio fluxes of known extrasolar planets.* Astronomy and Astrophysics, vol. 475, pages 359–368, November 2007. (Cited on pages 3, 16, 135 and 138.)

[Grießmeier 2011] J.-M. Grießmeier, P. Zarka and J. N. Girard. *Observation of planetary radio emissions using large arrays.* Radio Science, vol. 46, page 0, December 2011. (Cited on pages iii, 17 and 135.)

[Hallinan 2013] G. Hallinan, S. K. Sirothia, A. Antonova, C. H. Ishwara-Chandra, S. Bourke, J. G. Doyle, J. Hartman and A. Golden. *Looking for a Pulse: A Search for Rotationally Modulated Radio Emission from the Hot Jupiter, τ Boötis b.* The Astrophysical Journal, vol. 762, page 34, January 2013. (Cited on page 20.)

[Han 2006] J. L. Han, R. N. Manchester, A. G. Lyne, G. J. Qiao and W. van Straten. *Pulsar Rotation Measures and the Large-Scale Structure of the Galactic Magnetic Field.* The Astrophysical Journal, vol. 642, pages 868–881, May 2006. (Cited on page 9.)

[Hankins 1975] T. H. Hankins and B. J. Rickett. *Pulsar signal processing.* Methods in computational physics. Volume 14 - Radio astronomy, vol. A76-22804 09-89, no. 1, pages 55–129, 1975. (Cited on page 57.)

[Hankins 2003] T. H. Hankins, J. S. Kern, J. C. Weatherall and J. A. Eilek. *Nanosecond radio bursts from strong plasma turbulence in the Crab pulsar.* Nature, vol. 422, pages 141–143, March 2003. (Cited on page 9.)

[Hankins 2007] T. H. Hankins and J. A. Eilek. *Radio Emission Signatures in the Crab Pulsar.* The Astrophysical Journal, vol. 670, pages 693–701, November 2007. (Cited on pages iii, 4 and 9.)

[Hassall 2012] T. E. Hassall, B. W. Stappers, J. W. T. Hessels, M. Kramer, A. Alexov, K. Anderson, T. Coenen, A. Karastergiou, E. F. Keane, V. I. Kondratiev, K. Lazaridis, J. van Leeuwen, A. Noutsos, M. Serylak, C. Sobey, J. P. W. Verbiest, P. Weltevrede, K. Zagkouris, R. Fender, R. A. M. J. Wijers,

L. Bähren, M. E. Bell, J. W. Broderick, S. Corbel, E. J. Daw, V. S. Dhillon, J. Eislöffel, H. Falcke, J.-M. Grießmeier, P. Jonker, C. Law, S. Markoff, J. C. A. Miller-Jones, R. Osten, E. Rol, A. M. M. Scaife, B. Scheers, P. Schellart, H. Spreeuw, J. Swinbank, S. ter Veen, M. W. Wise, R. Wijnands, O. Wucknitz, P. Zarka, A. Asgekar, M. R. Bell, M. J. Bentum, G. Bernardi, P. Best, A. Bonafede, A. J. Boonstra, M. Brentjens, W. N. Brouw, M. Brüggen, H. R. Butcher, B. Ciardi, M. A. Garrett, M. Gerbers, A. W. Gunst, M. P. van Haarlem, G. Heald, M. Hoeft, H. Holties, A. de Jong, L. V. E. Koopmans, M. Kuniyoshi, G. Kuper, G. M. Loose, P. Maat, J. Masters, J. P. McKean, H. Meulman, M. Mevius, H. Munk, J. E. Noordam, E. Orrú, H. Paas, M. Pandey-Pommier, V. N. Pandey, R. Pizzo, A. Polatidis, W. Reich, H. Röttgering, J. Sluman, M. Steinmetz, C. G. M. Sterks, M. Tagger, Y. Tang, C. Tasse, R. Vermeulen, R. J. van Weeren, S. J. Wijnholds and S. Yatawatta. *Wide-band simultaneous observations of pulsars: disentangling dispersion measure and profile variations.* Astronomy and Astrophysics, vol. 543, page A66, July 2012. (Cited on page 14.)

[Hermsen 2013] W. Hermsen, J. W. T. Hessels, L. Kuiper, J. van Leeuwen, D. Mitra, J. de Plaa, J. M. Rankin, B. W. Stappers, G. A. E. Wright, R. Basu, A. Alexov, T. Coenen, J.-M. Grießmeier, T. E. Hassall, A. Karastergiou, E. Keane, V. I. Kondratiev, M. Kramer, M. Kuniyoshi, A. Noutsos, M. Serylak, M. Pilia, C. Sobey, P. Weltevrede, K. Zagkouris, A. Asgekar, I. M. Avruch, F. Batejat, M. E. Bell, M. R. Bell, M. J. Bentum, G. Bernardi, P. Best, L. Bîrzan, A. Bonafede, F. Breitling, J. Broderick, M. Brüggen, H. R. Butcher, B. Ciardi, S. Duscha, J. Eislöffel, H. Falcke, R. Fender, C. Ferrari, W. Frieswijk, M. A. Garrett, F. de Gasperin, E. de Geus, A. W. Gunst, G. Heald, M. Hoeft, A. Horneffer, M. Iacobelli, G. Kuper, P. Maat, G. Macario, S. Markoff, J. P. McKean, M. Mevius, J. C. A. Miller-Jones, R. Morganti, H. Munk, E. Orrú, H. Paas, M. Pandey-Pommier, V. N. Pandey, R. Pizzo, A. G. Polatidis, S. Rawlings, W. Reich, H. Röttgering, A. M. M. Scaife, A. Schoenmakers, A. Shulevski, J. Sluman, M. Steinmetz, M. Tagger, Y. Tang, C. Tasse, S. ter Veen, R. Vermeulen, R. H. van de Brink, R. J. van Weeren, R. A. M. J. Wijers, M. W. Wise, O. Wucknitz, S. Yatawatta and P. Zarka. *Synchronous X-ray and Radio Mode Switches: A Rapid Global Transformation of the Pulsar Magnetosphere.* Science, vol. 339, pages 436–, January 2013. (Cited on pages 9 and 14.)

[Hess 2011] S. L. G. Hess and P. Zarka. *Modeling the radio signature of the orbital parameters, rotation, and magnetic field of exoplanets.* Astronomy and Astrophysics, vol. 531, page A29, July 2011. (Cited on page 18.)

[Hessels 2006] J. W. T. Hessels, S. M. Ransom, I. H. Stairs, P. C. C. Freire, V. M. Kaspi and F. Camilo. *A Radio Pulsar Spinning at 716 Hz.* Science, vol. 311, pages 1901–1904, March 2006. (Cited on page 9.)

[Hessels 2008] J. W. T. Hessels, S. M. Ransom, V. M. Kaspi, M. S. E. Roberts, D. J. Champion and B. W. Stappers. *The GBT350 Survey of the Northern Galactic Plane for Radio Pulsars and Transients.* In C. Bassa, Z. Wang, A. Cumming and V. M. Kaspi, editeurs, 40 Years of Pulsars: Millisecond Pulsars, Magnetars and More, volume 983 of *American Institute of Physics Conference Series*, pages 613–615, February 2008. (Cited on pages 13, 102 and 134.)

[Hessels 2010] J. W. T. Hessels, B. Stappers, A. Alexov, T. Coenen, T. Hassall, A. Karastergiou, V. K. Kondratiev, M. Kramer, J. van Leeuwen, J. D. Mol, A. Noutsos and P. Weltevrede. *Early Pulsar Observations with LOFAR.* In ISKAF2010 Science Meeting, page 25, 2010. (Cited on page 14.)

[Hessels 2011] J. W. T. Hessels, M. S. E. Roberts, M. A. McLaughlin, P. S. Ray, P. Bangale, S. M. Ransom, M. Kerr, F. Camilo and M. E. Decesar. *A 350-MHz GBT Survey of 50 Faint Fermi γ-ray Sources for Radio Millisecond Pulsars.* In M. Burgay, N. D'Amico, P. Esposito, A. Pellizzoni and A. Possenti, editeurs, American Institute of Physics Conference Series, volume 1357 of *American Institute of Physics Conference Series*, pages 40–43, August 2011. (Cited on page 10.)

[Hewish 1968] A. Hewish, S. J. Bell, J. D. H. Pilkington, P. F. Scott and R. A. Collins. *Observation of a Rapidly Pulsating Radio Source.* Nature, vol. 217, pages 709–713, February 1968. (Cited on page 10.)

[Hulse 1974] R. A. Hulse and J. H. Taylor. *A High-Sensitivity Pulsar Survey.* Astrophysical Journal, vol. 191, page L59, July 1974. (Cited on page 11.)

[Jackson 1989] P. D. Jackson, M. R. Kundu and S. M. White. *Quiescent and flaring radio emission from the flare stars AD Leonis, EQ Pegasi, UV Ceti, Wolf 630, YY Geminorum and YZ Canis Minoris.* Astronomy and Astrophysics, vol. 210, pages 284–294, February 1989. (Cited on pages iii and 4.)

[Johnston 1992] S. Johnston, A. G. Lyne, R. N. Manchester, D. A. Kniffen, N. D'Amico, J. Lim and M. Ashworth. *A high-frequency survey of the southern Galactic plane for pulsars.* Monthly Notices of the Royal Astronomical Society, vol. 255, pages 401–411, April 1992. (Cited on page 12.)

[Johnston 2003] S. Johnston and R. W. Romani. *Giant Pulses from PSR B0540-69 in the Large Magellanic Cloud.* The Astrophysical Journal, vol. 590, pages L95–L98, June 2003. (Cited on page 9.)

[Karako-Argaman 2015] C. Karako-Argaman, V. M. Kaspi, R. S. Lynch, J. W. T. Hessels, V. I. Kondratiev, M. A. McLaughlin, S. M. Ransom, A. M. Archibald, J. Boyles, F. A. Jenet, D. L. Kaplan, L. Levin, D. R. Lorimer, E. C. Madsen, M. S. E. Roberts, X. Siemens, I. H. Stairs, K. Stovall, J. K.

Swiggum and J. van Leeuwen. *Discovery and Follow-up of Rotating Radio Transients with the Green Bank and LOFAR Telescopes.* Astrophysical Journal, vol. 809, page 67, August 2015. (Cited on page 13.)

[Kaspi 2004] V. M. Kaspi, S. M. Ransom, D. C. Backer, R. Ramachandran, P. Demorest, J. Arons and A. Spitkovsky. *Green Bank Telescope Observations of the Eclipse of Pulsar "A" in the Double Pulsar Binary PSR J0737-3039.* The Astrophysical Journal, vol. 613, pages L137–L140, October 2004. (Cited on page 9.)

[Keane 2010] E. F. Keane, D. A. Ludovici, R. P. Eatough, M. Kramer, A. G. Lyne, M. A. McLaughlin and B. W. Stappers. *Further searches for Rotating Radio Transients in the Parkes Multi-beam Pulsar Survey.* Monthly Notices of the Royal Astronomical Society, vol. 401, pages 1057–1068, January 2010. (Cited on page 10.)

[Keane 2011] E. F. Keane, M. Kramer, A. G. Lyne, B. W. Stappers and M. A. McLaughlin. *Rotating Radio Transients: new discoveries, timing solutions and musings.* Monthly Notices of the Royal Astronomical Society, vol. 415, no. 4, pages 3065–3080, 2011. (Cited on pages iii, 4, 9 and 10.)

[Keane 2015] E. Keane, B. Bhattacharyya, M. Kramer, B. Stappers, E. F. Keane, B. Bhattacharyya, M. Kramer, B. W. Stappers, S. D. Bates, M. Burgay, S. Chatterjee, D. J. Champion, R. P. Eatough, J. W. T. Hessels, G. Janssen, K. J. Lee, J. van Leeuwen, J. Margueron, M. Oertel, A. Possenti, S. Ransom, G. Theureau and P. Torne. *A Cosmic Census of Radio Pulsars with the SKA.* Advancing Astrophysics with the Square Kilometre Array (AASKA14), page 40, 2015. (Cited on pages viii, 105 and 106.)

[Keith 2010] M. J. Keith, A. Jameson, W. van Straten, M. Bailes, S. Johnston, M. Kramer, A. Possenti, S. D. Bates, N. D. R. Bhat, M. Burgay, S. Burke-Spolaor, N. D'Amico, L. Levin, P. L. McMahon, S. Milia and B. W. Stappers. *The High Time Resolution Universe Pulsar Survey - I. System configuration and initial discoveries.* Monthly Notices of the Royal Astronomical Society, vol. 409, pages 619–627, December 2010. (Cited on page 12.)

[Keith 2011] M. J. Keith, S. Johnston, P. S. Ray, E. C. Ferrara, P. M. Saz Parkinson, Ö. Çelik, A. Belfiore, D. Donato, C. C. Cheung, A. A. Abdo, F. Camilo, P. C. C. Freire, L. Guillemot, A. K. Harding, M. Kramer, P. F. Michelson, S. M. Ransom, R. W. Romani, D. A. Smith, D. J. Thompson, P. Weltevrede and K. S. Wood. *Discovery of millisecond pulsars in radio searches of southern Fermi Large Area Telescope sources.* Monthly Notices of the Royal Astronomical Society, vol. 414, pages 1292–1300, June 2011. (Cited on page 10.)

[Keith 2012] M. J. Keith, S. Johnston, M. Bailes, S. D. Bates, N. D. R. Bhat, M. Burgay, S. Burke-Spolaor, N. D'Amico, A. Jameson, M. Kramer, L. Levin,

S. Milia, A. Possenti, B. W. Stappers, W. van Straten and D. Parent. *The High Time Resolution Universe Pulsar Survey - IV. Discovery and polarimetry of millisecond pulsars.* Monthly Notices of the Royal Astronomical Society, vol. 419, pages 1752–1765, January 2012. (Cited on page 12.)

[Knight 2006] H. S. Knight, M. Bailes, R. N. Manchester, S. M. Ord and B. A. Jacoby. *Green Bank Telescope Studies of Giant Pulses from Millisecond Pulsars.* The Astrophysical Journal, vol. 640, pages 941–949, April 2006. (Cited on page 9.)

[Kondratiev 2009] V. I. Kondratiev, M. A. McLaughlin, D. R. Lorimer, M. Burgay, A. Possenti, R. Turolla, S. B. Popov and S. Zane. *New Limits on Radio Emission from X-ray Dim Isolated Neutron Stars.* The Astrophysical Journal, vol. 702, pages 692–706, September 2009. (Cited on pages iii, 7, 95, 107 and 134.)

[Konovalenko 2014] O. O. Konovalenko, P. L. Tokarsky and S. N. Yerin. *Effective area of phased antenna array of GURT radio telescope.* In The 7th International Conference On Ultrawideband and Ultrashort Impulse Signals UWBUSIS-2014, 2014. (Cited on pages iv and 37.)

[Kozhin 2007] R. V. Kozhin, V. V. Vinogradov and D. M. Vavriv. *Low-noise, high dynamic range digital receiver-spectrometer for radio astronomy applications.* In MSMW Symp. Proc., Kharkov, Ukraine, 736-738, 2007., pages 736–738, 2007. (Cited on page 35.)

[Kramer 2006a] M. Kramer, A. G. Lyne, J. T. O'Brien, C. A. Jordan and D. R. Lorimer. *A Periodically Active Pulsar Giving Insight into Magnetospheric Physics.* Science, vol. 312, pages 549–551, April 2006. (Cited on pages 8 and 9.)

[Kramer 2006b] M. Kramer, I. H. Stairs, R. N. Manchester, M. A. McLaughlin, A. G. Lyne, R. D. Ferdman, M. Burgay, D. R. Lorimer, A. Possenti, N. D'Amico, J. M. Sarkissian, G. B. Hobbs, J. E. Reynolds, P. C. C. Freire and F. Camilo. *Tests of General Relativity from Timing the Double Pulsar.* Science, vol. 314, pages 97–102, October 2006. (Cited on page 9.)

[Kuz'min 1978] A. D. Kuz'min, V. M. Malofeev, Y. P. Shitov, J. G. Davies, A. G. Lyne and B. Rowson. *Spectra of nine pulsars at 61 - 1420 MHz.* Monthly Notices of the Royal Astronomical Society, vol. 185, pages 441–449, November 1978. (Cited on page 8.)

[Large 1971] M. L. Large and A. E. Vaughan. *A search of the galactic plane for high dispersion pulsars.* Monthly Notices of the Royal Astronomical Society, vol. 151, page 277, 1971. (Cited on page 11.)

[Lawson 1987] K. D. Lawson, C. J. Mayer, J. L. Osborne and M. L. Parkinson. *Variations in the Spectral Index of the Galactic Radio Continuum Emission*

in the Northern Hemisphere. Monthly Notices of the Royal Astronomical Society, vol. 225, page 307, March 1987. (Cited on page 12.)

[Lazarus 2015] P. Lazarus, A. Brazier, J. W. T. Hessels, C. Karako-Argaman, V. M. Kaspi, R. Lynch, E. Madsen, C. Patel, S. M. Ransom, P. Scholz, J. Swiggum, W. W. Zhu, B. Allen, S. Bogdanov, F. Camilo, F. Cardoso, S. Chatterjee, J. M. Cordes, F. Crawford, J. S. Deneva, R. Ferdman, P. C. C. Freire, F. A. Jenet, B. Knispel, K. J. Lee, J. van Leeuwen, D. R. Lorimer, A. G. Lyne, M. A. McLaughlin, X. Siemens, L. G. Spitler, I. H. Stairs, K. Stovall and A. Venkataraman. *Arecibo Pulsar Survey Using ALFA. IV. Mock Spectrometer Data Analysis, Survey Sensitivity, and the Discovery of 41 Pulsars*. ArXiv e-prints, April 2015. (Cited on page 13.)

[Lazio 2004] T. J. W. Lazio and W. M. Farrell. *Radio Detection of Extrasolar Planets: Present and Future Prospects*. In American Astronomical Society Meeting Abstracts, volume 36 of *Bulletin of the American Astronomical Society*, page 135.08, December 2004. (Cited on page 135.)

[Lazio 2007] T. J. W. Lazio and W. M. Farrell. *Magnetospheric Emissions from the Planet Orbiting τ Bootis: A Multiepoch Search*. The Astrophysical Journal, vol. 668, pages 1182–1188, October 2007. (Cited on page 19.)

[Lazio 2010] T. J. W. Lazio, S. Carmichael, J. Clark, E. Elkins, P. Gudmundsen, Z. Mott, M. Szwajkowski and L. A. Hennig. *A Blind Search for Magnetospheric Emissions from Planetary Companions to Nearby Solar-Type Stars*. The Astronomical Journal, vol. 139, pages 96–101, January 2010. (Cited on page 19.)

[Lecavelier des Etangs 2009] A. Lecavelier des Etangs, S. K. Sirothia, Gopal-Krishna and P. Zarka. *GMRT radio observations of the transiting extrasolar planet HD 189733 b at 244 and 614 MHz*. Astronomy and Astrophysics, vol. 500, pages L51–L54, June 2009. (Cited on page 20.)

[Lecavelier des Etangs 2013] A. Lecavelier des Etangs, S. K. Sirothia, Gopal-Krishna and P. Zarka. *Hint of 150 MHz radio emission from the Neptune-mass extrasolar transiting planet HAT-P-11b*. Astronomy and Astrophysics, vol. 552, page A65, April 2013. (Cited on page 20.)

[Lorimer 1993] D. R. Lorimer, M. Bailes, R. J. Dewey and P. A. Harrison. *Pulsar Statistics - the Birthrate and Initial Spin Periods of Radio Pulsars*. Monthly Notices of the Royal Astronomical Society, vol. 263, page 403, July 1993. (Cited on page 10.)

[Lorimer 1995] D. R. Lorimer, J. A. Yates, A. G. Lyne and D. M. Gould. *Multi-frequency flux density measurements of 280 pulsars*. Monthly Notices of the Royal Astronomical Society, vol. 273, pages 411–421, March 1995. (Cited on page 11.)

[Lorimer 2006] D. R. Lorimer, A. J. Faulkner, A. G. Lyne, R. N. Manchester, M. Kramer, M. A. McLaughlin, G. Hobbs, A. Possenti, I. H. Stairs, F. Camilo, M. Burgay, N. D'Amico, A. Corongiu and F. Crawford. *The Parkes Multibeam Pulsar Survey - VI. Discovery and timing of 142 pulsars and a Galactic population analysis.* Monthly Notices of the Royal Astronomical Society, vol. 372, pages 777–800, October 2006. (Cited on pages 6, 10 and 12.)

[Lorimer 2007] D. R. Lorimer, M. Bailes, M. A. McLaughlin, D. J. Narkevic and F. Crawford. *A Bright Millisecond Radio Burst of Extragalactic Origin.* Science, vol. 318, pages 777–, November 2007. (Cited on pages iii, 3 and 4.)

[Lynch 2013] R. S. Lynch, J. Boyles, S. M. Ransom, I. H. Stairs, D. R. Lorimer, M. A. McLaughlin, J. W. T. Hessels, V. M. Kaspi, V. I. Kondratiev, A. M. Archibald, A. Berndsen, R. F. Cardoso, A. Cherry, C. R. Epstein, C. Karako-Argaman, C. A. McPhee, T. Pennucci, M. S. E. Roberts, K. Stovall and J. van Leeuwen. *The Green Bank Telescope 350 MHz Drift-scan Survey II: Data Analysis and the Timing of 10 New Pulsars, Including a Relativistic Binary.* The Astrophysical Journal, vol. 763, page 81, February 2013. (Cited on page 13.)

[Lyne 1993] A. G. Lyne, J. D. Biggs, P. A. Harrison and M. Bailes. *A long-period globular-cluster pulsar in an eclipsing binary system.* Nature, vol. 361, pages 47–49, January 1993. (Cited on page 9.)

[Lyne 1998] A. G. Lyne, R. N. Manchester, D. R. Lorimer, M. Bailes, N. D'Amico, T. M. Tauris, S. Johnston, J. F. Bell and L. Nicastro. *The Parkes Southern Pulsar Survey - II. Final results and population analysis.* Monthly Notices of the Royal Astronomical Society, vol. 295, pages 743–755, April 1998. (Cited on page 12.)

[Lyne 2004] A. G. Lyne, M. Burgay, M. Kramer, A. Possenti, R. N. Manchester, F. Camilo, M. A. McLaughlin, D. R. Lorimer, N. D'Amico, B. C. Joshi, J. Reynolds and P. C. C. Freire. *A Double-Pulsar System: A Rare Laboratory for Relativistic Gravity and Plasma Physics.* Science, vol. 303, pages 1153–1157, February 2004. (Cited on page 9.)

[Lyne 2010] A. Lyne, G. Hobbs, M. Kramer, I. Stairs and B. Stappers. *Switched Magnetospheric Regulation of Pulsar Spin-Down.* Science, vol. 329, pages 408–, July 2010. (Cited on page 9.)

[Majid 2006] W. Majid, D. Winterhalter, I. Chandra, T. Kuiper, J. Lazio, C. Naudet and P. Zarka. *Search for Radio Emission from Extrasolar Planets: Preliminary Analysis of GMRT Data.* In H. O. Rucker, W. Kurth and G. Mann, editeurs, Planetary Radio Emissions VI, page 589, 2006. (Cited on page 19.)

[Malofeev 1994] V. M. Malofeev, J. A. Gil, A. Jessner, I. F. Malov, J. H. Seiradakis, W. Sieber and R. Wielebinski. *Spectra of 45 pulsars.* Astronomy and Astrophysics, vol. 285, pages 201–208, May 1994. (Cited on page 8.)

[Manchester 1978] R. N. Manchester, A. G. Lyne, J. H. Taylor, J. M. Durdin, M. I. Large and A. G. Little. *The second Molonglo pulsar survey - discovery of 155 pulsars.* Monthly Notices of the Royal Astronomical Society, vol. 185, pages 409–421, November 1978. (Cited on page 11.)

[Manchester 1996] R. N. Manchester, A. G. Lyne, N. D'Amico, M. Bailes, S. Johnston, D. R. Lorimer, P. A. Harrison, L. Nicastro and J. F. Bell. *The Parkes Southern Pulsar Survey. I. Observing and data analysis systems and initial results.* Monthly Notices of the Royal Astronomical Society, vol. 279, pages 1235–1250, April 1996. (Cited on page 12.)

[Manchester 2001] R. N. Manchester, A. G. Lyne, F. Camilo, J. F. Bell, V. M. Kaspi, N. D'Amico, N. P. F. McKay, F. Crawford, I. H. Stairs, A. Possenti, M. Kramer and D. C. Sheppard. *The Parkes multi-beam pulsar survey - I. Observing and data analysis systems, discovery and timing of 100 pulsars.* Monthly Notices of the Royal Astronomical Society, vol. 328, pages 17–35, November 2001. (Cited on page 12.)

[Manchester 2005] R. N. Manchester, G. B. Hobbs, A. Teoh and M. Hobbs. *The Australia Telescope National Facility Pulsar Catalogue.* The Astronomical Journal, vol. 129, pages 1993–2006, April 2005. (Cited on pages 84, 94 and 102.)

[Markwardt 2009] C. B. Markwardt. *Non-Linear Least Squares Fitting in IDL with MPFIT.* In Proceedings of Astronomical Data Analysis Software and Systems XVIII, Quebec, Canada, ASP Conference Series, volume 411, 2009. (Cited on page 77.)

[Maron 2000] O. Maron, J. Kijak, M. Kramer and R. Wielebinski. *Pulsar spectra of radio emission.* Astronomy and Astrophysics Supplement, vol. 147, pages 195–203, December 2000. (Cited on page 6.)

[McLaughlin 2006] M. A. McLaughlin, A. G. Lyne, D. R. Lorimer, M. Kramer, A. J. Faulkner, R. N. Manchester, J. M. Cordes, F. Camilo, A. Possenti, I. H. Stairs, G. Hobbs, N. D'Amico, M. Burgay and J. T. O'Brien. *Transient radio bursts from rotating neutron stars.* Nature, vol. 439, pages 817–820, 2006. (Cited on pages 9 and 12.)

[Morris 1997] D. Morris, M. Kramer, C. Thum, R. Wielebinski, M. Grewing, J. Penalver, A. Jessner, G. Butin and W. Brunswig. *Pulsar detection at 87GHz.* Astronomy and Astrophysics, vol. 322, pages L17–L20, June 1997. (Cited on page 5.)

[Mottez 2014] F. Mottez and P. Zarka. *Radio emissions from pulsar companions: a refutable explanation for galactic transients and fast radio bursts.* Astronomy and Astrophysics, vol. 569, page A86, September 2014. (Cited on page 9.)

[Ng 2014] C. Ng, M. Bailes, S. D. Bates, N. D. R. Bhat, M. Burgay, S. Burke-Spolaor, D. J. Champion, P. Coster, S. Johnston, M. J. Keith, M. Kramer, L. Levin, E. Petroff, A. Possenti, B. W. Stappers, W. van Straten, D. Thornton, C. Tiburzi, C. G. Bassa, P. C. C. Freire, L. Guillemot, A. G. Lyne, T. M. Tauris, R. M. Shannon and N. Wex. *The High Time Resolution Universe pulsar survey - X. Discovery of four millisecond pulsars and updated timing solutions of a further 12.* Monthly Notices of the Royal Astronomical Society, vol. 439, pages 1865–1883, April 2014. (Cited on page 12.)

[Nichols 2011] J. D. Nichols. *Magnetosphere-ionosphere coupling at Jupiter-like exoplanets with internal plasma sources: implications for detectability of auroral radio emissions.* Monthly Notices of the Royal Astronomical Society, vol. 414, pages 2125–2138, July 2011. (Cited on page 18.)

[Offringa 2010] A. R. Offringa, A. G. de Bruyn, M. Biehl, S. Zaroubi, G. Bernardi and V. N. Pandey. *Post-correlation radio frequency interference classification methods.* Monthly Notices of the Royal Astronomical Society, vol. 405, no. 1, pages 155–167, 2010. (Cited on pages vi, 47, 49, 51, 68, 69 and 70.)

[Offringa 2012a] A. R. Offringa. *Algorithms for Radio Interference Detection and Removal.* PhD thesis, http://andreoffringa.org/pdfs/thesis/thesis-aroffringa.pdf, 2012. (Cited on pages 47 and 49.)

[Offringa 2012b] A. R. Offringa, J. J. van de Gronde and J. B. T. M. Roerdink. *A morphological algorithm for improving radio-frequency interference detection.* Astronomy & Astrophysics, vol. A95, no. 1, page 539, 2012. (Cited on page 71.)

[Page 1954] E. S. Page. *Continuous inspection schemes.* Biometrika, vol. 41, no. 1, pages 100–115, 1954. (Cited on page 49.)

[Petroff 2015] E. Petroff, E. F. Keane, E. D. Barr, J. E. Reynolds, J. Sarkissian, P. G. Edwards, J. Stevens, C. Brem, A. Jameson, S. Burke-Spolaor, S. Johnston, N. D. R. Bhat, P. C. S. Kudale and S. Bhandari. *Identifying the source of perytons at the Parkes radio telescope.* Monthly Notices of the Royal Astronomical Society, vol. 451, pages 3933–3940, August 2015. (Cited on page 133.)

[Petrova 2010] S. A. Petrova. *The Mechanism of Component Formation Out of the Main Pulse of a Radio Pulsar. I. The Precursor.* Radio Physics and Radio Astronomy, vol. 1, pages 19–26, 2010. (Cited on page 83.)

[Rankin 1986] J. M. Rankin. *Toward an empirical theory of pulsar emission. III - Mode changing, drifting subpulses, and pulse nulling.* Astrophysical Journal, vol. 301, pages 901–922, February 1986. (Cited on page 83.)

[Ransom 2011] S. M. Ransom, P. S. Ray, F. Camilo, M. S. E. Roberts, Ö. Çelik, M. T. Wolff, C. C. Cheung, M. Kerr, T. Pennucci, M. E. DeCesar, I. Cognard, A. G. Lyne, B. W. Stappers, P. C. C. Freire, J. E. Grove, A. A. Abdo, G. Desvignes, D. Donato, E. C. Ferrara, N. Gehrels, L. Guillemot, C. Gwon, A. K. Harding, S. Johnston, M. Keith, M. Kramer, P. F. Michelson, D. Parent, P. M. Saz Parkinson, R. W. Romani, D. A. Smith, G. Theureau, D. J. Thompson, P. Weltevrede, K. S. Wood and M. Ziegler. *Three Millisecond Pulsars in Fermi LAT Unassociated Bright Sources.* The Astrophysical Journal Letters, vol. 727, page L16, January 2011. (Cited on page 10.)

[Rees 1977] M. J. Rees. *A better way of searching for black-hole explosions.* Nature, vol. 266, page 333, March 1977. (Cited on page 4.)

[Ruderman 1975] M. A. Ruderman and P. G. Sutherland. *Theory of pulsars - Polar caps, sparks, and coherent microwave radiation.* Astrophysical Journal, vol. 196, pages 51–72, February 1975. (Cited on page 83.)

[Ryabov 2004] V. B. Ryabov, P. Zarka and B. P. Ryabov. *Search of exoplanetary radio signals in the presence of strong interference: enhancing sensitivity by data accumulation.* Planetary and Space Science, vol. 52, pages 1479–1491, December 2004. (Cited on page 20.)

[Ryabov 2010] V. B. Ryabov, D. M. Vavriv, P. Zarka, B. P. Ryabov, R. Kozhin, V. V. Vinogradov and L. Denis. *A low-noise, high-dynamic-range, digital receiver for radio astronomy applications: an efficient solution for observing radio-bursts from Jupiter, the Sun, pulsars, and other astrophysical plasmas below 30 MHz.* Astronomy & Astrophysics, vol. A16, no. 1, page 510, 2010. (Cited on pages 35 and 62.)

[Sagiv 2002] A. Sagiv and E. Waxman. *Collective Processes in Relativistic Plasma and Their Implications for Gamma-Ray Burst Afterglows.* The Astrophysical Journal, vol. 574, pages 861–872, August 2002. (Cited on page 4.)

[Sirothia 2014] S. K. Sirothia, A. Lecavelier des Etangs, Gopal-Krishna, N. G. Kantharia and C. H. Ishwar-Chandra. *Search for 150 MHz radio emission from extrasolar planets in the TIFR GMRT Sky Survey.* Astronomy and Astrophysics, vol. 562, page A108, February 2014. (Cited on page 20.)

[Slee 1986] O. B. Slee, S. K. Alurkar and A. D. Bobra. *Flux densities, spectra and variability of pulsars at metre wavelengths.* Australian Journal of Physics, vol. 39, pages 103–114, 1986. (Cited on page 8.)

[Spitler 2014] L. G. Spitler, J. M. Cordes, J. W. T. Hessels, D. R. Lorimer, M. A. McLaughlin, S. Chatterjee, F. Crawford, J. S. Deneva, V. M. Kaspi, R. S.

Wharton, B. Allen, S. Bogdanov, A. Brazier, F. Camilo, P. C. C. Freire, F. A. Jenet, C. Karako-Argaman, B. Knispel, P. Lazarus, K. J. Lee, J. van Leeuwen, R. Lynch, S. M. Ransom, P. Scholz, X. Siemens, I. H. Stairs, K. Stovall, J. K. Swiggum, A. Venkataraman, W. W. Zhu, C. Aulbert and H. Fehrmann. *Fast Radio Burst Discovered in the Arecibo Pulsar ALFA Survey.* The Astrophysical Journal, vol. 790, page 101, August 2014. (Cited on page 13.)

[Staelin 1968] D. H. Staelin and E. C. Reifenstein III. *Pulsating Radio Sources near the Crab Nebula.* Science, vol. 162, pages 1481–1483, December 1968. (Cited on page 10.)

[Stanislavsky 2011] A. A. Stanislavsky, E. P. Abranin, A. A. Konovalenko and A. A. Koval. *Heliograph of the UTR-2 Radio Telescope. I. General Scheme.* Radio Physics and Radio Astronomy (in Russian), 2011. (Cited on page 137.)

[Stappers 1996] B. W. Stappers, M. Bailes, A. G. Lyne, R. N. Manchester, N. D'Amico, T. M. Tauris, D. R. Lorimer, S. Johnston and J. S. Sandhu. *Probing the Eclipse Region of a Binary Millisecond Pulsar.* Astrophysical Journal Letters, vol. 465, page L119, July 1996. (Cited on page 9.)

[Stappers 2011] B. W. Stappers, J. W. T. Hessels, A. Alexov, K. Anderson, T. Coenen, T. Hassall, A. Karastergiou, V. I. Kondratiev, M. Kramer, J. van Leeuwen, J. D. Mol, A. Noutsos, J. W. Romein, P. Weltevrede, R. Fender, R. A. M. J. Wijers, L. Bähren, M. E. Bell, J. Broderick, E. J. Daw, V. S. Dhillon, J. Eislöffel, H. Falcke, J. Griessmeier, C. Law, S. Markoff, J. C. A. Miller-Jones, B. Scheers, H. Spreeuw, J. Swinbank, S. Ter Veen, M. W. Wise, O. Wucknitz, P. Zarka, J. Anderson, A. Asgekar, I. M. Avruch, R. Beck, P. Bennema, M. J. Bentum, P. Best, J. Bregman, M. Brentjens, R. H. van de Brink, P. C. Broekema, W. N. Brouw, M. Brüggen, A. G. de Bruyn, H. R. Butcher, B. Ciardi, J. Conway, R.-J. Dettmar, A. van Duin, J. van Enst, M. Garrett, M. Gerbers, T. Grit, A. Gunst, M. P. van Haarlem, J. P. Hamaker, G. Heald, M. Hoeft, H. Holties, A. Horneffer, L. V. E. Koopmans, G. Kuper, M. Loose, P. Maat, D. McKay-Bukowski, J. P. McKean, G. Miley, R. Morganti, R. Nijboer, J. E. Noordam, M. Norden, H. Olofsson, M. Pandey-Pommier, A. Polatidis, W. Reich, H. Röttgering, A. Schoenmakers, J. Sluman, O. Smirnov, M. Steinmetz, C. G. M. Sterks, M. Tagger, Y. Tang, R. Vermeulen, N. Vermaas, C. Vogt, M. de Vos, S. J. Wijnholds, S. Yatawatta and A. Zensus. *Observing pulsars and fast transients with LOFAR.* Astronomy and Astrophysics, vol. 530, page A80, June 2011. (Cited on pages 13, 14 and 105.)

[Stokes 1985] G. H. Stokes, J. H. Taylor, J. M. Welsberg and R. J. Dewey. *A survey for short-period pulsars.* Nature, vol. 317, page 787, October 1985. (Cited on page 11.)

[Stokes 1986] G. H. Stokes, D. J. Segelstein, J. H. Taylor and R. J. Dewey. *Results of two surveys for fast pulsars.* Astrophysical Journal, vol. 311, pages 694–700, December 1986. (Cited on page 11.)

[Stovall 2014] K. Stovall, R. S. Lynch, S. M. Ransom, A. M. Archibald, S. Banaszak, C. M. Biwer, J. Boyles, L. P. Dartez, D. Day, A. J. Ford, J. Flanigan, A. Garcia, J. W. T. Hessels, J. Hinojosa, F. A. Jenet, D. L. Kaplan, C. Karako-Argaman, V. M. Kaspi, V. I. Kondratiev, S. Leake, D. R. Lorimer, G. Lunsford, J. G. Martinez, A. Mata, M. A. McLaughlin, M. S. E. Roberts, M. D. Rohr, X. Siemens, I. H. Stairs, J. van Leeuwen, A. N. Walker and B. L. Wells. *The Green Bank Northern Celestial Cap Pulsar Survey. I. Survey Description, Data Analysis, and Initial Results.* The Astrophysical Journal, vol. 791, page 67, August 2014. (Cited on pages 9 and 13.)

[Thorsett 1991] S. E. Thorsett. *Frequency dependence of pulsar integrated profiles.* Astrophysical Journal, vol. 377, pages 263–267, August 1991. (Cited on pages vii and 86.)

[Tkachov 2013] V. M. Tkachov, V. V. Zakharenko, Ia. Yu. Vasylieva, Yu. A. Tsarin, E. Yu. Bannikova, V. V. Ilyushin, V. E. Savanevych, O. V. Gerasimenko, O. B. Annenkov, S. F. Kulishenko and D. F. Kulishenko. *Using grid-technologies for solving problems in radio physics and radio astronomy.* Radio Physics and Radio Astronomy (in Russian), vol. 18, no. 2, 2013. (Cited on page 59.)

[Treumann 2006] R. A. Treumann. *The electron-cyclotron maser for astrophysical application.* The Astronomy and Astrophysics Review, vol. 13, pages 229–315, August 2006. (Cited on page 14.)

[Ulyanov 2006] O. M. Ulyanov, V. V. Zakharenko, A. A. Konovalenko, A. Lecacheux, C. Rosolen and H. O. Rucker. *Detection Of The Individual Pulses Of The Pulsars 0809+74; 0834+06; 0950+08; 0943+10; 1133+16 At Decameter Wave Range.* In IAU Joint Discussion, volume 2 of *IAU Joint Discussion*, page 12, August 2006. (Cited on pages 9, 52 and 134.)

[Ulyanov 2012] O. M. Ulyanov and V. V. Zakharenko. *Energy of anomalously intense pulses of pulsars in decameter range.* Astronomical journal (in Russian), 2012. (Cited on page 105.)

[Ulyanov 2015] O.M. Ulyanov, M.A. Sidorchuk, V.V. Zakharenko, S.N. Yerin, I.N. Bubnov, A.A. Skoryk, A.I. Shevtsova, M.S. Plakhov, D.V. Mukha and E.R. Rudavin. *New technique of testing and calibration of the UTR-2 radio telescope.* In Proceedings of International Conference on Antenna Theory and Techniques (ICATT), 2015. (Cited on pages 46 and 134.)

[Usov 2000] V. V. Usov and J. I. Katz. *Low frequency radio pulses from gamma-ray bursts?* Astronomy and Astrophysics, vol. 364, pages 655–659, December 2000. (Cited on page 4.)

[van Haarlem 2013] M. P. van Haarlem, M. W. Wise, A. W. Gunst, G. Heald, J. P. McKean, J. W. T. Hessels, A. G. de Bruyn, R. Nijboer, J. Swinbank, R. Fallows, M. Brentjens, A. Nelles, R. Beck, H. Falcke, R. Fender, J. Hörandel, L. V. E. Koopmans, G. Mann, G. Miley, H. Röttgering, B. W. Stappers, R. A. M. J. Wijers, S. Zaroubi, M. van den Akker, A. Alexov, J. Anderson, K. Anderson, A. van Ardenne, M. Arts, A. Asgekar, I. M. Avruch, F. Batejat, L. Bähren, M. E. Bell, M. R. Bell, I. van Bemmel, P. Bennema, M. J. Bentum, G. Bernardi, P. Best, L. Bîrzan, A. Bonafede, A.-J. Boonstra, R. Braun, J. Bregman, F. Breitling, R. H. van de Brink, J. Broderick, P. C. Broekema, W. N. Brouw, M. Brüggen, H. R. Butcher, W. van Cappellen, B. Ciardi, T. Coenen, J. Conway, A. Coolen, A. Corstanje, S. Damstra, O. Davies, A. T. Deller, R.-J. Dettmar, G. van Diepen, K. Dijkstra, P. Donker, A. Doorduin, J. Dromer, M. Drost, A. van Duin, J. Eislöffel, J. van Enst, C. Ferrari, W. Frieswijk, H. Gankema, M. A. Garrett, F. de Gasperin, M. Gerbers, E. de Geus, J.-M. Grießmeier, T. Grit, P. Gruppen, J. P. Hamaker, T. Hassall, M. Hoeft, H. A. Holties, A. Horneffer, A. van der Horst, A. van Houwelingen, A. Huijgen, M. Iacobelli, H. Intema, N. Jackson, V. Jelic, A. de Jong, E. Juette, D. Kant, A. Karastergiou, A. Koers, H. Kollen, V. I. Kondratiev, E. Kooistra, Y. Koopman, A. Koster, M. Kuniyoshi, M. Kramer, G. Kuper, P. Lambropoulos, C. Law, J. van Leeuwen, J. Lemaitre, M. Loose, P. Maat, G. Macario, S. Markoff, J. Masters, R. A. McFadden, D. McKay-Bukowski, H. Meijering, H. Meulman, M. Mevius, E. Middelberg, R. Millenaar, J. C. A. Miller-Jones, R. N. Mohan, J. D. Mol, J. Morawietz, R. Morganti, D. D. Mulcahy, E. Mulder, H. Munk, L. Nieuwenhuis, R. van Nieuwpoort, J. E. Noordam, M. Norden, A. Noutsos, A. R. Offringa, H. Olofsson, A. Omar, E. Orrú, R. Overeem, H. Paas, M. Pandey-Pommier, V. N. Pandey, R. Pizzo, A. Polatidis, D. Rafferty, S. Rawlings, W. Reich, J.-P. de Reijer, J. Reitsma, G. A. Renting, P. Riemers, E. Rol, J. W. Romein, J. Roosjen, M. Ruiter, A. Scaife, K. van der Schaaf, B. Scheers, P. Schellart, A. Schoenmakers, G. Schoonderbeek, M. Serylak, A. Shulevski, J. Sluman, O. Smirnov, C. Sobey, H. Spreeuw, M. Steinmetz, C. G. M. Sterks, H.-J. Stiepel, K. Stuurwold, M. Tagger, Y. Tang, C. Tasse, I. Thomas, S. Thoudam, M. C. Toribio, B. van der Tol, O. Usov, M. van Veelen, A.-J. van der Veen, S. ter Veen, J. P. W. Verbiest, R. Vermeulen, N. Vermaas, C. Vocks, C. Vogt, M. de Vos, E. van der Wal, R. van Weeren, H. Weggemans, P. Weltevrede, S. White, S. J. Wijnholds, T. Wilhelmsson, O. Wucknitz, S. Yatawatta, P. Zarka, A. Zensus and J. van Zwieten. *LOFAR: The LOw-Frequency ARray.* Astronomy and Astrophysics, vol. 556, page A2, August 2013. (Cited on page 13.)

[van Leeuwen 2010] J. van Leeuwen and B. W. Stappers. *Finding pulsars with LOFAR.* A&A, vol. 509, page A7, 2010. (Cited on pages 10 and 14.)

[Vaughan 1969] A. E. Vaughan and M. I. Large. *Pulsar observations at Molonglo.* Proceedings of the Astronomical Society of Australia, vol. 1, page 220, March 1969. (Cited on page 11.)

[Vranesevic 2004] N. Vranesevic, R. N. Manchester, D. R. Lorimer, G. B. Hobbs, A. G. Lyne, M. Kramer, F. Camilo, I. H. Stairs, V. M. Kaspi, N. D'Amico, A. Possenti, F. Crawford, A. J. Faulkner and M. A. McLaughlin. *Pulsar Birthrates from the Parkes Multibeam Survey.* The Astrophysical Journal, vol. 617, pages L139–L142, December 2004. (Cited on page 6.)

[Walter 1996] F. M. Walter, S. J. Wolk and R. Neuhäuser. *Discovery of a nearby isolated neutron star.* Nature, vol. 379, pages 233–235, January 1996. (Cited on page 10.)

[Weekes 2001] T. C. Weekes. *Radio pulses from cosmic ray air showers.* In D. Saltzberg and P. Gorham, editeurs, Radio Detection of High Energy Particles, volume 579 of *American Institute of Physics Conference Series*, pages 3–13, July 2001. (Cited on page 3.)

[Weltevrede 2006] P. Weltevrede, R. T. Edwards and B. W. Stappers. *The subpulse modulation properties of pulsars at 21 cm.* Astronomy And Astrophysics, vol. 445, pages 243–272, January 2006. (Cited on page 83.)

[Winglee 1986] R. M. Winglee, G. A. Dulk and T. S. Bastian. *A search for cyclotron maser radiation from substellar and planet-like companions of nearby stars.* The Astrophysical Journal, vol. 309, pages L59–L62, October 1986. (Cited on page 19.)

[Winkel 2006] B. Winkel, J. Kerp and S. Stanko. *RFI detection by automated feature extraction and statistical analysis.* Astron. Nachr., vol. AN 999, no. 88, pages 789–801, 2006. (Cited on page 64.)

[Winterhalter 2006] D. Winterhalter, T. Kuiper, W. Majid, I. Chandra, J. Lazio, P. Zarka, C. Naudet, G. Bryden, W. Gonzalez and R. Treumann. *Search for Radio Emissions from Extrasolar Planets: the Observation Campaign.* In H. O. Rucker, W. Kurth and G. Mann, editeurs, Planetary Radio Emissions VI, page 595, 2006. (Cited on page 19.)

[Woods 2006] P. M. Woods and C. Thompson. Soft gamma repeaters and anomalous X-ray pulsars: magnetar candidates, pages 547–586. April 2006. (Cited on page 10.)

[Yantis 1977] W. F. Yantis, W. T. Sullivan III and W. C. Erickson. *A Search for Extra-Solar Jovian Planets by Radio Techniques.* In Bulletin of the American Astronomical Society, volume 9 of *Bulletin of the American Astronomical Society*, page 453, June 1977. (Cited on page 19.)

[Zakharenko 2011] V. V. Zakharenko, A. V. Markova and Y. Y. Vasylyeva. *Search for Pulsed Radio Emission from X-Ray DIM Isolated Neutron Stars at Decameter Wavelengths.* Radio Physics and Radio Astronomy, vol. 2, pages 15–21, 2011. (Cited on page 95.)

[Zakharenko 2013] V. V. Zakharenko, I. Y. Vasylieva, A. A. Konovalenko, O. M. Ulyanov, M. Serylak, P. Zarka, J.-M. Griessmeier, I. Cognard and V. S. Nikolaenko. *Detection of decametre-wavelength pulsed radio emission of 40 known pulsars.* Mon. Not. R. Astron. Soc., vol. 431, no. 1, pages 3624–3641, 2013. (Cited on pages v, vi, vii, 5, 21, 47, 48, 54, 56, 57, 83, 85, 86, 88, 94, 102, 103, 134 and 135.)

[Zarka 1997] Philippe Zarka, Julien Queinnec, Boris P. Ryabov, Vladimir B. Ryabov, Vyacheslav A. Shevchenko, Alexei V. Arkhipov, Helmut O. Rucker, Laurent Denis, Alain Gerbault, Patrick Dierich and Carlo Rosolen. *Ground-based high sensitivity radio astronomy at decameter wavelengths.* In Proceedings of "Planetary Radio Emissions IV" (Graz, 9/1996), pages 101–127, 1997. (Cited on pages 3, 80 and 119.)

[Zarka 1998] P. Zarka. *Auroral radio emissions at the outer planets: Observations and theories.* Journal of Geophysical Research, vol. 103, pages 20159–20194, September 1998. (Cited on page 14.)

[Zarka 2000] P. Zarka. *Radio Emissions from the Planets and their Moons.* Washington DC American Geophysical Union Geophysical Monograph Series, vol. 119, pages 167–178, 2000. (Cited on page 14.)

[Zarka 2001] Philippe Zarka, Rudolf A. Treumann, Boris P. Ryabov and Vladimir B. Ryabov. *Magnetically-Driven Planetary Radio Emissions and Application to Extrasolar Planets.* Astrophysics and Space Science, vol. 277, no. 1-2, pages 293–300, 2001. (Cited on pages 3 and 15.)

[Zarka 2002] Philippe Zarka, Vladimir Ryabov and Boris Ryabov. *Post-detection interference rejection and weak burst detection in time-frequency spectrograms.* URSI, no. 1, 2002. (Cited on page 61.)

[Zarka 2007] Philippe Zarka. *Plasma interactions of exoplanets with their parent star and associated radio emissions.* Planetary and Space Science, vol. 55, no. 1, pages 598–617, 2007. (Cited on pages 15 and 60.)

[Zarka 2015] P. Zarka, J. Lazio and G. Hallinan. *Magnetospheric Radio Emissions from Exoplanets with the SKA.* Advancing Astrophysics with the Square Kilometre Array, page 120, 2015. (Cited on pages iii, 15, 16, 17 and 137.)

Pulsars and transients survey and exoplanet search at low-frequencies with the UTR-2 radio telescope: methods and first results

Abstract: The search and study of transient sources of radio emission, especially at low frequencies, is one of the key projects for the new generation of radio telescopes such as SKA and its precursors among which LOFAR, NenuFAR and GURT. These sources include neutrons stars - producing a rotation modulated signal and detected as pulsars -, other compact highly magnetized objects or very dynamic or explosive events - producing non-periodic transients -, and exoplanets - some of which are expected to emit Jupiter-like decameter-wave radio bursts.
Low-frequency surveys are expected to reveal nearby pulsars "missed" by high-frequency surveys, due to the "unfavorable" orientation of their emission cones, that broaden at low frequencies, and to better characterize the spectrum of pulsars detected at both high and low frequencies. Surveys of non-periodic transients may reveal unique astrophysical phenomena, such as the mysterious extragalactic "fast radio bursts" or their galactic analogs. Radio bursts from the magnetospheres of exoplanets or from exoplanet-star plasma interaction has been theoretically predicted to exist preferably at low frequencies (as Jupiter's decameter-wave radio emission), although none has been detected so far; first detection and subsequent study will result in better understanding of emission processes and unique measurements of exoplanets' magnetic fields, that have implications on their habitability.
The aim of this work was (i) to carry out a survey for sources of transient and pulsed radio emission, and (ii) to attempt to detect radio emission from known exoplanets (discovered from optical measurements), by using the decameter radio telescope UTR-2 in Ukraine in beamformed (phased array) mode. Both topics imply to process large volumes of data, including RFI (Radio Frequency Interference) mitigation, calibration, and detection of low intensity bursts. Thus, I developed generic software tools from which I built an automated processing pipeline for UTR-2 data, that can be easily adapted to other radio telescopes observing in beamformed mode (LOFAR, NenuFAR and GURT).
Keywords: Low-frequency radio astronomy, data analysis, pulsars, transients, exoplanets, sky survey

Recherche de pulsars, transitoires et exoplanètes à basses fréquences avec le radiotélescope UTR-2: méthodes et premiers résultats

Résumé: La recherche et l'étude de sources radio transitoires, en particulier à basses fréquences, est un des projets clés de la nouvelle génération de radiotélescopes comme SKA et ses précurseurs, parmi lesquels LOFAR, NenuFAR et GURT. Ces sources incluent les étoiles à neutrons - produisant un signal périodique, détectées comme pulsars -, d'autres objets très magnétisés compacts ou des événements très dynamiques ou explosifs - produisant des transitoires non périodiques -, et des exoplanètes - dont certaines sont, comme Jupiter, susceptibles d'émettre des sursauts radio décamétriques.

Les "surveys" observations systématiques à basses fréquences peuvent révéler des pulsars proche, "manqués" par les surveys à plus hautes fréquences en raison de l'orientation "défavorable" de leurs cônes d'émission, qui s'élargissent aux basses fréquences. Ils devraient également permettre de mieux caractériser le spectre des pulsars détectés à la fois à hautes et basses fréquences. Les surveys de transitoires non périodiques peuvent révéler des phénomènes astrophysiques uniques, tels que les mystérieux "sursauts radio rapides" d'origine extragalactique ou leurs analogues galactiques. L'existence de sursauts radio produits par les magnétosphères exoplanètaires ou les interactions plasma exoplanète- étoile a été prédite par la théorie, en particulier aux basses fréquences (comme l'émission décamétrique de Jupiter). Mais aucun n'a été détecté jusqu'à présent. La première détection, et les études qui la suivront, ouvriront à une meilleure compréhension des processus d'émission radio et à des mesures uniques des champs magnétiques des exoplanètes, avec des répercussions sur leur habitabilité.

L'objectif de cette thèse était (i) effectuer un survey de sources d'émissions radio pulsées et transitoires, et (ii) tenter de détecter l'émission de radio d'une exoplanètes connue (découverte par mesures optiques), en utilisant le radiotélescope décamètrique UTR-2 en Ukraine, en mode de réseau phasé. Les deux sujets impliquent le traitement de grands volumes de données, avec notamment des étapes d'élimination des RFI (parasites radio), d'étalonnage du signal, et de détection de sursauts faible. J'ai développé des outils logiciels génériques à partir desquels j'ai construit un pipeline de traitement automatisé des données d'UTR-2, qui peut être facilement adapté à d'autres radiotélescopes observant en mode réseau phasé (LOFAR, NenuFAR et GURT).

Mots-clés: Radioastronomie basses fréquences, traitement de données, pulsars, transitoires, exoplanètes, surveys du ciel